VILNIUS UNIVERSITY
CENTER FOR PHYSICAL SCIENCES AND TECHNOLOGY

Tomas
ANDRIJAUSKAS

Artificial Magnetic Field for Ultracold Atoms in Optical Lattices

DOCTORAL DISSERTATION

Physical Sciences,
Physics (02P)

VILNIUS 2018

The dissertation has been developed during the years 2013–2018 in Vilnius University.

Supervisor:

prof. habil. dr. Gediminas Juzeliūnas (Vilnius University, Physical Sciences, Physics – 02P).

Defend council:

Chairman – **prof. habil. dr. Darius Abramavičius** (Vilnius University, Physical Sciences, Physics – 02P).

Members:

dr. Audrius Alkauskas (Center for Physical Sciences and Technology, Physical Sciences, Physics – 02P);

habil. dr. Gediminas Gaigalas (Vilnius University, Physical Sciences, Physics – 02P);

doc. dr. Vygandas Jarutis (Vilnius University, Physical Sciences, Physics – 02P);

prof. dr. Paulius Miškinis (Vilnius Gediminas Technical University, Physical Sciences, Physics – 02P).

Dissertation will be defended in the open session on 28th of September, 2018 at 14 o'clock in auditorium D401 at Center for Physical Sciences and Technology. Address: Saulėtekio av. 3, LT-10257, Vilnius, Lithuania, tel. no. +37052648884; email office@ftmc.lt.

Dissertation will be available for viewing in the Vilnius University Library and Vilnius University webpage:
`https://www.vu.lt/naujienos/ivykiu-kalendorius`

VILNIAUS UNIVERSITETAS
FIZINIŲ IR TECHNOLOGIJOS MOKSLŲ CENTRAS

Tomas
ANDRIJAUSKAS

Dirbtinis magnetinis laukas labai šaltiems atomams optinėse gardelėse

DAKTARO DISERTACIJA

Fiziniai mokslai,
Fizika (02P)

VILNIUS 2018

Disertacija rengta 2013–2018 metais Vilniaus universitete.

Mokslinis vadovas:

prof. habil. dr. Gediminas Juzeliūnas (Vilniaus universitetas, Fiziniai mokslai, Fizika – 02P).

Gynimo taryba:

Pirmininkas – **prof. habil. dr. Darius Abramavičius** (Vilniaus universitetas, fiziniai mokslai, fizika – 02P).

Nariai:

dr. Audrius Alkauskas (Fizinių ir technologijos mokslų centras, fiziniai mokslai, fizika – 02P);

habil. dr. Gediminas Gaigalas (Vilniaus universitetas, fiziniai mokslai, fizika – 02P);

doc. dr. Vygandas Jarutis (Vilniaus universitetas, fiziniai mokslai, fizika – 02P);

prof. dr. Paulius Miškinis (Vilniaus Gedimino technikos universitetas, fiziniai mokslai, fizika – 02P).

Disertacija ginama viešame Gynimo tarybos posėdyje 2018 m. rugsėjo mėn. 28 d. 14 val. Fizinių ir technologijos mokslų centro D401 auditorijoje. Adresas: Saulėtekio al. 3, LT-10257, Vilnius, Lietuva, tel. +37052648884; el. paštas office@ftmc.lt.

Disertaciją galima peržiūrėti Vilniaus universiteto bibliotekoje ir Vilniaus Universiteto interneto svetainėje adresu:
`https://www.vu.lt/naujienos/ivykiu-kalendorius`

CONTENTS

ABBREVIATIONS

BEC	Bose-Einstein condensation
QHE	Quantum Hall effect
FQHE	Fractional quantum Hall effect
BZ	Brillouin zone
FBZ	First Brillouin zone (in the context of dissertation it is the same as BZ)

INTRODUCTION

During the last few decades there were lots of advances in the physics of ultra-cold atoms and quantum optics [1]. Now it is possible to prepare and control ultra-cold atomic gases very precisely. This allows to do precision experiments on the resulting quantum systems. Cooling methods make it possible to decrease a temperature of atomic gases down to the order of nano-Kelving or even less. In 1997 the works in atom cooling and trapping were awarded by the Nobel prize to S. Chu, C. Cohen-Tannoudji and W. D. Phillips [2, 3, 4]. Such success in this field allowed to experimentally observe a Bose-Einstein condensation (BEC) in 1995. Because of this, E. A. Cornell, C. E. Wieman and W. Ketterle were awarded by another Nobel prize in 2001 [5, 6].

Ultra-cold atom systems can be applied to simulate condensed matter phenomena [7, 8, 1]. Moreover, creation of optical lattices for ultra-cold atoms started an experimental study of quantum computers and quantum information that can allow to understand quantum correllations and quantum entanglement more deeply. One of important quantum effects is a phase transition from a superconductor to a Mott insulator [9]. The superconductive phase exhibits very strong quantum correlations while the Mott insulator phase is convenient in quantum computing because of fixed number of atoms in each lattice site. It is possible that the first quantum computers, designed as quantum simulators [10], will be created using ultra-cold atoms in optical lattices.

Quantum computers and quantum simulators could solve some complicated problems that arise in condensed matters and high-energy physics. For the most time it is very difficult to numerically model correllated many-body quantum systems. In such cases quantum simulators may help to save time and money. Some examples of correlated quantum systems are Hubbard and spin models. While the Hubbard model does not approximate the condensed matter well, it can be used to describe ultra-cold atom dynamics in optical lattices. Since there is a big variety of optical lattices, one can construct a lot of different Hubbard models that exhibit many different quantum effects. On the other hand, some of such models simplify to various systems of interacting spins. Because of this, we can use ultra-cold atoms in optical lattices to simulate various spin models and solve related problems in condensed matter physics. Similar spin systems can also be simulated using ultra-cold ions. Since ions have a charge, it is easy to trap and cool them. It is also easy to manipulate and observe them. In addition, it is easy control and change various parameters of both ultra-cold atom and ion systems.

The ultra-cold atoms are usually electrically neutral and the conventional magnetic

field does not affect them in the same way as it affects point charges. Various methods have been used to create artificial magnetic field and simulate two-dimensional systems that exhibit the quantum Hall effect (QHE). One such way is to implement rotating systems [11, 12, 13, 14, 15, 16]. Another way is to create light-induced geometric potentials [17, 18]. Large magnetic fluxes can be created by shaking the lattice potential [19, 20, 21, 22] or implementing a laser-assisted (pseudo-)spin coupling [17, 18, 23, 24, 25, 26, 27, 28, 29].

Since it is possible to create artificial magnetic field for ultra-cold atoms in optical lattices [17], we can use such lattices to explore fractional Hall effect. This effect is already analyzed in two-dimensional systems, but there are still some unanswered questions like how to observe anyon and other correlated states. In optical lattices we can easily observe and explore this effect [30].

In this work we deal with two different aspects of artificial magnetic fields for ultracold atoms in optical lattices. In the first part we describe single-particle physics of ultra-cold atoms in optical lattices that have hexagonal geometry. We briefly describe the famous Haldane model: a two-dimensional hexagonal lattice with broken time-reversal symmetry which leads to a presence of the artificial magnetic field. This model was already experimentally realized [20]. Then we we describe our original work [31] on a three-level extension of the Haldane model. We derive the Bloch quasi-momentum space Hamiltonian, compute it's spectrum and analyze topological properties of the resulting energy bands by calculating Chern numbers for each band.

In the second part of the work we introduce an optical lattice with a different kind of artificial magnetic field which produces non-staggered magnetic flux [32]. We desribe how such optical lattice can be created using the real non-artificial magnetic field gradient and multi-frequency radiation that perturbs ultracold atoms trapped in this system. We also show how topologically rich is the band structure of the introduced optical flux lattice. This novel technique for creating the artificial magnetic field differs from the others we mentioned in the way that it produces stronger magnetic field. This allows to more easily realize the integer QHE. We show how the resulting band structure exhibits a Landau-level like levels with unit Chern numbers. In addition we show a few different topological phases with different distribution of Chern numbers.

Main objective of the thesis

To explore the QHE of two different types of artificial magnetic fields (staggered and non-staggered) for ultracold atoms in optical lattices by describing the dice optical lattice and the optical flux lattice and calculating topological Chern numbers of their energy bands.

Goals and tasks of the work

1. To introduce the dice lattice, a theoretical three-level extension of the two-level Haldane model, by deriving a lattice Hamiltonian in the Bloch quasi-momentum space using tight-binding model.
2. To calculate the band structure of the dice lattice and analyze its topological properties by calculating the topological Chern number for each band.
3. To present a theoretical model of an optical flux lattice created using multi-frequency radiation and develop an effective Hamiltonian using stroboscopic approximation.
4. To calculate the band structure of the resulting flux lattice and analyze its topological properties by calculating the topological Chern number for several lowest energy bands.

Statements to defend

1. The two-level Haldane model can be extended to a three-level model using dice optical lattice by applying the laser-assisted tunneling between the nearest neighbor sites.
2. The extended three-level Haldane-like model produces an easy access to topological semimetal phases and topological bands with Chern numbers higher than one.
3. The optical flux lattice with non-staggered magnetic flux can be realized using two-level atoms trapped in a magnetic gradient and perturbed by a multi-frequency radiation which resonantly couples internal states in different spatial positions.
4. The model of the flux optical lattice created using multi-frequency radiation exhibit topologically rich bands that in some cases resemble Landau levels and in other cases contain Chern numbers higher than one.

Scientific novelty

1. One of the simpliest two-dimensional lattice with artificial magnetic field is the famous Haldane model [33], which is already experimentally implemented [20]. The model produces topologically non-trivial bands that are characterized by non-zero topological invariant Chern number.

2. The Haldane model is essentially a two-level model in the momentum space, because its hexagonal geometry consists of two triangle sub-lattices. In the disertation it is suggested to use the dice geometry, which consists of three triangle sub-lattices. This produces a theoretical three-level analogue of the Haldane model which exhibits rich band topology of Chern numbers that are larger than one in modulus.

3. Optical flux lattices are new types of optical lattices with different type of artificial magnetic field. In conventional optical lattices the artificial magnetic field is usually staggered which means it is nonzero, but its flux over some elementary cell or superlattice cell is zero. In optical flux lattices, the magnetic flux is nonstaggered.

4. Non-staggered magnetic flux in optical flux lattices adds up over lattice cells and resembles uniform magnetic field. In this way optical flux lattices can produce Landau-like levels. In certain cases a set of the lowest bands of the optical flux lattice may exhibit rich topology, described by Chern numbers that are larger than one in modulus.

List of publications

Publications of the doctoral dissertation

1. E. Anisimovas, F. Gerbier, T. Andrijauskas, and N. Goldman, *Design of laser-coupled honeycomb optical lattices supporting Chern insulators*, Physical Review A **89**, 013632 (2014).

2. T. Andrijauskas, E. Anisimovas, M. Račiūnas, A. Mekys, V. Kudriašov, I. B. Spielman, and G. Juzeliūnas, *Three-level Haldane-like model on a dice optical lattice*, Physical Review A **92**, 033617 (2015).

3. Tomas Andrijauskas, I B Spielman and Gediminas Juzeliūnas, *Topological lattice using multi-frequency radiation*, New Journal of Physics **20**, 055001 (2018).

Other publications by the author

1. T. Andrijauskas, A. A. Shylau, and I. V. Zozoulenko, *Thomas-Fermi and Poissons modeling of gate electrostatics in graphene nanoribbon*, Lithuanian Journal of Physics **52**, 63-69 (2012).

2. I. I. Beterov, T. Andrijauskas, D. B. Tretyakov, V. M. Entin, E. A. Yakshina, I. I. Ryabtsev, and S. Bergamini, *Jaynes-Cummings dynamics in mesoscopic ensembles of Rydberg-blockaded atoms*, Physcal Review A **90**, 043413 (2014).

3. J. Ruseckas, V. Kudriašov, A. Mekys, T. Andrijauskas, Ite A. Yu and G. Juzeliūnas, *Nonlinear quantum optics for spinor slow light*, Physical Review A **98**, 013846 (2018).

International conferences attended by the author

1. G. Juzeliūnas, T. Andrijauskas, C. Wu, M. Lewenstein, *Many-body effects for cold atoms in line-centered lattices*, 75th Annual Meeting of the DPG and DPG Spring Meeting, Dresden, Germany, 2011 March 13-18 (poster).

2. T. Andrijauskas, G. Juzeliūnas, C. Wu, M. Lewenstein, *Line-Centered Square Optical Lattices: Many Body Effects*, Quantum Technologies Conference II, Manipulating photons, atoms, and molecules, Krakow, Poland, 2011 August 30 - September 4 (oral presentation).

3. Tomas Andrijauskas, Gediminas Juzeliūnas, Matteo Rizzi, Maciej Lewenstein, *Analysis of Band structure for Lieb and s-p optical lattices*, Advanced Materials and Technologies, 14th Internation Conference-School, Palanga, Lithuania, 2012 August 27-31 (poster).

4. T. Andrijauskas, E. Anisimovas, N. Goldman, G. Juzeliūnas, *Topological properties of band structure of coupled honeycomb and triangle optical lattices*, Advanced Materials and Technologies, 15th International Conference-School, Palanga, Lithuania, 2013 August 27-31 (poster).

5. T. Andrijauskas, E. Anisimovas, N. Goldman, G. Juzeliūnas, *Topological properties of band structure of complex optical lattices*, Quantum Technologies Conference IV, Manipulating photons, atoms, and molecules, Warsaw, Poland, 2013 September 15-20 (oral presentation).

6. E. Anisimovas, F. Gerbier, T. Andrijauskas, N. Goldman, *Design of laser-coupled honeycomb optical lattices supporting Chern insulators*, BEC 2014:

Quantum Gases and Quantum Coherence, Trento, Italy, 2014 May 28-31 (poster).

7. T. Andrijauskas, G. Juzeliūnas, *Flux lattices for periodically driven ultra-cold atoms*, Advanced Materials and Technologies, 16th International Conference-School, Palanga, Lithuania, 2014 August 27-31 (poster).

8. T. Andrijauskas, G. Juzeliūnas, *Flux lattices for periodically driven ultra-cold atoms*, Quantum Technologies Conference V, Manipulating photons, atoms, and molecules, Krakow, Poland, 2014 September 7-13 (oral presentation).

9. T. Andrijauskas, *Dice optical lattice and Haldane-like model for quasi-spin-1*, 17th Symposium on Topological Quantum Information, Munich, Germany, 2015 April 16-17 (poster).

10. T. Andrijauskas, G. Juzeliūnas, I. B. Spielman, *Creating optical flux lattice using multi-frequency radiation*, Atomic Physics, Gordon Research Conference, From Ultracold to Strongly Interacting Quantum Systems, Newport RI, JAV, 2015 June 14-19 (poster).

11. T. Andrijauskas, G. Juzeliūnas, I. B. Spielman, *Optical flux lattice using multi-frequency radiation*, EGAS, 47th Conference of the European Group on Atomic Systems, Ryga, Latvia, 2015 July 14-17 (poster).

12. T. Andrijauskas, G. Juzeliūnas, I. B. Spielman, *Optical flux lattice using multi-frequency radiation*, Synthetic Quantum Magnetism, International Workshop, Dresden, Germany, 2015 August 31 – September 4 (poster).

13. Tomas Andrijauskas, Ian B. Spielman, Gediminas Juzeliunas, *Topological properties of optical flux lattice created with multi-frequency radiation*, Quantum Technologies Conference VII, Manipulating photons, atoms, and molecules, Warsaw, Poland, 2016 September 20-25 (oral presentation).

14. T. Andrijauskas, I. B. Spielman and G. Juzeliūnas, *Topological flux lattice from multi-frequency radiation*, Humboldt Kolleg, Controlling quantum matter: From ultracold atoms to solids, Vilnius, 2018 July 29 – August 2 (poster).

Local conferences attended by the author

1. T. Andrijauskas, A. Shylau, I. V. Zozoulenko, *Elektronų tarpusavio sąveikos įtaka Anderson'o lokalizacijai grafeno juostelėje*, Lietuvos Nacionalinė fizikos konferencija LNFK-39, Vilnius, 2011 October 6-8 (poster).

2. T. Andrijauskas, E. Anisimovas, N. Goldman, G. Juzeliūnas, *Topological properties of band structure of T3 optical lattice*, Open Readings, 56th Scientific Conference for Young Students of Physics and Natural Sciences, Vilnius, 2013 March 20-23 (oral presentation).

3. I.I. Beterov, T. Andrijauskas, D. B. Tretyakov, V. M. Entin, E. Y. Yakshina, I. I. Ryabtsev, S. Bergamini, *Simulating Jaynes-Cummings Dynamics in Mesoscopic Ensembles of Interacting Atoms*, Open Readings, 57th Scientific Conference for Young Students of Physics and Natural Sciences, Vilnius, 2014 March 19-21 (oral presentation).

4. T. Andrijauskas, E. Anisimovas, M. Račiūnas, A. Mekys, V. Kurdiašov, I. B. Spielman, G. Juzeliūnas, *Dice optinė gardelė ir Haldane tipo modelis trijų lygmenų sistemai*, Penktoji jaunųjų mokslininkų konferencija, Fizinių ir technologijos mokslų tarpdalykiniai tyrimai, Vilnius, 2015 February 10 (oral presentation).

Personal contribution of the author

Author of the thesis has performed all the analytical analysis and numerical calculations. Author developed and used all computer programs needed for numerical analysis. Author wrote the whole text of this dissertation and created all the figures. This excludes dissertation publications that are attached at the end of the dissertation.

Acknowledgements

I am very grateful to my supervisor, Prof. Habil. Dr. Gediminas Juzeliūnas for invaluable discussions and guidance.

I am also grateful to Prof. Dr. Egidijus Anisimovas, Dr. Julius Ruseckas for great discussions that helped me to do the analytical and numerical calculations for this work.

1 REVIEW OF OPTICAL LATTICES AND ARTIFICIAL MAGNETIC FIELDS

1.1 Review of literature

Let us review various literature on a physics of ultracold atoms in optical lattices and artificial magnetic fields. The physics of ultracold atoms in optical lattices and the most important research that was made in this area are best presented in the review article by M. Lewenstein *et. al.* [1] and in the book *Ultracold Atoms in Optical Lattices* by M. Lewenstein *et. al.* [34]. More specifically, the physics of artificial magnetic fields for ultracold atoms are presented in a review article by J. Dalibard *et. al.* [17]. Here we summarize the main literature that is cited in the identified sources and review the various phenomena that ultracold atoms in optical lattices exhibit and developments that were made in this area of physics.

Over the last 20-25 years there were several important discoveries in quantum optics and atomic physics that revoliutionized the science of ultracold atoms. Over the years researchers in quantum optics and atomic physics reached a high levels in quantum engineering – preparation, manipulation, control and detection of quantum systems. Cooling of atoms have reached a level of very low temperatures and precision. Because of the developments in the laser cooling of atoms S. Chu [2], C. Cohen-Tannoudji [3] and W. D. Phillips [4] were awarded the Nobel Prize in 1997. Such achievements allowed to experimentally observe Bose-Einstein condensation (BEC) in 1995 [35, 36]. In 2001 E. A. Cornell and C. E. Wieman [5] and W. Ketterle [6] received the Nobel Prize for the successful Bose-Einstein condensation in dilute gases of akali atoms.

In addition to the mentioned experimental research there was a lot of theoretical research, such as the proposals of quantum cryptography [37], quantum communication [38, 39], quantum computer [40] and discovery of the quantum factorizing algorithm [41]. These works motivated experimental studies of quantum information [42].

The combinations of the experimental studies of quantum optics and atomic physics and theoretical and experimental studies of quantum information let to massive progress in the research of quantum correlations and quantum entanglement. A part of experimental and theoretical research of cold atoms, molecules and ions focused to quantum information and quantum simulators – quantum computers that have a purpose of simulating quantum many body systems that cannot be simulated using conventional classical computers [10].

The physics of ultracold atoms now study various interesting phenomena that mimick condensed matter physics. There are many specific directions of study such as 1D systems [43, 44, 45], spin-boson model [46, 47], 2D systems [48], Hubbard and spin models [49, 50, 51, 52, 53, 54, 55], spin glasses [56, 57, 58, 59], large effects induced by small disorder [60], high T_c superconductivity [50, 61, 62, 63], frustrated antiferromagnets and spin liquids [64, 65, 66], systems with higher spins [67, 68, 69], fractional quantum Hall effect (FQHE) [70, 71, 72, 73, 74, 75, 76] and lattice gauge fields [77, 29, 78, 79].

For the basics of quantum optics and atom optics the books Introduction to *Quantum Optics, From the Semi-classical Approach to Quantized Light* by Gilbert Grynberg *et. al.* [80], *Elements of Quantum Optics* by Pierre Meystre and Murray Sargent III [81], *Atom Optics* by Pierre Meystre [82] and *Quantum Optics* by Werner Vogel and Dirk-Gunnar Welsch [83] are recommended. For the review of Bose-Einstein Condensation the book *Bose-Einstein Condensation* by Lev Pitaevski and Sandro Stringari [84] is recommended.

1.2 Forces acting on ultracold atoms

Before talking about ultra-cold atoms in optical lattices and how an artificial magnetic field is created for them, we need to understand how atomic gases are cooled down and how atoms in such gases are manipulated. We begin with a simple model of a two-level atom in electromagnetic field. We will describe what forces act on such atom and how they can be used to create optical lattice – a spatially periodic potential.

A general Hamiltonian of a two-level atom in electromagnetic field consists of three terms [82]:

$$H = H_{\mathrm{A}} + H_{\mathrm{F}} + H_{\mathrm{AF}}. \tag{1.1}$$

Here the first term H_{A} describes a center of mass motion and internal levels of the atom. Let us denote the ground internal state by $|g\rangle$ and the excited internal state by $|e\rangle$. If we fix the ground state level energy to zero, then H_{atom} is explicitly written as

$$H_{\mathrm{A}} = \frac{\boldsymbol{p}^2}{2M} + \hbar\omega_0 |e\rangle\langle e|.$$

Here $\boldsymbol{p}$ is atomic momentum, M is mass. $\hbar\omega$ is energy of the excited state $|e\rangle$.

The second term H_{F} describes the electromagnetic (EM) field. Usually this term is

expressed in creation and annihilation operators:

$$H_{\mathrm{F}} = \sum_{\boldsymbol{k},\epsilon} \hbar\omega_{\boldsymbol{k},\epsilon} a^{\dagger}_{\boldsymbol{k},\epsilon} a_{\boldsymbol{k},\epsilon}.$$

Here we sum over all modes of the electromagnetic field that are numbered by the wavelength $\boldsymbol{k}$ and polarization ϵ. In ultra-cold atom systems one or more EM modes are filled up macroscopically, so they are treated clasically. Because of this we split H_{F} into two parts:

$$H_{\mathrm{F}} = H_{\mathrm{L}} + H_{\mathrm{R}}.$$

Here H_{L} describes the classical EM field while H_{R} consists of all other modes.

The third term H_{AF} describes interaction between the atom and EM field. We use electric dipole approximation and express it as

$$H_{\mathrm{AF}} = -\boldsymbol{d} \cdot \hat{\boldsymbol{E}}(\boldsymbol{r}, t). \tag{1.2}$$

Here $\boldsymbol{d}$ is the electric dipole moment of the atom,

$$\boldsymbol{d} = d\boldsymbol{e}_{\zeta} \left(|e\rangle\langle g| + |g\rangle\langle e| \right). \tag{1.3}$$

The vector $\boldsymbol{e}_{\zeta}$ points along axis of the dipole.

Ultra-cold atoms are usually manipulated by monochormatic electromagnetics fields created by lasers. The classical electric field of such lasers is written as

$$\boldsymbol{E}_{\mathrm{L}}(\boldsymbol{r}, t) = \boldsymbol{e}_{\epsilon}(\boldsymbol{r}) \mathcal{E}(\boldsymbol{r}) \cos\left[\omega t - \Phi(\boldsymbol{r})\right]. \tag{1.4}$$

Here ω is the electromagnetic field frequency, $\boldsymbol{e}_{\epsilon}(\boldsymbol{r})$ is poloarization vector, $\mathcal{E}(\boldsymbol{r})$ is slowly varying field amplitude and $\Phi(\boldsymbol{r})$ is phase. In a long-wavelength approximation we treat the atom as a point particle and the radius-vector $\boldsymbol{r}$ in (1.2) and (1.4) points to the atom center of mass position.

We split the interaction term H_{AF} into two terms in the same way as we did with the H_{F}:

$$H_{\mathrm{AF}} = H_{\mathrm{AL}} + H_{\mathrm{AR}}. \tag{1.5}$$

The first term H_{AL} describes the dipole interaction with the classical electromagnetic field. In the long-wavelength approximation the electric field operator $\hat{\boldsymbol{E}}(\boldsymbol{r}, t)$ in (1.2) is the classical field $\boldsymbol{E}_{\mathrm{L}}(\boldsymbol{r}, t)$ expressed in (1.4). By substituting (1.4) to (1.2) we get the explicit expression of H_{AL}:

$$H_{\mathrm{AL}} = \hbar\Omega_{\mathrm{R}}(\boldsymbol{r}) \left\{ \cos\left[\omega t - \Phi(\boldsymbol{r})\right] |e\rangle\langle g| + \text{H. c.} \right\}. \tag{1.6}$$

Here "H. c." denotes the Hermitian-conjugate expression of the first term in the sum inside the parentheses "{}". In (1.6) we introduced Rabi frequency:

$$\Omega_{\mathrm{R}}(\boldsymbol{r}) = -d\left[\boldsymbol{e}_\zeta \cdot \boldsymbol{e}_\epsilon(\boldsymbol{r})\right] \frac{\mathcal{E}(\boldsymbol{r})}{\hbar}. \tag{1.7}$$

This quantity measures interaction strength between the atom and the classical electromagnetic field.

The second term H_{AR} in (1.5) couples the internal atomic states with other modes of the electromagentic field, that are not filled up. This term describes the spontaneous emission of photons from the atom. Usually, this effect is included via phenomenological parameter, a spontaneous emission rate Γ.

Let us explore the quantum mechanical motion of the described tow-level atom in the given electromagnetic field using Heisenberg's equation of motion for the momentum operator $\boldsymbol{p}$:

$$\frac{\mathrm{d}\boldsymbol{p}}{\mathrm{d}t} = \frac{1}{\mathrm{i}\hbar}\left[\boldsymbol{p},\, H_{\mathrm{A}} + H_{\mathrm{AL}}\right]. \tag{1.8}$$

We calculate an average force $\boldsymbol{F}$ acting on the atom as the expectation value of (1.8):

$$\boldsymbol{F} = \left\langle \frac{\mathrm{d}\boldsymbol{p}}{\mathrm{d}t} \right\rangle. \tag{1.9}$$

Following [82] we find that in the end there are the two most important forces acting on the atom: the dissipative force $\boldsymbol{F}_{\mathrm{dissip}}$ and the reactive force $\boldsymbol{F}_{\mathrm{react}}$:

$$\boldsymbol{F}_{\mathrm{dissip}} = \hbar \boldsymbol{k}_{\mathrm{L}} \frac{\Gamma}{2} \frac{\Omega_{\mathrm{R}}^2/2}{\delta^2 + (\Gamma/2)^2 + \Omega_{\mathrm{R}}^2/2}, \tag{1.10}$$

$$\boldsymbol{F}_{\mathrm{react}} = -\frac{\hbar\delta}{2} \frac{\nabla\left(\Omega_{\mathrm{R}}^2\right)}{\delta^2 + (\Gamma/2)^2 + \Omega_{\mathrm{R}}^2/2}. \tag{1.11}$$

Here δ is detuning of the electromagnetic frequency from the resonant frequency ω_0 of the internal atomic states:

$$\delta = \omega - \omega_0. \tag{1.12}$$

The $\boldsymbol{k}_{\mathrm{L}}$ present in the dissipative force $\boldsymbol{F}_{\mathrm{dissip}}$ is the wavevector of the plane wave (1.4). Here effects of H_{AR} are indirectly included via the spontaneous emission rate Γ.

The dissipative force $\boldsymbol{F}_{\mathrm{dissip}}$ is responsible of electromagnetic pressure which decreases the kinetic energy of the atom. This force has important role in cooling processes. The dipole force $\boldsymbol{F}_{\mathrm{react}}$ is important in description of optical atom traps and creation of optical lattices, because it is proportional to the gradient $\nabla(\Omega_{\mathrm{R}}^2)$ and is non-zero only if the Rabi frequency Ω_{R} and subsequently the electric field

intensity $I \propto \Omega_{\mathrm{R}}^2$ vary in the space.

1.3 Cooling of atomic gases

Here we briefly describe the two most important methods of cooling of atomic gases: the Doppler cooling and the evaporative cooling. The first method is usually used in the beginning of a cooling process. The second is used in the end. Other cooling methods are described in [3, 82].

Let us consider an atom moving with a velocity $\boldsymbol{v}_0$ in the following field of a monochromatic electromagnetic wave, created by a laser:

$$\boldsymbol{E}(\boldsymbol{r}, t) = \boldsymbol{e}_\epsilon \mathcal{E} \cos\left(\omega t - \boldsymbol{k} \cdot \boldsymbol{r}\right). \tag{1.13}$$

In the long-wavelength approximation we insert the center of atom mass and get

$$\boldsymbol{E}(\boldsymbol{r}, t) = \boldsymbol{e}_\epsilon \mathcal{E} \cos\left[(\omega - \omega_{\mathrm{D}})t\right]. \tag{1.14}$$

Here $\boldsymbol{k} \cdot \boldsymbol{r} = \boldsymbol{k} \cdot \boldsymbol{v}_0 t = \omega_{\mathrm{D}} t$ and ω_{D} describes the frequency shift which is a result of the Doppler effect. The detuning δ changes to $\delta_{\mathrm{D}} = \delta - \omega_{\mathrm{D}}$. If the atom moves in the opposite direction than the electromagnetic wave, it experiences larger electromagnetic field frequency. If the atom moves in the same direction as the electromagnetic wave, it experiences the opposite effect.

Suppose that the laser is red-detuned ($\delta < 0$). Then slower atoms in the atomic gas cloud that move in the opposite direction to the electromagnetic wave experience the wave with the frequency which is close to the resonance frequency ω_0. Faster atoms will experience the wave which has a frequency further from the resonance. Because of this the atoms that move in the opposite direction to the wave are slowed down more than the atoms that move in the same direction to the wave. In this way we can slow down the atoms by combining two counter-propagating waves that both are red-detuned. For weak electromagnetic waves, the dissipative force $\boldsymbol{F}_{\mathrm{dissip}}$ simplifies [82]:

$$\boldsymbol{F}_{\mathrm{Doppler}} \approx -2\mu v_0. \tag{1.15}$$

Here μ is the resulting friction coefficient.

There is a temperature limit of the Doppler cooling because of spontanaeus emission of other atoms in the atomic cloud. The limit depends on a type of atoms. For alkali atoms this limit is of the order of several hundreds of micro-Kelvins. In order to cool the atomic cloud further other methods must be applied.

In the end of a cooling process one usually employs the evaporative cooling. The idea of such cooling is very simple: the trap barrier is lowered for a certain amount of time and the atoms with higher kinetic energy simply evaporate away. This process allows to decrease the atomic cloud temperature down to the order of nano-Kelvins.

1.4 Magnetic and optical traps

Almost all atomic gases in low enough temperatures make a phase transition to a solid state. The exception is helium, which stays in a liquid phase if we decrease a temperature while maintaining pressure. It may look that ultra-cold gases should not exist. However, we should mention that the transition to the solid state happens mostly because of three-body interactions [84]. If we decrease the density of atomic gases enough (to $10^{13} - 10^{15}\,\mathrm{cm}^{-3}$), then we also decrease a chance of three-body collisions to happen. In this way we can maintain a gas state. In order to reach quantum regime, the temperature needs to be very low (about of an order of 10^{-6} kelvins). In addition, the atomic gas cloud must be separated from other materials, because the atoms from the cloud may collide with the atoms of other materials and cause a phase transition from gas to solid state. Polarization of atom spins also helps to maintain the gas phase, because this increases repulsive interaction between the atoms.

We can satisfy mentioned requirements by collecting and cooling down low-density atomic gases with polarized spins inside a magnetic and/or optical traps. Such systems are long-lived (usually about several seconds before evaporating away from the trap or condensint into the solid state) compared to an average time between two-body collisitions that allow the temperature to distribute evenly in the atomic cloud.

Magnetic traps work because of Zeeman effect. In order to understand how they work, let us consider Alkali atoms. These types of atoms have only a single outermost electron. In the ground state, the projection of the full electron angular momentum $\boldsymbol{J}$ to the z axis is $1/2$. Then we can categorize such atoms into two groups according to their nuclear angular momentum. Any alkali atom has an odd number of protons. If such atom also has an odd number of neutrons, then it is a fermion. Otherwise it is a boson. The full atomic angular momentum is $\boldsymbol{F} = \boldsymbol{I} + \boldsymbol{J}$. Depending on $\boldsymbol{I}$, the projection values of $\boldsymbol{F}$ are $F = I \pm 1/2$. If there are no magnetic field, a degeneracy between both hyperfine levels is eliminated by interaction between electron angular momentum and nuclear angular momentum:

$$H_{\mathrm{hf}} = a\boldsymbol{I} \cdot \boldsymbol{J}.$$

Here a is an interaction strength.

In the presence of a magnetic field $\boldsymbol{B} = B\boldsymbol{e}_z$ we include additional term:

$$H_{\text{hf}} = a\boldsymbol{I} \cdot \boldsymbol{J} + 2\mu_B J_z B.$$

This term splits each hyperfine energy level into a several sub-levels depending on the nuclear angular momentum $\boldsymbol{I}$. Here μ_B is Bohr's magneton. For example, for ^{23}Na and ^{87}Rb, the nuclear angular momentum is $I = 3/2$ and both hyperfine levels split into 8 sub-levels: two levels with $m_F = \pm 2$ and two levels each for $m = -1, 0, 1$. In the limit of very strong magnetic field the splitted levels approach two levels $E = \pm\mu_B B$. Moreover, the interaction between the atoms in different hyperfine levels can be different and this allows to create many different interacting ultra-cold atomic systems.

A magnetic trap is created by using a magnetic field $\boldsymbol{B}(\boldsymbol{r})$ which varies spatially. In a situation when the adiabatic approximation holds – when the moving atom stays in the same internal state – the total energy of the atom depends on the magnetic field. If the atoms have lower energy where the magnetic field is stronger, they will move to the direction of the increasing magnetic field. If the atoms have lower energy where the magnetic field is lower, they will move to the direction of the decreasing magnetic field. From Maxwell's equations we know that it is impossible to create a static magnetic field with a maximum, so we are left with the second choice. The magnetic trap contains only the atoms that are in such internal state that they move to the direction of the decreasing magnetic field. For ^{23}Na and ^{87}Rb the internal states are $F = 2$, $m_F = +2, +1$ and $F = 1$, $m_F = -1$.

Another type of atom trap is the optical trap. The reactive force $\boldsymbol{F}_{\text{react}}$ in (1.11) can be expressed as a gradient of a potential function $V_{\text{eff}}(\boldsymbol{r})$:

$$\begin{aligned} \boldsymbol{F}_{\text{react}}(\boldsymbol{r}) &= -\nabla V_{\text{eff}}(\boldsymbol{r}), \\ V_{\text{eff}}(\boldsymbol{r}) &= \frac{\hbar\delta}{2} \ln\left(1 + \frac{\Omega_{\text{R}}^2/2}{\delta^2 + (\Gamma/2)^2}\right). \end{aligned}$$

The effective potential $V_{\text{eff}}(\boldsymbol{r})$ is a result of electromagnetic field of a laser.

Observe that for a small Rabi frequency, the effective potential is approximately proportional to Ω_{R}^2 and as a consequence it is proportional to the intensity of the electromagnetic field:

$$V_{\text{eff}}(\boldsymbol{r}) \propto |\mathcal{E}(\boldsymbol{r})|^2 .$$

If the laser is red-detuned ($\delta < 0$), the atom will have lower potential energy where the electromagnetic field intensity is higher. If the laser is blue-detuned ($\delta > 0$),

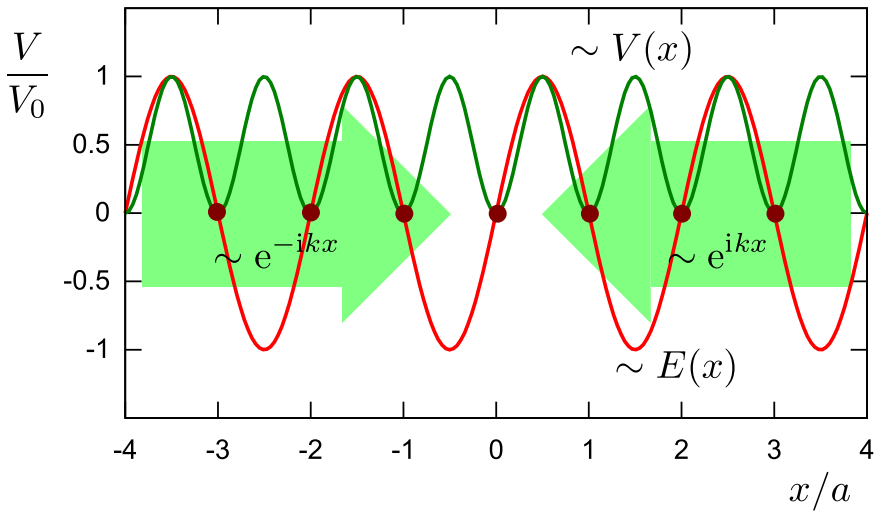

Figure 1.1: A simple one-dimensional optical lattice, created from two counter-propagating lasers. The green line is the potential $V(\boldsymbol{r})$ which is proportional to the intensity of the electromagnetic field of the resulting standing wave. Here V_0 is a maximum of the potential, $a = \pi/k_\mathrm{L}$ is the lattice constant. The red line is the electric field value of the created standing wave at some specific time moment.

the atoms will experience lower potential energy where the intensity is lower. The effective potential then can be expressed as

$$V_\mathrm{eff}(\boldsymbol{r}) = \mathrm{sgn}(\delta) V(\boldsymbol{r}) = \pm V(\boldsymbol{r}).$$

Here $V(\boldsymbol{r})$ is a dipole potential – a positive function, proportional to the electromagnetic field intensity. The effective potential $V_\mathrm{eff}(\boldsymbol{r})$ is then either $V(\boldsymbol{r})$ or $-V(\boldsymbol{r})$ depending on the sign of the detuning δ.

The optical trap is created by using red-detuned laser. The lasers, used in ultra-cold atom laboratories, have a Gaussian profile and the atoms will move to the where the laser has the maximum intensity. In this way, using one or more overlapping lasers we can contain atoms in a specific region of space. Usually the optical traps are stronger than magnetic ones.

1.5 Optical lattices

Since the created optical potential $V(\boldsymbol{r})$ is proportional to the intensity of the electric field $|\mathcal{E}(\boldsymbol{r})|^2$ we can now create simple periodic potentials by using standing waves. For example two counter-propagating waves produces the potential which is proportional to

$$\mathcal{E}^2 \left| \mathrm{e}^{\mathrm{i}(\omega t - k_\mathrm{L} x)} + \mathrm{e}^{\mathrm{i}(\omega t + k_\mathrm{L} x + \phi)} \right|^2 .$$

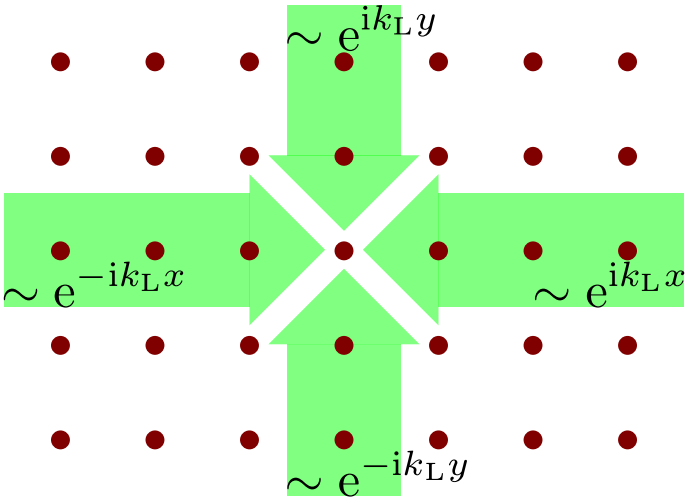

Figure 1.2: Square optical lattice

Then the potential $V(\boldsymbol{r})$ is expressed as

$$V(\boldsymbol{r}) = V_0 \sin^2\left(k_L x + \frac{\phi}{2}\right). \tag{1.16}$$

Here ϕ is a possible phase difference between the counter-propagating waves. Such periodic potential is presented in the fig. 1.1 and describes a one-dimensional optical lattice with a lattice constant $a = \pi/k_L$.

A simple two-dimensional square lattice is created by using two pairs of counter-propagating waves that are perpendicular to each other. In this case the produced optical potential is

$$V(\boldsymbol{r}) = V_0 \left[\sin^2(k_L x) + \sin^2(k_L y)\right]. \tag{1.17}$$

Such form of two-dimensional potential is corrent in case the is a slight frequency difference between two standing waves, so the fast-varying interference term can be ignored.

In order to create a simle hexagonal or triangle lattice, we can use three lasers with wavevectors (see fig. 1.3):

$$\boldsymbol{k}_1 = -\frac{k_L}{2}(\boldsymbol{e}_x + \sqrt{3}\boldsymbol{e}_y), \quad \boldsymbol{k}_2 = \frac{k_L}{2}(\boldsymbol{e}_x - \sqrt{3}\boldsymbol{e}_y), \quad \boldsymbol{k}_3 = k_L \boldsymbol{e}_y.$$

The total electric field is

$$\boldsymbol{E}(\boldsymbol{r}, t) = \boldsymbol{e}_z E_0 \sum_{j=1}^{3} \exp\left[\mathrm{i}\left(\boldsymbol{k}_j \cdot \boldsymbol{r} - \omega t + \phi_j\right)\right].$$

Here the lasers are linearly polarized along the z dimension. We can make a simple

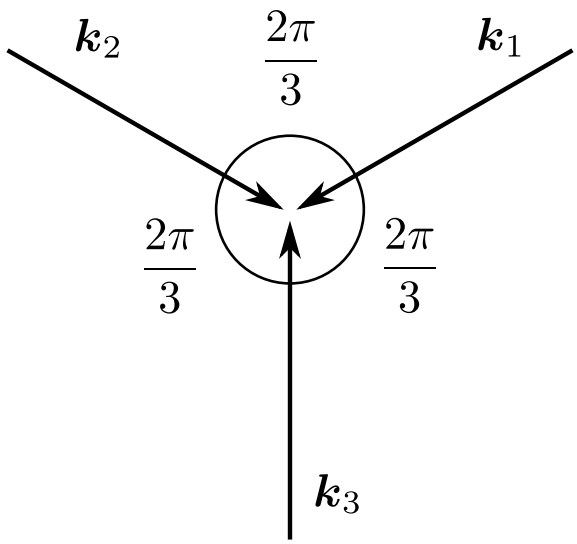

Figure 1.3: Laser beams configuration when creating a hexagonal or triangle optical lattice. The sum of the wavevectors $\boldsymbol{k}_1$, $\boldsymbol{k}_2$ and $\boldsymbol{k}_3$ is zero.

translation in space and time and eliminate the phases ϕ_j. The resulting effective dipole potential has a form

$$V(\boldsymbol{r}) = V_0 v(\boldsymbol{r}) = V_0 |f(\boldsymbol{r})|^2 \propto |\boldsymbol{E}(\boldsymbol{r}, t)|^2. \tag{1.18}$$

Here

$$\begin{aligned} f(\boldsymbol{r}) &= 1 + \exp\left(\mathrm{i}\boldsymbol{b}_1 \cdot \boldsymbol{r}\right) + \exp\left[\mathrm{i}\left(\boldsymbol{b}_1 + \boldsymbol{b}_2\right) \cdot \boldsymbol{r}\right], \\ v(\boldsymbol{r}) &= 3 + 2\cos\left(\boldsymbol{b}_1 \cdot \boldsymbol{r}\right) + 2\cos\left(\boldsymbol{b}_2 \cdot \boldsymbol{r}\right) + 2\cos\left[\left(\boldsymbol{b}_1 + \boldsymbol{b}_2\right) \cdot \boldsymbol{r}\right] \end{aligned}$$

and

$$\boldsymbol{k}_2 - \boldsymbol{k}_1 = \boldsymbol{b}_1 + \boldsymbol{b}_2, \quad \boldsymbol{k}_3 - \boldsymbol{k}_1 = \boldsymbol{b}_1.$$

The created dipole potential for the hexagonal/triangle lattice is presented in fig. 1.4. The effective potential $V_{\text{eff}}(\boldsymbol{r}) = \pm V(\boldsymbol{r})$ describes either the hexagonal lattice or the triangle lattice. If the lasers are red-detuned, then we get the triangle lattice, $V_{\text{eff}}(\boldsymbol{r}) = -V(\boldsymbol{r})$. If the lasers are blue-detuned, we get the hexagonal lattice, $V_{\text{eff}}(\boldsymbol{r}) = V(\boldsymbol{r})$.

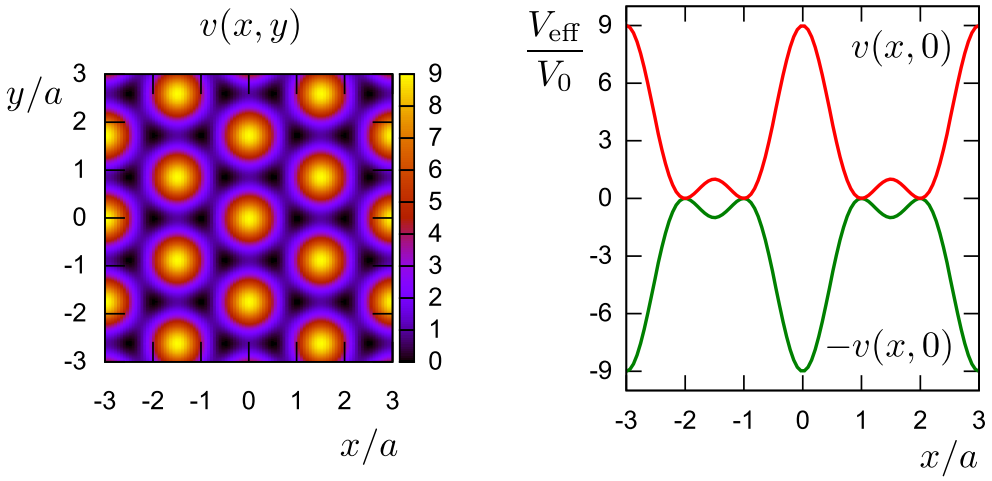

Figure 1.4: Optical potential for a hexagonal or triangle lattice. *Left*: the dipole potential $v(\boldsymbol{r})$. *Right*: effective lattice potential along the line $y = 0$. If the laser is red-detuned ($\delta < 0$), then $V_{\text{eff}}(\boldsymbol{r}) = -V_0 v(\boldsymbol{r})$ and we get the triangle lattice. If the laser is blue-detuned ($\delta > 0$), then $V_{\text{eff}}(\boldsymbol{r}) = V_0 v(\boldsymbol{r})$ and we get the hexagonal lattice.

2 CALCULATION METHODS AND ANALYSIS USED IN THIS WORK

2.1 Periodic quantum systems

2.1.1 General eigenproblem and Bloch states

The first step in any quantum mechanical problem is to find relevant eigenvalues and eigenstates of a Hamiltonian of a quantum system. In other words, the first step is to solve the stationary Schrodinger's equation (SE):

$$H\psi = E\psi. \tag{2.1}$$

Here H is the Hamiltonian – the quantum mechanical energy operator of a quantum system. Usually, for periodic quantum systems, one starts with a single-particle problem and then moves to many-body problems. In this work we explore only single-particle effects in two-dimensional systems. We will describe the analytic and numeric methods to explore such systems in great detail. In this way this chapter will also act as a great reference of solution methods for similar quantum problems.

A quantum mechanical particle in a periodic system – either an electron in a solid state or an ultra-cold atom in optical lattice – is described by a Hamiltonian which

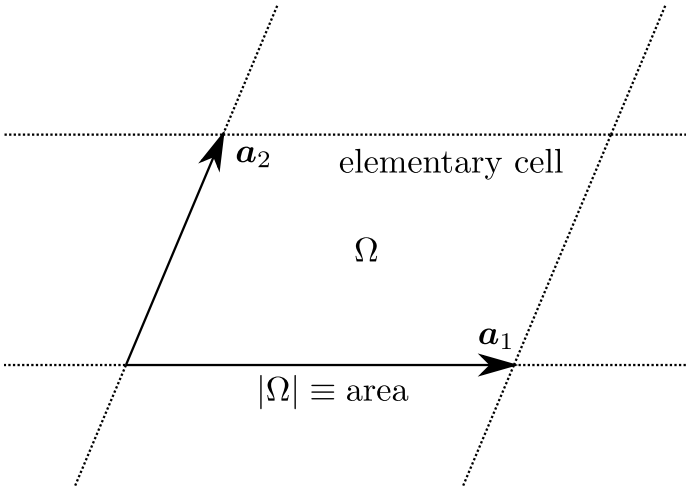

Figure 2.1: General 2D elementary cell: a region in $\mathbb{R}^2$ bounded by the parallelogram made from the elementary lattice vectors $\boldsymbol{a}_1$ and $\boldsymbol{a}_2$. The cell is denoted by Ω, its area by $|\Omega|$ and the integration element by $\mathrm{d}\Omega$.

includes kinetic and potential energy. In the coordinate representation it has a form

$$H = -\frac{\hbar^2}{2m}\nabla^2 + V. \tag{2.2}$$

Here $\hbar$ is the reduced Planck's constant, M is particle's mass, ∇^2 is the 2D laplacian, $\boldsymbol{r} \in \mathbb{R}^2$ is a 2D radius-vector, which is a position of an electron in a solid or a center of mass of an ultra-cold atom in an optical lattice. V is a potential which is periodic with respect to a lattice vector $\boldsymbol{r_n}$, $V(\boldsymbol{r} + \boldsymbol{r_n}) = V(\boldsymbol{r})$. The general lattice vector $\boldsymbol{r_n} \in \mathbb{R}^2$ is expressed in the elementary lattice vectors $\boldsymbol{a}_1, \boldsymbol{a}_2 \in \mathbb{R}^2$ as

$$\boldsymbol{r_n} = n_1\boldsymbol{a}_1 + n_2\boldsymbol{a}_2. \tag{2.3}$$

Here $\boldsymbol{n}$ denotes two integer indices, $\boldsymbol{n} \equiv (n_1, n_2)$, $n_1, n_2 \in \mathbb{Z}$. The region bounded by the parallelogram made from the elementary lattice vectors $\boldsymbol{a}_1$ and $\boldsymbol{a}_2$ is called the elementary cell and is denoted by Ω (see fig. 2.1). Its area is denoted by

$$|\Omega| := \int_\Omega \mathrm{d}\Omega = |\boldsymbol{a}_1 \times \boldsymbol{a}_2|. \tag{2.4}$$

Here $\mathrm{d}\Omega$ is the integration element inside the elementary cell Ω. The area $|\Omega|$ in (2.4) is expressed as the integral of unit function over the whole elementary cell.

Let us introduce a reciprocal lattice vector

$$\boldsymbol{G} = m_1\boldsymbol{b}_1 + m_2\boldsymbol{b}_2. \tag{2.5}$$

Here $\boldsymbol{b}_1, \boldsymbol{b}_2 \in \mathbb{R}^2$ are elementary reciprocal lattice vectors, that satisfy

$$\boldsymbol{b}_i \cdot \boldsymbol{a}_j = 2\pi\delta_{ij}, \qquad i, j = 1, 2. \tag{2.6}$$

Note that we don't put an index $\boldsymbol{m} \equiv (m_1, m_2)$ to the reciprocal vector $\boldsymbol{G}$, because we don't use the symbol $\boldsymbol{G}$ for other quantities and there are no such ambiguity as with the vectors $\boldsymbol{r}$ and $\boldsymbol{r_n}$. From eq. (2.6) we get convenient identity, which we will use later: $\exp(\boldsymbol{G} \cdot \boldsymbol{r_n}) = 1$.

The eigenvalue equation of the presented Hamiltonian is explicitly written as

$$-\frac{\hbar^2}{2m}\nabla^2\psi + V\psi = E\psi. \tag{2.7}$$

Here ψ is the particle's wavefunction and E is the corresponding energy.

The eq. (2.7) is defined over the whole coordinate space $\boldsymbol{r} \in \mathbb{R}^2$, which complicates the problem. Since the potential is periodic, we simplify the problem using Bloch's theorem, which states that the solution wavefunction ψ (eigenfunction) has the form

$$\psi(\boldsymbol{r}) \equiv \psi_{\boldsymbol{k}}(\boldsymbol{r}) = \mathrm{e}^{\mathrm{i}\boldsymbol{k}\cdot\boldsymbol{r}} u_{\boldsymbol{k}}(\boldsymbol{r}). \tag{2.8}$$

Here we introduced the Bloch's wavevector $\boldsymbol{k}$ which is one of quantities to number different solutions to the eq. (2.7). The new function $u_{\boldsymbol{k}}$ has the same periodicity as the potential V:

$$u_{\boldsymbol{k}}(\boldsymbol{r} + \boldsymbol{r_n}) = u_{\boldsymbol{k}}(\boldsymbol{r}). \tag{2.9}$$

As one can see, the Bloch's theorem (2.8) states that the eigenfunction ψ is a product of two terms. First term is the phase factor where the phase linearly depends on the position $\boldsymbol{r}$. Second term is the periodic function $u_{\boldsymbol{k}}$, which is called the periodic part of $\psi_{\boldsymbol{k}}$. Since the eigenfunctions $\psi_{\boldsymbol{k}}$ are now numbered by $\boldsymbol{k}$, we also need to number corresponding energy values $E \equiv E(\boldsymbol{k})$. The wavefunction of the form (2.8) is called Bloch wavefunction.

The Bloch's wavevector $\boldsymbol{k}$ is defined over the First Brillouin Zone (FBZ), which is a Wigner-Seitz primitive cell in the reciprocal space.

From the equations (2.8) and (2.9) we find that the eigenfunctions $\psi_{\boldsymbol{k}}$ satisfy the condition

$$\psi_{\boldsymbol{k}}(\boldsymbol{r} + \boldsymbol{r_r}) = \mathrm{e}^{\mathrm{i}\boldsymbol{k}\cdot\boldsymbol{r_r}} \psi_{\boldsymbol{k}}(\boldsymbol{r}). \tag{2.10}$$

This means that we can focus our attention to a single elementary cell instead of

the whole coordinate space $\mathbb{R}^2$. We reformulate our eigenvalue problem (2.7) to

$$-\frac{\hbar^2}{2m}\nabla^2\psi_{\boldsymbol{k}} + V\psi_{\boldsymbol{k}} = E(\boldsymbol{k})\psi_{\boldsymbol{k}} \tag{2.11}$$

with the Bloch-periodic condition (2.10).

Sometimes it is convenient to formulate this eigenproblem in terms of the periodic functions $u_{\boldsymbol{k}}$. By inserting (2.8) into (2.11) we get

$$-\frac{\hbar^2}{2m}\left(\nabla^2 u_{\boldsymbol{k}} + 2\mathrm{i}\boldsymbol{k}\cdot\nabla u_{\boldsymbol{k}} - \boldsymbol{k}^2 u_{\boldsymbol{k}}\right) + V u_{\boldsymbol{k}} = E(\boldsymbol{k})u_{\boldsymbol{k}}. \tag{2.12}$$

Here $\boldsymbol{k}^2 \equiv \boldsymbol{k}\cdot\boldsymbol{k}$ is a squared length of the Bloch wavevector $\boldsymbol{k}$.

2.1.2 Discrete problem: tight-binding model

The discrete description of opticall lattices uses tight-binding approximation, which in principle always leads to a finite-dimensional Hilbert spaces. The tight-binding approximation is used very widely to describe many-body effects, so usually one starts from particle creation and annihilation operators. We don't directly analyze many-body states, but we still use creation and annihilation operator language, since on single particle level it is equivalent to the usual one-particle Hilbert space description.

The tight-binding approximation limits the full quantum mechanical Hilbert space to a set of states that are localized near each lattice site. In this way we have convenient set of basis states and this set can be made into a finite set by chooosing suitable boundary conditions for the whole lattice. An example of such boundary conditions are periodic boundary conditions: we pick certain numbers of elementary cells in each dimension and wrap the whole lattice into two-dimensionall thorus. Such description can give very good description of bulk lattice properties if we include enough elementary cells in each dimension.

In general we start with a set of lattice sites positioned in the points $\boldsymbol{r}_j$, where j numbers each elementary cell. For more complex lattices a single elementary cell may contain more than one lattice site. It becomes convenient to use different indices for an elementary cell and specific sites and states in it. We will use a two-dimensional vector $\boldsymbol{n} \equiv (n_1, n_2)$ with integer indices n_1 and n_2 to denote the elementary cell and additional index s to denote different type of lattice sites. In this way we describe the position of each lattice site by the vector $\boldsymbol{r}_{\boldsymbol{n},s}$. Using this we denote creation and annihilation operators by $c^\dagger(\boldsymbol{r}_{\boldsymbol{n},s})$ and $c(\boldsymbol{r}_{\boldsymbol{n},s})$. This notation is useful when we don't want to specify a specific site and use general position vector $\boldsymbol{r}$. Then we will write

$c^\dagger(\boldsymbol{r})$ and $c(\boldsymbol{r})$, where the only requirement is that the vector $\boldsymbol{r}$ is not arbitrary, but points to some lattice site. In addition, it is convenient to pick a specific site in the elementary cell as a reference point to describe position of the that elementary cell. We do this by choosing specific s, for example $s = 0$ (if zero is in the set of possible values of s) and denote $\boldsymbol{r}_{\boldsymbol{n},0} \equiv \boldsymbol{r}_{\boldsymbol{n}}$. In this way the vectors $\boldsymbol{r}_{\boldsymbol{n}}$ coincide with the lattice vectors defined in (2.3).

Having introduced the creation and annihilation operators we now can build the general Hamiltonian H of a lattice. The dynamics of a single particle is described with terms of the form $t_{\boldsymbol{n},s,\boldsymbol{n}',s'}c^\dagger(\boldsymbol{r}_{\boldsymbol{n},s})c(\boldsymbol{r}_{\boldsymbol{n}',s'})$. Such terms remove the existing particle from the site $\boldsymbol{r}_{\boldsymbol{n}',s'}$ and create another particle in the site $\boldsymbol{r}_{\boldsymbol{n},s}$. Effectively, this process, called *hopping*, moves existing particle from one site to another. $t_{\boldsymbol{n},s,\boldsymbol{n}',s'}$ are called hopping parameters, that describe hopping rate and any additional phases that may appear when particle moves from one lattice site to another. Usually the hopping parameters don't include diagonal terms $t_{\boldsymbol{n},s,\boldsymbol{n},s}$ (with $\boldsymbol{n} = \boldsymbol{n}'$ and $s = s'$) as they describe the on-site energy and a possible additional potential. These terms are separated and denoted by another letter, for example $\varepsilon_{\boldsymbol{n},s} \equiv t_{\boldsymbol{n},s,\boldsymbol{n},s}$.

For a single particle in a lattice the general tight-binding Hamiltonian is written as

$$H = \sum_{\boldsymbol{n},s} \varepsilon_{\boldsymbol{n},s} c^\dagger(\boldsymbol{r}_{\boldsymbol{n},s})c(\boldsymbol{r}_{\boldsymbol{n},s}) + \sum_{\boldsymbol{n},s,\boldsymbol{n}',s'} t_{\boldsymbol{n},s,\boldsymbol{n}',s'} c^\dagger(\boldsymbol{r}_{\boldsymbol{n},s})c(\boldsymbol{r}_{\boldsymbol{n}',s'}). \tag{2.13}$$

Here the second term excludes the terms with $\boldsymbol{n} = \boldsymbol{n}'$ and $s = s'$ as they are expressed in the first term. If we don't have any kind of external potential or magnetic field, we have fully periodic quantum system and the on-site energies don't depend on the index $\boldsymbol{n}$. In the same way the hopping parameters $t_{\boldsymbol{n},s,\boldsymbol{n}',s'}$ depend only on the difference $\boldsymbol{n} - \boldsymbol{n}'$.

The core idea of tight-binding approximation is to cut off hopping parameters between lattice sites that are not near each other. Most of the time only the nearest neighbour (NN) sites are considered, but sometimes we include the next-nearest neighbour (NNN) sites into analysis as such terms may become important in order to describe certain lattice properties.

The single-particle physics are analyzed by switcing into $\boldsymbol{k}$-space. We do this using Fourier transform of the creation and annihilation operators $c^\dagger(\boldsymbol{r})$ and $c(\boldsymbol{r})$:

$$c_s(\boldsymbol{k}) = \frac{1}{\sqrt{N}} \sum_{\boldsymbol{k}} c(\boldsymbol{r}_{\boldsymbol{n},s}) \mathrm{e}^{-\mathrm{i}\boldsymbol{k}\cdot\boldsymbol{r}_{\boldsymbol{n}}},$$
$$c(\boldsymbol{r}_{\boldsymbol{n},s}) = \frac{1}{\sqrt{N}} \sum_{\boldsymbol{k}} c_s(\boldsymbol{k}) \mathrm{e}^{\mathrm{i}\boldsymbol{k}\cdot\boldsymbol{r}_{\boldsymbol{n}}}.$$

Here N is the total number of elementary cells in a quantization volume, meaning that if N_1 is the number of cells in one dimension and N_2 is the number of cells in another, the total number of cells is $N = N_1 N_2$. After this transformation the index $\boldsymbol{n}$ is changed into $\boldsymbol{k}$. For single-particle case, the Hamiltonian H becomes diagonal in $\boldsymbol{k}$. Then we write

$$H = \sum_{\boldsymbol{k}} H_{\boldsymbol{k}}$$

and problem is simplified to the eigenvalue problem of the block $H_{\boldsymbol{k}}$, which can be represented as a square matrix, which has the same size as the number of lattice sites in a single elementary cell. We will denote matrix representation of $H_{\boldsymbol{k}}$ by $\mathcal{H}_{\boldsymbol{k}}$. Eigenvalues of $H_{\boldsymbol{k}}$ form energy bands, denoted by $E_n(\boldsymbol{k})$.

2.1.3 Wannier states

Although Bloch functions (2.8) are eigenfunctions of the single-particle Hamiltonian and form a full basis in the quantum mechanical Hilbert space, they are not convenient when we explore certain types of optical lattices. Here we introduce alternative basis of Wannier functions that are constructed using Wannier functions [85, 86, 87, 88] that are built from solutions to the equation (2.11) with the corresponding boundary conditions (2.10). In addition, the Wannier functions establich a relation between the first-principles description (2.7) and the tigh-binding approximation (2.13).

Let us pick a specific energy band n which is separated from other bands by band gaps. The Wannier function $W_{\boldsymbol{R},n}$ is defined as a Fourier transformation of Bloch states $\psi_{\boldsymbol{k},n}$:

$$W_{\boldsymbol{R},n}(\boldsymbol{r}) = \sqrt{\frac{|\Omega|}{(2\pi)^2}} \int_{\mathrm{FBZ}} \mathrm{d}^2\boldsymbol{k}\, \mathrm{e}^{-\mathrm{i}\boldsymbol{k}\cdot\boldsymbol{R}} \psi_{\boldsymbol{k},n}(\boldsymbol{r}). \tag{2.14}$$

Here we integrate over the first Brillouin zone. If we pick a large but finite number of elementary cells and introduce periodic boundary conditions for the whole lattice, then we change the integration into a finite sum:

$$W_{\boldsymbol{R},n}(\boldsymbol{r}) = \frac{1}{\sqrt{N_{\mathrm{cells}}}} \sum_{\boldsymbol{k}} \mathrm{e}^{-\mathrm{i}\boldsymbol{k}\cdot\boldsymbol{R}} \psi_{\boldsymbol{k},n}(\boldsymbol{r}). \tag{2.15}$$

Here N_{cells} is the total number of cells in our lattice. In addition, we have the same number of $\boldsymbol{k}$-points in the first Brillouin zone.

Such Wannier functions have several important properties:

- $W_{\boldsymbol{R},n}$ are periodic functions with respect to the index $\boldsymbol{R}$:

$$W_{\boldsymbol{R},n}(\boldsymbol{r}) = W_{\boldsymbol{R}+\boldsymbol{R}',n}(\boldsymbol{r}+\boldsymbol{R}').$$

  Here $\boldsymbol{R}'$ is a lattice vector. This property shows that each Wannier function is its own translated copy. If we know the Wannier function for for one elementary cell, we easilty find others by translating it by the lattice vector $\boldsymbol{R}'$. This allows us to denote the Wannier functions simpler:

$$W_n(\boldsymbol{r}-\boldsymbol{R}) := \phi_{\boldsymbol{R},n}(\boldsymbol{r}).$$

- $W_{\boldsymbol{R},n}$ is not uniquely defined. If we change overal phases of the Bloch functions,

$$\tilde{\psi}_{\boldsymbol{k},n}(\boldsymbol{r}) = \exp(\mathrm{i}\varphi_{\boldsymbol{k},n})\psi_{\boldsymbol{k},n}(\boldsymbol{r}), \tag{2.16}$$

  then we construct a different set of Wannier functions. In addition, if we have several overlaping energy bands, then, before constructing Wannier functions, we can mix the Bloch functions:

$$\tilde{\psi}_{\boldsymbol{k},m}(\boldsymbol{r}) = \sum_n U^{(\boldsymbol{k})}_{m,n}\psi_{\boldsymbol{k},n}(\boldsymbol{r}). \tag{2.17}$$

  Here $U^{(\boldsymbol{k})}$ is unitary matrix, which mixes the Bloch functions in each $\boldsymbol{k}$-point. A phase choice (2.16) for a Bloch functions from a single energy band is a specific case of Bloch function mixing (2.17) when the matrix $U^{(\boldsymbol{k})}$ is diagonal unitary matrix.

- Wannier functions $W_{\boldsymbol{R},m}$ form an orthogonal basis for a Hilbert space subset for a selected energy bands.

Non-uniqueness of Wannier functions is a complication and it would seem that they are not very useful. However, it is shown that it is possible to choose the matrices $U^{(\boldsymbol{k})}$ in such a way that the resulting Wannier functions are maximally localized around lattice sites [88]. Such optimal matrices $U^{(\boldsymbol{k})}$ can be constructed using some criteria or measure of Wannier function localization. Such measure can be a functional

$$\sum_m \left(\langle \boldsymbol{r}^2\rangle_m - \langle \boldsymbol{r}\rangle_m^2\right). \tag{2.18}$$

This parameter measures the localization of all Wannier functions, defined in a single elementary cells and numbered by the index m. Here by $\langle \boldsymbol{r}\rangle$ and $\langle \boldsymbol{r}^2\rangle$ we denoted the quantum expectation values of the coordinate operator $\boldsymbol{r}$ and the squared coordiante

operator $\boldsymbol{r}$:

$$\langle \boldsymbol{r} \rangle = \langle \mathbf{0}, m | \boldsymbol{r} | \mathbf{0}, m \rangle,$$
$$\langle \boldsymbol{r}^2 \rangle = \langle \mathbf{0}, m | \boldsymbol{r}^2 | \mathbf{0}, m \rangle.$$

Here $|\mathbf{0}, m\rangle$ is a ket vector corresponding to the Wannier function $W_m \equiv W_{\mathbf{0},m}$. In order to the find maximally localized Wannier functions, we have to minimize the functional (2.18) by choosing optimal unitary matrices $U^{(\boldsymbol{k})}$.

The maximally localized Wannier functions have certain important properties:

- If the initial single-particle Hamiltonian has a time reverse symmetry, then there are no initial magnetic field and the maximally localized Wannier functions $\phi_n(\boldsymbol{r})$ are essentially real (ignoring the global phase factor).
- Maximally localized Wannier functions decrease exponentially if we move away from their centers. In the same way corresponding matrix elements of the Hamiltonian between these Wannier functions also decrease.

All the properties of Wannier functions allow us to use them as a basis for the tight-binding approximation.

2.1.4 Tight-binding model from Wannier functions

When we construct a set of maximally localized Wannier states $|\boldsymbol{R}, m\rangle$, we can use it as a basis for the tight-binding approximation. Because of localization, the matrix elements of the Hamiltonian between Wannier functions that are further away from each other are close to zero and can be ignored. When we construct the Hamiltonian in the Wannier function basis, we express a general state vector as

$$|\Psi\rangle = \sum_{\boldsymbol{R},m} c_{\boldsymbol{R},m} |\boldsymbol{R}, m\rangle. \tag{2.19}$$

Here $c_{\boldsymbol{R},m}$ are the expansion coefficients. Using this expansion and the fact, that Wannier states are orthonormal, we transform the Shrodinger's equation, $H|\Psi\rangle = E|\Psi\rangle$ into a system of equations for the expansion coefficients $c_{\boldsymbol{R},m}$:

$$\sum_{\boldsymbol{R}',m'} c_{\boldsymbol{R}',m'} \langle \boldsymbol{R}, m | H | \boldsymbol{R}', m' \rangle = E c_{\boldsymbol{R},m}. \tag{2.20}$$

Here $\langle \boldsymbol{R}, m | H | \boldsymbol{R}', m' \rangle$ are matrix elements of the Hamiltonian in the Wannier basis.

It is convenient to write the resulting Hamiltonian in the Wannier basis in a form with separated diagonal and off-diagonal elements:

$$H = \sum_{\boldsymbol{R},m} \varepsilon_{\boldsymbol{R},m} |\boldsymbol{R}, s\rangle\langle \boldsymbol{R}, s| + \sum_{(\boldsymbol{R},m)\neq(\boldsymbol{R}',m')} t_{\boldsymbol{R},m,\boldsymbol{R}',m'} |\boldsymbol{R}, m\rangle\langle \boldsymbol{R}', m'|. \tag{2.21}$$

Here $\varepsilon_{\boldsymbol{R},m} = \langle \boldsymbol{R}, m|H|\boldsymbol{R}, m\rangle$ are the diagonal matrix elements and $t_{\boldsymbol{R},m,\boldsymbol{R}',m'}$ are the off-diagonal matrix elements. The diagonal matrix elements correspond to the average Wannier state energies. The off-diagonal matrix elements describe hoppings between the lattice sites.

The single-particle tight-binding model (as described in the section 2.1.2) is constructed by identifying the Wannier function index $\boldsymbol{R}$ with the lattice vector $\boldsymbol{r_n}$, the index m with the sublattice index s and substituting

$$|\boldsymbol{R}, m\rangle\langle \boldsymbol{R}', m'| \to c^\dagger(\boldsymbol{r}_{\boldsymbol{n},s}) c(\boldsymbol{r}_{\boldsymbol{n}',s'}),$$
$$\varepsilon_{\boldsymbol{R},m} \to \varepsilon_{\boldsymbol{n},s},$$
$$t_{\boldsymbol{R},m,\boldsymbol{R}',m'} \to t_{\boldsymbol{n},s,\boldsymbol{n}',s'}.$$

In this way we get the tight-binding Hamiltonian (2.13).

Note that this way of building the tight-binding model works only for a single-particle case. If your model includes interaction terms, you need to start from the second-quantized version of initial Hamiltonian in the coordinate representation and then use Wannier basis in order to calculate not only the on-site energies and tunneling parameters, but also interaction terms.

2.1.5 Topological Chern number

If a certain energy band $E_n(\boldsymbol{k})$ does not touch the nearby energy bands,

$$|E_n(\boldsymbol{k}) - E_{n\pm1}(\boldsymbol{k})| \neq 0, \tag{2.22}$$

then we can define a topological invariant, call Chern number. We express the n-th band Chern number c_n using the TKNN (Thouless-Kohmoto-Nightingale-Nijs) formula:

$$c_n = \frac{1}{2\pi} \int_{\mathrm{FBZ}} \mathrm{d}^2\boldsymbol{k}\, F_n(\boldsymbol{k}), \tag{2.23}$$

$$F_n(\boldsymbol{k}) = \mathrm{i} \left(\frac{\partial \langle u_{\boldsymbol{k},n}|}{\partial k_x} \frac{\partial |u_{\boldsymbol{k},n}\rangle}{\partial k_y} - \frac{\partial \langle u_{\boldsymbol{k},n}|}{\partial k_y} \frac{\partial |u_{\boldsymbol{k},n}\rangle}{\partial k_x} \right). \tag{2.24}$$

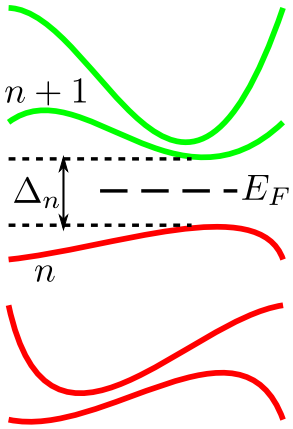

Figure 2.2: Schematic example of energy bands. The red color indicates the filled energy bands. The green color indicates the empty bands. Here E_F is the Fermi energy, Δ_n is the band gap between the n-th and $(n+1)$-th bands.

Here $F_n(\boldsymbol{k})$ is the Berry curvature of the n-th energy band, which is defined using the periodic parts $|u_{\boldsymbol{k},n}\rangle$ of the Bloch functions. We integrate this curvate over the whole FBZ. An alternative way to express the Berry curvate $F_n(\boldsymbol{k})$ is to use the Berry connection $\boldsymbol{A}_n(\boldsymbol{k})$ – a gauge field in the FBZ:

$$F_n(\boldsymbol{k}) = \boldsymbol{e}_z \cdot \nabla_{\boldsymbol{k}} \times \boldsymbol{A}_n(\boldsymbol{k}),$$
$$\boldsymbol{A}_n(\boldsymbol{k}) = \langle u_{\boldsymbol{k},n} | \mathrm{i}\nabla_{\boldsymbol{k}} | u_{\boldsymbol{k},n} \rangle.$$

The gauge field $\boldsymbol{A}_n(\boldsymbol{k})$ describes the parallel transport of the eigenstates $|u_{\boldsymbol{k},n}\rangle$ in the reciprocal space.

The topological Chern number c_n has several important properties:

- c_n is strictly integer, $c_n \in \mathbb{Z}$.
- If the n-th energy band touches at least one of the nearby (lower or higher) energy band, then c_n is undefined.
- c_n is robust to lattice perturbations under the condition that the n-th energy band does not touch any of the nearby energy bands. This means that the Chern number c_n can only be changed during a phase transition when the n-th band touches another energy band and then separates again.
- If there is a phase transition, then all the bands that are participating in that transition (all bands that touch and then separate) have a property that the sum of all Chern number of such energy bands is constant. This means that the Chern number can be "exchanged" between bands by a process of touching and separating.

Physical interpretation c_n is closely related to the quantum Hall conductivity. Let us assume that the atomic gas cloud is perturbed by an additional force field $\boldsymbol{F}(\boldsymbol{r})$. As an example, in a solid state systems such field can be a created using a conventional electric field $\boldsymbol{E}(\boldsymbol{r})$. Such external force field created non-zero density current $\boldsymbol{j}(\boldsymbol{r})$. In general, this density current depends linearly on the force field $\boldsymbol{F}(\boldsymbol{r})$:

$$\boldsymbol{j}(\boldsymbol{r}) = \hat{\sigma}\boldsymbol{F}(\boldsymbol{r}).$$

Here $\hat{\sigma}$ is a conductivity tensor. Its off-diagonal component $\sigma_{xy} \equiv \sigma_{\mathrm{H}}$ is called the Hall conductivity. Suppose we have n filled bands, that are separated by a band gap Δ_n from the empty higer bands (see fig. t2.2). Then the Hall conductivity is proportional to the sum the Chern number of the filled bands:

$$\sigma_{\mathrm{H}} \propto \sum_{i=1}^{n} c_i. \tag{2.25}$$

This means that Chern number c_n indicates how much Hall conductivity changes when we fill the n-th band. If the n-th band is not fully filled up or if there are no energy gap between the n-th and $(n+1)$-th bands, then the Hall conductivity σ_{H} not precisely defined by (2.25).

Mathematical interpretation We can express the Chern number directly in the gauge field $\boldsymbol{A}_n(\boldsymbol{r})$ using Stokes theorem on (2.23–2.24):

$$c_n = \frac{1}{2\pi\mathrm{i}} \oint_{\mathrm{FBZ}} \boldsymbol{A}(\boldsymbol{k}) \cdot \mathrm{d}\boldsymbol{k}. \tag{2.26}$$

This expression of c_n shows that if the gauge field $\boldsymbol{A}_n(\boldsymbol{r})$ is continuouos over the FBZ, then the corresponding Chern number c_n is zero. In order to explain this we mentally separate the contour integral in (2.26) into two parts: the part around the FBZ and the contribution of possible singularities. The former part is identically zero because of periodicity of $\boldsymbol{A}(\boldsymbol{r})$. The latter part may give a non-zero contribution (we will give explicit examples in the end of the chapter on the optical Dice lattice). If the field $\boldsymbol{A}_n(\boldsymbol{r})$ is continouos then it doesn't contain any singularities and the total contribution to the Chern number c_n is zero.

The Chern number c_n characterizes a topological structure of the complex fiber bundle built up from the eigenstates $|u_{\boldsymbol{k},n}\rangle$. Each ket vector $|u_{\boldsymbol{k},n}\rangle$ is defined up to arbitrary overall phase choice. We can restrict this phase choice, so $|u_{\boldsymbol{k},n}\rangle$ becomes continuous in the FBZ. Then by moving the state vector around some closed curve in the FBZ we get additional Berry phase. This phase doesn't depend on our choice

of phases (as long as this choice gives a continuous field of ket vectors $|u_{\boldsymbol{k},n}\rangle$). If we move the state vector around the whole FBZ, we get a Berry phase which is now a multiple of 2π. This multiplication constant is the Chern number c_n.

Classification of topological phases From (2.25) we see that we can classify different topological matter phases according to the Chern numbers c_i and the band gap Δ_n into four groups:

- *Topologically trivial insulator* – the sum of the Chern numbers of the filled energy bands is zero, $\sum_i c_i = 0$, and there is non-zero band gap $\Delta_n > 0$.
- *Chern insulator* (or a *topological insulator*) – The Chern number sum is not zero, $\sum_i c_i \neq 0$, and there is still the non-zero band gap, $\Delta_n > 0$.
- *Topologically trivial metal* or *semi-metal* – the Chern number sum is zero, $\sum_i c_i = 0$, and the Fermi energy level is not in the band gap. This happens when either the Fermi energy level is inside a gap or if there are no band gap at all ($\Delta_n = 0$).
- *Chern metal* or *semi-metal* – Chern number sum is non-zero, $\sum_i c_i \neq 0$, and the Fermi energy level is not inside a band gap (again: either there is no band gap or the Fermi energy level is inside a partially filled band).

One of the most interesting topological phasese are *Chern insulators*. In such cases we can observe Quantum Hall Effect (QHE). Suppose we start filling up the bands from the lowest one. When the Fermi energy level is inside the band gap, then the Hall conductivity σ_{H} doesn't change. When the Fermi level crosses the energy band, the Hall conductivity changes from one quantized value to another according the Chern number of the band.

Chern metal and Chern semi-metal phases can also be interesting to study. Howeber, in such cases the Hall conductivity σ_{H} may not be quantized.

2.2 Numerical calculation of band structure

2.2.1 Dimensionless units

For numerical analysis it is convenient to switch to dimensionless units. In general the procedure is to express the position $\boldsymbol{r}$ and energy quantities like the potential

V and the total energy E as

$$\begin{aligned} \boldsymbol{r} &\equiv \tilde{\boldsymbol{r}} r_{\mathrm{d}}, \\ V &\equiv \tilde{V} E_{\mathrm{d}}, \\ E &\equiv \tilde{E} E_{\mathrm{d}}. \end{aligned}$$

Here r_{d} and E_{d} are the chosen distance and energy units respectively. $\tilde{\boldsymbol{r}}$, $\tilde{V}$ and $\tilde{E}$ are the resulting dimensionless position, potential and energy respectively. By choosing r_{d} we immediately define the dimensionless gradient and Laplacian operators

$$\begin{aligned} \nabla &\equiv \tilde{\nabla} r_{\mathrm{d}}^{-1}, \\ \nabla^2 &\equiv \tilde{\nabla}^2 r_{\mathrm{d}}^{-2}. \end{aligned}$$

In the similar way we define dimensionless lattice vectors, reciprocal lattice vectors and Bloch's wavevector. Explicitly, $\boldsymbol{k} = \tilde{\boldsymbol{k}} r_{\mathrm{d}}^{-1}$. Also, by choosing the energy unit $\tilde{E}$ we also automatically choose units of frequency and time.

In the new units the eigenvalue equation for the BLoch wavefunction $\psi_{\boldsymbol{k}}$ (eq. 2.11) becomes

$$-\alpha \tilde{\nabla}^2 \psi_{\boldsymbol{k}} + \tilde{V} \psi_{\boldsymbol{k}} = \tilde{E}(\boldsymbol{k}) \psi_{\boldsymbol{k}}. \tag{2.27}$$

In the same way the eigenvalue equation for the periodic part $u_{\boldsymbol{k}}$ (eq. 2.12) becomes

$$-\alpha \left(\tilde{\nabla}^2 u_{\boldsymbol{k}} + 2\mathrm{i} \tilde{\boldsymbol{k}} \tilde{\nabla} u_{\boldsymbol{k}} - \tilde{\boldsymbol{k}}^2 u_{\boldsymbol{k}} \right) + \tilde{V} u_{\boldsymbol{k}} = \tilde{E}(\boldsymbol{k}) u_{\boldsymbol{k}}. \tag{2.28}$$

In both equations (2.27), (2.28) we have the same dimensionless parameter

$$\alpha = \frac{\hbar^2}{2 M r_{\mathrm{d}}^2 E_{\mathrm{d}}}. \tag{2.29}$$

This parameter depends on the choice of units r_{d} and E_{d}.

Note that for the rest of this document we drop the tilde from the dimensionless units. The only exceptions will be short discussions about specific choices of dimensionless units.

2.2.2 Finite difference method for rectangle lattice

In this section we present how to numerically calculate energy spectrum of a particle in rectangle lattice using simple finite differences. The finite difference method (FDM) is probably the simplest way to discretize partial differential equations. Here describe the describe the application of second-order approximation of first and

second derivatives to a discretization of the Schrodinger's equation, which is a linear second-order partial differential equation.

The elementary lattice vectors of a rectangle cell are $\boldsymbol{a}_1 = a_x \boldsymbol{e}_x$ and $\boldsymbol{a}_2 = a_y \boldsymbol{e}_y$. The elementary reciprocal lattice vectors are $\boldsymbol{b}_1 = (2\pi/a_x)\boldsymbol{e}_x$ and $\boldsymbol{b}_2 = (2\pi/a_y)\boldsymbol{e}_y$. The Brillouin zone is a rectangle

$$-\frac{\pi}{a_x} \leq k_x < \frac{\pi}{a_y}, \tag{2.30}$$

$$-\frac{\pi}{a_y} \leq k_y < \frac{\pi}{a_y}. \tag{2.31}$$

The eigenvalue equation for the Bloch functions $\psi_{\boldsymbol{k}}$ in dimensionless form is

$$-\alpha \nabla^2 \psi_{\boldsymbol{k}} + V \psi_{\boldsymbol{k}} = E(\boldsymbol{k}) \psi_{\boldsymbol{k}}. \tag{2.32}$$

The Bloch's theorem allows us to only consider a single elementary cell and the Bloch-periodic condition (2.10) simplifies to boundary conditions with additional phase factors (squezed boundary conditions):

$$\psi_{\boldsymbol{k}}(a_x, y) = \mathrm{e}^{\mathrm{i}k_x a_x} \psi_{\boldsymbol{k}}(0, y), \tag{2.33}$$

$$\psi_{\boldsymbol{k}}(x, a_y) = \mathrm{e}^{\mathrm{i}k_y \cdot a_y} \psi_{\boldsymbol{k}}(x, 0). \tag{2.34}$$

We define a grid on the elementary cell. The grid consists of a set of points (x_i, y_j) with

$$x_i = i\frac{a_x}{N_x}, \qquad i = 0, \ldots, N_x,$$

$$y_j = j\frac{a_y}{N_y}, \qquad j = 0, \ldots, N_y.$$

Here the x coordinate of each discretization point is numbered by the index i, which runs from 0 to N_x. The y coordinate is numbered by the index j, which runs from 0 to N_y. $i = 0$ corresponds to the left side of the elementary cell, $i = N_x$ corresponds to the right side. In a similar way, $j = 0$ corresponds to the bottom of the elementary cell and $j = N_y$ corresponds to the top. Observe that $x_0 = 0$, $y_0 = 0$, $x_{N_x} = a_x$ and $y_{N_y} = a_y$. In total we have $(N_x + 1) \times (N_y + 1)$ discretization points. Let us denote the distances between nearest discretization points in each dimension by $h_x = a_x/N_x$ and $h_y = a_y/N_y$.

In order to make the equation (2.32) simpler, we drop the Bloch wavevector index $\boldsymbol{k}$ (we will leave it only in $E(\boldsymbol{k})$ and boundary conditions). We denote the wavefunction ψ values in each discretization point (x_i, y_j) by $\psi_{i,j} \equiv \psi(x_i, y_j)$. In the same way we

denote the potential values by $V_{i,j} \equiv V(x_i, y_j)$.

In order to discretize the laplacian $\nabla^2\psi$ we use the second-order central difference formulas for the second derivatives:

$$\left[\frac{\partial^2\psi}{\partial x^2}\right]_{x=x_i,y=y_j} \sim \frac{1}{h_x^2}\left(\psi_{i+1,j} + \psi_{i-1,j} - 2\psi_{i,j}\right) \quad \text{as } h_x \to 0, \tag{2.35}$$

$$\left[\frac{\partial^2\psi}{\partial y^2}\right]_{x=x_i,y=y_j} \sim \frac{1}{h_y^2}\left(\psi_{i,j+1} + \psi_{i,j-1} - 2\psi_{i,j}\right) \quad \text{as } h_y \to 0. \tag{2.36}$$

Here the limit $h_x \to 0$ ($h_y \to 0$) is equivalent to $N_x \to \infty$ ($N_y \to \infty$). Combining these expressions we find that the laplacian $\nabla^2\psi$ in the point (x_i, y_j) is approximated by

$$\left[\nabla^2\psi\right]_{x=x_i,y=y_j} \sim \frac{1}{h_x^2}\left(\psi_{i+1,j} + \psi_{i-1,j} - 2\psi_{i,j}\right) + \frac{1}{h_y^2}\left(\psi_{i,j+1} + \psi_{i,j-1} - 2\psi_{i,j}\right)$$

as $h_x \to 0$ and $h_y \to 0$. In this way we discretize the eigenvalue equation (2.32) and get

$$\begin{aligned} -\alpha\frac{1}{h_x^2}\left(\psi_{i+1,j} + \psi_{i-1,j} - 2\psi_{i,j}\right) \\ -\alpha\frac{1}{h_y^2}\left(\psi_{i,j+1} + \psi_{i,j-1} - 2\psi_{i,j}\right) \\ +V_{i,j}\psi_{i,j} = E(\boldsymbol{k})\psi_{i,j}. \end{aligned} \tag{2.37}$$

Here $i = 0, \ldots, N_x$ and $j = 0, \ldots, N_y$.

The equation (2.37) contains coefficients $\psi_{i,j}$ with indices that are negative or higher than N_x (N_y) values of i (j). In order to eliminate such coefficients we discretize the boundary conditions (2.33)–(2.34):

$$\psi_{N_x,j} = \mathrm{e}^{\mathrm{i}k_x a_x}\psi_{0,j}, \tag{2.38}$$

$$\psi_{i,N_y} = \mathrm{e}^{\mathrm{i}k_y a_y}\psi_{i,0}. \tag{2.39}$$

We see that the resulting expressions (2.38)–(2.39) connect the left size of the elementary cell with the right side and the bottom side with the top side. This means that we can ignore the right and top sides (the coefficients with $i = N_x$ or $j = N_y$). So we number our system of equations (2.37) by $i = 0, \ldots, N_x - 1$ and $j = 0, \ldots, N_y - 1$. Each time we encounter a coefficient $\psi_{i,j}$ with $i = N_x$ or $j = N_y$, we use (2.38)–(2.39) to replace them: $\psi_{N_x,j} = \exp(\mathrm{i}k_x a_x)\psi_{0,j}$, $\psi_{i,N_y} = \exp(\mathrm{i}k_y a_y)\psi_{i,0}$. In the same way we replace coefficients $\psi_{i,j}$ with $i = -1$ or $j = -1$: $\psi_{-1,j} = \exp(-\mathrm{i}k_x a_x)\psi_{N_x-1,j}$, $\psi_{i,-1} = \exp(-\mathrm{i}k_y a_y)\psi_{i,N_y-1}$.

In the end we have a set of linear equations

$$\begin{aligned}&\left[2\alpha\left(h_x^{-2}+h_y^{-2}\right)+V_{i,j}\right]\psi_{i,j}\\&-\alpha h_x^{-2}\psi_{i+1,j}-\alpha h_x^{-2}\psi_{i-1,j}\\&-\alpha h_y^{-2}\psi_{i,j+1}-\alpha h_y^{-2}\psi_{i,j-1}=E(\boldsymbol{k})\psi_{i,j},\end{aligned}\tag{2.40}$$

where $i=0,\ldots,N_x-1$, $j=0,\ldots,N_y-1$. Together with the equations we have the following boundary conditions

$$\psi_{N_x,j}=\mathrm{e}^{\mathrm{i}k_xa_x}\psi_{0,j},\tag{2.41}$$

$$\psi_{i,N_y}=\mathrm{e}^{\mathrm{i}k_ya_y}\psi_{i,0},\tag{2.42}$$

$$\psi_{-1,j}=\mathrm{e}^{-\mathrm{i}k_xa_x}\psi_{N_x-1,j},\tag{2.43}$$

$$\psi_{i,-1}=\mathrm{e}^{-\mathrm{i}k_ya_y}\psi_{i,N_y-1}.\tag{2.44}$$

If we start with the eigenvalue equation for the periodic part u,

$$-\alpha\left(\nabla^2u+2\mathrm{i}\boldsymbol{k}\nabla u-\boldsymbol{k}^2u\right)+Vu=E(\boldsymbol{k})u,\tag{2.45}$$

we also need to discretize the gradient ∇u. For this we use the following second-order central difference formulas for the first derivatives:

$$\left[\frac{\partial u}{\partial x}\right]_{x=x_i,y=y_j}\sim\frac{1}{2h_x}\left(u_{i+1,j}-u_{i-1,j}\right)\quad\text{as }h_x\to0,\tag{2.46}$$

$$\left[\frac{\partial u}{\partial y}\right]_{x=x_i,y=y_j}\sim\frac{1}{2h_y}\left(u_{i,j+1}-u_{i,j-1}\right)\quad\text{as }h_y\to0.\tag{2.47}$$

Here we denoted $u_{i,j}\equiv u(x_i,y_j)$ (in the same way as ψ). The eigenvalue equation (2.45) is then approximated by

$$\begin{aligned}&\left[2\alpha\left(h_x^{-2}+h_y^{-2}\right)+\alpha\boldsymbol{k}^2+V_{i,j}\right]u_{i,j}\\&+\alpha\left(-h_x^{-2}-\mathrm{i}k_xh_x^{-1}\right)u_{i+1,j}+\alpha\left(-h_x^{-2}+\mathrm{i}k_xh_x^{-1}\right)u_{i-1,j}\\&+\alpha\left(-h_y^{-2}-\mathrm{i}k_yh_y^{-1}\right)u_{i,j+1}+\alpha\left(-h_y^{-2}+\mathrm{i}k_yh_y^{-1}\right)u_{i,j-1}=E(\boldsymbol{k})u_{i,j}.\end{aligned}\tag{2.48}$$

Here $i = 0, \ldots, N_x - 1$ and $j = 0, \ldots, N_y - 1$. The boundary conditions are

$$u_{N_x,j} = u_{0,j}, \tag{2.49}$$

$$u_{i,N_y} = u_{i,0}, \tag{2.50}$$

$$u_{-1,j} = u_{N_x-1,j}, \tag{2.51}$$

$$u_{i,-1} = u_{i,N_y-1}. \tag{2.52}$$

For numerical calculations we need to represent the resulting system of linear equations (2.40) in a matrix form. This can be achieved by introducing a single index l which is calculated by

$$l = i + jN_x, \qquad i = 0, \ldots, N_x - 1, \qquad j = 0, \ldots, N_y - 1. \tag{2.53}$$

The index l runs from 0 to $N_xN_y - 1$. The mapping $(i, j) \mapsto l$ defined by (2.53) is bijective and suitable for our goal. The resulting matrix is Hermitian and has the size $N \times N$, where $N = N_xN_y$ is the total number of non-equivalent discretization points in the elementary cell. One can observe that the matrix is sparse. There are no more than 3 non-zero elements in each row (or column). These properties apply to both types of eigenvalues (both for $\psi_{i,j}$ and $u_{i,j}$),

The spectrum is calculated by calculating several lowest eigenvalues of the matrix. For smaller matrices ($N \leq 10\,000$) we ignore its sparsity and use the LAPACK numeric library [89], which is suitable for such case. For larger matrices ($N > 10\,000$) we use PETSc [90, 91, 92] and SLEPc [93, 94, 95] numeric libraries, which can handle large and sparse matrices.

2.2.3 Fourier series method

The finite difference method, described in the previous section, is weak in two respects. First, it is simple only for rectangular cells. Although it can be extended to triangular and hexagonal lattices, the finite difference schemes become more complex. Second, in order to get a better approximation one needs to take a larger number of grid points, which leads to a larger matrices and longer computation. One way to overcome the second problem is to take higher-order approximations. However, the higher-order finite difference shcemes require to couple grid points that are further away from each other and this makes the resulting matrices less and less sparse. Moreover, the higher-order approximations are not easy to implement in more than one dimension.

An alternative way to solve a general 2D (not neceserally rectangle) eigenproblem

$$-\alpha\nabla^2\psi_{\boldsymbol{k}} + V\psi_{\boldsymbol{k}} = E(\boldsymbol{k})\psi_{\boldsymbol{k}}, \tag{2.54}$$

$$\psi_{\boldsymbol{k}}(\boldsymbol{r} + \boldsymbol{r}_{\boldsymbol{r}}) = \mathrm{e}^{\mathrm{i}\boldsymbol{k}\cdot\boldsymbol{r}_{\boldsymbol{r}}}\psi_{\boldsymbol{k}}(\boldsymbol{r}) \tag{2.55}$$

is to use Fourier expansion of the periodic part of the Bloch wavefunction $\psi_{\boldsymbol{k}}$:

$$u_{\boldsymbol{k}}(\boldsymbol{r}) = \sum_{\boldsymbol{G}} u_{\boldsymbol{k},\boldsymbol{G}}\mathrm{e}^{\mathrm{i}\boldsymbol{G}\cdot\boldsymbol{r}}. \tag{2.56}$$

Here $u_{\boldsymbol{k},\boldsymbol{G}}$ are Fourier coefficients, indexed by a reciprocal lattice vectors $\boldsymbol{G}$. The inverse transformation is

$$u_{\boldsymbol{k},\boldsymbol{G}} = \frac{1}{|\Omega|}\int_{\Omega}\mathrm{d}\Omega\, u_{\boldsymbol{k}}(\boldsymbol{r})\mathrm{e}^{-\mathrm{i}\boldsymbol{G}\cdot\boldsymbol{r}}. \tag{2.57}$$

Here Ω denotes the elementary cell over which we integrate. $|\Omega|$ is area of the elementary cell and $\mathrm{d}\Omega$ represents area unit used in the integration.

The presented form of $u_{\boldsymbol{k}}$ satisfies the Bloch-periodic condition (2.55) identically while the eigenvalue equation (2.54) becomes

$$\alpha|\boldsymbol{k} + \boldsymbol{G}|^2 u_{\boldsymbol{k},\boldsymbol{G}} + \sum_{\boldsymbol{G}'} V_{\boldsymbol{G}-\boldsymbol{G}'}u_{\boldsymbol{k},\boldsymbol{G}'} = E(\boldsymbol{k})u_{\boldsymbol{k},\boldsymbol{G}}. \tag{2.58}$$

Here $V_{\boldsymbol{G}}$ denotes the Fourier coefficients of the potential function V:

$$V_{\boldsymbol{G}} = \frac{1}{|\Omega|}\int_{\Omega}\mathrm{d}\Omega\, V(\boldsymbol{r})\mathrm{e}^{-\mathrm{i}\boldsymbol{G}\cdot\boldsymbol{r}}. \tag{2.59}$$

In order to calculate the Fourier coefficients $u_{\boldsymbol{k},\boldsymbol{G}}$ numerically we take a finite number of reciprocal lattice vectors $\boldsymbol{G} = m_1\boldsymbol{b}_1 + m_2\boldsymbol{b}_2$. Usually we limit the integers m_1 and m_2 by

$$-M_{\max} \leq m_1, m_2 \leq M_{\max}.$$

In this case we get $(2M_{\max} + 1)^2$ coefficients. The resulting matrix is real and symmetric. Non-diagonal elements comes only from the potential via its coefficients $V_{\boldsymbol{G}-\boldsymbol{G}'}$. The good choice of $M_{\max}$ depends on the potential V and on the number the lowest of bands we require. If the potential V is very oscillating, it has higher Fourier coefficients that are significant and must be included. If we are calculating a large number of bands or if we are interested in higher bands we have to take larger value of $M_{\max}$ to capture such bands. This is because the periodic parts $u_{\boldsymbol{k}}$of eigenfunctions of higher bands are more oscillating over the period and has higher significant Fourier coefficients. For simple optical lattices the potential is

created with standing laser waves and, so usually it is described by a combination of a sine and cosine functions. In such cases there are a finite number of non-zero Fourier coefficients $V_{\boldsymbol{G}}$. In addition, ultracold atoms in optical lattices usually are not excited to higher bands because of low temperature and their wavefunctions are not very oscillating over the elementary cell. This allows to take a small value of $M_{\max}$ (up to 10).

2.2.4 Fourier series method in coordinate representation

The Fourier series method is based on the momentum representation of a stationary Schrodinger's equation.

Here we start with a finite-dimensional Hilbert space which we get after limiting a number of reciprocal lattice vectors $\boldsymbol{G}$:

$$\boldsymbol{G} = m_1\boldsymbol{b}_1 + m_2\boldsymbol{b}_2, \qquad -M_{\max} \le m_1, m_2 \le M_{\max}.$$

We denote the total number of reciprocal lattice vectors by N,

$$N = (2M_{\max} + 1)^2, \tag{2.60}$$

and the set of these reciprocal lattice vectors by $\mathcal{G}$.

Observe that the Fourier series of the periodic part $u_{\boldsymbol{k}}$ (eq. 2.56) is now equivalent to a basis choice of

$$\phi_{\boldsymbol{G}}(\boldsymbol{r}) = \mathrm{e}^{\mathrm{i}\boldsymbol{G}\cdot\boldsymbol{r}}. \tag{2.61}$$

The periodic part is now expressed as

$$u_{\boldsymbol{k}}(\boldsymbol{r}) = \sum_{\boldsymbol{G}\in\mathcal{G}} \phi_{\boldsymbol{G}}(\boldsymbol{r}) u_{\boldsymbol{k},\boldsymbol{G}}. \tag{2.62}$$

Before we continue, let us introduce a specific type functions $\delta_{\boldsymbol{a}}$, that can be called "finite-dimensional" delta functions:

$$\delta_{\boldsymbol{a}}(\boldsymbol{r}) = \frac{1}{|\Omega|} \sum_{\boldsymbol{G}\in\mathcal{G}} \phi_{\boldsymbol{G}}(\boldsymbol{r} - \boldsymbol{a}). \tag{2.63}$$

These functions behave like Dirac delta functions, except they work only with functions, constructed from our finite basis (2.61):

$$\int_\Omega \mathrm{d}\Omega\, \delta^*_{\boldsymbol{a}}(\boldsymbol{r}) f(\boldsymbol{r}) = f(\boldsymbol{a}). \tag{2.64}$$

The equation (2.64) also shows that $\delta_{\boldsymbol{a}}(\boldsymbol{r})$ act as coordinate representation basis function.

Let us define a finite set of elementary cell points

$$\boldsymbol{r}_{\boldsymbol{j}} = \frac{j_1\boldsymbol{a}_1 + j_2\boldsymbol{a}_2}{2M_{\max}+1}, \qquad j_1 = 0,\ldots,2M_{\max}, \qquad j_2 = 0,\ldots,2M_{\max}. \tag{2.65}$$

There are in total N points – the same number as reciprocal lattice vectors $\boldsymbol{G}$. We denote this set of grid points by $\mathcal{R}$. The set $\mathcal{R}$ is the grid (not neceserally rectangle) on the elementary cell Ω.

The points $\mathcal{R}$ have one imporant property: the "finite-dimensional" delta functions $\delta_{\boldsymbol{a}}(\boldsymbol{r})$ constructed on this set of points form an orthogonal set. Observe,

$$\begin{aligned}
&\sum_{\boldsymbol{G}\in\mathcal{G}}\sum_{\boldsymbol{G}'\in\mathcal{G}}\int_\Omega \mathrm{d}\Omega\, \phi^*_{\boldsymbol{G}}(\boldsymbol{r}-\boldsymbol{r}_{\boldsymbol{j}})\phi_{\boldsymbol{G}'}(\boldsymbol{r}-\boldsymbol{r}_{\boldsymbol{j}'}) \\
=&\sum_{\boldsymbol{G}\in\mathcal{G}}\sum_{\boldsymbol{G}'\in\mathcal{G}} \mathrm{e}^{\mathrm{i}\boldsymbol{G}\cdot\boldsymbol{r}_{\boldsymbol{j}}}\mathrm{e}^{-\mathrm{i}\boldsymbol{G}'\cdot\boldsymbol{r}_{\boldsymbol{j}'}}\int_\Omega \mathrm{d}\Omega\, \mathrm{e}^{-\mathrm{i}(\boldsymbol{G}-\boldsymbol{G}')\cdot\boldsymbol{r}} \\
=&|\Omega|\sum_{\boldsymbol{G}\in\mathcal{G}} \mathrm{e}^{\mathrm{i}\boldsymbol{G}\cdot(\boldsymbol{r}_{\boldsymbol{j}}-\boldsymbol{r}_{\boldsymbol{j}'})}
\end{aligned} \tag{2.66}$$

The phase in the summand of the last line is explicitly

$$\begin{aligned}
\boldsymbol{G}\cdot(\boldsymbol{r}_{\boldsymbol{j}}-\boldsymbol{r}_{\boldsymbol{j}'}) &= \frac{1}{2M_{\max}+1}(\boldsymbol{b}_1 m_1 + \boldsymbol{b}_2 m_2)\cdot[(j_1-j_1')\boldsymbol{a}_1 + (j_2-j_2')\boldsymbol{a}_2] \\
&= 2\pi\left[m_1\frac{(j_1-j_1')}{2M_{\max}+1} + m_2\frac{(j_2-j_2')}{2M_{\max}+1}\right].
\end{aligned}$$

If $j_1 = j_1'$ and $j_2 = j_2'$, then $\boldsymbol{G}\cdot(\boldsymbol{r}_{\boldsymbol{j}}-\boldsymbol{r}_{\boldsymbol{j}'}) = 0$ and the sum in (2.66) simply gives the total number of grid points $(2M_{\max}+1)^2$. Otherwise all the exponents add up to zero. Thus we have

$$\sum_{\boldsymbol{G}\in\mathcal{G}} \mathrm{e}^{\mathrm{i}\boldsymbol{G}\cdot(\boldsymbol{r}_{\boldsymbol{j}}-\boldsymbol{r}_{\boldsymbol{j}'})} = (2M_{\max}+1)^2\delta_{\boldsymbol{j},\boldsymbol{j}'}. \tag{2.67}$$

Note that other choices of grids on the elementary cell may give a non-orthogonal sets of "finite-dimensional" delta functions.

The orthogonality property (2.67) allows us to use the "finite-dimensional" delta functions $\delta_{\boldsymbol{a}}(\boldsymbol{r})$ with $\boldsymbol{a} \equiv \boldsymbol{r}_{\boldsymbol{j}}$ as the new basis:

$$\delta_{\boldsymbol{j}}(\boldsymbol{r}) := \frac{\sqrt{|\Omega|}}{2M_{\max}+1}\delta_{\boldsymbol{r}_{\boldsymbol{j}}}(\boldsymbol{r}) = \frac{1}{2M_{\max}+1}\frac{1}{\sqrt{|\Omega|}}\sum_{\boldsymbol{G}\in\mathcal{G}} \mathrm{e}^{\mathrm{i}\boldsymbol{G}\cdot(\boldsymbol{r}-\boldsymbol{r}_{\boldsymbol{j}})}. \tag{2.68}$$

This "coordinate-representation" basis allows us to combine the Fourier method and the coordinate representation.

In practice, we construct the kinetic energy and/or momentum operators in the Fourier basis. Then we use the numerically constructed unitary matrix to transform from this basis into the coordinate-like basis, defined by the functions (2.68). In this new basis we include potential and other operators, that have simple expressions in the coordinate represenation. We use this method in the numerical band calculation of the optical flux lattice (chapter 4).

2.3 Numerical calculation of Chern number

In this section we summarize the numerical algorithm [96] that we use to calculate the Chern number of energy bands of the Dice lattice (chapter 3) or the total magnetic flux of the optical flux lattice (chapter 4). This algorithm is useful in case the band structure calculation is expensive – it allows to use a small grid of $\boldsymbol{k}$-points in the FBZ.

Let us assume that the lattice in question is rectangle and the $\boldsymbol{k}$-points form a rectangle grid:

$$k_x = \frac{2\pi}{a_x N_x} i, \quad k_y = \frac{2\pi}{a_y N_y} j, \quad i = 1, \ldots, N_x, \quad j = 1, \ldots, N_y. \tag{2.69}$$

Here a_x and a_y are sizes of the rectangle elementary cell in the x and y dimensions. N_x and N_y denote the numbers of $\boldsymbol{k}$-grid points in the k_x and k_y dimensions (don't confuse these numbers with the similar ones defined in the section 2.2.2). Usually we pick N_x and N_y in such a way that each elementary cell in the $\boldsymbol{k}$-grid is close to a square: $2\pi/(a_x N_x) \approx 2\pi/(a_y N_y)$.

Let us define normalized link variables between the eigenstates $|u_{\boldsymbol{k},n}\rangle$ in the $\boldsymbol{k}$-grid:

$$\boldsymbol{U}^{(n)}(\boldsymbol{k}) = \boldsymbol{e}_{\Delta\boldsymbol{k}} \frac{\langle u_{\boldsymbol{k},n} | u_{\boldsymbol{k}+\Delta\boldsymbol{k},n} \rangle}{|\langle u_{\boldsymbol{k},n} | u_{\boldsymbol{k}+\Delta\boldsymbol{k},n} \rangle|}. \tag{2.70}$$

Here the vector $\Delta\boldsymbol{k}$ points to the nearby $\boldsymbol{k}$-point on the grid depending on the component of $\boldsymbol{U}^{(n)}(\boldsymbol{k})$. If we consider the component $U_x^{(n)}(\boldsymbol{k})$, then $\Delta\boldsymbol{k} = 2\pi\boldsymbol{e}_x/(a_x N_x)$. In the same way, if we consider the component $U_y^{(n)}(\boldsymbol{k})$, then $\Delta\boldsymbol{k} = 2\pi\boldsymbol{e}_y/(a_y N_y)$. These link variables are well-defined if $\langle u_{\boldsymbol{k},n} | u_{\boldsymbol{k}+\Delta\boldsymbol{k},n} \rangle \neq 0$.

Now we can define a field on the $\boldsymbol{k}$-grid:

$$\tilde{F}_n(\boldsymbol{k}) = -\mathrm{i} \ln \left[U_x(\boldsymbol{k}) U_y \left(\boldsymbol{k} + \frac{2\pi}{a_x N_x} \boldsymbol{e}_x \right) U_x^{-1} \left(\boldsymbol{k} + \frac{2\pi}{a_y N_y} \boldsymbol{e}_y \right) U_y^{-1}(\boldsymbol{k}) \right]. \tag{2.71}$$

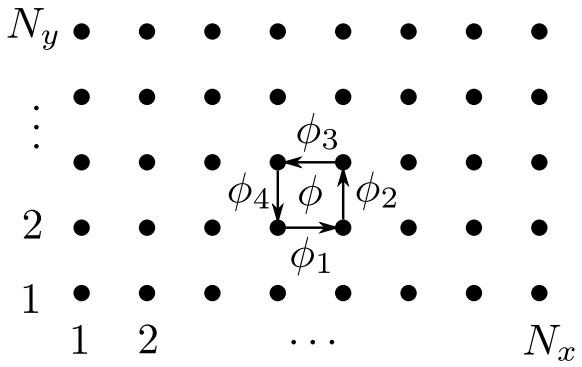

Figure 2.3: Discrete $\boldsymbol{k}$-grid in the FBZ. We calculate the discrete Berry curvature $\tilde{F}_n(\boldsymbol{k})$ by multiplying the phases, $\phi = \phi_1 + \phi_2 + \phi_3 + \phi_4$ of each link variable (after fixing the gauge for at least presented four grid points).

Since the link variables $U_x(\boldsymbol{k})$ and $U_y(\boldsymbol{k})$ are normalized, the logarithm in (2.71) returns overal phase of the multiplication of the four presented link variables (multiplied by the imaginary unit i). We chose the value of logarithm from the interval between $-\mathrm{i}\pi$ and $\mathrm{i}\pi$. One can notice that (2.71) is a discrete analogue of the Berry curvature $F_n(\boldsymbol{k})$ (eq. 2.24). We compute the numerical value of the Chern number by summing the discrete field $\tilde{F}_n(\boldsymbol{k})$ over all $\boldsymbol{k}$-grid points:

$$\tilde{c}_n = \frac{1}{2\pi} \sum_{\boldsymbol{k}} \tilde{F}_n(\boldsymbol{k}). \tag{2.72}$$

This "numerical" Chern number does not depend on our gauge choice: we can use any phases for the eigenstates $|u_{\boldsymbol{k},n}\rangle$. Another important property of $\tilde{c}_n$ is that by definition (meaning: up to the numerical precision) it is integer, independent on how many grid points we choose.

In practice, we don't have normalize link variables $U_x(\boldsymbol{k})$ and $U_y(\boldsymbol{k})$. Since the discrete Berry curvature $\tilde{F}_n(\boldsymbol{k})$ depends only on the overall phase of the multiplication of link variables, we can simply multiply all the required link variables (2.71) and then extract the phase. On the other hand, if we want to add separate phases of each link variables, then we get the correct overall phase only if we fix the gauge. By looking into the eq. 2.71 more closely, we can notice that we build up the discrete Berry curvature by adding up phases around a small rectangle loop near each $\boldsymbol{k}$-point on the grid (see fig. 2.3). In the limit $N_x, N_y \to \infty$, we get $\tilde{c}_n \to c_n$. Since the numeric Chern number $\tilde{c}_n$ can have only integer values (up to the numerical precision), then it cannot get close to the actual Chern number c_n continuously. By making the grid finer and finer, the value of $\tilde{c}_n$ jumps from one integer value to another while it reaches the correct one. In this way we can numerically calculate the exact value of Chern number c_n.

3 DICE OPTICAL LATTICE AS AN EXTENSION OF HALDANE MODEL

3.1 Haldane model

Let us review Haldane model before we continue with introducing its extension.

The original Haldane model [33] is a two-dimensional hexagonal lattice. The honeycomb structure can be viewed as two interpenetrating triangular lattices (see fig. 3.1).

The lattice is described by tight-binding model with two types of hoppings. There is a real hopping matrix element between nearest-neighbors on different triangular sublattices. The second type of hopping is between the next-nearest neighbors and couples each triangular sublattices separately.

We add a periodic local magnetic field in the direction perpendicular to the 2D plane of the lattice. The field has the full symmetry of the lattice. In addition the total flux over the unit cell is zero. Because of this the next-nearest neighbor hopping matrix elements acquire a non-trivial phase and become complex. This results in two energy bands that acquire nonzero Chern numbers.

The significant feature of the Haldane model is that it describes a two-dimensional lattice that exhibits nonzero Chern numbers (and thus a nonzero quantizuation of the Hall conductance σ_{H}) in the absence of an external magnetic field. In other words, the Haldane model is an example of how quantum Hall effect can appear as an intrinsic property of a band structure without external magnetic field.

Originally, Haldane mentioned that it is unlikely that his model will be physically realized [33]. However, in recent years it was experimentally realized using ultracold fermions [20].

3.2 The Dice optical lattice model

3.2.1 Lattice geometry

We consider a dice lattice, which consists of three triangle sub-lattices. One of them is called the *hub* sub-lattice. It is coupled to other two *rim* sub-lattices, that in turn are not coupled with each other. Let us denote the hub sub-lattice by B and the rim sub-lattice by A and C. The vectors that connect the nearest lattice sites are (fig. 3.2):

$$\boldsymbol{\delta}_1 = \frac{a}{2}(\boldsymbol{e}_x + \sqrt{3}\boldsymbol{e}_y), \quad \boldsymbol{\delta}_2 = \frac{a}{2}(\boldsymbol{e}_x - \sqrt{3}\boldsymbol{e}_y), \quad \boldsymbol{\delta}_3 = -a\boldsymbol{e}_x\,, \tag{3.1}$$

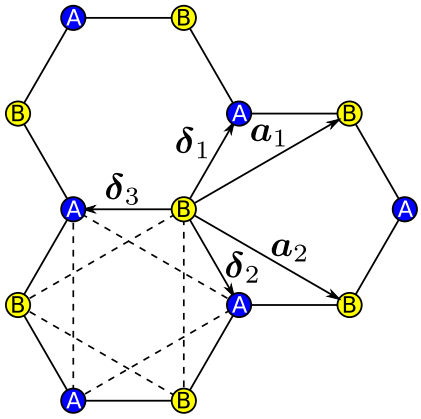

Figure 3.1: Hexagonal optical lattice of the Haldane model. The blue and yellow sites correspond to two triangular sub-lattices A and B. Solid lines show nearest-neighbor couplings between these sub-lattices. Dashed lines show next-nearest-neighbor couplings in each sub-lattice. The primitive lattice vectors are $\boldsymbol{a}_1$ and $\boldsymbol{a}_2$. Nearest sites are connected with the vectors $\boldsymbol{\delta}_1$, $\boldsymbol{\delta}_2$ and $\boldsymbol{\delta}_3$.

where a is the distance between two such sites. The basic lattice vectors

$$\boldsymbol{a}_1 = a(3\boldsymbol{e}_x + \sqrt{3}\boldsymbol{e}_y)/2, \quad \boldsymbol{a}_2 = a(3\boldsymbol{e}_x - \sqrt{3}\boldsymbol{e}_y)/2 \tag{3.2}$$

make a rhombic elementary cell. Using these vectors we define a set of lattice vectors $\boldsymbol{r_n} = n_1\boldsymbol{a}_1 + n_2\boldsymbol{a}_2$ (with integers n_1 and n_2) spaning the hub sub-lattice B (Bravais lattice). The two rim sub-lattices are defined in the following way. The first rim sub-lattice A is shifted from the hub sub-lattice B by the vector $\boldsymbol{\delta}_1$ in such way that sub-lattices A and B alone make a honeycomb lattice. The second rim sub-lattice C is shifted to the opposite direction by $-\boldsymbol{\delta}_1$ (see fig. 3.2). Let us introduce a set of vectors, that span all the lattice sites:

$$\boldsymbol{r}_{\boldsymbol{n},s} = \boldsymbol{r_n} + s\boldsymbol{\delta}_1. \tag{3.3}$$

Here the index $s = 0, \pm 1$ labels the three sublattices. The sites of the hub sub-lattice ($s = 0$) coinside with the lattice vectors: $\boldsymbol{r}_{\boldsymbol{n},0} = \boldsymbol{r_n}$. The sites of the rim sub-lattices A and C shifted by $\pm\boldsymbol{\delta}_1$, i.e. $\boldsymbol{r}_{\boldsymbol{n},+1} = \boldsymbol{r_n} + \boldsymbol{\delta}_1$ and $\boldsymbol{r}_{\boldsymbol{n},-1} = \boldsymbol{r_n} - \boldsymbol{\delta}_1$.

It is convenient to introduce an additional lattice vector $\boldsymbol{a}_3 = \boldsymbol{a}_1 - \boldsymbol{a}_2$. A set of the three lattice vectors $\boldsymbol{a}_i$ ($i = 1, 2, 3$) together with the opposite vectors $-\boldsymbol{a}_i$ connect all next-nearest lattice sites, and can be related to $\boldsymbol{\delta}_i$ as: $\boldsymbol{a}_1 = \boldsymbol{\delta}_1 - \boldsymbol{\delta}_3$, $\boldsymbol{a}_2 = \boldsymbol{\delta}_2 - \boldsymbol{\delta}_3$ and $\boldsymbol{a}_3 = \boldsymbol{\delta}_1 - \boldsymbol{\delta}_2$.

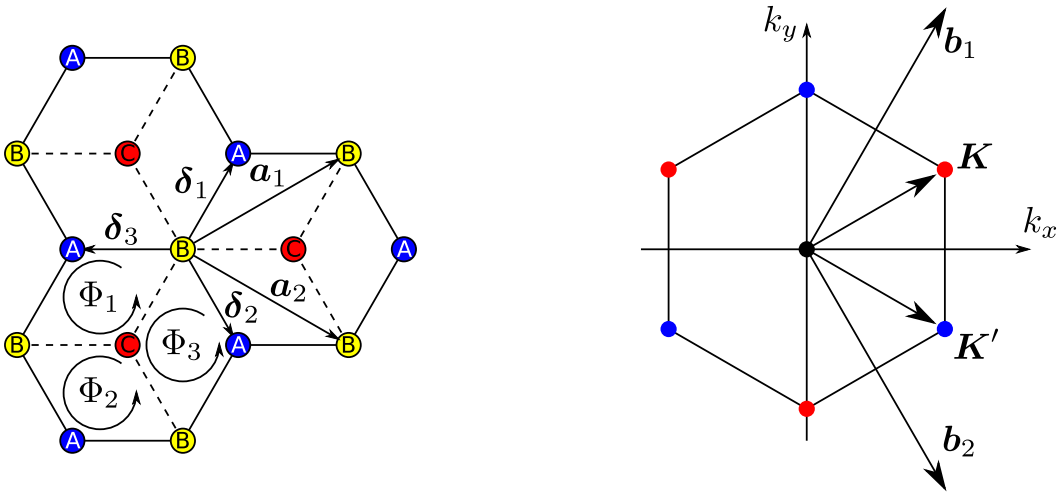

Figure 3.2: *Left*: dice lattice. The blue, green and red sites correspond to three different triangular sub-lattices A, B and C. Solid lines show couplings between the sites A and B. Dashed lines show couplings between the sites B and C. The primitive lattice vectors are $\boldsymbol{a}_1$ and $\boldsymbol{a}_2$. Nearest sites are connected with the vectors $\boldsymbol{\delta}_1$, $\boldsymbol{\delta}_2$ and $\boldsymbol{\delta}_3$. *Right*: hexagonal first Brillouin zone of the reciprocal lattice defined by the primitive reciprocal lattice vectors $\boldsymbol{b}_1$ and $\boldsymbol{b}_2$. Two inequivalent corners are at the points $\boldsymbol{K}$ (red) and $\boldsymbol{K}'$ (blue).

The basic reciprocal lattice vectors

$$\boldsymbol{b}_1 = \frac{2\pi}{3a}(\boldsymbol{e}_x + \sqrt{3}\boldsymbol{e}_y), \quad \boldsymbol{b}_2 = \frac{2\pi}{3a}(\boldsymbol{e}_x - \sqrt{3}\boldsymbol{e}_y) \tag{3.4}$$

are orthogonal to the lattice vectors, $\boldsymbol{a}_i \cdot \boldsymbol{a}_j = 2\pi\delta_{ij}$, $i, j = 1, 2$. The first Brillouin zone is hexagonal with two inequivalent corners $\boldsymbol{K}$ and $\boldsymbol{K}'$ positioned at $\boldsymbol{K} = (2\boldsymbol{b}_1 + \boldsymbol{b}_2)/3$ and $\boldsymbol{K}' = (\boldsymbol{b}_1 + 2\boldsymbol{b}_2)/3$. In terms of the Cartesian coordinates these points are given by

$$\boldsymbol{K} = \frac{2\pi}{9a}(3\boldsymbol{e}_x + \sqrt{3}\boldsymbol{e}_y), \quad \boldsymbol{K}' = \frac{2\pi}{9a}(3\boldsymbol{e}_x - \sqrt{3}\boldsymbol{e}_y), \tag{3.5}$$

as one can see in fig. 3.2.

3.2.2 Tight-binding model

We shall make use of the tight-binding model in which the single particle states $|\boldsymbol{r}_{\boldsymbol{n},s}\rangle$ represent the Wannier-type wave-functions localised at each lattice site $\boldsymbol{r}_{\boldsymbol{n},s}$, with $s = 0, \pm 1$ being the sub-lattice index. In the language of the second quantisation these single-partice states read $|\boldsymbol{r}_{\boldsymbol{n},s}\rangle = c^\dagger(\boldsymbol{r}_{\boldsymbol{n},s})|\text{vac}\rangle$, where $|\text{vac}\rangle$ is the Fock vacuum state, $c^\dagger(\boldsymbol{r}_{\boldsymbol{n},s})$ and $c(\boldsymbol{r}_{\boldsymbol{n},s})$ being the creation and annihilation operators of an atom in the corresponding localized state.

The full Hamiltonian of the system consist of three terms,

$$H = H_1 + H_2 + H_3. \tag{3.6}$$

The first term H_1 describes the laser-assisted tunneling of atoms between the sites of the hub sublattice B ($s = 0$) and its nearest neighbouring sites that belong to the rim sublatices A and C with $s = \pm 1$:

$$H_1 = \sum_{\boldsymbol{n}} \sum_{s=\pm 1} J^{(s)} \sum_{i=1}^{3} \mathrm{e}^{\mathrm{i}\boldsymbol{p}_s \cdot (\boldsymbol{r}_{\boldsymbol{n}} + s\boldsymbol{\delta}_i/2)} c^\dagger(\boldsymbol{r}_{\boldsymbol{n}}) c(\boldsymbol{r}_{\boldsymbol{n}} + s\boldsymbol{\delta}_i) + \mathrm{H.\,c.}\,, \tag{3.7}$$

where $J^{(s)}$ are the coupling amplitudes. The laser assisted tunneling (considered in refs. [18, 26, 97, 17, 98, 99]) is accompanied by the transfer of the recoil momentum $\boldsymbol{p}_s$ with $s = \pm 1$, to be labelled simply by $\boldsymbol{p}_\pm \equiv \boldsymbol{p}_{\pm 1}$. In the present situation $\boldsymbol{p}_+$ can generally differ from $\boldsymbol{p}_-$ because the transitions between the different sublattices can be induced by different lasers. Note that the nearest neighbour hopping alone is sufficient to generate fluxes through rhombic plaquettes

$$\Phi_i = \pm(\boldsymbol{p}_+ - \boldsymbol{p}_-) \cdot \boldsymbol{a}_i/2\,, \tag{3.8}$$

with $\boldsymbol{a}_i$ representing a diagonal vector of the plaquette in question. Yet the magnetic flux over the whole hexagonal plaquette remains zero.

The second term H_2 takes into account the tunneling between the next-nearest neighbouring sites belonging to the same sublattice with $s = 0, \pm 1$:

$$H_2 = \sum_{\boldsymbol{n}} \sum_{s=0,\pm 1} J_2^{(s)} \sum_{i=1}^{3} c^\dagger(\boldsymbol{r}_{\boldsymbol{n},s}) c(\boldsymbol{r}_{\boldsymbol{n},s} + \boldsymbol{a}_i) + \mathrm{H.\,c.} \tag{3.9}$$

This term describes the usual (not laser-assisted) hopping transitions between nearest sites in each of the three triangular sublattices, and $J_2^{(s)}$ with $s = 0, \pm 1$ are the correspoding matrix elements for the tunneling between the atoms belonging to the s-th sublattice.

The third therm H_3 desribes the energy mismatch for the particles populating the different sublattices:

$$H_3 = \sum_{\boldsymbol{n}} \sum_{s=0,\pm 1} \varepsilon_s c^\dagger(\boldsymbol{r}_{\boldsymbol{n},s}) c(\boldsymbol{r}_{\boldsymbol{n},s}). \tag{3.10}$$

The on-site energies ε_s are the diagonal matrix elements of the Hamiltonian in the basis of the Wannier states. Without a loss of generality we can take the on-site energy of the hub sublattice B to be zero: $\varepsilon_0 = 0$. The on-site energies of other *rim*

sublattices are to be labelled as $\varepsilon_{\pm 1} \equiv \varepsilon_{\pm}$.

Since the first term H_1 involves complex phase factors that depend on the elementary cell number $\boldsymbol{n}$, the full Hamiltonian H is not translationary invariant. Yet, we will transform the annihilation operators according to $c(\boldsymbol{r}_{\boldsymbol{n},0}) \to c(\boldsymbol{r}_{\boldsymbol{n},0})$ and $c(\boldsymbol{r}_{\boldsymbol{n},s}) \to c(\boldsymbol{r}_{\boldsymbol{n},s}) \exp(-\mathrm{i}\boldsymbol{p}_s \cdot \boldsymbol{r}_{\boldsymbol{n}})$ with $s = \pm 1$, and perform the corresponding transformation for the creation operators. This gauge transformation makes the full Hamiltonian (3.6) translationary invariant.

Transition to the reciprocal space is carried out by introducing new operators

$$c_s(\boldsymbol{k}) = \frac{1}{\sqrt{N}} \sum_{\boldsymbol{n}} c(\boldsymbol{r}_{\boldsymbol{n},s}) \mathrm{e}^{-\mathrm{i}\boldsymbol{k}\cdot\boldsymbol{r}_{\boldsymbol{n}}}\,, \quad c(\boldsymbol{r}_{\boldsymbol{n},s}) = \frac{1}{\sqrt{N}} \sum_{\boldsymbol{k}} c_s(\boldsymbol{k}) \mathrm{e}^{\mathrm{i}\boldsymbol{k}\cdot\boldsymbol{r}_{\boldsymbol{n}}}\,, \tag{3.11}$$

together with the Hermitian conjugated creation operators $c_s^\dagger(\boldsymbol{k})$. Here N is a number of elementary cells in the quantisation area, and the vectors $\boldsymbol{r}_{\boldsymbol{n}} = \boldsymbol{r}_{\boldsymbol{n},0}$ are located at the sites of the hub lattice. In terms of the new operators the Hamiltonian (3.6) splits into its $\boldsymbol{k}$-components:

$$H = \sum_{\boldsymbol{k}} H(\boldsymbol{k})\,, \quad H(\boldsymbol{k}) = \left[\begin{array}{ccc} c_+^\dagger(\boldsymbol{k}) & c_0^\dagger(\boldsymbol{k}) & c_-^\dagger(\boldsymbol{k}) \end{array}\right] \mathcal{H}(\boldsymbol{k}) \left[\begin{array}{c} c_+(\boldsymbol{k}) \\ c_0(\boldsymbol{k}) \\ c_-(\boldsymbol{k}) \end{array}\right], \tag{3.12}$$

where $\mathcal{H}(\boldsymbol{k})$ is a 3×3 matrix:

$$\mathcal{H}(\boldsymbol{k}) = \left[\begin{array}{ccc} \varepsilon_+ + 2J_2^{(+)} f(\boldsymbol{k}-\boldsymbol{p}_+) & J^{(+)} g(\boldsymbol{k}-\boldsymbol{p}_+/2) & 0 \\ J^{(+)} g^*(\boldsymbol{k}-\boldsymbol{p}_+/2) & 2J_2^{(0)} f(\boldsymbol{k}) & J^{(-)} g(\boldsymbol{k}-\boldsymbol{p}_-/2) \\ 0 & J^{(-)} g^*(\boldsymbol{k}-\boldsymbol{p}_-/2) & \varepsilon_- + 2J_2^{(-)} f(\boldsymbol{k}-\boldsymbol{p}_-) \end{array}\right]. \tag{3.13}$$

It is convenient to add an extra phase factor to the transformed operators $c_s(\boldsymbol{k}) \to c_s(\boldsymbol{k}) \mathrm{e}^{\mathrm{i}\boldsymbol{p}_s \cdot s\boldsymbol{\delta}_1/2}$. In that case the functions

$$f(\boldsymbol{k}) = \sum_{i=1}^{3} \cos(\boldsymbol{k}\cdot\boldsymbol{a}_i), \quad g(\boldsymbol{k}) = \mathrm{e}^{\mathrm{i}\boldsymbol{k}\cdot\boldsymbol{\delta}_1} \sum_{i=1}^{3} \mathrm{e}^{-\mathrm{i}\boldsymbol{k}\cdot\boldsymbol{\delta}_i} \tag{3.14}$$

entering Eq. (3.13) are translationally symmetric in the reciprocal space

$$f(\boldsymbol{k}+\boldsymbol{G}) = f(\boldsymbol{k})\,, \quad g(\boldsymbol{k}+\boldsymbol{G}) = g(\boldsymbol{k})\,, \tag{3.15}$$

where $\boldsymbol{G} = n_1\boldsymbol{b}_1 + n_2\boldsymbol{b}_2$ is a reciprocal lattice vector, n_1 and n_2 being integers. Consequently the matrix-Hamiltonian $\mathcal{H}(\boldsymbol{k})$ is also fully tranlationary invariant in the reciprocal space $\mathcal{H}(\boldsymbol{k}) = \mathcal{H}(\boldsymbol{k}+\mathbf{G})$. Furthermore, the functions $f(\boldsymbol{k})$ and $g(\boldsymbol{k})$

obey the following reflection properties

$$f(\boldsymbol{k}) = f(-\boldsymbol{k})\,, \quad g(\boldsymbol{k}) = g^*(-\boldsymbol{k})\,. \tag{3.16}$$

All this helps to consider various symmetries of the matrix-Hamiltonian (3.13).

3.3 Phases of non-interacting fermions

3.3.1 Chern numbers and symmetries of the system

Since the momentum-space Hamiltonian (3.13) represents a three level system, there are three energy bands $E_n(\boldsymbol{k})$, where $n = 1, 2, 3$, and associate to each of them an integer Chern number $c_n = 1, 2, 3$. We also identify two possible band gaps. The first band gap Δ_{12} is defined between the first ($n = 1$) and second ($n = 2$) bands and the second band gap Δ_{23} is defined between the second ($n = 2$) and the third ($n = 3$) bands.

The Chern number c_n for the n-th band is defined as a surface integral of a Berry curvature over the first Brillouin zone (FBZ) [**?**, 18]:

$$c_n = -\frac{1}{2\pi} \int_{\mathrm{FBZ}} \mathrm{d}^2 k\, F_n(\boldsymbol{k}). \tag{3.17}$$

The Berry curvature $F_n(\boldsymbol{k})$ can be expressed in terms of the eigenvectors $|u_{n,\boldsymbol{k}}\rangle$ of the Hamiltonian (3.13) as

$$F_n(\boldsymbol{k}) = \mathrm{i} \left(\frac{\partial}{\partial k_x} \langle u_{n,\boldsymbol{k}}| \right) \left(\frac{\partial}{\partial k_y} |u_{n,\boldsymbol{k}}\rangle \right) - \mathrm{i} \left(\frac{\partial}{\partial k_y} \langle u_{n,\boldsymbol{k}}| \right) \left(\frac{\partial}{\partial k_x} |u_{n,\boldsymbol{k}}\rangle \right) . \tag{3.18}$$

It is well defined as long the eigen-energies $E_n(\boldsymbol{k})$ are not degenerate for any fixed value of $\boldsymbol{k}$. Therefore the Chern number c_n can be ascribed to the n-th band if the latter does not touch any other bands. If the Fermi energy is situated in a band gap, the Chern number is directly related to Hall conductivity due to chiral edge states of the occupied bands [100] via $\sigma_{xy} = -e^2 c_n/\hbar$ [101]. For numerical calculation we make use of the discretised version of the Berry curvature (3.18), as described in [96].

For both *rim* sublattices A and C, we set on-site energies of to be symmetrially shifted away from the zero point $\varepsilon_+ = -\varepsilon_- = \varepsilon$. We also take the tunneling amplitudes to be equal $J^{(+)} = J^{(-)} = J$, $J_2^{(+)} = J_2^{(0)} = J_2^{(-)} = J_2$ and assume the recoil momenta to be opposite $\boldsymbol{p}_+ = -\boldsymbol{p}_- = \boldsymbol{p}$ for both *rim* sublattices A and C. The choice of opposite recoil momenta ensures the maximum flux, because the

magnetic flux through a rhombic plaquette Φ_i given by Eq. (3.8) is proportional to the difference of these vectors. Under these conditions, the matrix representation of the $\boldsymbol{k}$-space Hamiltonian becomes

$$\mathcal{H}(\boldsymbol{k}) = \begin{bmatrix} \varepsilon + 2J_2 f(\boldsymbol{k}-\boldsymbol{p}) & Jg(\boldsymbol{k}-\boldsymbol{p}/2) & 0 \\ Jg^*(\boldsymbol{k}-\boldsymbol{p}/2) & 2J_2 f(\boldsymbol{k}) & Jg(\boldsymbol{k}+\boldsymbol{p}/2) \\ 0 & Jg^*(\boldsymbol{k}+\boldsymbol{p}/2) & -\varepsilon + 2J_2 f(\boldsymbol{k}+\boldsymbol{p}) \end{bmatrix}. \tag{3.19}$$

This form of the Hamiltonian exhibits some symmetries. The first symmetry involves inversion of the onsite energies $\varepsilon \to -\varepsilon$ follwed by the unitary transformation that changes the first row with the third one (i.e. interchanges the *rim* sublattices A and C), as well as the momentum inversion $\boldsymbol{k} \to -\boldsymbol{k}$. Using the reflection properties of the functions f and g given by Eq. (3.16), one arrives at the same Hamiltonian (3.19). The second symmetry is $J \to -J$, which is a simple gauge transformation. Using these two symmetries we see that the change $J_2 \to -J_2$ gives $\mathcal{H}(\boldsymbol{k}) \to -\mathcal{H}(\boldsymbol{k})$. To sum up, all the three mentioned symmetries are: $(\varepsilon \to -\varepsilon, \mathcal{H} \to \mathcal{H})$, $(J \to -J, \mathcal{H} \to \mathcal{H})$ and $(J_2 \to -J_2, \mathcal{H} \to -\mathcal{H})$.

3.3.2 Numerical analysis

In this section, we numerically study the Chern phases of non-interacting fermions. In order to present dependence of the Chern number on the parameters ε, J, J_2 and $\boldsymbol{p}$ we adopt a similar presentation of the phase diagram scheme as in [99]. We choose the energy unit to be the nearest-neighbour tunneling amplitude J. For the recoil momentum $\boldsymbol{p}$, we express the p_x component in the units of K_x and the component p_y in the units of K_y, where $\boldsymbol{K}$ is one of the FBZ corners, defined in (3.5). In all the phase diagrams we present the dependence of the Chern number $c_n = c_n(p_x, p_y)$ on the components of the recoil momentum $\boldsymbol{p}$ using different colours for each possible values of c_n. The areas corresponding to a topologically trivial phase with a zero Chern number are shown in green ($c_n = 0$). On the other hand, the areas corresponding to non-trivial Chern phases are shown in yellow ($c_n = 1$), red ($c_n = 2$), cyan ($c_n = -1$) and blue ($c_n = -2$).

First we characterise topological properties of the band structure if there are no next-nearest neighbour coupling ($J_2 = 0$). In the fig. 3.3 we show the Chern number phase diagrams for $\varepsilon = J$. One can identify regions where Chern numbers are $\{c_1, c_2, c_3\} = \{0, 0, 0\}$, $\{-1, 2, -1\}$ and $\{1, -2, 1\}$. In the first type of the regions (green colour) we have topologycally trivial regions. In other regions we have non-zero Chern numbers with band gaps $\Delta_{12} = \Delta_{23} = 0$. Analysis of a band structure in these regions shows that the bands do not overlap with each other, as one can see

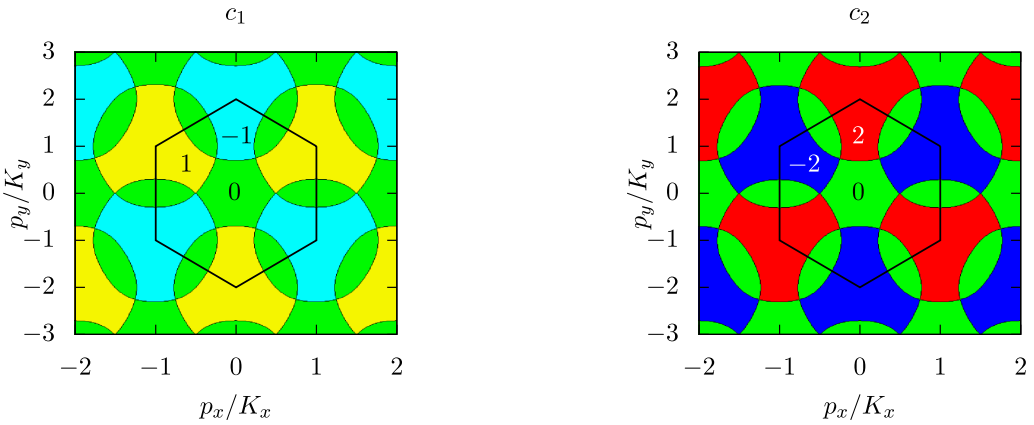

Figure 3.3: Chern number dependence on the recoil momentum $\boldsymbol{p}$ in the case $\varepsilon = J$ and $J_2 = 0$. In the left panel we present the phase diagram of the lowest band Chern number c_1. In the right panel we show corresponding phase diagram for the middle band. Since the sum of Chern numbers over all three bands is zero, the third band gives the same phase diagram as the first one ($c_1 = c_3$). The green regions correspond to the Chern number zero. The yellow, red, cyan and blue regions correspond to the Chern numbers 1, 2, -1 and -2 respectively. By the hexagon we show the FBZ in the $\boldsymbol{p}$-plane.

in fig. 3.6 presented in the next chapter. These are regions corresponding to semi-metallic Chern phases. Note that in the case $J_2 = 0$, the change $\boldsymbol{p} \to \boldsymbol{p} + \boldsymbol{G}$, where $\boldsymbol{G}$ is the reciprocal lattice vector, correspond to a gauge transformation. Thus there is a symmetry ($\boldsymbol{p} \to \boldsymbol{p} + \boldsymbol{G}, \mathcal{H} \to \mathcal{H}$). In the phase diagram (fig. 3.3) we also show the FBZ in the $\boldsymbol{p}$-plane, which is a hexagon with two inequivalent corners positioned at the points $\boldsymbol{K}$ and $\boldsymbol{K}'$.

Now let us analyse effects of the non-zero next-nearest neighbour coupling. For this we set $J_2 = 0.3J$ and $\varepsilon = 2J$. The Cher number phase diagrams are presented in the fig. 3.4. We can see regions with the Chern numbers corresponding to trivial phases $\{0, \pm 1, \mp 1\}$ and $\{\pm 1, 0, \mp 1\}$. In both regions we can find points where there is non-zero band gaps $\Delta_{12} > 0$ and/or $\Delta_{23} > 0$. This shows that there exist topological Chern insulating phases. For example in the point $\boldsymbol{p} = \boldsymbol{K}$, we have the Chern numbers $\{0, -1, 1\}$ and with the band gap between the middle and highest bands $\Delta_{23} \approx 0.26J$. By positioning the Fermi energy in the gap between the second and third bands we get the Chern insulating phase. Another interesting point is $\boldsymbol{p} = 2\boldsymbol{K}$, which gives the Chern numbers $\{-1, 0, 1\}$ and the band gaps $\Delta_{12} \approx 1.55J$ and $\Delta_{23} \approx 0.54J$. The bottom and top bands have non-zero Chern numbers, while it is zero for the middle band. Depending on the filling there are two types of topologically non-trivial phases. If the Fermi energy is positioned in one of the band

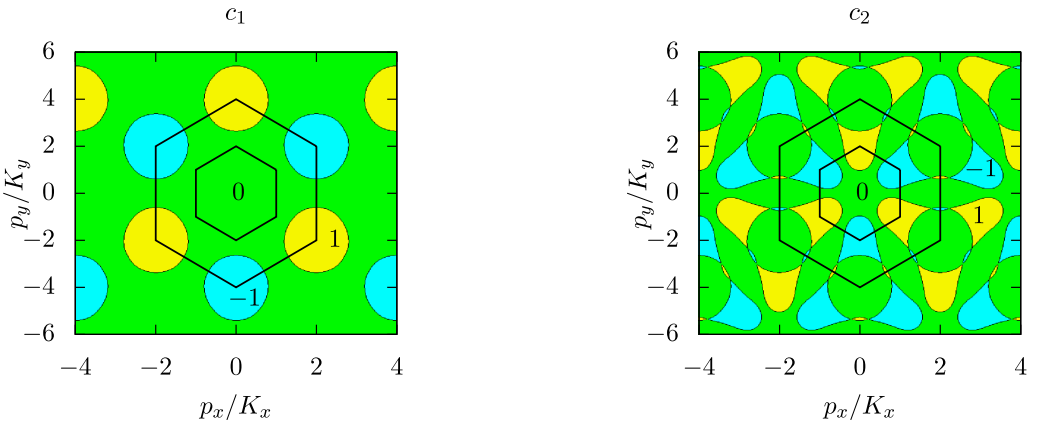

Figure 3.4: Chern number dependence on the recoil momentum $\boldsymbol{p}$ in the case $\varepsilon = 2J$ and $J_2 = 0.3J$. In the left panel we present the Chern number c_1 of the lowest band, while in the right panel we show the Chern number c_2 of the middle band. For the third band (not shown here) we have $c_3 = -(c_1 + c_2)$. The green, yellow, red, cyan and blue regions correspond to the Chern numbers 0, 1, 2, -1 and -2 respectively. By the smaller hexagon we show the FBZ, which was in the case $J_2 = 0$. Since the introduction of non-zero J_2 changes the periodicity of the $\boldsymbol{p}$-dependence, we also show a bigger hexagon, which is now the FBZ in the $\boldsymbol{p}$-plane.

gaps, we get a topological insulating phase. If the Fermi energy is in the middle band by partially filling it, we get Chern metallic phase. Note that in the case of non-zero NNN couplings ($J_2 \neq 0$) the translation symmetry in the recoil momentum $\boldsymbol{p}$ is smaller than in the case of zero NNN couplings: one has to shift the momentum by $2\boldsymbol{G}$ rather than $\boldsymbol{G}$. In the phase diagram fig. 3.4 we show this by extending the FBZ, which is now a bigger hexagon.

There are more types of Chern phases when the coupling J_2 is larger than in the previous discussion and comparable to the on-site energy ε. For $\varepsilon = J_2 = 0.5J$ we find insulating phases with Chern numbers $\{\pm 1, \pm 1, \mp 2\}$ and metallic phases with Chern numbers $\{\pm 2, 0, \mp 2\}$ (fig. 3.5). For example in the point $\boldsymbol{p} = 2\boldsymbol{K}$ we get Chern numbers $c_1 = c_2 = -1$ and $c_3 = 2$ with band gaps $\Delta_{12} \approx 0.61J$ and $\Delta_{23} \approx 0.54J$. Another interesting point is $\boldsymbol{p} = (2K_x, K_y)$ where the Chern numbers are $c_1 = -2$, $c_2 = 0$ and $c_3 = 2$ (white point in the fig. 3.5). The bulk spectrum in this point is given in the fig. 3.6. Note that there is a gap $\Delta_{13} \approx 1.35J$ between the lowest and highest bands. In this gap we have a middle band with the zero Chern number. By setting the Fermi energy in this gap one gets the Chern metallic phase with the Chern number $c_1 = -2$.

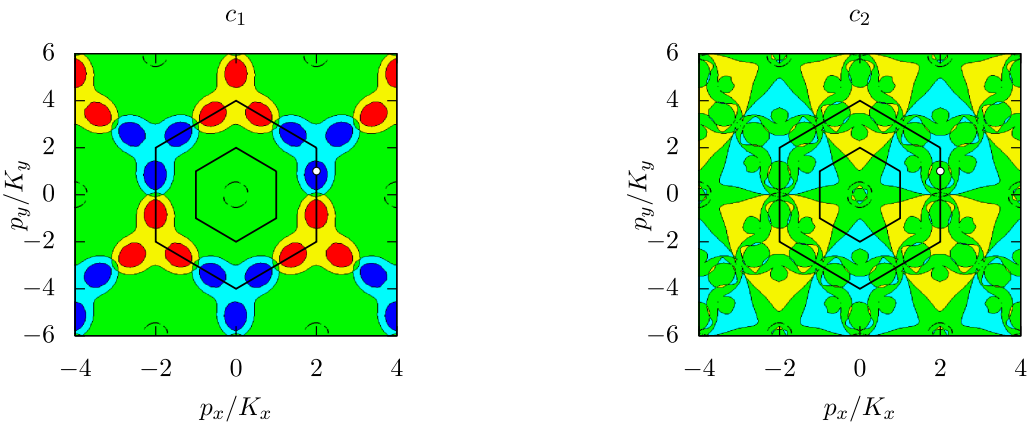

Figure 3.5: Chern number dependence on the recoil momentum in the case $\varepsilon = 0.5J$ and $J_2 = 0.5J$. *Left*: Chern number c_1 of the lowest band. *Right*: Chern number c_2 of the middle band. The colour scheme is the same as in the figs. 3.3 and 3.4. The white point is $\boldsymbol{p} = (2K_x, K_y)$ where the Chern numbers are $c_1 = -2$, $c_2 = 0$ and c_3 (see the spectrum in the fig. 3.6).

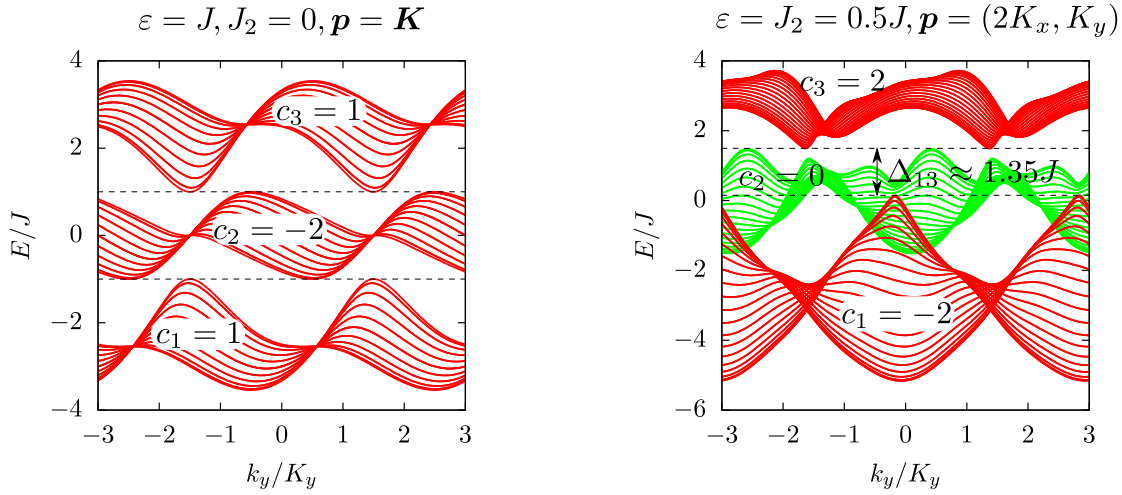

Figure 3.6: Bulk lattice spectrum, projected to $k_x = 0$ and plotted from $k_y = -3K_y$ to $3K_y$. From the fig. 3.2 we see that such kind of projection captures both inequivalent FBZ corners together with the centre point. *Left*: the spectrum for the point $\boldsymbol{p} = \boldsymbol{K}$ of the phase diagram for the case with no NNN-coupling (fig. 3.3). We show that the energy bands do not overlap and give semi-metallic phase if we fill the first one or the first two bands. *Right*: the spectrum for the point $\boldsymbol{p} = (2K_x, K_y)$ of the phase diagram fig. 3.5. There are two bands with non-zero Chern numbers ± 2 separated from the third band with the zero Chern number by the gap $\Delta_{13} \approx 1.35J$.

3.4 Analytic Chern number calculation

3.4.1 Berry connection

The Berry connection of the n-th band is defined as [102, 99]

$$\boldsymbol{A}_n(\boldsymbol{k}) = \mathrm{i}\langle u_{\boldsymbol{k},n}|\nabla_{\boldsymbol{k}}|u_{\boldsymbol{k},n}\rangle, \tag{3.20}$$

where $|u_{\boldsymbol{k},n}\rangle$ is denotes the n-th eigenvector of the matrix (3.13). We can express the Berry curvature (3.18) as the z component of the field $\boldsymbol{B}_n = \nabla \times \boldsymbol{A}$, namely $F_n(\boldsymbol{k}) = \boldsymbol{e}_z \cdot \boldsymbol{B}_n$. Now using the Stoke's theorem we change the integral featured in Eq.(3.17) over the FBZ to the contour integral around the FBZ,

$$\frac{1}{2\pi}\int_{\mathrm{FBZ}} \mathrm{d}^2k\, F_n(\boldsymbol{k}) \to \frac{1}{2\pi}\oint_{\mathrm{FBZ}} \mathrm{d}\boldsymbol{k}\cdot\boldsymbol{A}_n - \frac{1}{2\pi}\sum\oint_{\mathrm{singul}} \mathrm{d}\boldsymbol{k}\cdot\boldsymbol{A}_n\,.$$

where the last term excludes any contribution due to the gauge dependent singular points of the vector potential [99]. Since the $\boldsymbol{k}$-space Hamiltonian (3.13) and its eigenstates are periodic in the FBZ, $\boldsymbol{A}_n$ is also periodic. Thus the contour integral around the FBZ (the first term on the r.h.s. of the above equation) is zero. However the Berry connection $\boldsymbol{A}_n$ may contain unphysical singular points represented by the second term in above equaion. The Chern number then can be calculated by integrating $\boldsymbol{A}_n$ around each excluded singular point [99], giving

$$c_n = \frac{1}{2\pi}\sum\oint_{\mathrm{singul}} \mathrm{d}\boldsymbol{k}\cdot\boldsymbol{A}_n\,, \tag{3.21}$$

where the sum over all singular points.

3.4.2 Momentum space Hamiltonian and its eigenstates

Let us establishing a general structure of the eigenstates for the matrix Hamiltonian $\mathcal{H}(\boldsymbol{k})$, Eq.(3.19). For this we introduce a basis of our three-level system $|s\rangle$, with $s = 0, \pm 1$, and rewrite the matrix Hamiltonian in the state-vector notation as

$$H(\boldsymbol{k}) = \sum_{s=0,\pm1} |s\rangle d_s(\boldsymbol{k})\langle s| + \sum_{s=\pm1}\left(|s\rangle g_s(\boldsymbol{k})\mathrm{e}^{\mathrm{i}s\alpha_s(\boldsymbol{k})}\langle 0| + \mathrm{H.\,c.}\right), \tag{3.22}$$

where $d_s(\boldsymbol{k})$ stands for the diagonal matrix elements:

$$d_s(\boldsymbol{k}) = s\varepsilon + 2J_2 f(\boldsymbol{k} - s\boldsymbol{p})\,. \tag{3.23}$$

The off-diagonal matrix elements are represented in terms of the amplitude $g_{\pm 1}(\boldsymbol{k}) \equiv g_{\pm}(\boldsymbol{k})$ and the phase $\alpha_{\pm 1}(\boldsymbol{k}) \equiv \alpha_{\pm}(\boldsymbol{k})$ as:

$$Jg(\boldsymbol{k} \mp \boldsymbol{p}/2) = g_{\pm}(\boldsymbol{k})\mathrm{e}^{\mathrm{i}\alpha_{\pm}(\boldsymbol{k})} \tag{3.24}$$

Since there is no coupling between the A and C sublattices, one can perform a $\boldsymbol{k}$-dependent unitary transformation eliminating the phase factors

$$|s\rangle \to |s, \boldsymbol{k}\rangle = |s\rangle \mathrm{e}^{\mathrm{i}s\alpha_s(\boldsymbol{k})}, \qquad s = \pm 1,$$

and leave the basis vector $|0\rangle$ unchanged ($|0\rangle = |0, \boldsymbol{k}\rangle$). In the new basis the Hamiltonian (3.22) is characterised by real and symmetric matrix elements. Its eigenvectors can be cast in terms of these vectors with real coefficients $C_{n,s}(\boldsymbol{k})$:

$$|u_{\boldsymbol{k},n}\rangle = \sum_{s=0,\pm 1} C_{n,s}(\boldsymbol{k})|s, \boldsymbol{k}\rangle \equiv \sum_{s=0,\pm 1} |s\rangle C_{n,s}(\boldsymbol{k})\mathrm{e}^{\mathrm{i}s\alpha_s(\boldsymbol{k})}\,, \tag{3.25}$$

Combining Eqs. (3.20) and (3.25), one arrives at the following expression for the Berry connection

$$\boldsymbol{A}_n(\boldsymbol{k}) = -\sum_{s=\pm 1} sC_{n,s}^2(\boldsymbol{k})\nabla_{\boldsymbol{k}}\alpha_s(\boldsymbol{k}). \tag{3.26}$$

This result together with Eq. (3.21) will be subsequently used in determining the Chern numbers.

3.4.3 Determination of the Chern numbers: general

To determine the Chern number given by (3.21), one needs to find a behaviour of the vector potential at its singular points. Singularities of the vector potential can emerge at the points where the phase of the coupling matrix element $g_{\pm}(\boldsymbol{k})\mathrm{e}^{\mathrm{i}\alpha_{\pm}(\boldsymbol{k})}$ given by eq. 3.24 is not determined. This happens if the function $g(\boldsymbol{k} - \boldsymbol{p}_{\pm}/2)$ goes to zero. The function $g(\boldsymbol{k})$ given by eq. 3.14 is zero at the corners of the FBZ, namely at two inequivalent points $\boldsymbol{K}$ and $\boldsymbol{K}'$. Thus there two pairs of points

$$\boldsymbol{K}_{\pm} = \pm\boldsymbol{p}/2 + \boldsymbol{K}\,, \quad \boldsymbol{K}'_{\pm} = \pm\boldsymbol{p}/2 + \boldsymbol{K}'\,. \tag{3.27}$$

at which the function $g(\boldsymbol{k} \mp \boldsymbol{p}/2)$ goes to zero and its phase $\alpha_{\pm}(\boldsymbol{k})$ is undefined. Let us determine the coupling matrix elemement $g_{\pm}(\boldsymbol{k})\mathrm{e}^{\mathrm{i}\alpha_{\pm}(\boldsymbol{k})}$ in a vicitity of these points. Combing eqs. 3.14 and 3.24, the amplitude and phase of the coupling element

reads up to the first-order in the dispacement vector $\boldsymbol{q}$, i.e. for $qa \ll 1$ with $q = |\boldsymbol{q}|$:

$$g_{\pm}(\boldsymbol{K}_{\pm} + \boldsymbol{q}) \approx \frac{3}{2} qaJ\,, \quad \alpha_{\pm}(\boldsymbol{K}_{\pm} + \boldsymbol{q}) \approx \frac{\pi}{3} - \varphi, \tag{3.28}$$

$$g_{\pm}(\boldsymbol{K}'_{\pm} + \boldsymbol{q}) \approx \frac{3}{2} qaJ\,, \quad \alpha_{\pm}(\boldsymbol{K}'_{\pm} + \boldsymbol{q}) \approx -\frac{\pi}{3} + \varphi, \tag{3.29}$$

where φ is a phase of the complex number $q_x + \mathrm{i}q_y = q\mathrm{e}^{\mathrm{i}\varphi}$. Integrating over a small circle centered at $\mathbf{q} = 0$ surrounding each singular point of the phase, one finds:

$$\oint_{|\mathbf{q}|\to 0} \mathrm{d}\boldsymbol{q} \cdot \nabla_q \alpha_{\pm}(\boldsymbol{K}_{\pm} + \boldsymbol{q}) = -2\pi$$

$$\oint_{|\mathbf{q}|\to 0} \mathrm{d}\boldsymbol{q} \cdot \nabla_q \alpha_{\pm}(\boldsymbol{K}'_{\pm} + \boldsymbol{q}) = 2\pi$$

These equations together with eqs. 3.21 and 3.26 provide the following result for the Chern number

$$c_n = \sum_{s=\pm 1} s \left[C^2_{n,s}(\boldsymbol{K}'_{\pm}) - C^2_{n,s}(\boldsymbol{K}_{\pm}) \right] , \tag{3.30}$$

where the different signs appear due to the opposite phases in the phases appearing in eqs. 3.28 and 3.29. Therefore to find the Chern number one needs to determined the coeficients $C_{n,s}$ entering the state-vector at the points $\boldsymbol{K}_{\pm}$ and $\boldsymbol{K}'_{\pm}$. If $C^2_{n,\pm} = 1$ the particular singular point contributes to the Chern number of the n-th band. In the following we shall consider two different situations.

3.4.4 Determination of the Chern numbers: specific cases

The case where $\boldsymbol{p} = \mathbf{G}$ Suppose first that the difference in the recoil momenta coincides with the inverse lattice vector $\boldsymbol{p} = \mathbf{G}$. In that case the coupling completely vanishes both for $\boldsymbol{k} = \boldsymbol{K}_{\pm}$ and also for $\boldsymbol{k} = \boldsymbol{K}'_{\pm}$. At these points $g(\boldsymbol{k} - \boldsymbol{p}/2) = g(\boldsymbol{k}+\boldsymbol{p}/2) = 0$, so all the states $|s\rangle$, $s = 0, \pm 1$ are decoupled, and thus the eigenstates are the bare states $|s\rangle$. The corresponding eigen-energies of the matrix Hamiltonian $\mathcal{H}(\boldsymbol{k})$, Eq.(3.22), coinside with its diagonal elements $d_s(\boldsymbol{k})$ for $\boldsymbol{k} = \boldsymbol{K}_{\pm}$ and $\boldsymbol{k} = \boldsymbol{K}'_{\pm}$. Furthermore, for $\boldsymbol{p} = \mathbf{G}$ one has $f(\boldsymbol{k} - \boldsymbol{p}) = f(\boldsymbol{k}) = f(\boldsymbol{k} + \boldsymbol{p})$, giving $d_s(\boldsymbol{k}) = s\varepsilon + 2J_2 f(\boldsymbol{k})$. Therefore both for $\boldsymbol{k} = \boldsymbol{K}_{\pm}$ and $\boldsymbol{k} = \boldsymbol{K}'_{\pm}$, the eigenstates are ordered in the same manner $d_{+1}(\boldsymbol{k}) > d_0(\boldsymbol{k}) > d_{-1}(\boldsymbol{k})$. Thus the Chern number given by eq. 3.30 is identially equal to zero. In this way, for $\boldsymbol{p} = \mathbf{G}$ the system does not exhibit any topologically non-trivial phases. This is because in that case the flux over the rhombic plaquettes $\Phi_i = \pm \boldsymbol{p} \cdot \boldsymbol{a}_i$ is zero (modulus 2π), and there is no breaking of the time-reversal symmetry.

3.4.5 The case where $\boldsymbol{p} \neq \mathbf{G}$

For$\boldsymbol{p} \neq \mathbf{G}$ situations is as follows. If $\mathbf{k} = \boldsymbol{K}_\pm$ or $\mathbf{k} = \boldsymbol{K}'_\pm$, one has $g(\boldsymbol{k} \mp \boldsymbol{p}/2) = 0$ and $g(\boldsymbol{k} \pm \boldsymbol{p}/2) \neq 0$, so only the phase $\alpha_\pm(\boldsymbol{k})$ is undefined. Consequently, the Hamiltonian (3.22) splits into two independent parts with $|\pm\rangle$ decoupled from $|0\rangle$ and $|\mp\rangle$. Thus only the state $|\pm\rangle$ contributes to the Chern number, the other two states giving no contribution to it. To find the Chern number it is important to identify to which dispersion branch belongs the state $|\pm\rangle$ at two momentum point $\mathbf{k} = \boldsymbol{K}_\pm$ and $\mathbf{k} = \boldsymbol{K}'_\pm$. If it belong to different dispersion branches, the difference $C^2_{n,s}(\boldsymbol{K}'_\pm) - C^2_{n,s}(\boldsymbol{K}_\pm)$ is non-zero and contributes to the Chern number in eq. 3.30. In the following we explore this issue in more detail without including the NNN-hopping to the Hamiltonian (3.19) or (3.22).

Assuming $J_2 = 0$ and the on-site energy ε becomes the only independend parameter with J being only the energy unit.

$$\mathcal{H}(\boldsymbol{k}) = \begin{bmatrix} \varepsilon & Jg(\boldsymbol{k} - \boldsymbol{p}/2) & 0 \\ Jg^*(\boldsymbol{k} - \boldsymbol{p}/2) & 0 & Jg(\boldsymbol{k} + \boldsymbol{p}/2) \\ 0 & Jg^*(\boldsymbol{k} + \boldsymbol{p}/2) & -\varepsilon \end{bmatrix}. \tag{3.31}$$

As an illustration we pick $\boldsymbol{p} = \boldsymbol{K}$ for which the numerically calculated Chern numbers are $c_1 = 1$, $c_2 = -2$ and $c_3 = 1$. First we consider the point $\mathbf{k} = \boldsymbol{K}_+$ or $\mathbf{k} = \boldsymbol{K}'_+$ for which $g(\boldsymbol{k} - \boldsymbol{p}/2) = 0$. Furthermore, $g(\boldsymbol{k} + \boldsymbol{p}/2) =$ ....for $\mathbf{k} = \boldsymbol{K}_+$, and $g(\boldsymbol{k} + \boldsymbol{p}/2) =$ .... for $\mathbf{k} = \boldsymbol{K}_-$. Therefore for $\mathbf{k} = \boldsymbol{K}_+$ the eigenvalues are ... . On the other hand, for $\mathbf{k} = \boldsymbol{K}_+$ the eigenvalues are ...

The function $g(\boldsymbol{k})$ is zero and has undefined phase in the points $\boldsymbol{k} = \boldsymbol{K}$ and $\boldsymbol{k} = \boldsymbol{K}'$, while the function $g(\boldsymbol{k} + \boldsymbol{K})$ is zero in the points $\boldsymbol{k} = 0$ and $\boldsymbol{k} = \boldsymbol{K}' - \boldsymbol{K}$. The point $\boldsymbol{K}' - \boldsymbol{K}$ is equivalent to the point $\boldsymbol{K}$, so we consider only three points in the FBZ: $\boldsymbol{k}_1 = 0$, $\boldsymbol{k}_2 = \boldsymbol{K}$ and $\boldsymbol{k}_3 = \boldsymbol{K}'$. Near each of these point the Hamiltonian (3.31) becomes

$$H(\boldsymbol{q}) \approx \varepsilon \sum_{s=\pm} s|s\rangle\langle s| + 3J\left(|+\rangle\langle 0| + |0\rangle\frac{1}{2}qa\mathrm{e}^{-\mathrm{i}\varphi}\langle -| + \mathrm{h.\,c.}\right), \tag{3.32}$$

$$H(\boldsymbol{K} + \boldsymbol{q}) \approx \varepsilon \sum_{s=\pm} s|s\rangle\langle s| + \frac{3}{2}Jqa\left(|+\rangle\mathrm{e}^{-\mathrm{i}\varphi}\langle 0| + |0\rangle\mathrm{e}^{\mathrm{i}\varphi}\langle -| + \mathrm{h.\,c.}\right), \tag{3.33}$$

$$H(\boldsymbol{K}' + \boldsymbol{q}) \approx \varepsilon \sum_{s=\pm} s|s\rangle\langle s| + 3J\left(|+\rangle\frac{1}{2}qa\mathrm{e}^{\mathrm{i}\varphi}\langle 0| + |0\rangle\langle -| + \mathrm{h.\,c.}\right). \tag{3.34}$$

Here we ignored the constant phases $\pm\pi/3$ that come from the expansions (3.28) and (3.29) of the function $g(\boldsymbol{k})$, because it is not important in the Berry connection

(3.26). Moreover, it can be eliminated by a simple $\boldsymbol{k}$-independent transformation near each point $\boldsymbol{k}_i$, $i = 1, 2, 3$.

From (3.32)–(3.34) we see that in the first point $\boldsymbol{k}_1 = 0$ only the phase $\alpha_-(\boldsymbol{q})|_{qa\to 0} = -\varphi$ is undefined. In the second point $\boldsymbol{k}_2 = \boldsymbol{K}$ both phases $\alpha_+(\boldsymbol{K}+\boldsymbol{q})|_{qa\to 0} = -\varphi$ and $\alpha_-(\boldsymbol{K}+\boldsymbol{q})|_{qa\to 0} = \varphi$ are undefined. In the third point $\boldsymbol{k}_3 = \boldsymbol{K}'$ only the phase $\alpha_+(\boldsymbol{K}'+\boldsymbol{q})|_{qa\to 0} = \varphi$ is undefined.

Having all the required phases we can now check the behaviour of the coefficients $C_{n,\pm}(\boldsymbol{k})$. We have to solve eigenvalue equations of the Hamiltonians (3.32)–(3.34) in the corresponding points $\boldsymbol{k}_i$, $i = 1, 2, 3$ by setting $\boldsymbol{q} = 0$.

First we consider the first point $\boldsymbol{k}_1 = 0$. From the Hamiltonian (3.32) we get eigenvalues $E^{(\pm)} = \frac{1}{2}\varepsilon \pm \sqrt{(3J)^2 + \left(\frac{\varepsilon}{2}\right)^2}$ and $E^{(0)} = -\varepsilon$ with the corresponding required eigenvector coefficients $C_{n,-} = 0$ for the first two eigenvalues and $C_{n,-} = 1$ for the third eigenvalue. In order to find to which energy bands these eigenvalues belong we must order them to the ascending order. First we note that if the on-site energy value is $\varepsilon_0 = \frac{3\sqrt{2}}{2}J$ the get $E^{(0)} = E^{(-)}$, so the corresponding bads touch each other and the Chern number is undefined. For $0 < \varepsilon < \varepsilon_0$. The eigenvalues are ordered as $\frac{1}{2}\varepsilon - \sqrt{(3J)^2 + \left(\frac{\varepsilon}{2}\right)^2} < -\varepsilon < \frac{1}{2}\varepsilon + \sqrt{(3J)^2 + \left(\frac{\varepsilon}{2}\right)^2}$. This gives the coefficients $C_{1,-} = C_{3,-} = 0$ and $C_{2,-} = 1$. For $\varepsilon > \varepsilon_0$ the eigenvalues are ordered as $-\varepsilon < \frac{1}{2}\varepsilon - \sqrt{(3J)^2 + \left(\frac{\varepsilon}{2}\right)^2} < \frac{1}{2}\varepsilon + \sqrt{(3J)^2 + \left(\frac{\varepsilon}{2}\right)^2}$ and the coefficients are $C_{1,-} = 1$ and $C_{2,-} = C_{3,-} = 0$. From this analysis we find that for $0 < \varepsilon < \varepsilon_0$ the Berry connection $\boldsymbol{A}_2(\boldsymbol{k})$ of the middle band has a singularity at the point $\boldsymbol{k} = 0$. For $\varepsilon > \varepsilon_0$ this singularity moves from the middle band to the lowest one and the Berry connection $\boldsymbol{A}_1(\boldsymbol{k})$ gets a singularity.

Similar analysis of the Hamiltonian (3.33) shows that the Berry connections $\boldsymbol{A}_1(\boldsymbol{k})$ and $\boldsymbol{A}_3(\boldsymbol{k})$ always have singularities in the point $\boldsymbol{k} = \boldsymbol{K}$. The corresponding non-zero coefficients are $C_{1,-} = 1$ and $C_{3,+} = 1$.

Finally the third Hamiltonian (3.34) gives a similar results as the first one (3.32). For $0 < \varepsilon < \varepsilon_0$ the Berry connection $\boldsymbol{A}_2(\boldsymbol{k})$ has singularity in the point $\boldsymbol{k} = \boldsymbol{K}'$ with $C_{2,+} = 1$ and for $\varepsilon > \varepsilon_0$, $\boldsymbol{A}_3(\boldsymbol{k})$ has a singularity in the same point with $C_{3,+} = 1$.

Now we can combine this analysis with the phases $\alpha_\pm$ and write Berry connection (3.26) of each band near all their singular points:

- For $0 < \varepsilon < \varepsilon_0$ we have $\boldsymbol{A}_1(\boldsymbol{K}+\boldsymbol{q}) \approx -\nabla_{\boldsymbol{q}}\varphi$, $\boldsymbol{A}_2(\boldsymbol{q}) \approx \nabla_{\boldsymbol{q}}\varphi$, $\boldsymbol{A}_2(\boldsymbol{K}'+\boldsymbol{q}) \approx \nabla_{\boldsymbol{q}}\varphi$

and $\boldsymbol{A}_3(\boldsymbol{K}+\boldsymbol{q}) \approx -\nabla_{\boldsymbol{q}}\varphi$. The Chern numbers (3.21) are

$$
\begin{aligned}
c_1 &= -\frac{1}{2\pi} \oint_{q\to 0} \mathrm{d}\boldsymbol{q} \cdot \boldsymbol{A}_1(\boldsymbol{K}+\boldsymbol{q}) = 1, \\
c_2 &= -\frac{1}{2\pi} \oint_{q\to 0} \mathrm{d}\boldsymbol{q} \cdot \boldsymbol{A}_2(\boldsymbol{q}) - \frac{1}{2\pi} \oint_{q\to 0} \mathrm{d}\boldsymbol{q} \cdot \boldsymbol{A}_2(\boldsymbol{K}'+\boldsymbol{q}) = -2, \\
c_3 &= -\frac{1}{2\pi} \oint_{q\to 0} \mathrm{d}\boldsymbol{q} \cdot \boldsymbol{A}_3(\boldsymbol{K}+\boldsymbol{q}) = 1.
\end{aligned}
$$

- For $\varepsilon > \varepsilon_0$ we have $\boldsymbol{A}_1(\boldsymbol{q}) \approx \nabla_{\boldsymbol{q}}\varphi$, $\boldsymbol{A}_1(\boldsymbol{K}+\boldsymbol{q}) \approx -\nabla_{\boldsymbol{q}}\varphi$, $\boldsymbol{A}_3(\boldsymbol{K}+\boldsymbol{q}) \approx -\nabla_{\boldsymbol{q}}\varphi$ and $\boldsymbol{A}_3(\boldsymbol{K}'+\boldsymbol{q}) \approx \nabla_{\boldsymbol{q}}\varphi$. In this case the Berry connection $\boldsymbol{A}_2(\boldsymbol{k})$ does not have any singularities, while other connections $\boldsymbol{A}_1(\boldsymbol{k})$ and $\boldsymbol{A}_3(\boldsymbol{k})$ have two each. In these Berry connections the two singularities compensate each other. Thus all Chern numbers are zeroes.

We see that in the on-site energy interval from 0 to $\varepsilon_0 = \frac{3\sqrt{2}}{2}J$ the dispersion bands contain non-zero Chern numbers $c_1 = c_3 = 1$, $c_2 = -2$. In the point ε_0 there is a phase transition which distributes the Chern number $c_2 = 2$ to other bands, which gives all the Chern numbers equal to zeroes. At higher on-site energy values we loose all topological phenomena. Finally with an additional numerical analysis we approximately got the same value of ε_0.

We calculated Chern numbers for the case without no NNN-hopping for the specific recoil momentum value $\boldsymbol{p} = \boldsymbol{K}$. We can get similar results for different corners of the FBZ in the $\boldsymbol{p}$-plane as well. For an arbitrary point $\boldsymbol{p}$ this analysis becomes difficult, because in general we get four points where one or both of the phases $\alpha_\pm$ are undefined. Additionally the sorting of Hamiltonian eigenvalues in each of these points becomes complex because of dependence on three parameters – the on-site energy ε and the components of the recoil momentum $\boldsymbol{p}$ (and NNN-hopping amplitudes if we include them). However, all Chern numbers in principle can be calculated analytically because it requires to diagonalise at most 2-by-2 matrices.

Summary

We considered ultra-cold atoms in a two-dimensional dice optical lattice in a tight-binding approximation. We created an artificial magnetic field using a laser-assisted tunneling between the nearest neighbor sites. In this way we engineered staggered magnetic fluxes. The dice optical lattice represents a triangular Bravais laattice with a three-site basis consisting of a hub site connected to the two rim sites. In this way our model can be intepreted as an extension of the famous Haldane model which is reproduced if one of the two rim sublattices is eliminted.

We demonstrated that the proposed upgrade of the Haldane model created a significant added value, including an easy access to topological semimetal phases relying only on the nearest-neighbor coupling, as well as enhanced topological band structure featuring Chern numbers higher than one leading to physics beyond the usual quantum Hall effect.

4 OPTICAL FLUX LATTICE CREATED USING MULTI-FREQUENCY RADIATION

4.1 Two level atom with frequency comb coupling

4.1.1 General model

Let us consider an ultra-cold spin-1/2 atom in a magnetic field gradient along the x direction. The resulting Zeeman effect gives a position-dependent detuning between the spin up $|\uparrow\rangle$ and down $|\downarrow\rangle$ states. Assuming the gradient to be linear, it splits the internal atom levels as $\sim x\sigma_3$, with $\sigma_3 = |\uparrow\rangle\langle\uparrow| - |\downarrow\rangle\langle\downarrow|$ (see fig. 4.1). The Hamiltonian of the atom in this regime can be written as

$$H_0 = \frac{\boldsymbol{p}^2}{2M} + \frac{\Delta(x)}{2}\sigma_3. \tag{4.1}$$

Here the first term is a kinetic energy of the atom, in which $\boldsymbol{p}$ and M is a momentum and a mass of the atom. The second term describes the magnetic Zeeman shift represented by the potential function $\Delta(x)$, which we assume to be linear in x in the spatial region of interest: $\Delta(x) = \Delta_0 + \Delta' x$.

Let us introduce a Raman coupling between the internal atomic states of the form

$$V(y,t) = V_0 \sum_n \left[\mathrm{e}^{\mathrm{i}k_0 y}\mathrm{e}^{-\mathrm{i}2n\omega t} + \mathrm{e}^{-\mathrm{i}k_0 y}\mathrm{e}^{-\mathrm{i}(2n+1)\omega t}\right] |\downarrow\rangle\langle\uparrow| + \mathrm{H.\,c.} \tag{4.2}$$

The first term couples the internal states with a frequency comb electromagnetic wave, which is a superposition of plane waves of even frequencies $2n\omega$ propagating along y direction. Similarly, the second term corresponds to a coupling with frequency comb of odd frequencies $(2n+1)\omega$ propagating in the opposite direction. Both frequency combs couple internal atomic states resonantly in different positions along x direction (fig. 4.1). In writting Eq.(4.2) we have assumed that variations of the wave vectors and amplitudes of plane waves corresponding to different frequency components are negligible. Therefore we have taken pick a single value of the wave number k_0 and a single value of the coupling strength V_0. The coupling given by (4.2) has then a periodic time dependence with a period $T = 2\pi/\omega$.

Time evolution is described by the Schrödinger equation

$$\mathrm{i}\hbar\frac{\partial}{\partial t}|\psi(t)\rangle = H(t)|\psi(t)\rangle, \tag{4.3}$$

where

$$H(t) = H_0 + V(y,t) \tag{4.4}$$

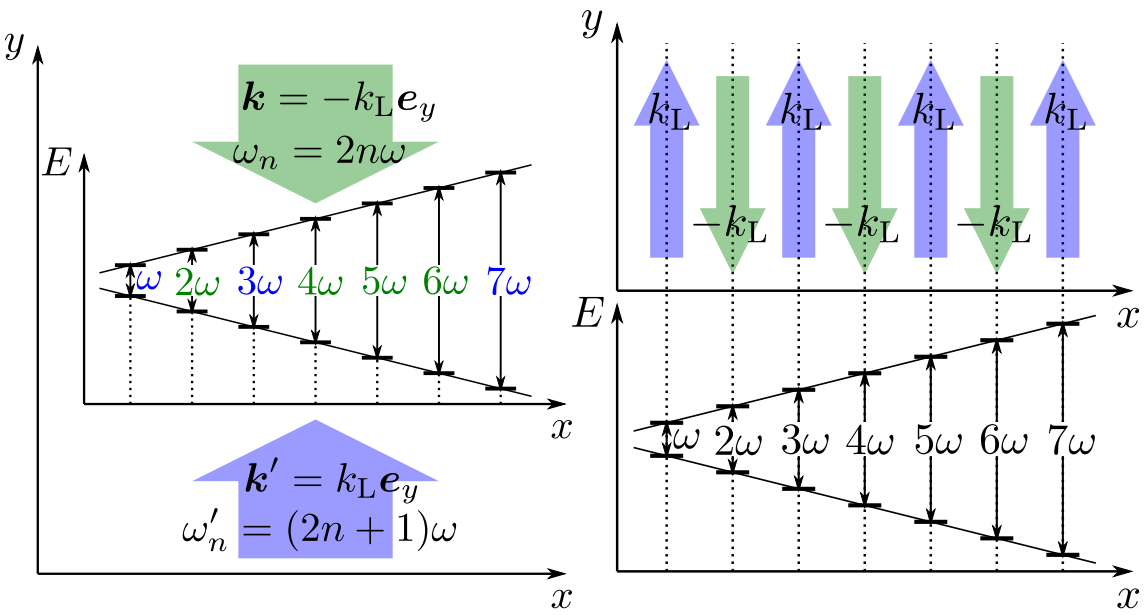

Figure 4.1: Coupling of two linearly shifted internal atomic states $|\uparrow\rangle$ and $|\downarrow\rangle$ with two frequency comb wave-packets. The first frequency comb propagates along the y direction and couples the internal states with even multiples of the Floquet frequency ω (green colour). The second frequency comb propagates in the opposite direction and couples the internal states with odd multiples of ω. The atom is in resonant with frequency combs in different positions along the x direction.

is the full time-dependent Hamiltonian, and

$$|\psi(\boldsymbol{r},t)\rangle = \sum_{\gamma=\downarrow\uparrow} \psi_\gamma(\boldsymbol{r},t)|\gamma\rangle$$

is the full atomic state-vector containing contributions due to both internal states $|\downarrow\uparrow\rangle$ and also center of mass wave-functions $\psi_{\downarrow\uparrow}(\boldsymbol{r},t)$. From (4.2) we see that the coupling $V(y,t)$ is periodic in y with a period of $2\pi/k_0$.

It is convenient to switch to a different gauge by changing the local phases of the atomic spin states $|\uparrow\rangle \to \exp(-\mathrm{i}k_0 y/2)|\uparrow\rangle$, $|\downarrow\rangle \to \exp(\mathrm{i}k_0 y/2)|\downarrow\rangle$. From this it follows that $|\downarrow\rangle\langle\uparrow| \to \exp(\mathrm{i}k_0 y)|\downarrow\rangle\langle\uparrow|$. Thus the coupling (4.2) transforms to

$$V(y,t) \to \tilde{V}(y,t) = V_0 \sum_n \left[\mathrm{e}^{\mathrm{i}2k_0 y}\mathrm{e}^{-\mathrm{i}2n\omega t} + \mathrm{e}^{-\mathrm{i}(2n+1)\omega t}\right]|\downarrow\rangle\langle\uparrow| + \mathrm{H.\,c.} \tag{4.5}$$

The momentum $\boldsymbol{p}$ also changes, $\boldsymbol{p} \to \boldsymbol{p} + \hbar k_0 \sigma_3 \boldsymbol{e}_y/2$, so the unperturbed Hamiltonian (4.1) in the new gauge is

$$\tilde{H}_0 = \frac{1}{2M}\left(\boldsymbol{p} + \hbar k_0 \sigma_3 \boldsymbol{e}_y/2\right)^2 + \frac{\Delta(x)}{2}\sigma_3. \tag{4.6}$$

On the other hand, going to a new gauge the coupling $\tilde{V}(y,t)$ has a twice smaller

period π/k_0. Subsequently, when exploring energy bands and their topological properties, this will prevent problems arrising from using a twice larger elementary cell.

4.1.2 Coupling as a series of pulses

We assume that there are enough plane waves in each frequency comb, so we can represent them as two overlapping series of short pulses in time. In the limit of the infinite summation over n from $-\infty$ to ∞, we can change the first sum of the complex exponents in the coupling (4.5) to the Dirac comb function

$$\sum_{n=-\infty}^{\infty} \mathrm{e}^{-\mathrm{i}2n\omega t} = \tau \sum_{l=-\infty}^{\infty} \delta(t - \tau l), \tag{4.7}$$

where τ denotes a half period $\tau = T/2 = \pi/\omega$. The second sum has an additional phase factor, which modifies the Dirac comb by including alternating signs:

$$\sum_{n=-\infty}^{\infty} \mathrm{e}^{-\mathrm{i}\omega t}\mathrm{e}^{-\mathrm{i}2n\omega t} = \tau \sum_{l=-\infty}^{\infty} (-1)^l \delta(t - \tau l). \tag{4.8}$$

We now rearrange all the terms from the both sums (4.7) and (4.8) in the coupling (4.5) into two groups containing even and odd value of the index l. In the first group the exponent $\exp(-\mathrm{i}\pi l)$ equals to a unity, while in the second group it is equal to a minus unity. In this way we rewrite the coupling (4.5) as

$$\tilde{V}(t, y) = V_+(y)\tau \sum_{\text{even } l} \delta(t - \tau l) + V_-(y)\tau \sum_{\text{odd } l} \delta(t - \tau l). \tag{4.9}$$

Here we introduced new operators

$$V_\pm(y) = V_0 \left(\mathrm{e}^{\mathrm{i}2k_0 y} \pm 1\right) |\downarrow\rangle\langle\uparrow| + \text{H. c.} \tag{4.10}$$

In this way we separated the spatial and temporal dependencies in the coupling (4.5).

4.2 Stroboscopic time evolution

4.2.1 Effective coupling

Let us consider the time evolution in a single period from $t = 0 - \epsilon$ to $t = T - \epsilon$ with $\epsilon \to 0$. Such evolution includes the first kick V_+ at the beginning of the period $t_+ = 0$ and the second kick V_- in the middle of the period $t_- = \tau$ and the free evolution

at other times. In this time interval one can represent the evolution operator as a product of four terms:

$$U(T,0) \equiv \lim_{\epsilon\to 0} U(T-\epsilon, 0-\epsilon) = U_0 U_- U_0 U_+. \tag{4.11}$$

Here

$$U_0 = \exp\left(-\frac{\mathrm{i}}{\hbar}\tilde{H}_0\tau\right) \tag{4.12}$$

is the evolution operator over the half period τ, generated by the unperturbed Hamiltonian $\tilde{H}_0$. Other two operators $U_\pm$ describe two different kicks at the time moments $t_\pm$:

$$U_\pm = \exp\left(-\frac{\mathrm{i}}{\hbar}V_\pm\tau\right). \tag{4.13}$$

We assume that the Floquet frequency ω is sufficiently larger than the recoil frequency $\omega_{\mathrm{rec}} = E_{\mathrm{rec}}/\hbar = \hbar k_0^2/2M$, so the momentum $\boldsymbol{p}$ of the atom varies sufficiently slowly in each period. Therefore we treat the momentum as a C-number during the evolution of the system from $t = 0-\epsilon$ to $t = T-\epsilon$. Then we rearrange terms in the full time evolution operator (4.11) and approximate it by

$$U_{\mathrm{eff}} = \exp\left\{-\frac{\mathrm{i}}{\hbar}\left[\frac{1}{2M}\left(\boldsymbol{p} + \hbar k_0 \sigma_3 \boldsymbol{e}_y/2\right)^2 + V_{\mathrm{eff}}\right]T\right\}, \tag{4.14}$$

where V_{eff} is an effective coupling, given by

$$\exp\left(-\frac{\mathrm{i}}{\hbar}V_{\mathrm{eff}}T\right) = \mathrm{e}^{-\mathrm{i}\sigma_3 f_3/2} U_- \mathrm{e}^{-\mathrm{i}\sigma_3 f_3/2} U_+. \tag{4.15}$$

Here we introduced a function $f_3(\boldsymbol{r}) = \pi\Delta(x)/(\hbar\omega)$. From now on we set $\Delta_0 = 0$ and denote

$$\beta = \frac{\Delta'}{\hbar\omega}.$$

This allows to express the function f_3 as

$$f_3(\boldsymbol{r}) = \pi\beta x. \tag{4.16}$$

The introduced parameter β has an inverse length dimension and characterizes natural distance along the x direction.

Let us write the effective coupling V_{eff} in a form

$$V_{\mathrm{eff}} = \frac{\hbar}{2}\boldsymbol{\sigma}\cdot\boldsymbol{\Omega}, \tag{4.17}$$

where $\boldsymbol{\sigma} \equiv (\sigma_1, \sigma_2, \sigma_3)$ is a three-dimensional vector with Pauli matrices $\sigma_1 = |{\downarrow}\rangle\langle{\uparrow}$

$|+\text{H.c.}$, $\sigma_2 = \mathrm{i}|\downarrow\rangle\langle\uparrow| + \text{H.c.}$ and $\sigma_3 = |\uparrow\rangle\langle\uparrow| - |\downarrow\rangle\langle\downarrow|$ as components. Here also $\boldsymbol{\Omega} \equiv (\Omega_1, \Omega_2, \Omega_3) \equiv \boldsymbol{\Omega}(\boldsymbol{r})$ is an effective magnetic field. In this way the effective coupling (4.17) is characterised by three real functions Ω_i, $i = 1, 2, 3$. Note that this effective potential does not have component near the unit matrix I. In fact, since the four exponents in the right hand side of (4.15) represent four subsequent rotations in a three-dimensional Euclidean space, the product of these exponents also represents a three-dimensional rotation. The resulting rotation can be expressed as an imaginary exponent of a pure Pauli vector $\boldsymbol{\sigma} \cdot \boldsymbol{\Omega}$. This allows us to write the effective coupling in the given form (4.17).

The effective magnetic field can be presented in analytic expressions by denoting the operator (4.15) as

$$\exp\left(-\frac{\mathrm{i}}{\hbar} V_{\text{eff}} T\right) = q_0 - \mathrm{i}\sigma_1 q_1 - \mathrm{i}\sigma_2 q_2 - \mathrm{i}\sigma_3 q_3. \tag{4.18}$$

Here q_0, q_1, q_2 and q_3 are real functions of the coordinate $\boldsymbol{r} \equiv (x, y)$. Comparing (4.15) and (4.18) and multiplying four matrix exponents we find:

$$q_0 = \cos f_1 \cos f_2 \cos f_3, \tag{4.19}$$

$$q_1 = \sin f_1 \cos f_2 \cos\left(k_0 y + f_3\right) - \cos f_1 \sin f_2 \sin\left(k_0 y\right), \tag{4.20}$$

$$q_2 = \sin f_1 \cos f_2 \sin\left(k_0 y + f_3\right) + \cos f_1 \sin f_2 \cos\left(k_0 y\right), \tag{4.21}$$

$$q_3 = \cos f_1 \cos f_2 \sin f_3 - \sin f_1 \sin f_2. \tag{4.22}$$

Here we introduced two additional functions,

$$f_1(y) = 2\pi v_0 \cos\left(k_0 y\right), \tag{4.23}$$

$$f_2(y) = 2\pi v_0 \sin\left(k_0 y\right). \tag{4.24}$$

Knowing the functions (4.19)–(4.22) we take a logarithm of (4.18) and find the effective magnetic field

$$\boldsymbol{\Omega} = \omega \frac{\boldsymbol{q}}{\|\boldsymbol{q}\|} \pi^{-1} \arccos q_0. \tag{4.25}$$

Here we defined a three dimensional vector $\boldsymbol{q}$ as $(q_1, q_{2,} q_3)$ and its norm by $\|\boldsymbol{q}\|$. From (4.25) we see that the the effective magnetic field can also be expressed in its absolute value $\Omega \equiv \|\boldsymbol{\Omega}\| = \omega\pi^{-1} \arccos q_0$ together with a normalized direction vector $\boldsymbol{N} = \boldsymbol{q}/\|\boldsymbol{q}\|$.

The resulting effective magnetic field (4.25) and the effecitve coupling (4.17) are periodic along the both x and y directions. The spatial periods are $a_x = 2/\beta$ and $a_y = \pi/k_0$ respectively. The effective coupling functions Ω_1, Ω_2 and Ω_3 are presented

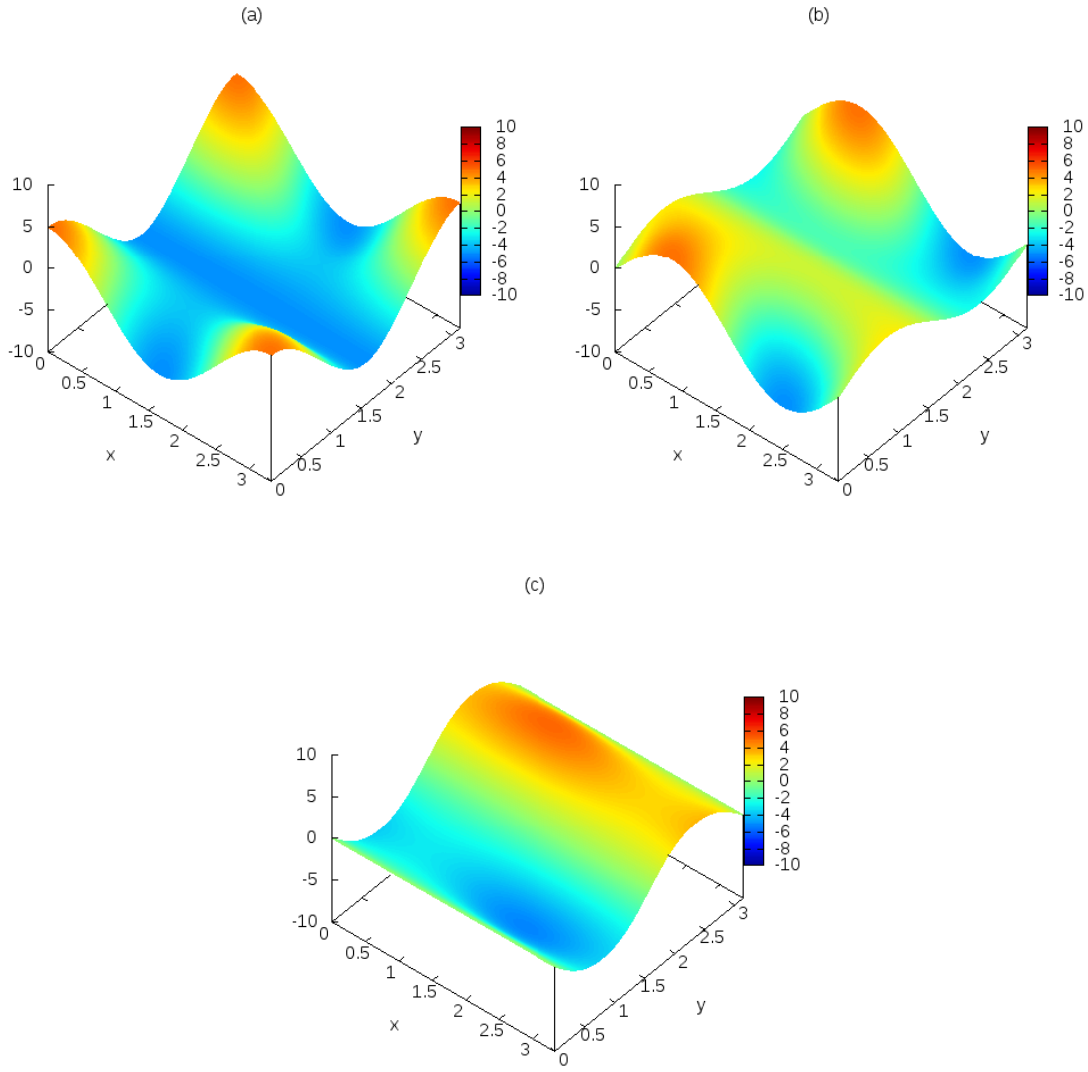

Figure 4.2: Coupling components (a) $\Omega_1(\boldsymbol{r})$, (b) $\Omega_2(\boldsymbol{r})$ and (c) $\Omega_3(\boldsymbol{r})$ in the adiabatic case, $V_0 = 0.25\hbar\omega$ with Floquet frequency $\hbar\omega = 10E_{\text{recoil}}$ and gradient $\beta = 0.6k_0$. The corresponding eigenvalues of the coupling are presented in the fig. 4.3(b). Here the coordinates x and y are expressed in units of k_0^{-1}.

in the fig. 4.2. We choose the Floquet frequency ω to be ten times higher tha the recoil energy, $\hbar\omega = E_{\text{recoil}}$. This helps the stroboscopic time evolution to be more precise. Moreover, we choose such gradient of the original magnetic field, that we approximately get a square elementary cell: $\beta = 0.6k_0$. This simplifies and stabilizies all numerical calculations. Finally, in the fig. 4.2 we present the effective coupling in the case of adiabatic regime, $V_0 = 0.25\hbar\omega$. In this case the absolute value of the effective coupling almost does not change (see fig. 4.3).

4.2.2 Eigen-structure of the effective coupling

Let us parametrise the coupling field $\boldsymbol{\Omega}(\boldsymbol{r})$ in the spherical co-ordinates $\Omega(\boldsymbol{r})$, $\theta(\boldsymbol{r})$ and $\phi(\boldsymbol{r})$:

$$\cos\theta = \frac{\Omega_3}{\Omega} = \frac{q_3}{\|\boldsymbol{q}\|}, \tag{4.26}$$

$$\tan\phi = \frac{\Omega_2}{\Omega_1} = \frac{q_2}{q_1}. \tag{4.27}$$

Following [**?**] we write the effective coupling (4.17) in a form

$$V_{\text{eff}} = \frac{\hbar}{2}\Omega \begin{bmatrix} \cos\theta & \mathrm{e}^{-\mathrm{i}\phi}\sin\theta \\ \mathrm{e}^{\mathrm{i}\phi}\sin\theta & -\cos\theta \end{bmatrix}. \tag{4.28}$$

The eigenvalues of the effective coupling (4.28) at a point $\boldsymbol{r}$ are

$$V_{\pm}(\boldsymbol{r}) = \pm\frac{\hbar}{2}\Omega(\boldsymbol{r}). \tag{4.29}$$

See fig. 4.3, where the eigenvalues of the effective coupling (4.28) are presented for three cases of the Raman coupling strength. The first case corresponds to a weak Raman coupling, $V_0 = 0.05\hbar\omega$. The spectrum $V_{\pm}(\boldsymbol{r})$ is close to a spectrum of $\sim \sigma_3 x$ and has a small gap. We expect this regime be not suitable for adiabatic time evolution because of high loses. The second case, $V_0 = 0.25\hbar\omega$, produces almost flat bands $V_{\pm}(\boldsymbol{r})$ with big gap between them compared to band widths. We expect this regime to be suitable for adiabatic time evolution. The last case describes strong Raman coupling, such that the bands are again separated by a small gap and close to touching each other.

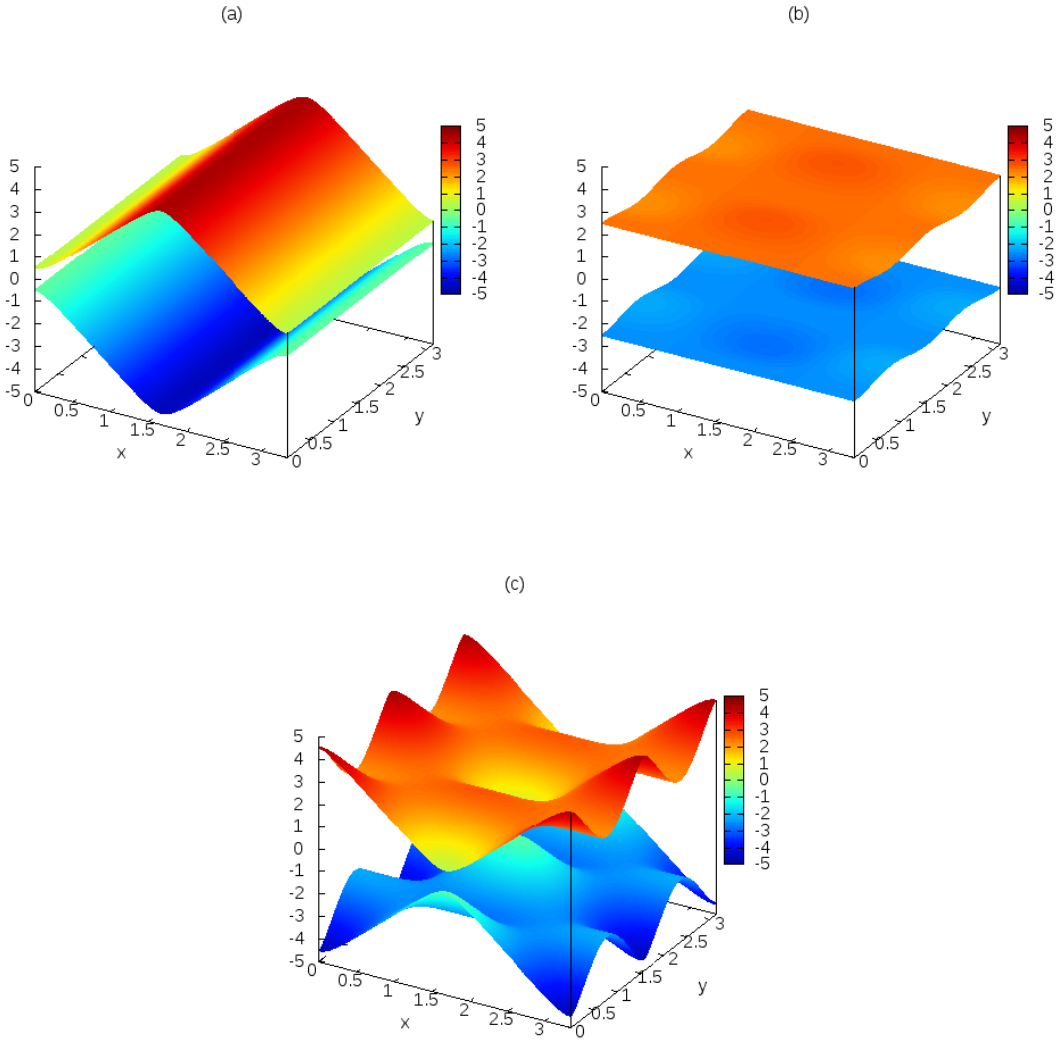

Figure 4.3: Eigenvalues $V_{\pm}(\boldsymbol{r})$ of the effective coupling in the cases of (a) weak coupling $V_0 = 0.05\hbar\omega$, (b) regime for adiabatic motion $V_0 = 0.25\hbar\omega$ and (c) strong coupling $V_0 = 0.45\hbar\omega$. In all three cases Floquet frequency is $\omega = 10E_{\mathrm{recoil}}/\hbar$ and gradient is $\beta = 0.6k_0$. Here the coordinates x and y are expressed in units of k_0^{-1}. The eigenvalues are expressed in the units of $\hbar\omega$. Only one window of eigenvalues is shown between $-\hbar\omega/2$ and $\hbar\omega/2$.

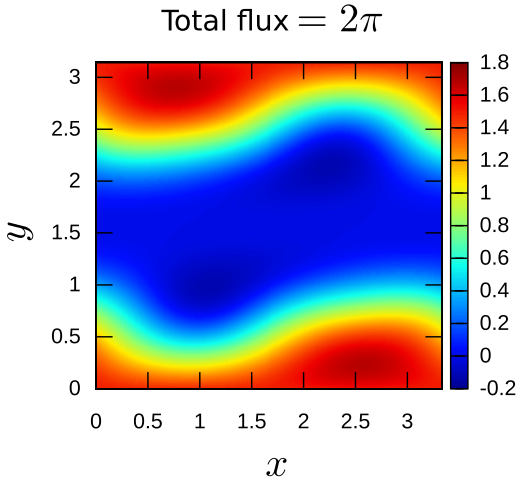

Figure 4.4: Geometric flux density $\boldsymbol{B} \equiv \boldsymbol{B}_+$ in the adiabatic regime with the Floquet frequeny $\hbar\omega = 10E_{\text{recoil}}$, the coupling strength $V_0 = 0.25\hbar\omega$ and the gradient $\beta = 0.6k_0$. The form this flux density does not depend on the gradient β as it just scales with corresponding lattice constant $a_x = 2/\beta$.

4.2.3 Adiabatic approximation

We consider adiabatic motion of the atom in one of its two internal states. The projection of Shrodinger's equation with the effective coupling (4.17) gives a geometric vector potential,

$$\boldsymbol{A}_\pm(\boldsymbol{r}) = \pm\frac{\hbar}{2}\left(\cos\theta - 1\right)\nabla\phi, \tag{4.30}$$

and a geometric scalar potential

$$W(\boldsymbol{r}) = \frac{\hbar^2}{8M}\left[(\sin\theta\nabla\phi)^2 + (\nabla\theta)^2\right]. \tag{4.31}$$

The geometric vector potential $\boldsymbol{A}_\pm(\boldsymbol{r})$ produces a synthetic magnetic flux density $\boldsymbol{B}_\pm(\boldsymbol{r}) = \nabla\times\boldsymbol{A}_\pm(\boldsymbol{r})$. The geometric vector potential $\boldsymbol{A}_\pm(\boldsymbol{r})$ may contain Aharonov-Bohm type singularities, that give rise to a synthetic magnetic flux over a single elementary cell:

$$\alpha_\pm = -\frac{1}{\hbar}\sum\oint_{\text{singul}} \mathrm{d}\boldsymbol{r}\cdot\boldsymbol{A}_\pm(\boldsymbol{r}). \tag{4.32}$$

Singularitites appear in the points where $\theta = \pi$. Then the angle ϕ and its gradient $\nabla\phi$ are undefined and $\cos\theta = -1$. The term $\cos\theta - 1$ in (4.30) is not zero and does not remove the undefined phase $\nabla\phi$. In our case we get two singularities that do not compensate each other, so the synthetic magnetic flux over a single elementary cell is $\pm 2\pi$.

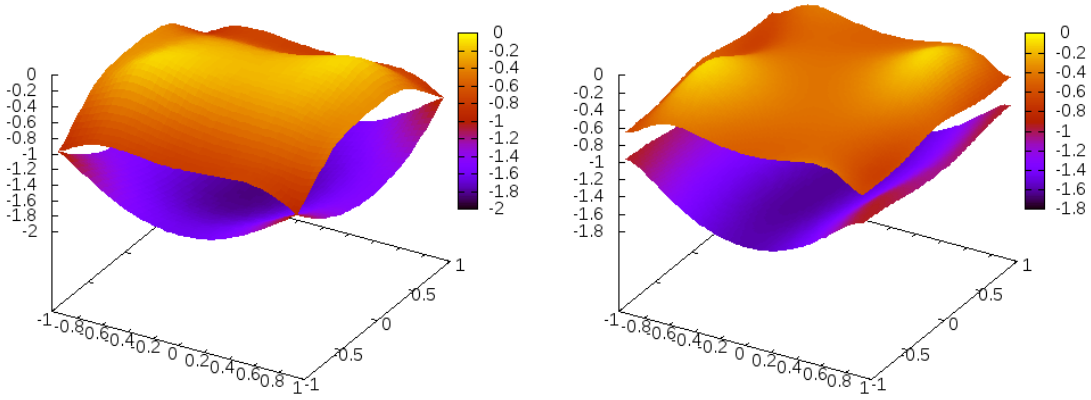

Figure 4.5: Dispersion surfaces for (left) $V_0 = 0.175\hbar\omega$ and (right) $V_0 = 0.25\hbar\omega$. Here Floquet frequency and gradient and gradient are $\hbar\omega = 10E_{\text{recoil}}$ and $\beta = 0.6k_0$. The first case (left) shows dispersion near a phase transition point, where Chern numbers are exchanged between the first and second bands. The second case (right) shows dispersion in the case of adiabatic regime with the effective coupling $\boldsymbol{\Omega}(\boldsymbol{r})$ presented in the fig. 4.2. Here the Bloch wavevector components k_x and k_y are expressed in the units of k_0. The energy is expressed in the recoil energy units E_{recoil}.

The geometric flux density $\boldsymbol{B}(\boldsymbol{r}) \equiv \boldsymbol{B}_+(\boldsymbol{r})$ and the geometric scalar potential $W(\boldsymbol{r})$ in the case of adiabatic regime ($\hbar\omega = 10E_{\text{recoil}}$, $V_0 = 0.25\hbar\omega$, $\beta = 0.6k_0$) are presented in the fig. 4.4. The total synthetic magnetic flux in a singe elementary cell here is 2π and is independent of the Floquet frequendy ω and the gradient β. The flux has a value 2π in the range of the coupling strength $0 < V_0 < 0.5\hbar\omega$.

4.2.4 Band structure and Chern numbers

We explore topological properties of the flux lattice, generated by the effective coupling (4.17), by numerically calculating band structure and Chern numbers. Again we choose the Floquet frequency to be ten times larger than the recoil energy, $\hbar\omega = 10E_{\text{recoil}}$ and the gradient of the original magnetic field such that we approximately get a square lattice, $\beta = 0.6k_0$. First, let us consider the adiabatic regime, $V_0 = 0.25\hbar\omega$. In this case the Chern numbers of the first five bands are equal to one (see fig. 4.6). Thus the Hall conductivity should monotonically increase when filling these bands. This resembles the Quantum Hall effect involving the Landau levels. One would expect that higher bands also have Chern numbers one. However we could not prove that, because of loss in the calculation precision when going to

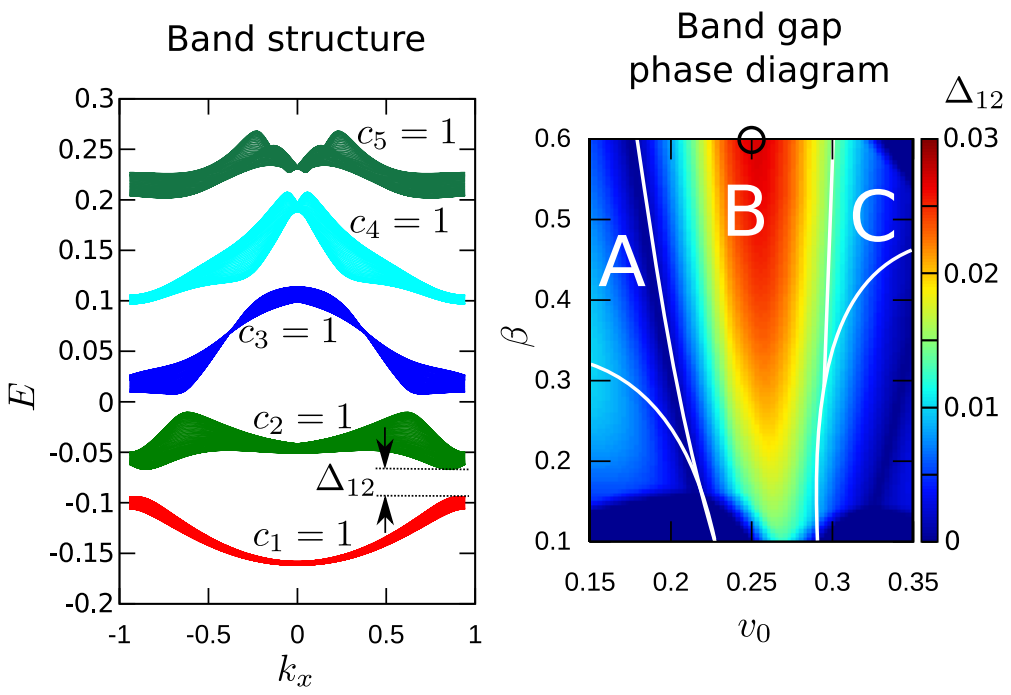

Figure 4.6: *Left*: dispersion surfaces, projected onto the k_x axis for $V_0 = 0.25\hbar\omega$. As in other figures, here $\hbar\omega = 10E_{\text{recoil}}$ and $\beta = 0.6k_0$. *Right*: band gap phase diagram for $\hbar\omega = 10E_{\text{recoil}}$. Here $v_0 \equiv V_0/\hbar\omega$.

the higher bands.

Next, we check what happens when we leave the regime $V_0 = 0.25\hbar\omega$ where the adiabatic potential is the most flat, and consider lower and higher values of the coupling strength V_0. Near $V_0 = 0.175\hbar\omega$ we find a topological phase transition with Chern numbers exchanging between the two lowest energy bands. Lower values of the coupling strength makes the lowest band have Chern number zero, $c_1 = 0$, the second band have Chern number two, $c_2 = 2$, while the topological properties of the higher bands does not change (up to our calculation precision). Near $V_0 = 0.3\hbar\omega$ we find another phase transition. But this time the Chern numbers are exchanged between the second and the third bands. After that point the Chern numbers are distributed as $c_1 = 1$, $c_2 = -1$, $c_3 = 3$, $c_4 = 1$, ... This phase transition is interesting, because the Chern number jumps by two units.

In the fig. 4.5 we show the dispersion surfaces near the first phase transition, $V_0 = 0.175\hbar\omega$ and in the case of adiabatic regime, $V_0 = 0.25\hbar\omega$. In the first case we can see one cone on the corner of the first Brillouin zone. The second case shows that there is a gap $\sim 0.27E_{\text{recoil}}$, which is comparable with the width of the first band $\sim 0.68E_{\text{recoil}}$. During this phase transition the second and third bands close and open in two different points in the first Brillouin zone simultaneously. This explains

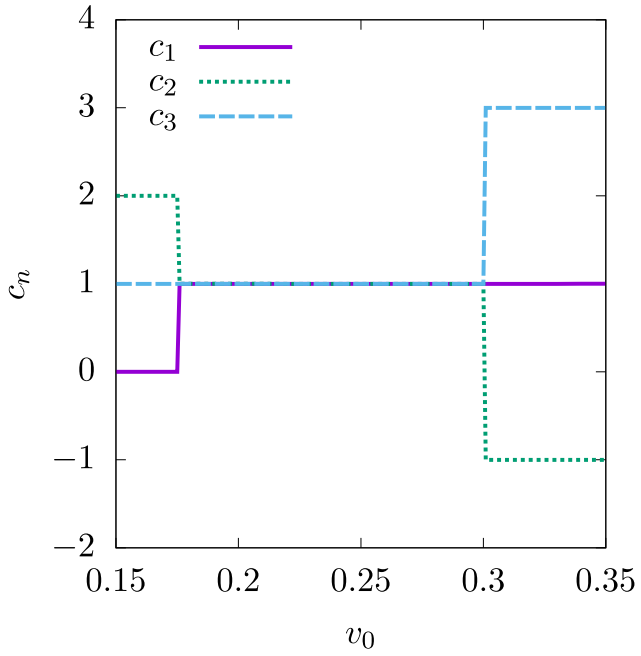

Figure 4.7: Chern number dependence on $v_0 \equiv V_0/\hbar\omega$ for $\beta = 0.6k_0$ and $\hbar\omega = 10E_{\text{recoil}}$.

why the corresponding Chern numbers jump by two units.

Finally, we explore the band gap dependence not only on the coupling strength V_0, but also on the gradient β. In the figure 4.7 we present how the Chern numbers of the first three bands depend on V_0. The figure 4.6 shows how the band gap between the first and second bands depends on the same parameters. Notice that in the same middle region the band gap is nonzero, but gets smaller when the gradient β decreases.

Summary

We described a novel technique for creating an artificial magnetic field for ultracold atoms using a periodically pulsed pair of counter-propagating Raman lasers that drive transitions between a pair of internal atomic states: a multi-frequency coupling term. Together with a magnetic field gradient, this creates a rectangular lattice with a non-staggered magnetic flux.

The described and analyzed model an optical flux lattice uses a temporally pulsed Raman coupling. Usually, techniques that rely on a temporal modulation of Hamiltonian parameters lead to heating problems. Our method is applied to atoms that are not initially in any optical lattice, so there are no initial constraints on modulation frequency to avoid transitions between original Bloch bands.

We calculated the resulting Bloch bands and explored their non-trivial topology. The analyzed optical flux lattice produces several Landau-like lowest energy bands. Under certain choice of lattice parameters the lowest bands have unit Chern numbers. In addition, the lattice may also produces rich topological bands that have Chern numbers largen than one in modulus.

CONCLUSIONS

1. The considered dice lattice represents a triangular Bravais lattice with a three-site basis consisting of a hub site connected to two rim sites. As a consequence, the dice lattice supports with three energy bands. In addition, the dice lattice contains *staggered* artificial magnetic field. Thus our model can be interpreted as a generalization of the paradigmatic Haldane model which is reproduced if one of the two rim sublattices is eliminated.

2. The proposed upgrade of the Haldane model a creates significant added value such as (i) an easy access to topological semimetal phases relying on only nearest neighbour coupling and (ii) enhanced topological band structures featuring Chern numbers higher than one.

3. The described and analyzed model an optical flux lattice uses a temporally pulsed Raman coupling. Using the stroboscopic approximation we derived an effective Hamiltonian which describes a 2D lattice with *non-staggered* magnetic field.

4. The analyzed optical flux lattice produces several Landau-like lowest energy bands. Under certain choice of lattice parameters the lowest bands have unit Chern numbers. In addition, the lattice may also produces rich topological bands that have Chern numbers largen than one in modulus.

APPENDIX

Chern numbers from the topolocial perspective

In this appendix we will very briefly describe how Chern number are related with topology. In order to avoid giving a lot of mathematical derivations we will limit ourselves only to the specific definitions that are most relevant to our case of 2D lattices that exhibit integer QHE. For more discussion on how tolopogy is used in physics we recommend to see the books *Topology and Geometry for Physicists* by Charles Nash and Siddhartha Sen [103] and Geometry, *Topology and Physics* by Mikio Nakahara [104]. For more mathematical discussion we recommend the classic book *General Topology* by John L. Kelley [105].

Topology is one of the core area of mathematics which usually comes immediately after axiomatic description of mathematical sets. At the most basic level topology gives the most abstract notions of a point in a space (not necesserally an Euclidean), neighborhood of a point, continuity, closed sets, open sets, closures of a set, boundaries, interiors, connectedness and compactness. Almost every mathematician and physicist use topology implicitly when talking about mentioned notions.

Let us begin with the basic definition of a topological space. Let X be any set and let $\mathcal{T}$ be a collection of subsets of X. Note that X may be either finite or infinite, so $\mathcal{T}$ may also contain either finite or infinite subsets. The pair $(X, \mathcal{T})$ is called a topological space if and only if (by definition):

- the empty set $\emptyset$ and the whole set X belong to $\mathcal{T}$ ($\emptyset \in \mathcal{T}, X \in \mathcal{T}$),
- any finite or infinte union of elements of $\mathcal{T}$ also belong to $\mathcal{T}$,
- any *finite* (and only finite) intersection of elements of $\mathcal{T}$ also belong to $\mathcal{T}$.

The set X is also called topological space (meaning that mathematicians imply the collections of sets $\mathcal{T}$, but simply don't write the full pair $(X, \mathcal{T})$). The elements of $\mathcal{T}$ are called open sets. The elements of the topological space X are called points.

We can now turn to the first important notion: continuous mapping. A function f mapping from one topological space X to another Y is called continuous if the inverse image of an open set in Y is an open set in X. One can check how this definition works specifically with a simple real functions $\mathbb{R} \to \mathbb{R}$ on a real number line and see that it corresponds to usual definitions given in various calculus books. The topological definition is simply a more abstract version which can be used to a much larger group of different types of mappings between more abstract spaces.

Equipped with this basic notions we can go to the core topic of topology: homeomorphisms and topological invariants. The main idea in topology is to study spaces that can be continuously deformed into one another. Let us take two topological spaces X and Y. Then a map f from X to Y ($f : X \to Y$) is called a homeomorphism if it is both continouos and has an inverse which is also continuous. The spaces X and Y are called homeomorphic with each other. From the definition we see that if f is homeomorphism, so is the inverse f^{-1}. Moreover, if we introduce the third topological space Z, then provided that X is homeomorphic to Y and Y is homeomorphic to Z, then X is also homeomorphig to Z. The last three properties show that we can characterize all topological spaces into equivalence classes: a pair of spaces X and Y belong to the same equivalence class if they are homeomorphic. The characterization is done using topological invariants – mathematical objects that characterize each class of equivalent topological spaces. The topological invariants can take many forms: they can be integers such as dimension or a Chern number as it is used in the main text of the dissertation. They can also be certain properties such as connectedness or compactness. They can even be whole mathematical structures such as groups.

We can now continue and introduce manifolds, or more specifically differentiable manifolds. Intuitively, a manifold M is a topological space which locally looks like Euclidean space $\mathbb{R}^n$ (where n is a dimension of the manifold M), but not necessarilly globally. This means that we can continuously map an open set of M to an open set of $\mathbb{R}^n$. If we have two overlapping open sets M_1 and M_2 of M and continuously map them to two open sets A_1 and A_2 of $\mathbb{R}^n$ by $f_1 : M_1 \to A_1$ and $f_2 : M_2 \to A_2$, then there is a mapping from A_1 to A_2 given by $f_2 \circ f_1^{-1}$. If we have a collection of such open sets of M that covers the whole manifold M and all mapping between the resulting open sets of $\mathbb{R}^n$ are infinitelly differentiable, then we call M a differentiable manifold.

As an example we can consider a sphere. We can define can define an open set on it by taking the whole sphere and excluding the poles: this is M_1. Then we can define spherical angles θ and ϕ as coordinates: they give a mapping f_1 to an open set A_1 of $\mathbb{R}^2$. In a similar way we can define another spherical coordinates by choosing a different pair of opposite sphere points as poles: this provides M_2, f_2 and A_2. One can check that the mapping between the open sets A_1 and A_2 of $\mathbb{R}^n$ is infinitelly differentiable. Thus a sphere is a two-dimensional differentiable manifold. Observe, that in this case we can't use only one set of spherical angles θ and ϕ, because ϕ is not defined in the poles, so the sphere is not globally homeomorphic to $\mathbb{R}^n$.

We skip such notions as orientability and now go directly to fiber bundles. Like a

manifold, a fiber bundle is, in intuitive terms, a topological space which is locally a product of two spaces (but not necessarily globally). The simple example is the Möbius strip. Let us take two one-dimensional manifolds: a line segment and a circle. The product of these spaces is a cylinder. This is a product space globally and locally. On the other hand, the Möbius strip is a product of a line segment and a circle locally, but not globally.

A fibre bundle consists of a topological space E (called the *total space*), a topological space X (called *the base space*), a topological space F (called the *fibre*) and a *projection* $\Pi : E \to X$. The local triviality of the bundle E is reflected by a set of open neighborhoods U_α covering X, meaning that for each U_α there is a homeomorphism $\phi_\alpha : \Pi^{-1}(U_\alpha) \to U_\alpha \times F$. In the previous example of the Möbius strip, the base space X is a circle and the fibre F is a line segment. For each point x on the circle there is the fibre $\Pi^{-1}(x)$. This example should give some understanding on how fiber bundles are defined.

A fiber bundle E is said to be a vector bundle if its fibre F is a vector space $\mathbb{R}^n$ or a complex vector space $\mathbb{C}^n$.

Let us now consider a two-dimensional lattice in a tight-binding approximation. The eigenstates of a single-particle Hamiltonian are Bloch wavefunctions indexed by the Bloch wavevector $\boldsymbol{k}$. This wavevector is defined over the FBZ which is a two-dimensional torus $\mathbb{T}^2$. In the $\boldsymbol{k}$-space representation the Hamiltonian is described by a collection of Hermitian operators $H(\boldsymbol{k})$ in the n-dimensional Hilbert space, where n is the total number of bands. In other words for each $\boldsymbol{k}$ we a have Hilbert space $\mathcal{H}_{\boldsymbol{k}} \cong \mathbb{C}^n$. The collection of spaces $\mathcal{H}_{\boldsymbol{k}}$ forms a complex vector bundle on the base space $\mathbb{T}^n$.

In the tight-binding models the full vector bundle is always trivial, meaning it is always homeomorphic to $\mathbb{T}^2 \times \mathbb{C}^n$. In an insulator we divide the bands into two groups: the filled bands and the empty bands. It may happen that the filled bands can form a subbundle of $\mathbb{T}^2 \times \mathbb{C}^n$ which is non-trivial. This non-triviality is measured by the Chern numbers of each filled band and is related to the integer QHE as explained in the chapter 2.1.5. The definition, interpretation and calculation methods of a Chern number are already given in the main text of the dissertation.

REFERENCES

[1] Maciej Lewenstein, Anna Sanpera, Veronica Ahufinger, Bogdan Damski, Aditi Sen(De), and Ujjwal Sen. Ultracold atomic gases in optical lattices: mimicking condensed matter physics and beyond. *Advances in Physics*, 56(2):243–379, 2007.

[2] Steven Chu. Nobel lecture: The manipulation of neutral particles. *Rev. Mod. Phys.*, 70:685–706, Jul 1998.

[3] Claude N. Cohen-Tannoudji. Nobel lecture: Manipulating atoms with photons. *Rev. Mod. Phys.*, 70:707–719, Jul 1998.

[4] William D. Phillips. Nobel lecture: Laser cooling and trapping of neutral atoms. *Rev. Mod. Phys.*, 70:721–741, Jul 1998.

[5] E. A. Cornell and C. E. Wieman. Nobel lecture: Bose-einstein condensation in a dilute gas, the first 70 years and some recent experiments. *Rev. Mod. Phys.*, 74:875–893, Aug 2002.

[6] Wolfgang Ketterle. Nobel lecture: When atoms behave as waves: Bose-einstein condensation and the atom laser. *Rev. Mod. Phys.*, 74:1131–1151, Nov 2002.

[7] Immanuel Bloch, Jean Dalibard, and Wilhelm Zwerger. Many-body physics with ultracold gases. *Rev. Mod. Phys.*, 80:885–964, Jul 2008.

[8] Markus Greiner, Olaf Mandel, Tilman Esslinger, Theodor W. Hänsch, and Immanuel Bloch. Quantum phase transition from a superfluid to a mott insulator in a gas of ultracold atoms. *Nature*, 415:39–44, Jan 2002.

[9] D. Jaksch, C. Bruder, J. I. Cirac, C. W. Gardiner, and P. Zoller. Cold bosonic atoms in optical lattices. *Phys. Rev. Lett.*, 81:3108–3111, Oct 1998.

[10] Richard P. Feynman. Quantum mechanical computers. *Foundations of Physics*, 16:507–531, Jun 1986.

[11] J. R. Abo-Shaeer, C. Raman, J. M. Vogels, and W. Ketterle. Observation of vortex lattices in bose-einstein condensates. *Science*, 292(5516):476–479, 2001.

[12] N.R. Cooper. Rapidly rotating atomic gases. *Advances in Physics*, 57(6):539–616, 2008.

[13] Alexander L. Fetter. Rotating trapped bose-einstein condensates. *Rev. Mod. Phys.*, 81:647–691, May 2009.

[14] K. W. Madison, F. Chevy, V. Bretin, and J. Dalibard. Stationary states of a rotating bose-einstein condensate: Routes to vortex nucleation. *Phys. Rev. Lett.*, 86:4443–4446, May 2001.

[15] M. R. Matthews, B. P. Anderson, P. C. Haljan, D. S. Hall, C. E. Wieman, and E. A. Cornell. Vortices in a bose-einstein condensate. *Phys. Rev. Lett.*, 83:2498–2501, Sep 1999.

[16] K. C. Wright, R. B. Blakestad, C. J. Lobb, W. D. Phillips, and G. K. Campbell. Driving phase slips in a superfluid atom circuit with a rotating weak link. *Phys. Rev. Lett.*, 110:025302, Jan 2013.

[17] Jean Dalibard, Fabrice Gerbier, Gediminas Juzeliūnas, and Patrik Öhberg. Colloquium: Artificial gauge potentials for neutral atoms. *Rev. Mod. Phys.*, 83:1523–1543, Nov 2011.

[18] N Goldman, G Juzeliūnas, P Öhberg, and I B Spielman. Light-induced gauge fields for ultracold atoms. *Reports on Progress in Physics*, 77(12):126401, 2014.

[19] André Eckardt. Colloquium: Atomic quantum gases in periodically driven optical lattices. *Rev. Mod. Phys.*, 89:011004, Mar 2017.

[20] Gregor Jotzu, Michael Messer, Rémi Desbuquois, Martin Lebrat, Thomas Uehlinger, Daniel Greif, and Tilman Esslinger. Experimental realization of the topological haldane model with ultracold fermions. *Nature*, 515:237–240, Nov 2014.

[21] J. Struck, C. Ölschläger, M. Weinberg, P. Hauke, J. Simonet, A. Eckardt, M. Lewenstein, K. Sengstock, and P. Windpassinger. Tunable gauge potential for neutral and spinless particles in driven optical lattices. *Phys. Rev. Lett.*, 108:225304, May 2012.

[22] Patrick Windpassinger and Klaus Sengstock. Engineering novel optical lattices. *Reports on Progress in Physics*, 76(8):086401, 2013.

[23] M. Aidelsburger, M. Atala, M. Lohse, J. T. Barreiro, B. Paredes, and I. Bloch. Realization of the hofstadter hamiltonian with ultracold atoms in optical lattices. *Phys. Rev. Lett.*, 111:185301, Oct 2013.

[24] N. R. Cooper. Optical flux lattices for ultracold atomic gases. *Phys. Rev. Lett.*, 106:175301, Apr 2011.

[25] N. Goldman, J. C. Budich, and P. Zoller. Topological quantum matter with ultracold gases in optical lattices. *Nature Physics*, 12:639–645, 2016.

[26] D Jaksch and P Zoller. Creation of effective magnetic fields in optical lattices: the hofstadter butterfly for cold neutral atoms. *New Journal of Physics*, 5(1):56, 2003.

[27] Juha Javanainen and Janne Ruostekoski. Optical detection of fractional particle number in an atomic fermi-dirac gas. *Phys. Rev. Lett.*, 91:150404, Oct 2003.

[28] Hirokazu Miyake, Georgios A. Siviloglou, Colin J. Kennedy, William Cody Burton, and Wolfgang Ketterle. Realizing the harper hamiltonian with laser-assisted tunneling in optical lattices. *Phys. Rev. Lett.*, 111:185302, Oct 2013.

[29] K. Osterloh, M. Baig, L. Santos, P. Zoller, and M. Lewenstein. Cold atoms in non-abelian gauge potentials: From the hofstadter "moth" to lattice gauge theory. *Phys. Rev. Lett.*, 95:010403, Jun 2005.

[30] N. Barberán, M. Lewenstein, K. Osterloh, and D. Dagnino. Ordered structures in rotating ultracold bose gases. *Phys. Rev. A*, 73:063623, Jun 2006.

[31] T. Andrijauskas, E. Anisimovas, M. Račiūnas, A. Mekys, V. Kudriašov, I. B. Spielman, and G. Juzeliūnas. Three-level haldane-like model on a dice optical lattice. *Phys. Rev. A*, 92:033617, Sep 2015.

[32] Tomas Andrijauskas, I B Spielman, and Gediminas Juzeliūnas. Topological lattice using multi-frequency radiation. *New Journal of Physics*, 20(5):055001, 2018.

[33] F. D. M. Haldane. Model for a quantum hall effect without landau levels: Condensed-matter realization of the "parity anomaly". *Phys. Rev. Lett.*, 61:2015–2018, Oct 1988.

[34] Maciej Lewenstein, Anna Sanpera, and Veronice Ahufinger. *Ultracold Atoms in Optical Lattices*. Oxford University Press, United Kingdom, 2012.

[35] M. H. Anderson, J. R. Ensher, M. R. Matthews, C. E. Wieman, and E. A. Cornell. Observation of bose-einstein condensation in a dilute atomic vapor. *Science*, 269(5221):198–201, 1995.

[36] K. B. Davis, M. O. Mewes, M. R. Andrews, N. J. van Druten, D. S. Durfee, D. M. Kurn, and W. Ketterle. Bose-einstein condensation in a gas of sodium atoms. *Phys. Rev. Lett.*, 75:3969–3973, Nov 1995.

[37] Artur K. Ekert. Quantum cryptography based on bell's theorem. *Phys. Rev. Lett.*, 67:661–663, Aug 1991.

[38] Charles H. Bennett and Stephen J. Wiesner. Communication via one- and two-particle operators on einstein-podolsky-rosen states. *Phys. Rev. Lett.*, 69:2881–2884, Nov 1992.

[39] Charles H. Bennett, Gilles Brassard, Claude Crépeau, Richard Jozsa, Asher Peres, and William K. Wootters. Teleporting an unknown quantum state via dual classical and einstein-podolsky-rosen channels. *Phys. Rev. Lett.*, 70:1895–1899, Mar 1993.

[40] J. I. Cirac and P. Zoller. Quantum computations with cold trapped ions. *Phys. Rev. Lett.*, 74:4091–4094, May 1995.

[41] P. W. Shor. Algorithms for quantum computation: discrete logarithms and factoring. In *Proceedings 35th Annual Symposium on Foundations of Computer Science*, pages 124–134, Nov 1994.

[42] D. Bouwmeester, A.K. Ekert, and A. Zeilinger. *The Physics of Quantum Information: Quantum Cryptography, Quantum Teleportation, Quantum Computation*. Springer, Berlin, 2000.

[43] A. Recati, P. O. Fedichev, W. Zwerger, and P. Zoller. Spin-charge separation in ultracold quantum gases. *Phys. Rev. Lett.*, 90:020401, Jan 2003.

[44] B. Paredes and J. I. Cirac. From cooper pairs to luttinger liquids with bosonic atoms in optical lattices. *Phys. Rev. Lett.*, 90:150402, Apr 2003.

[45] C. Kollath, U. Schollwöck, and W. Zwerger. Spin-charge separation in cold fermi gases: A real time analysis. *Phys. Rev. Lett.*, 95:176401, Oct 2005.

[46] A. J. Leggett, S. Chakravarty, A. T. Dorsey, Matthew P. A. Fisher, Anupam Garg, and W. Zwerger. Dynamics of the dissipative two-state system. *Rev. Mod. Phys.*, 59:1–85, Jan 1987.

[47] A. Recati, P. O. Fedichev, W. Zwerger, J. von Delft, and P. Zoller. Atomic quantum dots coupled to a reservoir of a superfluid bose-einstein condensate. *Phys. Rev. Lett.*, 94:040404, Feb 2005.

[48] Zoran Hadzibabic, Peter Krüger, Marc Cheneau, Baptiste Battelier, and Jean Dalibard. Berezinskii–kosterlitz–thouless crossover in a trapped atomic gas. *Nature*, 441:1118–1121, 2006.

[49] F.H.L. Essler, H. Frahm, F. Göhmann, A. Klümper, and V.E. Korepin. *The One-Dimensional Hubbard Model*. Oxford University Press, Oxford, 2005.

[50] A. Auerbach. *Interacting Electrons and Quantum magnetism*. Springer, New York, 1994.

[51] D. Jaksch and P. Zoller. The cold atom hubbard toolbox. *Annals of Physics*, 315(1):52 – 79, 2005. Special Issue.

[52] J. J. García-Ripoll, M. A. Martin-Delgado, and J. I. Cirac. Implementation of spin hamiltonians in optical lattices. *Phys. Rev. Lett.*, 93:250405, Dec 2004.

[53] L. Santos, M. A. Baranov, J. I. Cirac, H.-U. Everts, H. Fehrmann, and M. Lewenstein. Atomic quantum gases in kagomé lattices. *Phys. Rev. Lett.*, 93:030601, Jul 2004.

[54] L.-M. Duan, E. Demler, and M. D. Lukin. Controlling spin exchange interactions of ultracold atoms in optical lattices. *Phys. Rev. Lett.*, 91:090402, Aug 2003.

[55] U. Dorner, P. Fedichev, D. Jaksch, M. Lewenstein, and P. Zoller. Entangling strings of neutral atoms in 1d atomic pipeline structures. *Phys. Rev. Lett.*, 91:073601, Aug 2003.

[56] S F Edwards and P W Anderson. Theory of spin glasses. *Journal of Physics F: Metal Physics*, 5(5):965, 1975.

[57] David Sherrington and Scott Kirkpatrick. Solvable model of a spin-glass. *Phys. Rev. Lett.*, 35:1792–1796, Dec 1975.

[58] Daniel S. Fisher and David A. Huse. Ordered phase of short-range ising spin-glasses. *Phys. Rev. Lett.*, 56:1601–1604, Apr 1986.

[59] A. J. Bray and M. A. Moore. Chaotic nature of the spin-glass phase. *Phys. Rev. Lett.*, 58:57–60, Jan 1987.

[60] J. Wehr, A. Niederberger, L. Sanchez-Palencia, and M. Lewenstein. Disorder versus the mermin-wagner-hohenberg effect: From classical spin systems to ultracold atomic gases. *Phys. Rev. B*, 74:224448, Dec 2006.

[61] W. Hofstetter, J. I. Cirac, P. Zoller, E. Demler, and M. D. Lukin. High-temperature superfluidity of fermionic atoms in optical lattices. *Phys. Rev. Lett.*, 89:220407, Nov 2002.

[62] Arnaud Koetsier, D. B. M. Dickerscheid, and H. T. C. Stoof. Bec-bcs crossover in an optical lattice. *Phys. Rev. A*, 74:033621, Sep 2006.

[63] Michael Köhl, Henning Moritz, Thilo Stöferle, Kenneth Günter, and Tilman Esslinger. Fermionic atoms in a three dimensional optical lattice: Observing fermi surfaces, dynamics, and interactions. *Phys. Rev. Lett.*, 94:080403, Mar 2005.

[64] G. Misguich and C. Lhuillier. *Frustrated spin systems.* World Scientific, Singapore, 2004.

[65] B. Damski, H.-U. Everts, A. Honecker, H. Fehrmann, L. Santos, and M. Lewenstein. Atomic fermi gas in the trimerized kagomé lattice at 2/3 filling. *Phys. Rev. Lett.*, 95:060403, Aug 2005.

[66] B. Damski, H. Fehrmann, H.-U. Everts, M. Baranov, L. Santos, and M. Lewenstein. Quantum gases in trimerized kagomé lattices. *Phys. Rev. A*, 72:053612, Nov 2005.

[67] Eugene Demler and Fei Zhou. Spinor bosonic atoms in optical lattices: Symmetry breaking and fractionalization. *Phys. Rev. Lett.*, 88:163001, Apr 2002.

[68] Adilet Imambekov, Mikhail Lukin, and Eugene Demler. Spin-exchange interactions of spin-one bosons in optical lattices: Singlet, nematic, and dimerized phases. *Phys. Rev. A*, 68:063602, Dec 2003.

[69] S. K. Yip. Dimer state of spin-1 bosons in an optical lattice. *Phys. Rev. Lett.*, 90:250402, Jun 2003.

[70] R. B. Laughlin. Anomalous quantum hall effect: An incompressible quantum fluid with fractionally charged excitations. *Phys. Rev. Lett.*, 50:1395–1398, May 1983.

[71] N. K. Wilkin and J. M. F. Gunn. Condensation of "composite bosons" in a rotating bec. *Phys. Rev. Lett.*, 84:6–9, Jan 2000.

[72] N. R. Cooper, N. K. Wilkin, and J. M. F. Gunn. Quantum phases of vortices in rotating bose-einstein condensates. *Phys. Rev. Lett.*, 87:120405, Aug 2001.

[73] B. Paredes, P. Fedichev, J. I. Cirac, and P. Zoller. $\frac{1}{2}$-anyons in small atomic bose-einstein condensates. *Phys. Rev. Lett.*, 87:010402, Jun 2001.

[74] M. Popp, B. Paredes, and J. I. Cirac. Adiabatic path to fractional quantum hall states of a few bosonic atoms. *Phys. Rev. A*, 70:053612, Nov 2004.

[75] Anders S. Sørensen, Eugene Demler, and Mikhail D. Lukin. Fractional quantum hall states of atoms in optical lattices. *Phys. Rev. Lett.*, 94:086803, Mar 2005.

[76] R. N. Palmer and D. Jaksch. High-field fractional quantum hall effect in optical lattices. *Phys. Rev. Lett.*, 96:180407, May 2006.

[77] I. Montvay and G. Münster. *Quantum Fields of a Lattice*. Cambridge University Press, Cambridge, 1997.

[78] J. Ruseckas, G. Juzeliūnas, P. Öhberg, and M. Fleischhauer. Non-abelian gauge potentials for ultracold atoms with degenerate dark states. *Phys. Rev. Lett.*, 95:010404, Jun 2005.

[79] Sumanta Tewari, V. W. Scarola, T. Senthil, and S. Das Sarma. Emergence of artificial photons in an optical lattice. *Phys. Rev. Lett.*, 97:200401, Nov 2006.

[80] Gilbert Grynberg, Alain Aspect, and Claude Fabre. *Introduction to Quantum Optics, From the Semi-classical Approach to Quantized Light*. Cambridge University Press, Cambridge, 2010.

[81] Pierre Meystre and Murray Sargent III. *Elements of Quantum Optics*. Springer-Verlag Berlin Heidelberg, 2007.

[82] Pierre Meystre. *Atom Optics*. Springer-Verlag New York, Inc., 2001.

[83] Werner Vogel and Dirk-Gunnar Welsch. *Quantum Optics*. WILEY-VCH Verlag GmbH and Co. KGaA, Weinheim, 2006.

[84] Lev Pitaevski and Sandro Stringari. *Bose-Einstein Condensation*. Oxford University Press Inc., New York, 2003.

[85] Gregory H. Wannier. The structure of electronic excitation levels in insulating crystals. *Phys. Rev.*, 52:191–197, Aug 1937.

[86] W. Kohn. Analytic properties of bloch waves and wannier functions. *Phys. Rev.*, 115:809–821, Aug 1959.

[87] W. Kohn. Construction of wannier functions and applications to energy bands. *Phys. Rev. B*, 7:4388–4398, May 1973.

[88] Nicola Marzari and David Vanderbilt. Maximally localized generalized wannier functions for composite energy bands. *Phys. Rev. B*, 56:12847–12865, Nov 1997.

[89] E. Anderson, Z. Bai, C. Bischof, S. Blackford, J. Demmel, J. Dongarra, J. Du Croz, A. Greenbaum, S. Hammarling, A. McKenney, and D. Sorensen. *LAPACK Users' Guide*. Society for Industrial and Applied Mathematics, Philadelphia, PA, third edition, 1999.

[90] Satish Balay, Shrirang Abhyankar, Mark F. Adams, Jed Brown, Peter Brune, Kris Buschelman, Lisandro Dalcin, Victor Eijkhout, William D. Gropp, Dinesh Kaushik, Matthew G. Knepley, Dave A. May, Lois Curfman McInnes, Richard Tran Mills, Todd Munson, Karl Rupp, Patrick Sanan, Barry F. Smith, Stefano Zampini, Hong Zhang, and Hong Zhang. PETSc Web page. `http://www.mcs.anl.gov/petsc`, 2018.

[91] Satish Balay, Shrirang Abhyankar, Mark F. Adams, Jed Brown, Peter Brune, Kris Buschelman, Lisandro Dalcin, Victor Eijkhout, William D. Gropp, Dinesh Kaushik, Matthew G. Knepley, Dave A. May, Lois Curfman McInnes, Richard Tran Mills, Todd Munson, Karl Rupp, Patrick Sanan, Barry F. Smith, Stefano Zampini, Hong Zhang, and Hong Zhang. PETSc users manual. Technical Report ANL-95/11 - Revision 3.9, Argonne National Laboratory, 2018.

[92] Satish Balay, William D. Gropp, Lois Curfman McInnes, and Barry F. Smith. Efficient management of parallelism in object oriented numerical software libraries. In E. Arge, A. M. Bruaset, and H. P. Langtangen, editors, *Modern Software Tools in Scientific Computing*, pages 163–202. Birkhäuser Press, 1997.

[93] Vicente Hernandez, Jose E. Roman, and Vicente Vidal. SLEPc: A scalable and flexible toolkit for the solution of eigenvalue problems. *ACM Trans. Math. Software*, 31(3):351–362, 2005.

[94] V. Hernandez, J. E. Roman, and V. Vidal. SLEPc: Scalable Library for Eigenvalue Problem Computations. *Lect. Notes Comput. Sci.*, 2565:377–391, 2003.

[95] J. E. Roman, C. Campos, E. Romero, and A. Tomas. SLEPc users manual. Technical Report DSIC-II/24/02 - Revision 3.9, D. Sistemes Informàtics i Computació, Universitat Politècnica de València, 2018.

[96] Takahiro Fukui, Yasuhiro Hatsugai, and Hiroshi Suzuki. Chern numbers in discretized brillouin zone: Efficient method of computing (spin) hall conductances. *Journal of the Physical Society of Japan*, 74(6):1674–1677, 2005.

[97] Fabrice Gerbier and Jean Dalibard. Gauge fields for ultracold atoms in optical superlattices. *New Journal of Physics*, 12(3):033007, 2010.

[98] E. Alba, X. Fernandez-Gonzalvo, J. Mur-Petit, J. K. Pachos, and J. J. Garcia-Ripoll. Seeing topological order in time-of-flight measurements. *Phys. Rev. Lett.*, 107:235301, Nov 2011.

[99] N Goldman, E Anisimovas, F Gerbier, P Öhberg, I B Spielman, and G Juzeliūnas. Measuring topology in a laser-coupled honeycomb lattice: from chern insulators to topological semi-metals. *New Journal of Physics*, 15(1):013025, 2013.

[100] Yasuhiro Hatsugai. Chern number and edge states in the integer quantum hall effect. *Phys. Rev. Lett.*, 71:3697–3700, Nov 1993.

[101] D. J. Thouless, M. Kohmoto, M. P. Nightingale, and M. den Nijs. Quantized hall conductance in a two-dimensional periodic potential. *Phys. Rev. Lett.*, 49:405–408, Aug 1982.

[102] Di Xiao, Ming-Che Chang, and Qian Niu. Berry phase effects on electronic properties. *Rev. Mod. Phys.*, 82:1959–2007, Jul 2010.

[103] Charles Nash and Siddhartha Sen. *Topology and Geometry for Physicists*. Academic Press Inc. (London) LTD, 1983.

[104] Mikio Nakahara. *Geometry, Topology and Physics*. IOP Publishing Ltd, 2003.

[105] John L. Kelley. *General Toplogy*. Springer, 1955.

SANTRAUKA

TURINYS

ĮVADAS

Per paskutinius kelis dešimtmečius buvo pasiekta nemažai pasiekimų labai šaltų atomų ir kvantinės optikos fizikoje [1]. Šiuo metu įmanoma tiksliai paruošti ir valdyti labai šaltų atomų dujas. Tai leidžia atlikti tikslius kvantinių sistemų matavimus. Šaldymo metodai leidžia pasiekti atomų dujų temperatūras iki kelių nano-Kelvinų eilės ir net mažesenes. 1997 metais už darbą ir pasiekimus atomų šaldymo ir laikymo fizikoje S. Chu, C. Cohen-Tannoudji ir W. D. Phillips buvo apdovanoti Nobelio premija [2, 3, 4]. Šie pasiekimai leido eksperimentiškai stebėti Bose-Einsten kondensaciją. 2001 metais E. A. Cornell, C. E. Wieman ir W. Ketterle už tai buvo apdovanoti Nobelio premija [5, 6].

Labai šaltų atomų sistemos gali būti naudojamos kaip kietų kūnų ir kondensuotų sitemų simuliatoriai [7, 8, 1]. Be to, optinių gardelių sukūrimas labai šaltiems atomams pradėjo kvantinių kompiuterių ir kvantinės informacijos eksperimentinius tyrimus. Šie eksprimentai leidžia tyrinėti kvantines koreliacijas bei kvantinį susietumą. Vienas iš svarbesnių tiriamų efektų yra fazinis virsmas iš superlaidininko fazės į Mott izoliatoriaus fazę [9]. Superlaidininko fazė pasižymi itin stipria koreliacija. Tuo tarpu Mott izoliatoriaus fazė patogi kvantiniams kompiuteriams, nes atomai turi fiksuotą skaičių kiekviename gardelės mazge.

Kvantiniai kompiuteriai ir kvantiniai simuliatoriai [10] gali padėti išspręsti kai kuriuos sudėtingus uždavinius kondensuotų medžiagų bei didelių energijų fizikoje. Pavyzdžiui, itin koreliuotos daugiadalelinės kondensuotos sistemos yra per sudėtingos tyrinėti skaitmeniškai su kompiuteriu. Labai šalti atomai optinėse gardelėse gali būti naudojami kaip tokių sistemų simuliatoriai ir taip pagelbėti suskaičiuoti įvairius reikalingus dydžius.

Labai šalti atomai paprastai yra elektriškai neutralūs. Todėl jie nejaučia įprasto magnetiniu lauko kaip taškinės dalelės (tai yra jie nejaučia Lorentz'o jėgos). Per pastaruosius metus buvo sugalvota nemažai būdų kaip sukurti dirbtinį magnetinį lauką. Vienas iš būdų yra sukti labai šaltų atomų dujų debesėli kartu su gardele ir nagrinėti visą šią sistemą besisukančioje koordinačių sistemoje [11, 12, 13, 14, 15, 16]. Kitas dirbtinio magnetinio lauko sukūrimo būdas yra naudoti lazerių spinduliuotę, kuri sukuria geometrinius potencialus [17, 18]. Magnetiniai srautai taip pat gali būti sukurti periodiškai purtant gardelės potencialą [19, 20, 21, 22].

Kadangi dirbtinį magnetinį lauką labai šaltiems atomams optinėse gardelė yra įmanoma sukurti, mes galime tokias sistemas naudoti tyrinėjant sveikąjį ir trupmeninį kvantinius Hall'o efektus. Labai šalti atomai optinėse gardelėse yra vienas iš būdų giliau tyrinėti šiuos efektus.

Šiame darbe tyrinėjame dvi skirtingas labai šaltų atomų gardelėse sistemas. Pir-

moje dalyje aprašome viendalelines labai šaltų atomų dvimatėje *dice* optinėje gardelėje savybes. Ši gardelė geometriškai atrodo kaip lošimo kauliukų rinkinys (*dice*), pasižymi šešiakampe geometrija ir yra Haldane modelio, kuris jau yra eksperimentiškai įgyvendintas [20], išplėtimas.

Antroje dalyje pristatome optinę gardelę, kuri pasižymi magnetiniu srautu, kuris nekeičia ženklo (*non-staggered flux*) elementariuose gardelės mazguose. Mes aprašome kaip tokia gardelė gali būti sukurta naudojant įprasto magnetinio lauko gradientą ir dažnių šukų spinduliuotę. Šioje darbo dabo dalyje mes ištyrinėjame šios gardelės dirbitinio magnetinio srauto savybes bei juostinės sandaros topologines savybes. Parodome kaip gardelės juostinė sandara pasižymi Landau lygmenų savybėmis.

Pagrindinis disertacijos tikslas

Ištyrinėti kvantinį Hall'o effektą esant *kintamo ženklo* ir *nekintamo ženklo* dirbtiniams magnetiniams laukams, kuris veikia labai šaltus atomus optinėse gardelėse, skaičiuojant dice optinės gardelės ir optinės srauto gardelės energijų spektrus bei atitinkamus Chern'o skaičius.

Disertacijos uždaviniai

1. Pateikti ir aprašyti dviejų lygmenų Haldane modelio išplėtimą į tris lygmenis – dice optinę gardelę – išvedant gardelės Bloch'o Hamiltonianą stipriojo ryšio artinyje.

2. Ištyrinėti dice optinės gardelės juostinės sandaros topologines savybes suskaičiuojant jos energijų spektrą bei atitinkamus Chern'o skaičius.

3. Pateikti ir aprašyti srauto gardelę, kuri sukuriama naudojant dažnio šukų spinduliuotę, ir išvesti efektyvų Hamiltonianą naudojant stroboskopinį artinį.

4. Suskaičiuoti srauto gardelės juostinę sandarą ir ištyrinėti jos topologinęs savybes suskaičiuojant kelių žemiausių juostų Chern'o skaičių.

Ginamieji teiginiai

1. Dviejų lygmenų Haldane modelis gali būti išplėstas į trijų lygmenų modelį naudojant dice optinę gardelę ir lazeriais sukeltus šuolius tarp artimiausių gardelės mazgų.

2. Išplėstas trijų lygmenų Haldane tipo modelis pasižymi topologinėmis puslaidininkio bei kitomis fazėmis, kuriuos aprašomos topologiniais Chern'o skaičiais moduliu didesniais už vienetą.

3. Optinė srauto gardelė su nekintamo ženklo magnetiniu srautu gali būti sukurta naudojant dviejų lygmenų atomus, veikiamus įprasto magnetinio lauko gradientu ir dažnio šukų spinduliuote, kuri rezonansiškai sukabina atomo lygmenis skirtinguose erdvės taškuose.

4. Darbe pateiktas optinės srauto gardelės modelis pasižymi topologiškai turtinga juostine sandara, kuri kai kuriais atvejais atitinka Landau tipo lygmenis ir kitais atvejais turi topologinius Chern'o skaičius moduliu didesnius už vienetą.

Darbo naujumas ir aktualumas

1. Vienas iš paprasčiausių dvimačių gardelių su dirbtiniu magnetiniu lauku yra gerai žinomas Haldane modelis [23], kuris jau yra eksperimentiškai įgyvendintas [20]. Šis modelis pasižymi topologiškai netrivialiomis energijos juostomis, kurios yra apibūdinamos topologiniais Chern'o skaičiais nelygiais nuliui.

2. Impulsiniame atvaizdavime Haldane modelis yra iš esmės dviejų lygmenų sistema. Šiame darbe mes pateikiame šio modelio išplėtimą į tris lygmenis naudodami "Dice" (lošimo kauliuko) geometriją. Išplėstas modelis pasižymi topologiškai turtingesne juostine sandara, kuri gali turėti topologinius Chern'o skaičius moduliu didesnius už vienetą.

3. Optinės srauto gardelės yra naujo tipo optinės gardelės, kurios pasižymi nekintančio ženklo magnetniu srautu (*non-staggered flux*). Darbe aprašome tokio tipo gardelę, sukuriamą naudojant dažnių šukų spinduliuotę.

4. Nekintančio ženklo magnetinis srautas optinėse gardelėse pasižymi pastovaus magnetinio lauko savybėmis. Dėl to, optinių srauto gardelių juostinė sandara gali pasižymėti Landau lygmenų savybėmis. Kai kuriais atvejais nagrinėjama srauto gardelė taip pat pateikia topologiškai turtingą juostinę sandarą, kurią apibūdiną Chern'o skaičiai moduliu didesni už vienetą.

Autoriaus indėlis

Disertacijos autorius atliko visus analitinius ir skaitmeninius tyrimus. Autorius parašė visas kompiuterines programas skaitmeniniams tyrimams. Autorius parašė visą disertacijos tekstą ir sukūrė visus paveikslėlius. Į tai neįeina disertacijos publikacijos, kurios yra pridėtos disertacijos pabaigoje.

Trumpas autoriaus gyvenimo aprašymas

Tomas Andrijauskas gimė 1988 metų birželio 4 dieną Šiauliuose. Vidurinį išsilavinimą įgyjo baigęs Klaipėdos Ąžuolyno gimnaziją 2007 metais. Tais pačiais metais Tomas įstojo į Vilniaus universiteto fizikos fakultetą ir pradėjo bakalauro studijas fiziko specialybei įgyti. Per bakalauro studijas Tomas buvo išvykęs pusmečiui į Švediją pagal ERASMUS studentų apsikeitimo programą. 2011 metais Tomas baigė bakalauro studijas ir įstojo į magistrantūros studijas tame pačiame fakultete. 2013 metais Tomas baigė magistrantūros studijas su pagyrimu (Magna Cum Laude) ir įstojo į doktorantūros studijas, kurias baigia šio dokumento ruošimo metu – 2018 metais.

Po antrojo bakalauro studijų kurso Tomas susipažino su prof. habil. dr. Gediminu Juzeliūnu, kuris tapo pagrindiniu jo mokslinių vadovu bei yra vadovas iki šiol.

Nuo 2012 metų Tomas parašė 6-ias publikacijas recenzuojamuose žurnaluose, sudalyvavo 14-oje tarptautinių konferencijų ir 4-iose vietinėse konferencijose. Per bakalauro studijas Tomas du kartus sudalyvavo vasaros studentų mokslinėje praktikoje. Per magistrantūros studijas Tomas taip pat sudalyvavo papildomoje studentų praktikoje.

1 Optinių gardelių ir dirbtinio magnetinio lauko apžvalga

1.1 Atomą veikiančios jėgos

Kad galėtume suprasti kaip atomų dujos yra šaldomos ir laikomos gaudyklėse bei kaip sukuriama optinė gardelė yra svarbu panagrinėti jėgas, kurios veikia paprastą dviejų vidinių lygmenų atomą, esantį elektromagnetiniame lauke.

Bendru atveju vieno atomo, elektromagnetinio lauko ir sąveikos tarp jų hamiltonianas susideda iš trijų dalių [24]:

$$H = H_{\mathrm{A}} + H_{\mathrm{F}} + H_{\mathrm{AF}} \,. \tag{1.1}$$

- Pirmasis narys H_{A} aprašo atomo masės centro judėjimą ir vidines būsenas. Pasirinkę žemesnės atomo vidinės būsenos $|g\rangle$ energija lygia nuliui, atomo hamiltoniana užrašome kaip

$$H_{\mathrm{A}} = \frac{\boldsymbol{p}^2}{2M} + \hbar\omega_0 |e\rangle\langle e| \,. \tag{1.2}$$

  Čia $|e\rangle$ yra sužadinta vidinė atomo būsena, kurios energija lygi $\hbar\omega_0$, $\boldsymbol{p}$ – judesio kiekis ir M – masė.

- Antrasis narys H_{F} aprašo elektromagnetinį lauką. H_{F} paprastai išreiškiamas per atsiradimo ir išnykimo operatorius kiekvienoje lauko modoje sumą

$$H_{\mathrm{F}} = \sum_{\boldsymbol{k},\epsilon} \hbar\omega_{\boldsymbol{k},\epsilon} a^{\dagger}_{\boldsymbol{k},\epsilon} a_{\boldsymbol{k},\epsilon} \,, \tag{1.3}$$

  kur $\boldsymbol{k}$ yra modos bangos vektorius, o ϵ – poliarizacija. Šaltų atomų fizikoje dažniausiai viena arba keletas elektromagnetinio lauko modų yra makroskopiškai užpildytos ir gali būti įtrauktos į dinamiką kaip klasikinis laukas. Tokiu atveju elektromagnetinio lauko hamiltonianą išskaidome į dvi dalis:

$$H_{\mathrm{F}} = H_{\mathrm{L}} + H_{\mathrm{R}} \,, \tag{1.4}$$

  kur H_{L} aprašo klasikinį elektromagnetinį lauką, o H_{R} sudaro visas kitas modas.

- Trečiasis narys H_{AF} aprašo atomo sąveiką su elektromagnetiniu lauku. Apsiribodami elektrinio dipolio artiniu, šį operatorių užrašome kaip

$$H_{\mathrm{AF}} = -\boldsymbol{d} \cdot \hat{\boldsymbol{E}}(\boldsymbol{r}, t) \,, \tag{1.5}$$

kur $\boldsymbol{d}$ yra atomo elektrinis dipolinis momentas:

$$\boldsymbol{d} = d\boldsymbol{e}_\zeta \left(|e\rangle\langle g| + |g\rangle\langle e|\right) . \tag{1.6}$$

Čia $\boldsymbol{e}_\zeta$ yra vienetis vektorius nukreiptas išilgai kvantavimo krypties.

Labai šalti atomai paprastai veikiami lazerių kuriamomis monochromatinėmis elektromagnetinėmis bangomis, kurių klasikinį elektrinį lauką galime apytikriai užrašyti kaip

$$\boldsymbol{E}_{\mathrm{L}}(\boldsymbol{r}, t) = \boldsymbol{e}_\epsilon(\boldsymbol{r})\mathcal{E}(\boldsymbol{r}) \cos\left[\omega t - \Phi(\boldsymbol{r})\right] , \tag{1.7}$$

kur ω yra bangos dažnis, $\boldsymbol{e}_\epsilon(\boldsymbol{r})$ – poliarizacijos vektorius, $\mathcal{E}(\boldsymbol{r})$ – lėtai kintanti lauko amplitudė, o $\Phi(\boldsymbol{r})$ – bangos fazė. Reikai paminėti, kad Naudodami ilgabangį artinį (*long-wavelength approximation*), klasikinio elektrinio lauko operatorių pakeičiame atomo masės centro koordinačių ir laiko funkcija $\hat{\boldsymbol{E}}_{\mathrm{L}}(\boldsymbol{r}, t) \to \boldsymbol{E}_{\mathrm{L}}(\boldsymbol{r} \equiv \boldsymbol{r}_{\mathrm{atom}}, t)$.

Atitinkamai kaip ir elektromagnetinio lauko (1.3), atomo sąveikos su lauku hamiltonianą (1.5) išskaidome į dvi dalis:

$$H_{\mathrm{AF}} = H_{\mathrm{AL}} + H_{\mathrm{AR}} . \tag{1.8}$$

Pirmasis narys H_{AL} yra atsakingas už dipolinę atomo sąveiką su klaskiniu elektromagnetiniu lauku. Pasinaudoję klasikinio elektrinio lauko išraiška (1.7), šį narį išreiškiame kaip

$$H_{\mathrm{AL}} = \hbar\Omega(\boldsymbol{r}) \left\{\cos\left[\omega t - \Phi(\boldsymbol{r})\right] |e\rangle\langle g| + \mathrm{h.\,c.}\right\} . \tag{1.9}$$

Čia įvedėme vieną iš svarbiausių atomo optikoje dydį – Rabi dažnį

$$\Omega(\boldsymbol{r}) = -d\left[\boldsymbol{e}_\zeta \cdot \boldsymbol{e}_\epsilon(\boldsymbol{r})\right] \frac{\mathcal{E}(\boldsymbol{r})}{\hbar} , \tag{1.10}$$

kuris apibūdina atomo sąveikos su klasikiniu elektromagnetiniu lauku stiprumą. Antrasis sąveikos (1.8) narys H_{AR} sukabina atomo vidinių lygmenų sistemą su visomis kitomis neužpildytomis elektromagnetinio lauko modomis ir aprašo savaiminę spinduliuotę atomui pereinant iš sužadintos būsenos $|e\rangle$ į nesužadintą $|g\rangle$. Paprastai šio nario įtaką atomo judėjimui elektromagnetiniame lauke apibūdiname fenomenologiniu parametru – savaiminės spinduliuotės sparta Γ.

Toliau nagrinėkime atomo, esančio aprašytame klasikiniame elektromagnetiniame lauke (1.7), judesio kiekio momento operatoriaus $\boldsymbol{p}$ dinamiką, kurią aprašo Heisenberg'o judėjimo lygtis

$$\frac{\mathrm{d}\boldsymbol{p}}{\mathrm{d}t} = \frac{1}{\mathrm{i}\hbar}[\boldsymbol{p},\, H_{\mathrm{A}} + H_{\mathrm{AL}}] . \tag{1.11}$$

Vidutinę jėgą $\boldsymbol{F}$, kuri veikia atomą, galime suskaičiuoti kaip jo judesio kiekio operatoriaus $\boldsymbol{p}$ laikinės išvestinės kvantmechaninį vidurkį

$$\boldsymbol{F} = \left\langle \frac{\mathrm{d}\boldsymbol{p}}{\mathrm{d}t} \right\rangle . \tag{1.12}$$

Čia pilno vidutinės jėgos išvedimo, kurį galima rasti [24], nepateiksime. Paminėsime tik dvi svarbiausias jėgos komponentes – disipacinę jėgą $\boldsymbol{F}_{\mathrm{dissip}}$ ir reaktyvią (arba dipolinę) jėgą $\boldsymbol{F}_{\mathrm{react}}$:

$$\boldsymbol{F}_{\mathrm{dissip}} = \hbar \boldsymbol{k}_{\mathrm{L}} \frac{\Gamma}{2} \frac{\Omega^2/2}{\delta^2 + (\Gamma/2)^2 + \Omega^2/2} , \tag{1.13}$$

$$\boldsymbol{F}_{\mathrm{react}} = -\frac{\hbar\delta}{2} \frac{\nabla(\Omega^2)}{\delta^2 + (\Gamma/2) + \Omega^2/2} . \tag{1.14}$$

Čia δ yra elektromagnetinio lauko dažnio ω išderinimas lyginant su rezonansiniu atomo dažniu ω_0:

$$\delta = \omega - \omega_0 , \tag{1.15}$$

o $\boldsymbol{k}_L$ – plokščiosios elektromagnetinės bangos vektorius. Reikia paminėti, kad nors dinamikoje energijos operatorius H_{AR} ir nedalyvauja, jo įtaką įtraukiame per spinduliuotės spartą Γ.

Pateikta disipacinė jėga $\boldsymbol{F}_{\mathrm{dissip}}$ yra atsakinga už elektromagnetinės spinduliuotės slėgį, kuris mažina atomo kinetinę energiją ir yra svarbi nagrinėjant atomų dujų šaldymo procesus. Šios jėgos priklausomybė nuo išderinimo δ turi Lorenco funkcijos formą. Dipolinė jėga $\boldsymbol{F}_{\mathrm{react}}$ yra svarbi nagrinėjant optines atomų gaudykles ir optines gardeles. Galime pastebėti, kad ši jėga yra proporcinga Rabi dažnio kvadrato gradientui $\nabla(\Omega^2)$, todėl ji nelygi nuliui tik tuomet, jeigu elektrinio lauko intensyvumas erdvėje kinta.

1.2 Atomų dujų šaldymas

Šiame skyrelyje trumpai aprašysime du svarbiausius atomų dujų šaldymo būdus: Doppler'io šaldymą (*Doppler cooling*) ir garinimo šaldymą (*evaporative cooling*). Pirmasis paprastai atliekamas atomų šaldymo proceso pradžioje, o antrasis – pabaigoje. Kiti šaldymo būdai (*Sysiphus cooling, subrecoil cooling*) plačiau aprašyti [3, 24].

Nagrinėkime atomą, judantį greičiu $\boldsymbol{v}_0$ monochromatinės elektromagntinės bangos elektriniame lauke

$$\boldsymbol{E}(\boldsymbol{r}, t) = \boldsymbol{e}_\epsilon \mathcal{E} \cos(\omega t - \boldsymbol{k} \cdot \boldsymbol{r}) .$$

Naudodami ilgabangį artinį, atomo masės centro padėties vektorių tiesiog įstatome į šio elektrinio lauko išraišką:

$$\boldsymbol{E}(\boldsymbol{r},t) = \boldsymbol{e}_\epsilon \mathcal{E} \cos\left[(\omega - \omega_\mathrm{D})t\right] ,$$

kur $\boldsymbol{k}\cdot\boldsymbol{r} = \boldsymbol{k}\cdot\boldsymbol{v}_0 t = \omega_\mathrm{D} t$. Čia ω_D yra dėl Doppler'io efekto atsiradęs dažnio poslinkis. Atitinkamai lazerio elektromagnetinės bangos dažnio išderinimas (1.15), nuo kurio priklauso atomą veikianti disipacinė jėga (1.13), pasikeičia į $\delta_\mathrm{D} = \delta - \omega_\mathrm{D}$. Taigi dėl Doppler'io efekto, atomas, judantis prieš elektromagnetinės bangos sklidimo kryptį, jaučia didesnį bangos dažnį. Priešingai, atomas, judantis ta pačia kryptimi kaip ir sklindanti elektromagnetinė banga, jaučia mažesnį bangos dažnį.

Sakykime lazerio elektromagntinė banga yra išderinta į raudonąją pusę ($\delta < 0$). Tokiu atveju lėtesni atomai, judantis prieš elektromagnetinę bangą, dėl Doppler'io efekto jaus bangą, kurios dažnis yra artimesnis rezonansiniui atomo dažniui ω. Gretesni atomai jaus bangą, kurios dažnis yra toliau rezonansinio dažnio. Dėl to, atomai, judantis prieš bangą, yra labiau stabdomi, nei greitinami, judantis ta pačia kryptimi kaip ir banga. Šiuo atveju šaldymas vyksta sudedant dvi viena prieš kitą skilndančias elektromagnetines bangas, išderintas į raudonąją pusę. Esant pakankamai silpnoms bangoms, disipacinės jėgos išraiška (1.13) supaprastėja [**?**]:

$$\boldsymbol{F}_\mathrm{Doppler} \approx -2\eta v_0 , \tag{1.16}$$

kur η yra „trinties“ koeficientas.

Dėl savaiminės spinduliuotės ir atsitiktinės fotonų, išspinduliuotų kitų dujose esančių atomų, sugerties Doppler'io šaldymas turi tam tikrą apatinę temperatūros ribą, kuri priklauso nuo atomų rūšies. Šarminiams elementams ši temperatūra yra keleto šimtų mikro-Kelvinų eilės. Norint atomų dujas atšaldyti iki žemesnių tempratūrų, reikia naudoti kitus šaldymo būdus, pavyzdžiui Sysiphus šaldyma, kuriam paaiškinti dviejų vidinių atomo lygmenų neužtenka.

Atomų dujų šaldymo pabaigoje paprastai naudojamas gana paprastas garinimo šaldymas. Atomų gaudyklės potencialinis barjeras yra kuriam laikui sumažinamas taip leidžiant didesnės kinetinės energjos atomams iš jos pabėgti. Šis šaldymo būdas leidžia pasiekti itin mažas nano-Kelvinų eilės temperatūras.

1.3 Magnetinės ir optinės gaudyklės

Beveik visos sąveikaujančių atomų sistemos pakankamai žemose temperatūrose pereina į kieto kūno fazę. Išimtis gali būti Helio atomai, kurie išlieka skystoje fazėje jeigu mažindami temperatūrą nedidiname slėgio. Iš pirmo žvilgsnio pastebime, kad

labai šaltų atomų dujos ir Bose-Einstein'o kondendatai negalėtų egzistuoti. Tačiau reikia paminėti, kad perėjimas į kietojo kūno fazę yra labiausiai įtakotas dėl trijų kūnų susidūrinėjimų [**?**]. Taigi pakankamai sumažinus atomų tankį (paprastai Bose-Einstein'o kondensate atomu tankis yra $10^{13} - 10^{15}\,\mathrm{cm}^{-3}$) galime sumažinti trijų kūnų susidurinėjimų dažnį ir išlaikyti dujinę fazę. Tokiu atveju, kad būtų svarbūs kvantiniai reiškiniai, atomų dujų temperatūra turi ypač maža ($10^{-6}\,\mathrm{K}$ eilės). Be to, atomų dujos turi būti laikomos toliau nuo kitų medžiagų, nes atomai gali su jomis susidurinėti ir taip sukelti fazinį virsmą iš dujinės į kieto kūno fazę. Išlaikyti dujinę fazę taip pat padeda sukinių poliarizacija, kuri sustiprina stūmą tarp atomų.

Minėtos sąlygos sudaromos surenkant ir atšaldant labai grynas mažo tankio atomų dujas su poliarizuotais sukiniais magnetinėje gaudyklėje arba optinėje gaudyklėje. Sistema pakankamai ilgai išbūna tokioje nepusiausvyroje būsenoje (paprastai apie keletą sekundžių) lyginant su laiku tarp dviejų kūnų susidurinejimais, kurie leidžia temperatūrai tolygiai pasiskirstyti atomų dujų debesėlyje.

Magnetinių gaudyklių veikimas remiasi Zeeman'o efektu. Kad galėtume suprasti tokių gaudykliu veikimo principus, panagrinėkime sukinines šarminių elementų savybes. Šarminiai elementai turi tik vieną išorinį elektroną ir žemiausiosje būsenoje pilno elektrono judesio kiekio momento $\boldsymbol{J}$ projekcija į z ašį lygi $1/2$ (Planc'o konstantos $\hbar$ nerašome). Įtraukiant ir branduolio judesio kiekio momentą, atomus galime suskirstyti į dvi grupes. Jeigu atomo branduolio neutronų skaičius yra lyginis, tai žinant, kad protonų skaičius yra nelyginis, atomas yra bozonas. Kitu atveju atomas yra fermionas. Pilno atomo judesio kiekio momento $\boldsymbol{F} = \boldsymbol{I} + \boldsymbol{J}$ projekcijų vertes, priklausomai nuo branduolio judesio kiekio momento $\boldsymbol{I}$, galime suskirstyti į dvi grupes: $F = I \pm 1/2$. Kol nėra magnetinio lauko, energijos išsigimimą tarp abiejų hypersmulkiosios struktūros lygmenų pašalina elektrono judesio kiekio momento sąveika su branduolio judesio kiekio momentu:

$$H_{\mathrm{hf}} = a\boldsymbol{I} \cdot \boldsymbol{J}\,, \tag{1.17}$$

kur a yra sąveikos konstanta.

Esant magnetiniam laukui prie sąveikos (1.17) turime pridėti papildomą narį

$$H_{\mathrm{hf}} = a\boldsymbol{I} \cdot \boldsymbol{J} + 2\mu_B J_z B \tag{1.18}$$

kuris kiekvieną hypersmulkiosios spektro sandaros lygmenį suskaldo į keletą polygmenių, priklausomai nuo branduolio judesio kiekio momento $\boldsymbol{I}$. Čia μ_B yra Bohr'o magnetonas, o magnetinis laukas yra nukreiptas išilgai z ašies. Pavyzdžiui, natrio ^{23}Na ir rubidžio ^{87}Rb atveju $I = 3/2$ ir abu hypersmulkiosios sandaros lygmenys suskyla į aštuonis polygmenis: du lygmenis su $m_F = \pm 2$ ir po du lygmenis kiekvienu

kitu atveju: $m = -1, 0, 1$. Labai stipraus magnetinio lauko riboje abiejų suskilusių lygmenų energijos artėja prie dviejų lygmenų $E = \pm\mu_B B$. Sąveika tarp atomų kiekviename lygmenyje gali būti skirtinga. Tai leidžia nagrinėti nemažai skirtingų sąveikaujančių šaltų atomų dujų sistemų.

Aptarto tipo atomams magnetinė gaudyklė sudaroma sukuriant erdvėje kintančio stiprumo magnetinį lauką $\boldsymbol{B}(\boldsymbol{r})$. Esant sąlygoms, kai galioja adiabatinis artinys – atomas, judėdamas erdvėje, išlieka toje pačioje vidinėje būsenoje – atomo energija priklauso nuo magnetinio lauko erdvinio kitimo. Jeigu stiprėjant magnetiniam laukui atomo energija mažėja, atomai judės magnetinio lauko stiprėjimo kryptimi. Kitu atveju, jeigu stiprėjant laukui energija didėja, atomai judės lauko silpnėjimo kryptimi. Kadangi vakuume negalime sukurti statinio magnetinio lauko, kuris turėtų maksimumą (tai išplaukia iš Maxwell'o lygčių), tai pirmuoju atveju sudaryti magnetinės gaudyklės negalime. Lieka tos vidinės būsenos, kuriose esantys atomai juda magnetinio lauko silpnėjimo kryptimi. Natrio ir rubidžio atveju tokios būsenos yra $F = 2$, $m_F = +2, +1$ ir $F = 1$, $m_F = -1$.

Toliau aptarsime optinių gaudyklių veikimo principus. Prisimine praeitame skyrelyje pateiktą atomą veikiančios dipolinės jėgos $\boldsymbol{F}_{\text{react}}$ išraišką (1.14), pastebime, kad ją galime perrašyti kaip tam tikros potencinės funkcijos $V_{\text{eff}}(\boldsymbol{r})$ gradientą:

$$\begin{aligned} \boldsymbol{F}_{\text{react}}(\boldsymbol{r}) &= -\nabla V_{\text{eff}}(\boldsymbol{r}) \\ V_{\text{eff}}(\boldsymbol{r}) &= \frac{\hbar\delta}{2} \ln\left(1 + \frac{\Omega^2/2}{\delta^2 + (\Gamma/2)^2}\right) . \end{aligned} \tag{1.19}$$

Ši funkcija (1.19) yra efektyvus potencialas, atsiradęs dėl lazerio elektromagnetinio lauko.

Galime pastebėti, kad esant esant pakankamai mažam Rabi dažniui, efektyvus potencialas yra apytikriai proporcingas Rabi dažnio kvadratui, tuo pačiu ir elektrinio lauko intensyvumui:

$$V_{\text{eff}}(\boldsymbol{r}) \sim |\mathcal{E}(\boldsymbol{r})|^2 . \tag{1.20}$$

Jeigu lazerio lauko dažnis yra išderintas į raudonąją pusę ($\delta < 0$), atomas turės mažesnę energiją erdvės taškuose, kuriuose elektrinis laukas yra stipresnis. Priešingu atveju ($\delta > 0$), atomai turės turės mažesnę energiją taškuose, kur laukas silpnesnis. Efektyvų potencialą yra patogu perrašyti

$$V_{\text{eff}}(\boldsymbol{r}) = \operatorname{sgn}(\delta)\, V(\boldsymbol{r}) = \pm V(\boldsymbol{r}) ,$$

kur $V(\boldsymbol{r})$ – dipolinis potencialas, proporcingas elektrinio lauko inensyvumui, yra teigiama funkcija. Efektyvus potencialas $V_{\text{eff}}(\boldsymbol{r})$ atitinkamai yra lygus arba priešingas jam priklausomai nuo išderinimo δ.

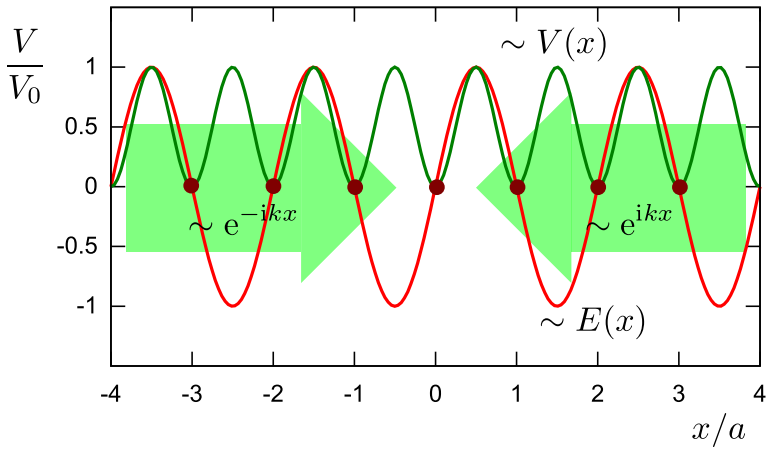

1.1 pav.: Paprasčiausia vienmatė optinė gardelė, sukurtą dviejų vienas prieš kitą bėgančių plokščių elektromagnetinių bangų. Žalia kreive pavaizduotas dipolinis potencialas $V(x)$. Čia V_0 yra potencialo gylis, o $a = \pi/k_\mathrm{L}$ – gardelės konstanta. Raudona kreive pavaizduotas elektrinio lauko, kuriančio tokį potencialą, kitimo dėsnis.

Optinė gaudyklė paprasčiausiu atveju sukuriama naudojant į raudonąją pusę išderintą lazerio lauką ($\delta < 0$). Žinant, kad lazerio elektrinis laukas statmenai bangos sklidimo krypčiai turi Gauss'o funkcijos formą, atomai judės link lauko maksimumo. Taip naudojant vieną arba daugiau persiklojančių lazerių pluoštų priverčiame atomus likti optinėje gaudyklėje. Paprastai optinės gaudyklės yra stipresnės už magnetines.

1.4 Optinės gardelės

Žinodami, kad atomą veikiantis dipolinis potencialas $V(\boldsymbol{r})$ yra proporcingas elektromagnetinės bangos elektrinio lauko intensyvumui $|\mathcal{E}(\boldsymbol{r})|^2$ (1.20), paprasčiausią periodinį potencialą sukuriame iš stovinčiosios bangos – dviejų vienas prieš kitą bėgančių bangų superpozicijos:

$$V(\boldsymbol{r}) \sim \mathcal{E}^2 \left|\mathrm{e}^{\mathrm{i}(\omega t - k_\mathrm{L}\cdot x)} + \mathrm{e}^{\mathrm{i}(\omega t + k_\mathrm{L}\cdot x + \phi)}\right|^2 ,$$
$$V(\boldsymbol{r}) = V_0 \sin^2(k_\mathrm{L}\cdot x + \tilde{\phi}) ,$$

kur k_L bangos vektoriaus modulis, o ϕ ir $\tilde{\phi} = \phi/2$ nurodo galimą fazių skirtumą tarp bangų. Toks periodinis potencialas yra vienmatė optinė gardelė, kuri pavaizduota 1.1 pav. Gardelės konstanta – atstumas tarp gretimų gardelės mazgų – yra $a = \pi/k_\mathrm{L}$.

Paprasčiausią dvimatę optinę gardelę sukuriame naudodami daugiau persiklojančių stovinčių bangų. 1.2 pav. pavaizduota kvadratinė optinė gardelė, kurios

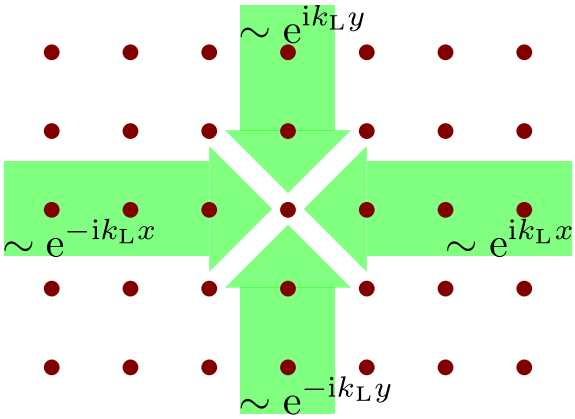

1.2 pav.: Kvadratinė optinė gardelė

dipolinis potencialas yra

$$V(\boldsymbol{r}) = V_0 \left[\sin^2(k_\mathrm{L}x) + \sin^2(k_\mathrm{L}y)\right] \ . \tag{1.21}$$

Reikia paminėti, kad tokia elektrinių laukų intensuvumo sudėtis teisinga tuomet, kai abiejų stovinčių bangų dažniai yra šiek tiek išderinti. Tokiu atveju papildomo greitai kintančio interferencinio nario galime į dinamiką neįtraukti (atlikti vidurkinimą laike ir apsiriboti tik lėtai kintančiais nariais).

2 Tyrimo metodai naudojami šiame darbe

2.1 Periodinis potencialas ir Bloch'o teorema

Pirmasis žingsnis bet kokiame kvantinės mechanikos uždavinyje yra išspręsti vienos dalelės stacionariąją Schrödinger'io lygtį

$$H|\psi\rangle = E|\psi\rangle\,, \tag{2.1}$$

kur H yra sistemos hamiltonianas – pilnutinės energijos operatorius. Ši lygtis kitaip vadinama hamiltoniano tikrinių verčių lygtimi ir jos sprendiniai sudaro galimas sistemos būsenas $|\psi\rangle$, kuriose tiksliai žinoma energija. Kadangi hamiltonianas yra ermitinis (*hermitian*), tai jo tikriniai būsenos vektoriai sudaro pilną bazę visoje nagrinėjamos kvantinės sistemos Hilbert'o erdvėje. Žinodami tokią pilną būsenų bazę ir jų energijas galime nagrinėti laikinius uždavinius (spręsti laikinę Schrödinger'io lygtį) bei konstruoti įvairius didelio dalelių skaičiaus modelius.

Nagrinėkime vienos kvantinės dalelės judėjimą dvimačiame periodiniame potenciniame lauke $V(\boldsymbol{r})$, kuris nepakinta atlikus transliaciją per vektorių $\boldsymbol{R} = n_1\boldsymbol{a}_1 + n_2\boldsymbol{a}_2$:

$$V(\boldsymbol{r} + \boldsymbol{R}) = V(\boldsymbol{r})\,, \tag{2.2}$$

kur n_i yra sveikieji skaičiai. Toks periodinis potencialas vadiamas gardele, vektorių rikinys $\boldsymbol{a}_i$ vadinamas gardelės vektoriais, o jų ilgiai $|\boldsymbol{a}_i|$ - gardelės konstantomis. Stačiakampis gretasienis, kurį sudaro gardelės vektoriai vadinamas elementariuoju narveliu. Pilnas vienos dalelės hamiltonianas bedimensiniuose dydžiuose

$$H = -\frac{1}{2}\boldsymbol{p}^2 + V(\boldsymbol{r}) \tag{2.3}$$

yra transliaciškai invariantinis per gardelės vektorių $\boldsymbol{R}$. Tai reiškia, kad hamiltonianas komutuoja su transliacijos operatoriumi $T_{\boldsymbol{R}}$, kurį galime apibrėžti per judesio kiekio operatorių $\boldsymbol{p}$:

$$[H,\, T_{\boldsymbol{R}}] = 0\,, \qquad T_{\boldsymbol{R}} = \exp(-\mathrm{i}\boldsymbol{p}\cdot\boldsymbol{R})\,. \tag{2.4}$$

Pasinaudodami operatoriaus $T_{\boldsymbol{R}}$ poveikio į banginę funkciją $\psi(\boldsymbol{r}) = \langle\boldsymbol{r}|\psi\rangle$ Teiloro (*Taylor*) eilutės skleidiniu pagal $\boldsymbol{R}$, galime nesudėtingai parodyti, kad šis operatorius, veikdamas į banginę funkciją, pastumia ją per vektorių $\boldsymbol{R}$:

$$T_{\boldsymbol{R}}\psi(\boldsymbol{r}) = \psi(\boldsymbol{r} - \boldsymbol{R})\,. \tag{2.5}$$

Kvantinės mechanikos uždaviniuose dažniausiai reikalaujame, kad ieškoma sistemos

banginė funkcija būtų tolydi ir turėtų tolydžias išvestines, taigi toks skleidimas Teiloro eilute yra teisingas.

Kadangi nagrinėjama kvantinė sistema yra periodinė, mes reikalaujame, kad perstumtos per vektorių $\boldsymbol{R}$ banginės funkcijos modulio kvadratas arba dalelės padėties tikimybės tankis nepasikeitų:

$$|T_{\boldsymbol{R}}\psi(\boldsymbol{r})|^2 = |\psi(\boldsymbol{r})|^2 \,. \tag{2.6}$$

Šios banginės funcijos sąvybės ir žinojimas, kad transliacijos operatoriaus tikrinės vertės yra $\exp(-\mathrm{i}\boldsymbol{k}\cdot\boldsymbol{R})$, leidžia šio operatoriaus poveikį banginei funkcijai užrašyti tokiu būdu

$$T_{\boldsymbol{R}}\psi(\boldsymbol{r}) = \exp(-\mathrm{i}\boldsymbol{k}\cdot\boldsymbol{R})\psi(\boldsymbol{r}) \,, \tag{2.7}$$

kur $\boldsymbol{k}$ yra tikrinė judesio kiekio operatoriaus vertė. Ši savybė parodo, kad banginę funciją galime išskaidyti į eksponentinę ir periodinę per gardelės vektorių $\boldsymbol{R}$ dalis:

$$\psi_{\boldsymbol{k}}(\boldsymbol{r}) = \exp(\mathrm{i}\boldsymbol{k}\cdot\boldsymbol{r})u_{\boldsymbol{k}}(\boldsymbol{r}) \,. \tag{2.8}$$

Tokios formos būsenos funkciją vadiname Bloch'o funkcija, o tokios formos sprendinio užrašymą esant periodiniam potencialui - Bloch'o teorema. Šia funkciją numeruojame indeksu $\boldsymbol{k}$ - Bloch'o banginiu vektoriumi. Trumpai tariant Bloch'o teorema teigia, kad dalelės, esančios periodiniame potenciale banginė funkcija yra moduliuota eksponentinė funkcija.

Iš Bloch'o funkcijos formos (2.8) matome, kad ji nesikeičia perstūmus Bloch'o banginį vektorių $\boldsymbol{k}$ per atvirkštinį vektorių $\boldsymbol{G} = n_1\boldsymbol{b}_1 + n_2\boldsymbol{b}_2$. Čia $\boldsymbol{b}_i$ yra atvirkštinės gardelės vektoriai, kurie pasirenkami taip, kad būtų tenkinama sąlyga

$$\boldsymbol{a}_i \cdot \boldsymbol{b}_j = 2\pi\delta_{i,j} \,. \tag{2.9}$$

Toks Bloch'o funkcijos periodiškumas atvirkštinėje gardelėje reiškia, kad mums užtenka nagrinėti tik dalį visų galimų $\boldsymbol{k}$ reikšmių arba kitaip tariant mums užtenka apsiriboti pirmąja Brillouin'o zona.

Bloch'o teorema padeda kvantinės mechanikos uždavinį supaprastinti iki elementaraus narvelio realioje erdvėje. Kitaip tariant, pasinaudodami stacionariąja Schrödinger'o lygtimi, galime užrašyti lygtį periodinei funkcijai $u_{\boldsymbol{k}}(\boldsymbol{r})$. Paprasčiausias būdas šią lygtį užrašyti yra paveikti Bloch'o funkciją (2.8) judesio kiekio operatoriumi $\boldsymbol{p}$ žinant, kad jis koordinatiniame atvaizdavime užrašomas kaip $-\mathrm{i}\nabla$. Diferencijuodami Bloch'o funciją $\psi_{\boldsymbol{k}}(\boldsymbol{r})$ pastebime, kad periodinės funkcijos $u_{\boldsymbol{k}}(\boldsymbol{r})$ atskyrimas

nuo eksponentės atitinka pakeitimą $\nabla \to \nabla + \mathrm{i}\boldsymbol{k}$. Taigi lygtis šiai funkcijai yra

$$-\frac{1}{2}(\nabla + \mathrm{i}\boldsymbol{k})^2 u_{\boldsymbol{k},n}(\boldsymbol{r}) + V(\boldsymbol{r}) u_{\boldsymbol{k},n}(\boldsymbol{r}) = E_{\boldsymbol{k},n} u_{\boldsymbol{k},n}(\boldsymbol{r})\,. \tag{2.10}$$

Šią lygtį užrašome kiekvienai skirtingai $\boldsymbol{k}$ reikšmei pirmojoje Brillouin'o zonoje ir pilnas sistemos hamiltonianas tampa diagonalus pagal indeksą $\boldsymbol{k}$. Kadangi bendru atveju ši tikrinių verčių lygtis gali duoti be galo daug sprendinių, mes taip pat įvedame papildomą indeksą n joms numeruoti.

Tikrinių energijos verčių rinkinys tam tikrai fiksuotai n reikšmei $(\boldsymbol{k}, E)$ erdvėje sudaro paviršių, kurį vadiname dispersijos juosta, o visą tokių paviršių rinkinį visoms n reikšmėms vadiname dispersija. Visų tikrinių energijos verčių $E_{\boldsymbol{k},n}$ ir atitinkamų tikrinių būsenos vektorių $|\psi_{\boldsymbol{k},n}\rangle$ (arba atitinkamų periodinių dalių $|u_{\boldsymbol{k},n}\rangle$) rinkinį vadiname juostine sandara.

2.2 Wannier būsenos

Nors Bloch'o funkcijos (2.8) yra tikrinės sistemos hamiltoniano būsenos ir sudaro pilną sistemos Hilberto erdvės bazę, jos nėra patogios nagrinėjant labai šaltus atomus optinėse gardelėse, ypač tiriant daugiadalelinius reiškinius, kuomet dažnai naudojamas stipriojo ryšio artinys. Šiame skyrelyje įvesime ir panagrinėsime kitą ortogonalių bazinių funkcijų – Wannier funkcijų – bazę [25, 26, 27, 28], kuri yra patogi minėtame artinyje.

Wannier funkciją $\phi_{\boldsymbol{R},n}(\boldsymbol{r})$ apibrėžiame kaip Bloch'o būsenų $\psi_{\boldsymbol{k},n}(\boldsymbol{r})$ Fourier transformaciją

$$\phi_{\boldsymbol{R},n}(\boldsymbol{r}) = \sqrt{\frac{V}{(2\pi)^3}} \int_{\mathrm{BZ}} \mathrm{d}^2\boldsymbol{k}\, \exp(-\mathrm{i}\boldsymbol{k}\cdot\boldsymbol{R}) \psi_{\boldsymbol{k},n}(\boldsymbol{r})\,, \tag{2.11}$$

kur integruojame per pirmą Brillouin'o zona. Raide V žymime elementaraus narvelio realioje erdvėje plotą. Jeigu, įvedę periodines kraštines salygas, nagrinėjame baigtinį elementarių narvelių skaičių, tai turime kvantuotas Bloch'o banginio vektoriaus $\boldsymbol{k}$ vertes ir integralą (2.11) pakeičiame suma

$$\phi_{\boldsymbol{R},n}(\boldsymbol{r}) = \frac{1}{\sqrt{N}} \sum_{\boldsymbol{k}} \exp(-\mathrm{i}\boldsymbol{k}\cdot\boldsymbol{R}) \psi_{\boldsymbol{k},n}(\boldsymbol{r})\,, \tag{2.12}$$

kur raide N pažymėjome skirtingų $\boldsymbol{k}$ verčių pirmojoje Brillouin'o zonoje skaičių, kuris lygus pilnam elementarių narvelių skaičiui kvantavimo tūryje.

Taip apibrėžtos Wannier funkcijos $\phi_{\boldsymbol{R},n}(\boldsymbol{r})$ turi keletą savybių:

- $\phi_{\boldsymbol{R},n}(\boldsymbol{r})$ yra periodinės funkcijos pagal indeksą $\boldsymbol{R}$:

$$\phi_{\boldsymbol{R},n}(\boldsymbol{r}) = \phi_{\boldsymbol{R}+\boldsymbol{R}',n}(\boldsymbol{r} + \boldsymbol{R}')\,. \tag{2.13}$$

Čia $\boldsymbol{R}'$ yra gardelės transliacijos vektorius. Ši savybė parodo, kad kiekviena Wannier funkcija yra viena kitos per tam tikrą elementarių narvelių skaičių perstumta kopija. Taigi, žinodami Wannier funkciją viename elementariame narvelyje, kitas sužinome atlike jos transliaciją per gardelės vektorių $\boldsymbol{R}'$. Tokia šių funkcijų savybė leidžia jas žymėti paprasčiau:

$$\phi_n(\boldsymbol{r} - \boldsymbol{R}) := \phi_{\boldsymbol{R},n}(\boldsymbol{r})\,. \tag{2.14}$$

- $\phi_{\boldsymbol{R},n}(\boldsymbol{r})$ nėra unikaliai apibrėžtos. Pasirinkus Bloch'o funkcijų rinkinį su kitomis globaliomis fazėmis

$$\tilde{\psi}_{\boldsymbol{k},n}(\boldsymbol{r}) = \exp(\mathrm{i}\varphi_{\boldsymbol{k},n})\psi_{\boldsymbol{k},n}(\boldsymbol{r})\,, \tag{2.15}$$

jų modulio kvadrato nepakeičiame $|\tilde{\psi}_{\boldsymbol{k},n}(\boldsymbol{r})|^2 = |\psi_{\boldsymbol{k},n}(\boldsymbol{r})|^2$, tačiau iš jų sukonstruojame jau kitokias Wannier funkcijas. Jeigu mes nagrinėsime keletą dispersijos juostų, kurios yra persiklojusios viena su kita, tai bendru atveju, prieš konstruodami Wannier funkcijas, galime pradines Bloch'o funkcijas sumaišyti, t. y. paimti jų superpozicijas:

$$\tilde{\psi}_{\boldsymbol{k},m}(\boldsymbol{r}) = \sum_n U^{(\boldsymbol{k})}_{mn}\psi_{\mathbf{k},n}(\boldsymbol{r})\,, \tag{2.16}$$

kur $U^{(\boldsymbol{k})}$ yra unitari matrica, kuri sumaišo Bloch'o būsenas viena su kita kiekviename pirmosios Brillouin'o zonos taške $\boldsymbol{k}$. Vienos dispersijos juostos atveju formulę (2.15) galime laikyti kaip atskiru formulės (2.16) atveju, kai ši matrica yra diagonali.

Toks Wannier funkcijų neunikalumas nėra patogus daugiadaleliniuose skaičiavimuose. Vis dėlto, yra parodyta, kad unitarias matricas $U^{(\boldsymbol{k})}$ įmanoma pasirinkti tokias, kad galutinės Wannier funkcijos būtų maksimaliai lokalizuotos ties jų centrais [**?**]. Kad galėtume rasti optimalias matricas $U^{(\boldsymbol{k})}$, kurias naudodami sukonstruotume maximaliai lokalizuotas Wannier funkcijas, reikia apibrėžti kriterijų arba parametrą, kurio pagalba galėtume nustatyti šių funkcijų išplitimą. Toks parametras gali būti funkcionalas

$$\Omega = \sum_m \left(\langle \boldsymbol{r}^2\rangle_m - \langle \boldsymbol{r}\rangle_m^2\right)\,, \tag{2.17}$$

kuriuo apibrėžiame visų Wanier funkcijų viename elementariame narvelyje deloka-

lizaciją. Čia pažymėjome

$$\langle \boldsymbol{r} \rangle_m = \langle \mathbf{0}, m | \boldsymbol{r} | \mathbf{0}, m \rangle$$
$$\langle \boldsymbol{r}^2 \rangle_m = \langle \mathbf{0}, m | \boldsymbol{r}^2 | \mathbf{0}, m \rangle$$

Kitaip šį funkcionalą galime perrašyti $\Omega = \sum_m \sigma_m^2$, kur σ_m - vidutinis m-tosios Wannier funcijos išplitimas. Norint rasti maksimaliai lokalizuotų Wannier funkcijų bazę, įvestas funkcionalas turi būti minimizuotas atitinkamai parenkant tinkamas unitarias matricas $U^{(\mathbf{k})}$.

Maksimaliai lokalizuotos Wannier funkcijos, kurių išplitimai σ_m yra minimalūs turi keletą labai svarbių savybių:

- Jeigu pradinė stacionari Schrödinger'io lygtis (2.1) yra simetriška laiko inversijos atžvilgiu, tai sistemoje magnetinio lauko nėra ir maksimaliai lokalizuotos Wannier funkcijos $\phi_n(\boldsymbol{r})$ yra realios nekreipiant dėmesio į globalų fazinį daugiklį.

- Maksimaliai lokalizuotos Wannier funkcijos tolstant nuo jų centrų padėčių mažėja eksponentiškai. Analogiškai mažėja ir hamiltoniano matriciniai elementai tarp toliau išdėstytų Wannier funkcijų.

2.3 Stipriojo ryšio modelis

Turėdami maksimaliai lokalizuotų Wannier būsenų $|\boldsymbol{R}, s\rangle$ rinkinį, jį galime panaudoti kaip bazę stipriojo ryšio artinyje. Kadangi joje galime atmesti hamiltiniano matricinius elementus tarp tolimesnių Wannier būsenų, jį atvaizduojanti matrica tampa reta. Konstruodami hamiltonianą, bendrą būsenos vektorių išreiškiame per Wannier būsenų superpoziciją

$$|\Psi\rangle = \sum_{\boldsymbol{R},m} c_{\boldsymbol{R},m} |\boldsymbol{R}, m\rangle \,, \tag{2.18}$$

kur $c_{\boldsymbol{R},m}$ yra skleidimo koeficientai. Naudodami tokią ieškomos tikrinės būsenos formą hamiltoniano tikrinių verčių lygtį užrašome tokiu būdu:

$$\sum_{\boldsymbol{R},m} c_{\boldsymbol{R},m} H |\boldsymbol{R}, s\rangle = \sum_{\boldsymbol{R},m} c_{\boldsymbol{R},m} E |\boldsymbol{R}, m\rangle \,. \tag{2.19}$$

Projektuodami šią lygtį į kiekvieną Wannier būseną ir pasinaudodami jų ortonormuotumu sukonstruojame tiesinių lygčių sistemą skleidimo koeficientams $c_{\boldsymbol{R},m}$ rasti:

$$\sum_{\boldsymbol{R}',m'} c_{\boldsymbol{R}',m'} \langle \boldsymbol{R}, m | H | \boldsymbol{R}', m' \rangle = E c_{\boldsymbol{R},m} \,. \tag{2.20}$$

Šiuo atveju sistemos hamiltonianą yra patogu užrašyti operatorine forma atskiriant diagonalius ir nediagonalius elementus:

$$H = \sum_{\boldsymbol{R},m} |\boldsymbol{R}, s\rangle \varepsilon_{\boldsymbol{R},m} \langle \boldsymbol{R}, s| + \sum_{(\boldsymbol{R},m)\neq(\boldsymbol{R}',m')} |\boldsymbol{R}, m\rangle J_{\boldsymbol{R},m,\boldsymbol{R}',m'} \langle \boldsymbol{R}', m'| \,, \tag{2.21}$$

kur raide $\varepsilon_{\boldsymbol{R},m} = \langle \boldsymbol{R}, m|H|\boldsymbol{R}, m\rangle$ pažymejome diagonalius hamiltoniano elementus, o raide $J_{\boldsymbol{R},m,\boldsymbol{R}',m'} = \langle \boldsymbol{R}, s|H|\boldsymbol{R}', s'\rangle$ - nediagonalius. Diagonalūs elementai yra Wannier būsenų vidutinės energijos, kurios dėl transliacinės simetrijos ir Wannier būsenų sąvybių nepriklauso nuo vektoriaus $\boldsymbol{R}$. Nediagonalūs hamiltoniano elementai yra proporcingi tikimybės amplitudei, kad atomas, esantis būsenoje $|\boldsymbol{R}', m'\rangle$, pereis į būseną $|\boldsymbol{R}, m\rangle$. Kadangi šie elementai nyksta nagrinėjant vis tolimesnes Wannier būsenas, patogu juos pernumeruoti atskirai nagrinėjant artimiausias būsenas, tolimesnes ir taip sluoksniais iki pačių tolimiausių. Matriciniai elementai tarp arčiausiai esančių Wannier būsenų paprastai žymimos $-t$ arba $-J$.

Kadangi optinių gardelių nagrinėjime stipriojo ryšio artinys paprastai naudojamas sprendžiant daugiadalelinius uždavinius, tai patogu sukonstruotą hamiltonianą perrašyti antriniame kvantavime. Tai atliekame Wannier būsenas pakeisdami atitinkamais antrinio kvantavimo operatoriais:

$$|\boldsymbol{R}, m\rangle\langle \boldsymbol{R}', m'| \to a^\dagger_{\boldsymbol{R},m} a_{\boldsymbol{R}',m'} \,. \tag{2.22}$$

Galiausiai, pasinaudojus visais žymejimų supaprastinimais sistemos hamiltonianą stipriojo ryšio artinyje užrašome tokiu būdu:

$$H = \sum_{\boldsymbol{R},m} \varepsilon_m a^\dagger_{\boldsymbol{R},m} a_{\boldsymbol{R},m} - J \sum_{\langle \boldsymbol{R},m,\boldsymbol{R}',m'\rangle} a^\dagger_{\boldsymbol{R},m} a_{\boldsymbol{R}',m'} + \ldots \tag{2.23}$$

kur skliaustai $\langle\cdot\rangle$ žymi sumavimą poromis tarp artimiausių gardelės mazgų.

2.4 Chern'o skaičius

Jeigu nagrinėjama n-toji energijos juosta nesiliečia su gretimomis

$$|E_n(\boldsymbol{k}) - E_{n\pm1}(\boldsymbol{k})| > 0 \,, \tag{2.24}$$

galime apbrėžti Chern'o skaičių [29, 30] – topologinį tvarkos parametrą, kuris priklauso nuo tikrinių būsenų vektorių $|u_{\boldsymbol{k},n}\rangle$. Chern'o skaičių galime išreikšti per

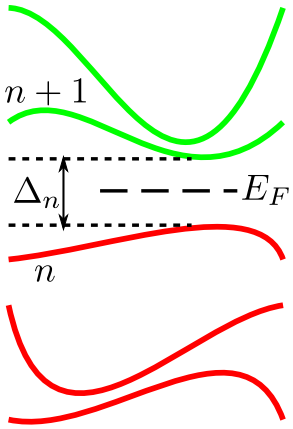

2.1 pav.: Energijos juostų pavyzdys. Raudona spalva pavaizduotos užpildytos juostos. Žalia - neužpildytos. E_F yra Fermi energijos vertė, o Δ_n – draustinis energijos tarpas.

TKNN (*Thouless-Kohmoto-Nightingale-Nijs*) formule [31, 32]:

$$c_n = \frac{1}{2\pi} \int_{\mathbb{T}^2} \mathrm{d}^2\boldsymbol{k}\, F_n(\boldsymbol{k})\,, \tag{2.25}$$

$$F_n(\boldsymbol{k}) = \mathrm{i}\left(\frac{\partial\langle u_{\boldsymbol{k},n}|}{\partial k_x} \frac{\partial|u_{\boldsymbol{k},n}\rangle}{\partial k_y} - \frac{\partial\langle u_{\boldsymbol{k},n}|}{\partial k_y} \frac{\partial|u_{\boldsymbol{k},n}\rangle}{\partial k_x} \right)\,, \tag{2.26}$$

kur $F_n(\boldsymbol{k})$ yra n-tosios juostos Berry kreivumas. Čia integruojame per pirmąją Brillouin'o zoną, kuri yra toroidas $\mathbb{T}^2$. Berry kreivumą $F_n(\boldsymbol{k})$ dar kitaip galime išreikšti per kalibruotinį potencialą $\boldsymbol{A}(\boldsymbol{k})$ Brillouin'o zonoje:

$$F_n(\boldsymbol{k}) = \boldsymbol{e}_z \cdot \nabla_{\boldsymbol{k}} \times \boldsymbol{A}_n(\boldsymbol{k})\,, \tag{2.27}$$

$$\boldsymbol{A}_n(\boldsymbol{k}) = \langle u_{\boldsymbol{k},n}|\mathrm{i}\nabla_{\boldsymbol{k}}|u_{\boldsymbol{k},n}\rangle\,, \tag{2.28}$$

kuris apibūdina tikrinių būsenų $|u_{\boldsymbol{k},n}\rangle$ lygiagrečius pernešimus (*parallel transport*) visoje pirmojoje Brillouin'o zonoje [**?**].

Topologinis Chern'o skaičius c_n pasižymi keleta svarbių savybių:

- c_n yra sveikasis skaičius: $c_n \in \mathbb{Z}$.
- Jeigu n-tasis dispesijos paviršius liečiasi su bent vienu gretimu (kai (2.24) nelygybė tampa lygybe), Chern'o skaičius c_n yra neapibrėžtas.
- c_n yra atsparus optinės gardelės perturbacijoms, kurios nepriverčia dispersijos n-tojo paviršiaus susiliesti su gretimais. Tai reiškia, kad Chern'o skaičius c_n gali pasikeisti, tik įvykus sistemos faziniui virsmui, kurio metu dispersijos paviršius susiliečia su bent vienu gretimu ir po to atsiskiria.

- Vykstant faziniam virsmui, kurios metu keičiasi Chern'o skaičius c_n, jame dalyvaujančių energijos juostų bendra Chern'o skaičių suma išlieka pastovi.

- c_n yra glaudžiai susijęs su sistemos Hall'o laidumu. Sakykime turime n užpildytų žemiausių energijos juostų (2.1 pav.), kurios yra atskirtos draustiniu enerijos tarpu nuo aukštesnių. Tuomet tokios sistemos Hall'o laidumas proporcingas užpildytų juostų Chern'o skaičių sumai:

$$\sigma_{\mathrm{H}} \sim \sum_{i=1}^{n} c_i \,. \tag{2.29}$$

  Tai reiškia, kad aukščiausios užpildytos (n-tosios) energijos juostos Chern'o skaičiaus vertė parodo, kiek ši juosta gali pasikeisti Hall'o laidumą σ_{H}. Jeigu draustinio energijų tarpo nėra, aukštesnės energijos juostos termodinaminėje pusiausvyroje yra dalinai užpildytos ir Hall'o laidumas (2.29) nėra tiksliai apibrėžtas.

Pasinaudoję Stokso (*Stokes*) teorema, Cherno skaičių c_n galime išreikšti kaip kalibruotinio potencialio $\boldsymbol{A}_n(\boldsymbol{k})$ kreivinį integralą aplink elementarųjį narvelį atvirkštinėje gardelėje:

$$c_n = \frac{1}{2\pi \mathrm{i}} \oint_{\mathbb{T}^2} \boldsymbol{A}(\boldsymbol{k}) \cdot \mathrm{d}\boldsymbol{k} \,. \tag{2.30}$$

Tai reiškia, kad jeigu kalibruotinis potencialas $\boldsymbol{A}(\boldsymbol{k})$ yra tolygus visoje pirmojoje Brillouin'o zonoje $\mathbb{T}^2$, tai Chern'o skaičius lygus nuliui. Taip yra todėl, kad integruojame per periodinės Brillouin'o zonos kraštus ir skirtingų kraštų integralai vienas kitą panaikina. Tokią pačią išvadą pateikia ir kompleksinių funkcijų analizė: jeigu integruojame kompleksinę funkciją uždaru kontūru, kurio viduje nėra polių, tai integralas yra lygus nuliui. Priešingai, jeigu kalibruotinis potencialinis laukas $\boldsymbol{A}(\boldsymbol{k})$ nėra tolygiai apibrėžtas visoje pirmojoje Brilllouin'o zonoje, kontūrinis integralas nera lygus nuliui ir Chern'o skaičius įgyja nenulinę reikšmę.

Iš (2.29) priklausomybės matome, kad pagal Chern'o skaičius c_i ir draustinį energijų tarpą $\Delta_{n,n+1}$ optinės gardelės fazes galime suskirstyti į trys grupes:

- Topologiškai trivialaus izoliatoriaus fazė – Chern'o skaičių suma iki n-tosios energijos juostos lygi nuliui. Aukštesnės energijos juostos yra atskirtos nuo n-tosios draustiniu energijos tarpu: $\Delta_{n,n+1} > 0$.

- Chern'o izoliatorius (arba topologinis izoliatorius) – Chern'o skaičų suma *nėra* lygi nuliui. Aukštesnės energijos juostos yra atskirtos draustiniu energijos tarpu: $\Delta_{n,n+1} > 0$.

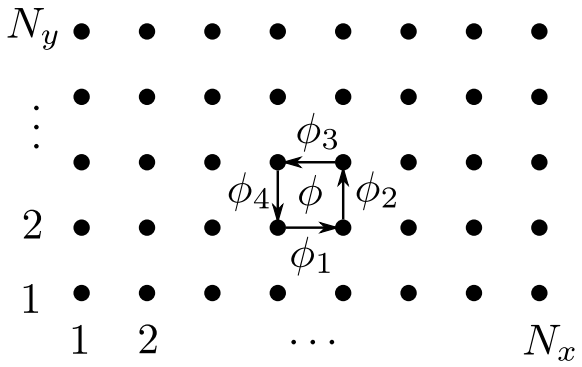

2.2 pav.: Diskretinis $\boldsymbol{k}$ tinklelis kvadratinėje Brillouin'o zonoje. Skaičiuodami lauko stiprumo $\tilde{F}_n(\boldsymbol{k})$ reikšmę apeiname keturis gretimus tinklelio taškus išeinant iš taško $\boldsymbol{k}$ ir sudedame ryšio kinatmųjų fazes: $\phi = \phi_1 + \phi_2 + \phi_3 + \phi_4$.

- Topologiškai trivialus metalas arba pusmetalis – Chern'o skaičių suma lygi nuliui. n-toji energijos juosta liečia aukštesnę arba persikloja su ja. Reikia paminėti, kad šiuo atveju juostos turėtų liestis skirtinguose $\boldsymbol{k}$ taškuose, kitaip Chern'o skaičius būtų neapibrėžtas.

- Chern'o metalas arba pusmetalis – Chern'o skaičių suma nėra lygi nuliui. Aukščiausia užpildyta (n-toji) energijos juosta liečia aukštesnę arba persikloja su ja.

Įdomiausia nagrinėti tokias optinių gardelių parametrų verčių sritis, kuriose galima Chern'o izoliatoriaus fazė. Tokiu atveju gali būti stebimas kvantinis Hall'o efektas. Sakykime šiuo atveju pildome energijos juostas nuo žemiausios. Kai Fermi energijos lygmuo yra draustiniame tarpe, Hall'o laidumas σ_{H} laidumas nesikeičia. Kai Fermi lygmuo kerta energijos juostą, Hall'o laidumas pasikeičia nuo vienos kvantuotos reikšmės iki kitos. Chern'o metalo ir pusmetalio fazės taip pat įdomios nagrinėti, tik tokiu atveju dėl draustinio energijos tarpo nebuvimo Hall'o laidumas σ_{H} nėra tiksliai kvantuotas.

2.5 Skaitmeninis Chern'o skaičiaus apskaičiavimas

Šiame skyrelyje pateiksime Chern'o skaičiaus apskaičiavimo algoritmą [**?**], kai sistemos juostinė sandara yra apibrėžta diskretinėje Brillouin'o zonoje, t. y. tokioje, kuri yra sudaryta iš baigtinio skaičiaus Bloch'o vektoriaus $\boldsymbol{k}$ verčių. Paprastai tokią diskretinę juostinę sandarą suskaičiuojame skaitmeniniais metodais, kai neturime galimybių rasti tikrinių būsenų kiekviename Brillouin'o zonos taške $\boldsymbol{k}$.

Tarkime, vektoriaus $\boldsymbol{k}$ reikšmės Brillouin'o zonoje sudaro stačiakampį diskretinį

tinklelį (2.2 pav.):

$$k_x = \frac{2\pi}{a_x N_x} i\,, \qquad k_y = \frac{2\pi}{a_y N_y} j\,, \qquad i = 1, \ldots, N_x\,, \qquad j = 1, \ldots, N_y\,, \tag{2.31}$$

kur a_x ir a_y yra stačiakampio elementaraus narvelio dydis x ir y kryptimis, o N_x ir N_y yra vektoriaus tinklelio taškų skaičiai atitinkamomis kryptimis. Paprastai N_x ir N_y pasirenkame tokius, kad elementarus stačiakampis narvelis vektoriaus $\boldsymbol{k}$ tinklelyje būtų kuo artimesnis kvadratui: $2\pi/a_x N_x \approx 2\pi/a_y N_y$. Toliau apibrėžiame normuotus ryšio kintamuosius tarp būsenų $|u_{\boldsymbol{k},n}\rangle$ $\boldsymbol{k}$-tinklelyje:

$$\boldsymbol{U}^{(n)}(\boldsymbol{k}) = \boldsymbol{e}_{\Delta\boldsymbol{k}} \frac{\langle u_{\boldsymbol{k},n} | u_{\boldsymbol{k}+\Delta\boldsymbol{k},n}\rangle}{|\langle u_{\boldsymbol{k},n} | u_{\boldsymbol{k}+\Delta\boldsymbol{k},n}\rangle|}\,, \tag{2.32}$$

kur vektorius $\Delta\boldsymbol{k}$ nukreiptas į gretimą $\boldsymbol{k}$ tinklelio tašką priklausomai nuo $\boldsymbol{U}^{(n)}(\boldsymbol{k})$ komponentės: jeigu turime komponentę $U_x^{(n)}(\boldsymbol{k})$, tai $\Delta\boldsymbol{k} = \frac{2\pi}{aM}\boldsymbol{e}_x$ ir analogiškai jeigu turime komponentę $U_y^{(n)}(\boldsymbol{k})$, tai $\Delta\boldsymbol{k} = \frac{2\pi}{bN}\boldsymbol{e}_y$. Ryšio kinamieji yra gerai apibrėžti jeigu $\langle u_{\boldsymbol{k},n} | u_{\boldsymbol{k}+\Delta\boldsymbol{k},n}\rangle = 0$.

Toliau apibrėžiame lauko stiprumą diskretinio tinklelio mazguose:

$$\tilde{F}_n(\boldsymbol{k}) = -\mathrm{i}\ln\left[U_x(\boldsymbol{k}) U_y\left(\boldsymbol{k} + \frac{2\pi}{aM}\boldsymbol{e}_x\right) U_x^{-1}\left(\boldsymbol{k} + \frac{2\pi}{bN}\boldsymbol{e}_y\right) U_y^{-1}(\boldsymbol{k})\right]\,. \tag{2.33}$$

Kadangi visi ryšio kintamieji yra normuoti, tai logaritminė funkcija gražina jų sandaugos fazę arba jų fazių sumą. Be to, logaritminės funkcijos reikšmę imame pagrindiniame intervale tarp $-\mathrm{i}\pi$ ir $\mathrm{i}\pi$. Šis lauko stiprumo apibrėžimas yra diskretinis Berry kreivumo (2.26) analogas. Chern'o skaičių suskaičiuojame susumavę lauko stiprumo (2.33) vertes visame diskretiniame tinklelyje:

$$\tilde{c}_n = \frac{1}{2\pi}\sum_{\boldsymbol{k}} \tilde{F}_n(\boldsymbol{k})\,. \tag{2.34}$$

Matome, kad lauko stiprumas (2.33) ir Chern'o skaičius (2.34) nepriklauso nuo kalibruotės pasirinkimo. Tuo galime įsitikinti kiekvieną vektorių $|u_{\boldsymbol{k},n}\rangle$ formulėje (2.33) padaugine iš bet kokio fazinio daugiklio ir parodę, kad tai neturi įtakos lauko stiprumui. Be to, įvedę kalibruotinį lauką $\tilde{\boldsymbol{A}}(\boldsymbol{k}) = \ln \boldsymbol{U}(\boldsymbol{k})$ galime parodyti, kad diskretiniame Brillouin'o zonos tinklelyje apibrėžtas Chern'o skaičius (2.34) yra sveikas skaičius nepriklausomai nuo tinklelio dydžio [**?**].

Praktiniame skaičiavime kiekvieno ryšio kintamojo normuoti nebūtina. Kadangi diskretinis lauko stiprumas priklauso tik nuo ryšio kintamųjų sandaugos fazės, tai užtenka sudauginti reikalingas keturias vektorių $|u_{\boldsymbol{k},n}\rangle$ skaliarines sandaugas ir suskaičiuoti gauto kompleksinio skaičiaus fazę pagrindiniame intervale. Labiau pa-

nagrinėję formulę (2.33) matome, kad daugindami ryšio kintamuosius apeiname ratu per keturis gretimus diskretinio tinklelio taškus. Tai atitinka vektorinės sandaugos $\nabla \times \boldsymbol{A}(\boldsymbol{k})$ komponentės z kryptimi skaičiavimą diskretiniame tiklelyje. Todėl riboje $M, N \to \infty$ turime $\tilde{c}_n \to c_n$. Kadangi Chern'o skaičius $\tilde{c}_n$ tolygiai kisti negali (jis yra sveikasis skaičius), tai smulkėjant tinkleliui (didėjant M ir N), jis šuoliškai kinta tol kol pasiekamas reikalingas tikslumas. Jį pasiekę galime teigti, kad Chern'o skaičius suskaičiuotas teisingai.

3 Dice optinė gardelė

3.1 Gardelės geometrija

Dice optinė gardelė yra hexagoninės struktūros dvimatė gardelė, sudaryta iš trijų trikampių subgardelių, kurių mazgus žymime raidėmis A, B ir C (žr. pav. 3.1). Subgardelė B yra sukabinta su kitomis subgardelėmis taip, kad kiekvienam B subgardelės mazgui artimiausi mazgai yra iš subgardelių A ir C. Vektoriai, kurie sujungia artimiausius dice gardelės mazgus yra

$$\boldsymbol{\delta}_1 = \frac{a}{2}(\boldsymbol{e}_x + \sqrt{3}\boldsymbol{e}_y), \quad \boldsymbol{\delta}_2 = \frac{a}{2}(\boldsymbol{e}_x - \sqrt{3}\boldsymbol{e}_y), \quad \boldsymbol{\delta}_3 = -a\boldsymbol{e}_x\,. \tag{3.1}$$

Čia a yra atstumas tarp artimiausių gardelės mazgų. Elementarūs gardelės vektoriai yra

$$\boldsymbol{a}_1 = a(3\boldsymbol{e}_x + \sqrt{3}\boldsymbol{e}_y)/2, \quad \boldsymbol{a}_2 = a(3\boldsymbol{e}_x - \sqrt{3}\boldsymbol{e}_y)/2. \tag{3.2}$$

Jie sudaro rombo formos elementarų gardelės narvelį. Iš šių vektorių sudarome bendrą gardelės vektorių $\boldsymbol{r}_{\boldsymbol{n}} = n_1\boldsymbol{a}_1 + n_2\boldsymbol{a}_2$, kur n_1 ir n_2 yra sveikieji skaičiai. Vektorių $\boldsymbol{r}_{\boldsymbol{n}}$ rinkinys sudaro B subgardelę. Visų trijų subgardelių (tai yra visos dice gardelės) mazgų padėtis aprašome vektoriais

$$\boldsymbol{r}_{\boldsymbol{n},s} = \boldsymbol{r}_{\boldsymbol{n}} + s\boldsymbol{\delta}_1. \tag{3.3}$$

Čia $s = 0, \pm 1$ nurodo kiekvieną subgardelę: pasirinkimas $s = 0$ duoda subgardelę B, o $s = \pm 1$ duoda atitinkamai subgardeles A ir B.

Patogu įvesti papildomą gardelės vektorių $\boldsymbol{a}_3 = \boldsymbol{a}_1 - \boldsymbol{a}_2$. Šis vektorius, jam priešingas vektorius $-\boldsymbol{a}_3$ kartu su vektoriais $\pm\boldsymbol{a}_1$ ir $\pm\boldsymbol{a}_2$ sujungia visas tolimesnių gardelės mazgų poras.

Elementarūs atvirkštinės gardelės vektoriai yra

$$\boldsymbol{b}_1 = \frac{2\pi}{3a}(\boldsymbol{e}_x + \sqrt{3}\boldsymbol{e}_y), \quad \boldsymbol{b}_2 = \frac{2\pi}{3a}(\boldsymbol{e}_x - \sqrt{3}\boldsymbol{e}_y). \tag{3.4}$$

Pirmoji Brillouin'o zona yra taisyklingas šešiakampis dviejomis neekvivalenčiomis viršūnėmis $\boldsymbol{K} = (2\boldsymbol{b}_1 + \boldsymbol{b}_2)/3$ ir $\boldsymbol{K}' = (\boldsymbol{b}_1 + 2\boldsymbol{b}_2)/3$ (žr. pav. 3.1).

3.2 Stipriojo ryšio modelis

Dice gardelės nagrinėjimui naudojame stipriojo ryšio modelį, kuriame Hilberto erdvės bazę sudaro viendalelinės būsenos $|\boldsymbol{r}_{\boldsymbol{n},s}\rangle$, kurios aprašo vieno atomo Wannier būsenas, lokalizuotas ties kiekvienu gardelės mazgu $\boldsymbol{r}_{\boldsymbol{r},s}$. Antrinio kvantavimo formalizme šios būsenos yra sukuriamos operatoriais $c^\dagger(\boldsymbol{r}_{\boldsymbol{r},s})$ ir sunaikinamos atitinka-

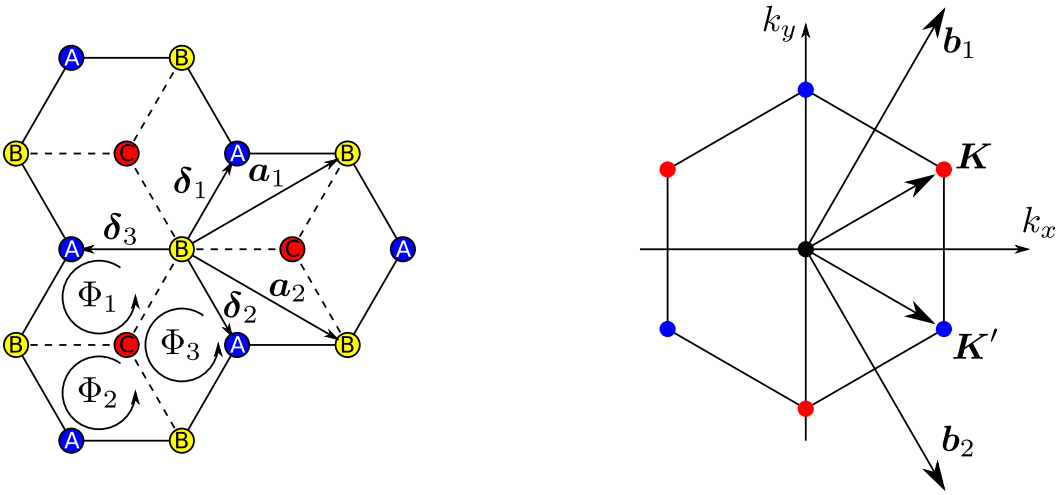

3.1 pav.: *Kairysis pav.*: dice gardelė. Mėlyni, žali ir raudoni mazgai atitinka tris skirtingas trikampes subgardeles A, B ir C. *Dešinysis pav.*: pirmoji Brillouin'o zona.

mais operatoriais $c(\boldsymbol{r}_{\boldsymbol{r},n})$.

Pilnas sistemos Hamiltonianas yra sudarytas iš trijų dalių

$$H = H_1 + H_2 + H_3. \tag{3.5}$$

Pirmasis narys aprašo lazeriais indukuotus šuolius tarp artimiausių gardelės mazgų:

$$H_1 = \sum_{\boldsymbol{n}} \sum_{s=\pm 1} J^{(s)} \sum_{i=1}^{3} \mathrm{e}^{\mathrm{i}\boldsymbol{p}_s\cdot(\boldsymbol{r}_{\boldsymbol{n}}+s\boldsymbol{\delta}_i/2)} c^\dagger(\boldsymbol{r}_{\boldsymbol{n}}) c(\boldsymbol{r}_{\boldsymbol{n}} + s\boldsymbol{\delta}_i) + \mathrm{H.\,c.} \tag{3.6}$$

Čia $J^{(s)}$ yra šuolių amplitudžių moduliai. Šie indukuoti šuoliai papildomai prideda ir fazę, kuri tiesiškai priklauso nuo atatrankos parametro $\boldsymbol{p}_s$.

Antrasis narys H_2 įtraukia naturalius atomo šuolius tarp tolimesnių gardelės narių (Šuolius, kurie nėra indukuoti lazeriais ir vyksta kiekvienoje trikampėje subgardelėje atskirai):

$$H_2 = \sum_{\boldsymbol{n}} \sum_{s=0,\pm 1} J_2^{(s)} \sum_{i=1}^{3} c^\dagger(\boldsymbol{r}_{\boldsymbol{n},s}) c(\boldsymbol{r}_{\boldsymbol{n},s} + \boldsymbol{a}_i) + \mathrm{H.\,c.} \tag{3.7}$$

Čia $J_2^{(s)}$ yra šuolių amplitudės, kurios atitinkamai pasirinkus kalibruotę, yra realios.

Trečiasis narys H_3 aprašo vidutinę atomo energiją kiekviename gardelės mazge:

$$H_3 = \sum_{\boldsymbol{n}} \sum_{s=0,\pm 1} \varepsilon_s c^\dagger(\boldsymbol{r}_{\boldsymbol{n},s}) c(\boldsymbol{r}_{\boldsymbol{n},s}). \tag{3.8}$$

Tai yra diagonalūs Hamiltoniano nariai.

Kadangi pirmasis narys H_1 turi kompleksinius matricinius elementus, kurių fazė tiesiškai priklauso nuo gardelės mazgų padėčių, tai Hamiltonianas nėra transliaciškai invariantinis. Mes galime atlikti kalibruotės transformaciją $c(\boldsymbol{r}_{\boldsymbol{n},s}) \to c(\boldsymbol{r}_{\boldsymbol{n},s}) \exp(-\mathrm{i}\boldsymbol{p}_s \cdot \boldsymbol{r}_{\boldsymbol{n}})$, kuri įveda šią simetriją.

Papildomai įvedę pakeitimą $c(\boldsymbol{r}_{\boldsymbol{r},n}) \to c(\boldsymbol{r}_{\boldsymbol{r},n})\mathrm{e}^{\mathrm{i}\boldsymbol{p}_s \cdot s\boldsymbol{\delta}_1/2}$ ir atlikę atsiradimo ir išnykimo operatorių Fourier transformaciją, sistemą galime impulisiname atvaizdavime aprašyti trijų lygmenų modeliu. Tokiu atveju Hamiltonianas yra aprašomas matrica

$$\mathcal{H}(\boldsymbol{k}) = \begin{bmatrix} \varepsilon_+ + 2J_2^{(+)} f(\boldsymbol{k}-\boldsymbol{p}_+) & J^{(+)} g(\boldsymbol{k}-\boldsymbol{p}_+/2) & 0 \\ J^{(+)} g^*(\boldsymbol{k}-\boldsymbol{p}_+/2) & 2J_2^{(0)} f(\boldsymbol{k}) & J^{(-)} g(\boldsymbol{k}-\boldsymbol{p}_-/2) \\ 0 & J^{(-)} g^*(\boldsymbol{k}-\boldsymbol{p}_-/2) & \varepsilon_- + 2J_2^{(-)} f(\boldsymbol{k}-\boldsymbol{p}_-) \end{bmatrix}. \tag{3.9}$$

Čia, funkcijos f ir g yra

$$f(\boldsymbol{k}) = \sum_{i=1}^{3} \cos(\boldsymbol{k} \cdot \boldsymbol{a}_i), \quad g(\boldsymbol{k}) = \mathrm{e}^{\mathrm{i}\boldsymbol{k}\cdot\boldsymbol{\delta}_1} \sum_{i=1}^{3} \mathrm{e}^{-\mathrm{i}\boldsymbol{k}\cdot\boldsymbol{\delta}_i}. \tag{3.10}$$

$\boldsymbol{k}$ yra Blocho banginis vektorius.

Toks modelis impulisiname atvaizdavime pasižymi transliacine simetrija atvirkštinėje gardelėje, $\mathcal{H}(\boldsymbol{k}) = \mathcal{H}(\boldsymbol{k} + \mathbf{G})$, ir yra patogus juostinės sandaros topologinių savybių tyrinėjimui.

3.3 Nesąveikaujančių fermionų topologinės fazės

Prieš atlikdami juostinės sandaros analizę mes pirmiausia sumažiname nepriklausomų gardelės parametrų skaičių pasirinkdami $\varepsilon_{+1} = -\varepsilon_{-1} = \varepsilon$, $J^{(+1)} = J^{(-1)} = J$, $J_2^{(+1)} = J_2^{(0)} = J_2^{(-1)}$ ir $\boldsymbol{p}_{+1} = -\boldsymbol{p}_{-1} = \boldsymbol{p}$. Tokiu atveju Hamiltoniano matrica supaprastėja į

$$\mathcal{H}(\boldsymbol{k}) = \begin{bmatrix} \varepsilon + 2J_2 f(\boldsymbol{k}-\boldsymbol{p}) & Jg(\boldsymbol{k}-\boldsymbol{p}/2) & 0 \\ Jg^*(\boldsymbol{k}-\boldsymbol{p}/2) & 2J_2 f(\boldsymbol{k}) & Jg(\boldsymbol{k}+\boldsymbol{p}/2) \\ 0 & Jg^*(\boldsymbol{k}+\boldsymbol{p}/2) & -\varepsilon + 2J_2 f(\boldsymbol{k}+\boldsymbol{p}) \end{bmatrix}. \tag{3.11}$$

Tokios formos Hamiltonianas pasižymi keliomis simetrijomis ($\varepsilon \to -\varepsilon, \mathcal{H} \to \mathcal{H}$), ($J \to -J, \mathcal{H} \to \mathcal{H}$) ir ($J_2 \to -J_2, \mathcal{H} \to -\mathcal{H}$).

Juostinę sandarą ir topologinį kiekvienos juostos Chern'o skaičių skaičiuojame skaitmeniškai. Rezultatams atvaizduoti naudojame panašią schemą kaip ir [**?**]. Energijos vienetu pasirenkame šuolių tarp artimiausių gardelės mazgų amplitudę, $J \equiv 1$. Atatrankos impulso $\boldsymbol{p}$ komponentę p_x išreiškiame per K_x, komponentę p_y išreiškiame per K_y, kur $\boldsymbol{K}$ yra vienas iš Brillouin'o zonos kampų. Visose fazinėse

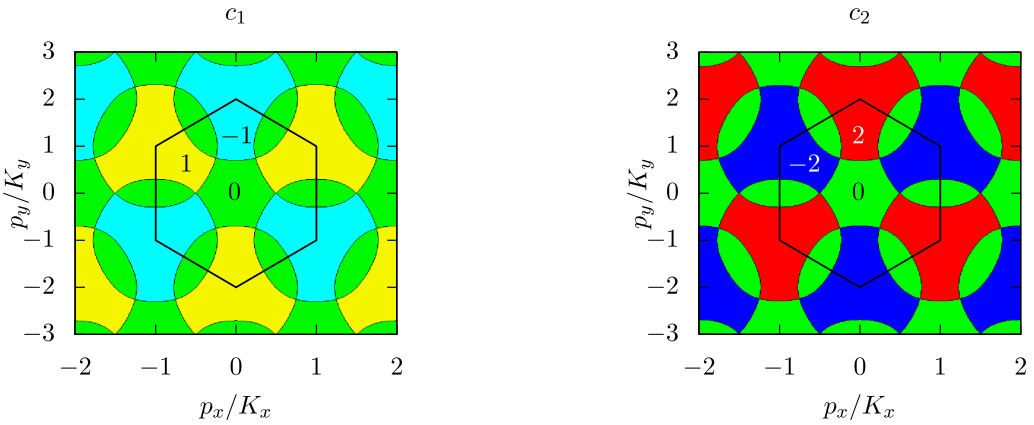

3.2 pav.: Chern'o skaičių priklausomybė nuo atatrankos impulso $\boldsymbol{p}$ kai $\varepsilon = J$ ir $J_2 = 0$. *Kairysis pav.*: žemiausios juostos Chern'o skaičius c_1. *Dešinysis pav.*: Vidurinės juostos Chern'o skaičius. Žalia spalva atitinka nulinį Chern'o skaičių. Geltona, raudona, žydra ir mėlyna – Chern'o skaičius 1, 2, -1 ir -2 atitinkamai.

diagramose Chern'o skaičių išreiškiame kaip funkciją $c_n = c_n(p_x, p_y)$. Skirtingas c_n reikšmes išreiškiame skirtingomis spalvomis: 0 – žalia, 1 – geltona, 2 – raudona, -1 – šviesiai mėlyna ir -2 – tamsiai mėlyna.

Pirmiausia nagrinėkime atvejį, kai nėra šuolių tarp tolimesnių gardelės mazgų ($J_2 = 0$). Pav. 3.2 pateikiame Chern'o skaičių fazines diagramas kai $\varepsilon = J$. Fazinėse diagramose yra sritys kur Chern'o skaičiai yra $\{c_1, c_2, c_3\} = \{0, 0, 0\}$, $\{-1, 2, -1\}$ ir $\{1, -2, 1\}$. Srityse kur Chern'o skaičiai yra nelygus nuliams, tarp energijos juostų nėra tarpų, $\Delta_{12} = \Delta_{23} = 0$. Juostinės sandaros analizė parodo, kad energijos juostos šiose srityse nepersikloja ir nesiliečia (t. y. liečiasi skirtinguose $\boldsymbol{k}$ taškuose).

Toliau patyrinėkime kas pasikeičia kai įtraukiame šuolius tarp tolimesnių gardelės mazgų. Kai $\varepsilon = J_2 = 0.5J$ gauname izoliatoriaus fazes su Chern'o skaičiais $\{\pm 1, \pm 1, \mp 2\}$ ir metalo fazes su Chern'o skaičiais $\{\pm 2, 0, \mp 2\}$ (pav. 3.3). Šios fazės pasižymi Chern'o skaičiais, kurie yra moduliu didesni už vienetą.

Apibendrinimas

Ištyrinėjome labai šaltus atomus esančius dvimatėje dice optinėje gardelėje naudodami stipriojo ryšio artinį. Gardelėje dirbtinis magnetinis laukas yra sukuriamas naudojant laserius, kurie indukuoja šuolius tarp skirtingų gardelės mazgų. Dice optinė gardelė yra trijų lygmenų išplėtimas Haldane modelio, kuris yra aprašomas naudojant dviejų lygmenų modelį.

Parodėme, kad toks Haldane modelio išplėtimas leidžia nesudėtingai gauti topologinę pusmetalio fazę. Tuo pačiu šis modelis turi ir kitų topologinių fazių, kurios

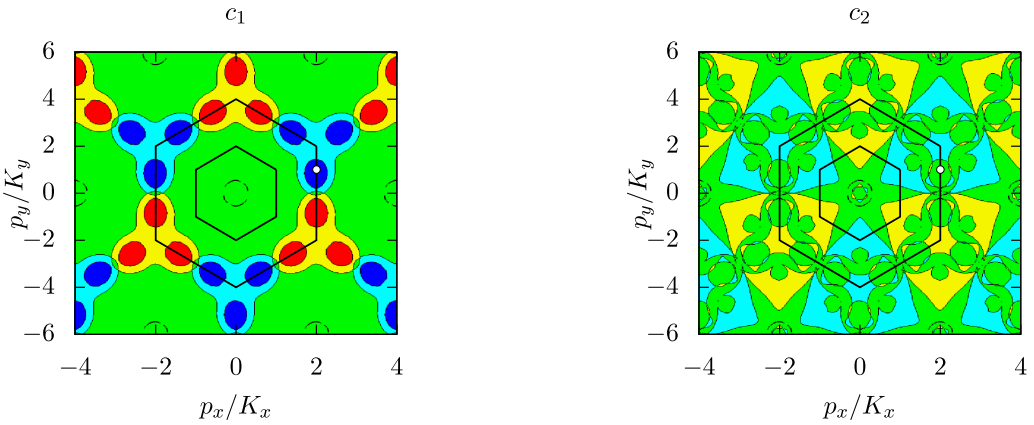

3.3 pav.: Chern'o skaičių priklausomybė nuo atatrankos impulso $\boldsymbol{p}$ kai $\varepsilon = 0.5J$ ir $J_2 = 0.5J$. *Kairysis pav.*: žemiausios juostos Chern'o skaičius c_1. Dešinysis pav.: vidurinės juostos Chern'o skaičius c_2. Baltas taškas yra $\boldsymbol{p} = (2K_x, K_y)$, kuriame Černo skaičiai yra $c_1 = -2$, $c_2 = 0$ ir c_3. Čia naudojame tą patį spalvų kodą kaip ir pav. 3.2.

pasižymi Chern'o skaičiais moduliu didesniais už vienetą.

4 Dažnio šukų gardelė

4.1 Gardelės modelis

Nagrinėkime dviejų lygmenų (sukinio 1/2) atomą, veikamą magnetinio lauko gradientu x kryptimi. Dėl Zeeman'o efekto atomo vidinių būsenų $|\uparrow\rangle$ ir $|\downarrow\rangle$ energija priklauso nuo atomo pozicijos erdvėje. Magnetinio lauko priklausomybę nuo x koordinatės laikome tiesine. Tokiu atveju atomo vidinė sandara aprašoma nariu $\sim x\sigma_3$, kur $\sigma_3 = |\uparrow\rangle\langle\uparrow| - |\downarrow\rangle\langle\downarrow|$ yra Pauli matrica (žr. pav. 4.1). Toks atomas, veikiamas minėtų magnetiniu lauku, aprašomas hamiltonianu

$$H_0 = \frac{\boldsymbol{p}^2}{2M} + \frac{\Delta(x)}{2}\sigma_3. \tag{4.1}$$

Čia pirmas narys yra atomo kinetinė energija, kur $\boldsymbol{p}$ yra atomo judesio kiekis ir M yra atomo masė. Antras narys aprašo Zeeman'o poslinkį, kuris apibūdinamas tiesine fukcija $\Delta(x) = \Delta_0 + \Delta' x$.

Įvedame Raman'o sukabinimą tarp abiejų atomo lygmenų:

$$V(y,t) = V_0 \sum_n \left[\mathrm{e}^{\mathrm{i}k_0 y}\mathrm{e}^{-\mathrm{i}2n\omega t} + \mathrm{e}^{-\mathrm{i}k_0 y}\mathrm{e}^{-\mathrm{i}(2n+1)\omega t}\right] |\downarrow\rangle\langle\uparrow| + \mathrm{H.\,c.} \tag{4.2}$$

Skliaustuose pirmasis narys aprašo atomo lygmenų sukabinimą lyginiais dažnio kartotiniais $2n\omega$. Antras narys aprašo lygmenų sukabinimą nelyginiais dažnio kartotiniais $(2n+1)\omega$.

Nagrinėjimą galime supaprastinti atlike kalibruotės transformaciją $|\uparrow\rangle \to \exp(-\mathrm{i}k_0 y/2)|\uparrow\rangle$, $|\downarrow\rangle \to \exp(\mathrm{i}k_0 y/2)|\downarrow\rangle$, kuri pakeičia hamiltonianą (4.1) į

$$H_0 \to \tilde{H}_0 = \frac{1}{2M}\left(\boldsymbol{p} + \hbar k_0 \sigma_3 \boldsymbol{e}_y/2\right)^2 + \frac{\Delta(x)}{2}\sigma_3. \tag{4.3}$$

ir Raman'o sukabinimą į

$$V(y,t) \to \tilde{V}(y,t) = V_0 \sum_n \left[\mathrm{e}^{\mathrm{i}2k_0 y}\mathrm{e}^{-\mathrm{i}2n\omega t} + \mathrm{e}^{-\mathrm{i}(2n+1)\omega t}\right] |\downarrow\rangle\langle\uparrow| + \mathrm{H.\,c.} \tag{4.4}$$

Pilnas sistemos Hamiltonianas yra

$$\tilde{H}(t) = \tilde{H}_0 + \tilde{V}(y,t) \tag{4.5}$$

Raman'o sukabinimas (4.4) gali būti atvazduotas per Dirac'o šukų funkcijas:

$$\tilde{V}(t,y) = V_+(y)\tau \sum_{\text{even } l} \delta(t - \tau l) + V_-(y)\tau \sum_{\text{odd } l} \delta(t - \tau l). \tag{4.6}$$

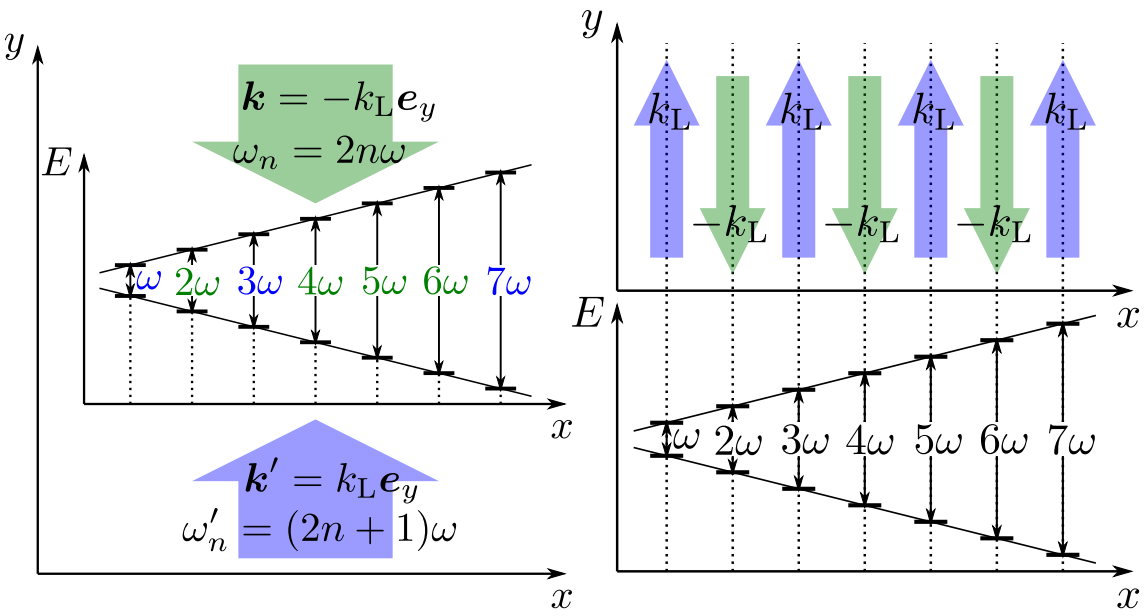

4.1 pav.: Atomo vidinių lygmenų $|\uparrow\rangle$ ir $|\downarrow\rangle$ sukabinimo schema.

Čia

$$V_{\pm}(y) = V_0\left(\mathrm{e}^{\mathrm{i}2k_0 y} \pm 1\right)|\downarrow\rangle\langle\uparrow| + \mathrm{H.\,c.} \tag{4.7}$$

Tokiu būdų galime atskirti sistemos laikine ir erdvinę priklausomybes.

4.2 Magnetinis srautas

Nagrinėkime mūsų modelinės kvantinės sistemos laikinę evoliuciją per viena laiko periodą, nuo $t = 0 - \epsilon$ iki $t = T - \epsilon$, kur $\epsilon \to 0$. Per šį periodą atomas patiria du spinduliuotės smūgius, kurie įvyksta laiko momentais $t_+ = 0$ ir $t_- = \tau$. Tarp šių smūgių atomas juda pagal hamiltonianą (4.3).

Floquet dažnį ω laikome dideliu lyginant su atatrankos dažniu $\omega_{\mathrm{rec}} = E_{\mathrm{rec}}/\hbar = \hbar k_0^2/2M$. Tokiu atveju atomo judesio kiekis $\boldsymbol{p}$ pakinta nežymiai tarp smūgių. Naudodami stroboskopinę aproksimaciją laikinė sistemos evoliucija aprašoma unitariu operatoriumi

$$U_{\mathrm{eff}} = \exp\left\{-\frac{\mathrm{i}}{\hbar}\left[\frac{1}{2M}\left(\boldsymbol{p} + \hbar k_0 \sigma_3 \boldsymbol{e}_y/2\right)^2 + V_{\mathrm{eff}}\right]T\right\}, \tag{4.8}$$

kur V_{eff} yra efektyvus atomo lygmenų sukabinimas:

$$V_{\mathrm{eff}} = \frac{\hbar}{2}\boldsymbol{\sigma}\cdot\boldsymbol{\Omega}, \tag{4.9}$$

Čia $\boldsymbol{\sigma} \equiv (\sigma_1, \sigma_2, \sigma_3)$ yra trimatis vektorius, kurio elementai yra Pauli matricos $\sigma_1 = |\downarrow\rangle\langle\uparrow| + \mathrm{H.c.}$, $\sigma_2 = \mathrm{i}|\downarrow\rangle\langle\uparrow| + \mathrm{H.c.}$ ir $\sigma_3 = |\uparrow\rangle\langle\uparrow| - |\downarrow\rangle\langle\downarrow|$. Sukabinimas apibūdinamas

trijomis realiomis koordinačių funkcijomis $\mathbf{\Omega} \equiv (\Omega_1, \Omega_2, \Omega_3) \equiv \mathbf{\Omega}(\boldsymbol{r})$.

Efektyvų sukabinimą (4.9) galime aprašyti išskaidę funkcijų vektorių $\mathbf{\Omega}$ į sferines komponentes $\Omega(\boldsymbol{r})$, $\theta(\boldsymbol{r})$ ir $\phi(\boldsymbol{r})$:

$$\cos\theta = \frac{\Omega_3}{\Omega} = \frac{q_3}{\|\boldsymbol{q}\|}, \tag{4.10}$$

$$\tan\phi = \frac{\Omega_2}{\Omega_1} = \frac{q_2}{q_1}. \tag{4.11}$$

Tikrinės efektyvaus sukabinimo vertės erdvės taške $\boldsymbol{r}$ yra

$$V_\pm(\boldsymbol{r}) = \pm\frac{\hbar}{2}\Omega(\boldsymbol{r}). \tag{4.12}$$

Nagrinėkime adiabatinę sistemos evoliuciją viename iš dviejų gautų energijos juostų (4.12). Suprojektave Schrodinger'io lygtį į vieną iš šių lygmenų gauname geometrinį vektorinį potencialą

$$\boldsymbol{A}_\pm(\boldsymbol{r}) = \pm\frac{\hbar}{2}\left(\cos\theta - 1\right)\nabla\phi, \tag{4.13}$$

kuris aprašo dirbtinį magnetinį lauką $\boldsymbol{B}_\pm(\boldsymbol{r}) = \nabla \times \boldsymbol{A}_\pm(\boldsymbol{r})$. Esant pakankamai silpnam Raman'o sukabinimui geometrinis vektorinis potencialas $\boldsymbol{A}_\pm(\boldsymbol{r})$ turi du singuliarumo taškus, kurie duodą netrivialų magnetinį srautą per elementarų gardelės narvelį:

$$\alpha_\pm = -\frac{1}{\hbar}\sum \oint_{\text{singul}} \mathrm{d}\boldsymbol{r} \cdot \boldsymbol{A}_\pm(\boldsymbol{r}). \tag{4.14}$$

Singuliarumai atsiranda dviejuose erdvėse taškuose ir jie vienas kito nekompensuoja. Taip gauname nekintamo ženklo magnetinį srautą.

Geometrinio srauto tankis $\boldsymbol{B}(\boldsymbol{r}) \equiv \boldsymbol{B}_+(\boldsymbol{r})$ adiabatiniame režime ($\hbar\omega = 10E_{\text{recoil}}$, $V_0 = 0.25\hbar\omega$, $\beta = 0.6k_0$) yra pavaizduotas pav. 4.2. Pilnas magnetinis srautas per elementarų narvelį yra lygus 2π ir nepriklauso nuo Floquet dažnio ω bei gradiento β. Srautą 2π turime tada, kai sukabinimo stiprumas yra $0 < V_0 < 0.5\hbar\omega$.

4.3 Juostinė sandara

Optinės srauto gardelės juostinė sandara pasižymi Landau tipo lygmenų savybėmis esant adiabatiniam režimui, kai $\hbar\omega = 10E_{\text{recoil}}$, $\beta = 0.6k_0$ ir $V_0 = 0.25\hbar\omega$. Šiuo atveju pirmų penkių žemiausių energijų juostų topologiniai Chern'o skaičiai lygus vienetui (žr. pav. 4.3). Taigi Hall'o laidumas monotoniškai didėja kai šias juostas pildome fermiono tipo atomais. Toks gaunamas kvantinis Hall'o efektas panašus į gaunamą iš Laundau lygmenų.

Sumažinę Raman'o sukabinimo stiprumą žemiau $V_0 = 0.175\hbar\omega$ gauname kitokio

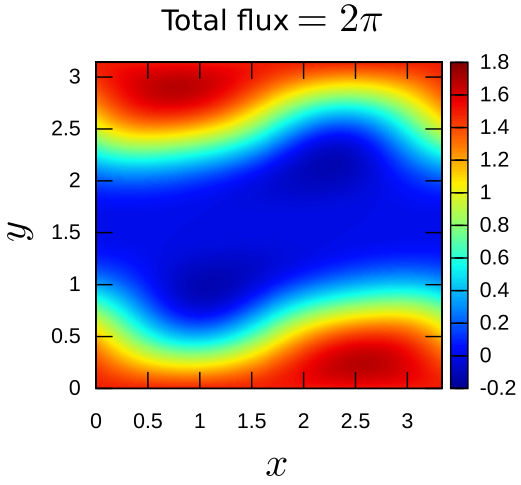

4.2 pav.: Dirbtinio magnetinio laukas per vieną elementarų narvelį adiabatiniame režime, kai $V_0 = 0.25\hbar\omega$ ir $\beta = 0.6k_0$.

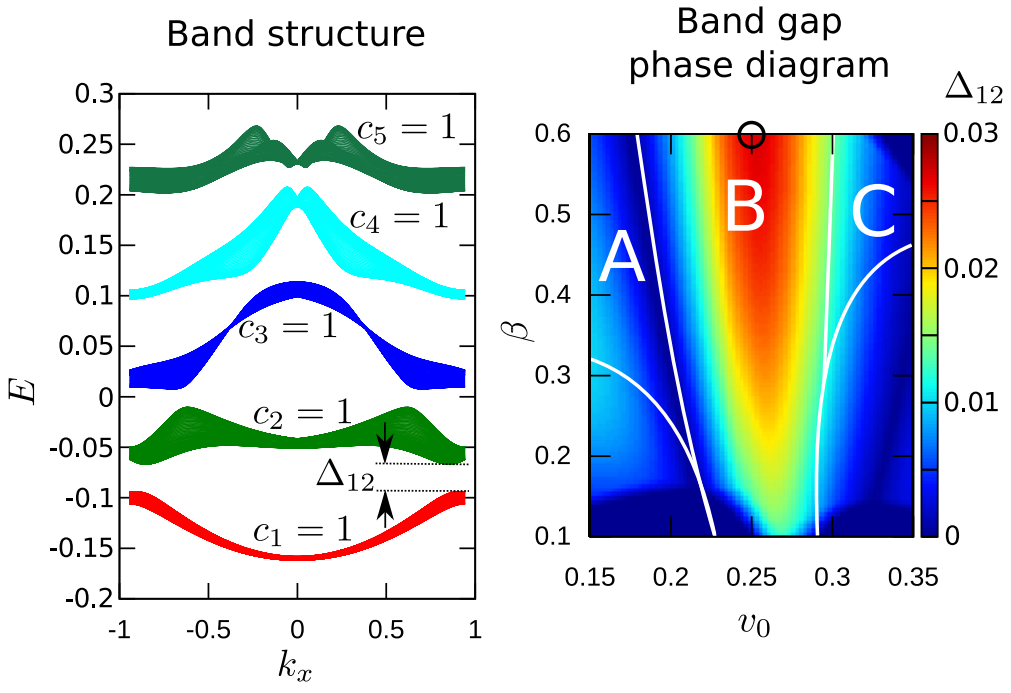

4.3 pav.: *Kairysis pav.*: srauto optinės gardelės juostinė sandara kai $V_0 = 0.25\hbar\omega$. Čia Floquet dažnis yra $\hbar\omega = 10E_{\text{recoil}}$, o pradinio magnetinio lauko gradientas $\beta = 0.6k_0$. *Dešinysis pav.*: draustinio juostų tarp tarp pirmųjų dviejų juostų fazinė diagrama. Čia $v_0 \equiv V_0/\hbar\omega$.

tipo topologinę fazę (pav. 4.3 sritis A), kurioje žemiausia juosta turi nulinį Chern'o skaičių, $c_1 = 0$, antra juosta turi Chern'o skaičių $c_2 = 2$, o kitų likusių juostų Chern'o skaičiai lieka nepasikeitę. Didinant Raman'o sukabinimą aukščiau $V_0 = 0.3\hbar\omega$ gauname kitą fazę su Chern'o skaičiais, $c_1 = 1$, $c_2 = -1$, $c_3 = 3$, $c_4 = 1$, ... (pav. 4.3 sritis B).

Apibendrinimas

Šiame skyriuje aprašėme naujovišką būdą sukurti dirbitinį magnetinį lauką labai šaltiems atomams naudojant dažnių šukų spinduliuotę, kuri sukabina du atomo vidinius lygmenis. Kartu su įprasto magnetinio lauko gradientu tokia sistema tampa stačiakampe optinę srauto gardele, kuri pasižymi nekintamo ženklo dirbitniu magnetiniu srautu bei topologiškai turtinga juostine sandara.

IŠVADOS

1. Darbe tyrinėta dice optinė gardelė yra sudaryta iš trijų sukabintų trikampių Bravais subgardelių. Todėl stipriojo ryšio artinyje gardelė turi tris energijos juostas. Dice gardelė tuo pačiu turi ir *kintamo ženklo* dirbtinį magnetinį lauką. Šis modelis išplečia dviejų lygmenų Haldane modelį į tris lygmenis. Haldane modelis gaunamas pašalinus vieną iš dice gardelės trikampių subgardelių.

2. Dice gardelė kaip Haldane modelio išplėtimas pateikia (i) galimybę pasiekti Chern'o puslaidininkio fazę neįtraukiant atomų šuolių tarp tolimesnių gardelės mazgų bei (ii) turtingą juostinę sandarą, kuri gali pateikti Chern'o skaičius moduliu didenius už vienetą.

3. Antroje darbo dalyje aprašyta ir ištyrinėta optinė srauto gardelė yra sudaroma naudojant dviejų lygmenų atomus, veikiamus įprasto magnetinio lauko gradientu ir dažnių šukų spinduliuotę. Stroboskopiniame artinyje gardelė yra dviejų dimensijų gardelė, kuri turi *nekintamo ženklo* dirbtinį magnetinį lauką.

4. Optinė srauto gardelė pasižymi Landau tipo energijos juostomis – esant tinkamiems parametrams kelios žemiausios energijos juostos turi Chern'o skaičių lygų vienetui. Be to, kaip ir dice optinė gardelė, ši gardelė gali turėti juostinę sandarą, apibūdinama Chern'o skaičiais moduliu didesniais už vienetą.

LITERATŪROS SĄRAŠAS

[1] Maciej Lewenstein, Anna Sanpera, Veronica Ahufinger, Bogdan Damski, Aditi Sen(De), and Ujjwal Sen. Ultracold atomic gases in optical lattices: mimicking condensed matter physics and beyond. *Advances in Physics*, 56(2):243–379, 2007.

[2] Steven Chu. Nobel lecture: The manipulation of neutral particles. *Rev. Mod. Phys.*, 70:685–706, Jul 1998.

[3] Claude N. Cohen-Tannoudji. Nobel lecture: Manipulating atoms with photons. *Rev. Mod. Phys.*, 70:707–719, Jul 1998.

[4] William D. Phillips. Nobel lecture: Laser cooling and trapping of neutral atoms. *Rev. Mod. Phys.*, 70:721–741, Jul 1998.

[5] E. A. Cornell and C. E. Wieman. Nobel lecture: Bose-einstein condensation in a dilute gas, the first 70 years and some recent experiments. *Rev. Mod. Phys.*, 74:875–893, Aug 2002.

[6] Wolfgang Ketterle. Nobel lecture: When atoms behave as waves: Bose-einstein condensation and the atom laser. *Rev. Mod. Phys.*, 74:1131–1151, Nov 2002.

[7] Immanuel Bloch, Jean Dalibard, and Wilhelm Zwerger. Many-body physics with ultracold gases. *Rev. Mod. Phys.*, 80:885–964, Jul 2008.

[8] Markus Greiner, Olaf Mandel, Tilman Esslinger, Theodor W. Hänsch, and Immanuel Bloch. Quantum phase transition from a superfluid to a mott insulator in a gas of ultracold atoms. *Nature*, 415:39–44, Jan 2002.

[9] D. Jaksch, C. Bruder, J. I. Cirac, C. W. Gardiner, and P. Zoller. Cold bosonic atoms in optical lattices. *Phys. Rev. Lett.*, 81:3108–3111, Oct 1998.

[10] Richard P. Feynman. Quantum mechanical computers. *Foundations of Physics*, 16:507–531, Jun 1986.

[11] J. R. Abo-Shaeer, C. Raman, J. M. Vogels, and W. Ketterle. Observation of vortex lattices in bose-einstein condensates. *Science*, 292(5516):476–479, 2001.

[12] N.R. Cooper. Rapidly rotating atomic gases. *Advances in Physics*, 57(6):539–616, 2008.

[13] Alexander L. Fetter. Rotating trapped bose-einstein condensates. *Rev. Mod. Phys.*, 81:647–691, May 2009.

[14] K. W. Madison, F. Chevy, V. Bretin, and J. Dalibard. Stationary states of a rotating bose-einstein condensate: Routes to vortex nucleation. *Phys. Rev. Lett.*, 86:4443–4446, May 2001.

[15] M. R. Matthews, B. P. Anderson, P. C. Haljan, D. S. Hall, C. E. Wieman, and E. A. Cornell. Vortices in a bose-einstein condensate. *Phys. Rev. Lett.*, 83:2498–2501, Sep 1999.

[16] K. C. Wright, R. B. Blakestad, C. J. Lobb, W. D. Phillips, and G. K. Campbell. Driving phase slips in a superfluid atom circuit with a rotating weak link. *Phys. Rev. Lett.*, 110:025302, Jan 2013.

[17] Jean Dalibard, Fabrice Gerbier, Gediminas Juzeliūnas, and Patrik Öhberg. Colloquium: Artificial gauge potentials for neutral atoms. *Rev. Mod. Phys.*, 83:1523–1543, Nov 2011.

[18] N Goldman, G Juzeliūnas, P Öhberg, and I B Spielman. Light-induced gauge fields for ultracold atoms. *Reports on Progress in Physics*, 77(12):126401, 2014.

[19] André Eckardt. Colloquium: Atomic quantum gases in periodically driven optical lattices. *Rev. Mod. Phys.*, 89:011004, Mar 2017.

[20] Gregor Jotzu, Michael Messer, Rémi Desbuquois, Martin Lebrat, Thomas Uehlinger, Daniel Greif, and Tilman Esslinger. Experimental realization of the topological haldane model with ultracold fermions. *Nature*, 515:237–240, Nov 2014.

[21] J. Struck, C. Ölschläger, M. Weinberg, P. Hauke, J. Simonet, A. Eckardt, M. Lewenstein, K. Sengstock, and P. Windpassinger. Tunable gauge potential for neutral and spinless particles in driven optical lattices. *Phys. Rev. Lett.*, 108:225304, May 2012.

[22] Patrick Windpassinger and Klaus Sengstock. Engineering novel optical lattices. *Reports on Progress in Physics*, 76(8):086401, 2013.

[23] F. D. M. Haldane. Model for a quantum hall effect without landau levels: Condensed-matter realization of the "parity anomaly". *Phys. Rev. Lett.*, 61:2015–2018, Oct 1988.

[24] Pierre Meystre. *Atom Optics*. Springer-Verlag New York, Inc., 2001.

[25] Gregory H. Wannier. The structure of electronic excitation levels in insulating crystals. *Phys. Rev.*, 52:191–197, Aug 1937.

[26] W. Kohn. Analytic properties of bloch waves and wannier functions. *Phys. Rev.*, 115:809–821, Aug 1959.

[27] W. Kohn. Construction of wannier functions and applications to energy bands. *Phys. Rev. B*, 7:4388–4398, May 1973.

[28] Nicola Marzari and David Vanderbilt. Maximally localized generalized wannier functions for composite energy bands. *Phys. Rev. B*, 56:12847–12865, Nov 1997.

[29] Charles Nash and Siddhartha Sen. *Topology and Geometry for Physicists*. Academic Press Inc. (London) LTD, 1983.

[30] Mikio Nakahara. *Geometry, Topology and Physics*. IOP Publishing Ltd, 2003.

[31] D. J. Thouless, M. Kohmoto, M. P. Nightingale, and M. den Nijs. Quantized hall conductance in a two-dimensional periodic potential. *Phys. Rev. Lett.*, 49:405–408, Aug 1982.

[32] Di Xiao, Ming-Che Chang, and Qian Niu. Berry phase effects on electronic properties. *Rev. Mod. Phys.*, 82:1959–2007, Jul 2010.

PUBLICATIONS OF THE DOCTORAL DISSERTATION

I E. Anisimovas, F. Gerbier, T. Andrijauskas, and N. Goldman, *Design of laser-coupled honeycomb optical lattices supporting Chern insulators*, Physical Review A **89**, 013632 (2014).

II T. Andrijauskas, E. Anisimovas, M. Račiūnas, A. Mekys, V. Kudriašov, I. B. Spielman, and G. Juzeliūnas, *Three-level Haldane-like model on a dice optical lattice*, Physical Review A **92**, 033617 (2015).

III Tomas Andrijauskas, I B Spielman and Gediminas Juzeliūnas, *Topological lattice using multi-frequency radiation*, New Journal of Physics **20**, 055001 (2018).

I

Design of laser-coupled honeycomb optical lattices supporting Chern insulators

E. Anisimovas, F. Gerbier, T. Andrijauskas, and N. Goldman

Physical Review A **89**, 013632 (2014).

as the work contains at least 10% new material not covered by APS's copyright and does not contain more than 50% of the text (including equations) of the original article. The APS will extend the author of a “derived work” the right to all papers published in APS journals.

As the author (or the author's employer) of an APS-published article, may I use copies of part or all of my article in the classroom?

Yes, the author or his/her employer may use all or part of the APS-prepared version for educational purposes without requesting permission from the APS as long as the appropriate bibliographic citation is included.

As the author of an APS-published article, may I use figures, tables, graphs, etc. in future publications?

Yes, as the author you have the right to use figures, tables, graphs, etc. in subsequent publications using files prepared and formatted by you or the APS-prepared versions. The appropriate bibliographic citation must be included.

As the author of an APS-published article, may I include my article or a portion of my article in my thesis or dissertation?

Yes, the author has the right to use the article or a portion of the article in a thesis or dissertation without requesting permission from APS, provided the bibliographic citation and the APS copyright credit line are given on the appropriate pages.

As the author of an APS-published article, may I give permission to a colleague or third party to republish all or part of the article in a print publication?

Yes, as the author you may grant permission to third parties to republish print versions of the article provided the APS-published version (e.g., the PDF from the online journal, or a copy of the article from the print journal) is not used for this purpose. The article may not be published in another journal, and the third party may not charge a fee. The appropriate bibliographic citation and notice of the APS copyright must be included.

As the author of an APS-published article, may I give permission to a colleague or third party to republish all or part of the APS-published version in an online journal, book, database compilation, etc.?

No, an author may not grant permission in this case. To request permission to republish APS-copyrighted material, please refer to the “Reuse & Permissions” link that can be found on each APS article page.

As the author of an APS-published article, may I provide a PDF of my paper to a colleague or third party?

The author is permitted to provide, for research purposes and as long as a fee is not charged, a PDF copy of his/her article using either the APS-prepared version or the author prepared version.

As a third party (not an author), may I republish an article or portion of an article published by APS?

Design of laser-coupled honeycomb optical lattices supporting Chern insulators

E. Anisimovas,[1,2,*] F. Gerbier,[3] T. Andrijauskas,[2] and N. Goldman[3,†]
[1]*Department of Theoretical Physics, Vilnius University, Saulėtekio 9, LT-10222 Vilnius, Lithuania*
[2]*Institute of Theoretical Physics and Astronomy, Vilnius University, Goštauto 12, LT-01108 Vilnius, Lithuania*
[3]*Laboratoire Kastler Brossel, CNRS, UPMC, ENS, 24 rue Lhomond, 75005, Paris, France*
(Received 30 December 2013; published 31 January 2014)

We introduce an explicit scheme to realize Chern insulating phases employing cold atoms trapped in a state-dependent optical lattice and laser-induced tunneling processes. The scheme uses two internal states, a ground state and a long-lived excited state, respectively trapped in separate triangular and honeycomb optical lattices. A resonant laser coherently coupling the two internal states enables hopping between the two sublattices with a Peierls-like phase factor. Although laser-induced hopping by itself does not lead to topological bands with nonzero Chern numbers, we find that such bands emerge when adding an auxiliary lattice that perturbs the lattice structure, effectively turning it at low energies into a realization of the Haldane model: a two-dimensional honeycomb lattice breaking time-reversal symmetry. We investigate the parameters of the resulting tight-binding model using first-principles band-structure calculations to estimate the relevant regime for experimental implementation.

DOI: 10.1103/PhysRevA.89.013632 PACS number(s): 67.85.−d, 37.10.Jk, 73.43.−f

I. INTRODUCTION

Lattice systems displaying topologically nontrivial band structures are currently attracting the curiosity of a large scientific community [1,2]. For systems breaking time-reversal invariance, the band topology is characterized by a topological invariant (the Chern number [3,4]) taking integer values. The presence of topological order is signaled by a nonzero value of the topological invariant and has experimental consequences, such as the existence of chiral edge states enforced by the bulk-edge correspondence [1,2] or the quantization of transport coefficients in electronic systems [5]. The universality of these topological properties suggests that they could be engineered not only in solid-state systems [2] but also in a wide range of physical systems characterized by spatially periodic structures, such as photonic lattices [6] or ultracold atoms trapped in optical lattices [7–9]. Progress towards realization of topological phases in cold atomic gases has been recently reported [10–12].

In two space dimensions, one of the simplest models supporting topological bands was proposed by Haldane [13]. This model features nearest-neighbor (NN) and *next*-nearest-neighbor (NNN) hoppings on a honeycomb lattice accompanied by complex (Peierls) phase factors such that the net flux through a unit hexagonal cell is zero. The Haldane model has never been realized in laboratories, but it has been suggested that it could be engineered through lattice shaking [14], rotation [15], or laser-induced methods [14,16–19]. In the present contribution, we consider a concrete experimental implementation of the Haldane-like optical lattice, initially introduced by Alba *et al.* [20]. This scheme, illustrated in Fig. 1(a), envisages trapping atoms with two internal states into two state-dependent triangular optical lattices. The two lattices are spatially distinct and intertwined to form a honeycomb pattern. A laser-induced coupling of the two internal states produces the NN hoppings within this "hybrid honeycomb" lattice, as shown by full red lines in Fig. 1(a). The properties of this model were explored in detail in Ref. [21] in terms of a simple two-band tight-binding model. However, the relation between the tight-binding model parameters and the realistic lattice potential was not explored in the previous works [20,21].

In this article, we go beyond the studies [20,21] and analyze an explicit experimental scheme that implements the Haldane-like optical lattice. We build on the scheme proposed in Ref. [22], and consider an atomic species with a long-lived metastable excited state e. The method is valid both for bosonic and fermionic species, and it does not suffer from spontaneous emission. We show that the Haldane-like optical lattice can be realized using a minimal set of ingredients: (a) a primary state-dependent lattice $V^{(1)}$, that traps the ground g and excited e states in a honeycomb or triangular hybrid lattice, (b) a laser that couples the two states $g \leftrightarrow e$, and (c) an auxiliary lattice $V^{(2)}$ periodic in one direction only. The main lattice $V^{(1)}_{g/e}$, depicted in Fig. 1(b), traps the ground state g in the triangular lattice represented by the C sites, while the excited state e is trapped in the complementary honeycomb lattice formed by the A and B sites. Additionally, the g and e states are coupled by a resonant laser-inducing hopping between the primary honeycomb and triangular lattices. Superimposing an auxiliary lattice $V^{(2)}_{g/e}$ chosen to shift the B sites in energy, one effectively removes these sites from the dynamics. The resulting "laser-coupled honeycomb" lattice is illustrated in Fig. 1(c). It is characterized by laser-induced NN hopping between A and C sites, with complex tunneling matrix elements $J_{AC}e^{i\boldsymbol{p}\cdot(\boldsymbol{r}_A+\boldsymbol{r}_C)/2}$, and natural NNN hopping between sites of the same nature, with amplitudes $J_A \approx J_C$. This laser-coupled honeycomb lattice is qualitatively equivalent to the Haldane-like model of Refs. [20,21], which was shown to host Chern insulating phases for specific values of the transferred momentum $\boldsymbol{p}$ and ratio J_A/J_{AC}. Thus the present scheme illustrated in Fig. 1(c) provides a realistic method to realize topological bands in optical-lattice systems. In the following, we investigate this strategy in detail and discuss its validity in terms of actual lattice parameters.

*egidijus.anisimovas@ff.vu.lt
†nathan.goldman@lkb.ens.fr

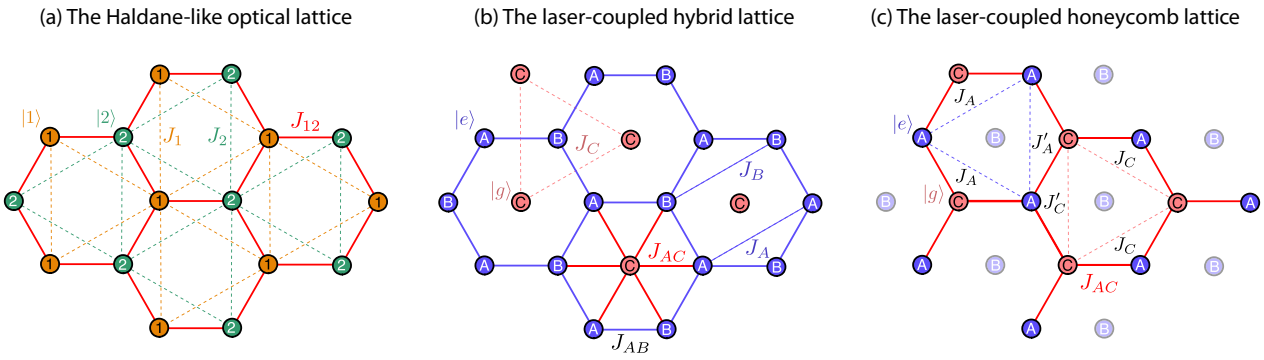

FIG. 1. (Color online) (a) Haldane-like optical lattice: atoms in states $|1\rangle$ and $|2\rangle$ are trapped in two state-dependent triangular optical lattices, with hopping amplitude J_1 and J_2, respectively. Coupling the states $1 \leftrightarrow 2$ induces hopping between the two triangular lattices, generating a Haldane-like honeycomb lattice with complex NN hopping matrix element J_{12}. (b) Sketch of the hybrid laser-coupled lattice generated by the potentials in Eq. (2). Atoms in the ground g (excited e) state are attracted to the intensity maxima (minima) that span the red triangular (blue honeycomb) sublattice. Full and dotted lines indicate the dominant NN and NNN tunnelings, which enter the tight-binding models of Sec. II. The two sublattices are coupled by direct laser-induced transitions indicated with full red lines, as described in Eq. (4). (c) Sketch of the final lattice geometry resulting from the addition of an auxiliary lattice (Sec. III), where B sites are blacked out to indicate that they correspond to higher bands of the hybrid lattice. A and C sites form a honeycomb lattice connected by NN laser-induced tunneling (full red lines) and natural NNN tunneling (dashed lines). Note that the NNN hopping amplitudes are slightly anisotropic: $J_A \neq J'_A$ and $J_C \neq J'_C$. The laser-coupled honeycomb lattice in (c) is qualitatively equivalent to the Haldane-like optical lattice (a) of Refs. [20,21].

The present work is structured as follows. In Sec. II, we discuss the atomic properties of two-electron atoms used in our proposal, taking the specific example of ytterbium atoms, introduce the main lattice $V^{(1)}$, and explore its band structure. In Sec. II C, we discuss the lattice structure emerging from the coupling between the ground g and excited e states. Then we add the auxiliary lattice $V^{(2)}$ in Sec. III, and we show how it leads to a Haldane-like model exhibiting reachable Chern insulating phases. We conclude with a summary and some final remarks in Sec. IV.

II. HYBRID TRIANGULAR-HONEYCOMB LATTICE

A. Atomic structure and light-shift potentials

We consider a gas of atoms with two internal states, denoted g and e, which are trapped in a potential landscape created by a set of lasers. A key requirement is to choose a long-lived excited state e to suppress heating due to spontaneous emission. This is, for instance, fulfilled in alkaline-earth-metal or ytterbium atoms [22], where g is chosen to be the electronic spin singlet ground state $^1S_0$, and e is a long-lived spin triplet excited state $^3P_0$. The transition between these two states has already been exploited to build atomic clocks [23,24], and proposed to be a good candidate for coherent operations in quantum information processing [25] or quantum simulation [22,26]. In the following we choose ytterbium atoms to be specific while the proposed method should work as well with other atoms featuring very long-lived excited states. For ytterbium, the lifetime of the $^3P_0$ excited state is estimated to be $\sim$20 s [27], and coupling to the ground state is achieved using a laser at the resonant wavelength $\lambda_{ge} \approx 578$ nm.

We consider here atoms confined to two dimensions by a strong trap in the z direction acting identically on both internal states. In general, the potentials $V_{g/e}(\boldsymbol{r})$ felt by the two states are different [28]. For the sake of simplicity, we choose the so-called "antimagic" wavelength λ_{am} at which the polarizabilities of the two relevant states are exactly opposite, $\alpha_g(\lambda_{am}) = -\alpha_e(\lambda_{am}) = \alpha_{am} > 0$ [22,25]. Generalizing to another wavelength is straightforward as long as the signs of the polarizabilities remain opposite. For a monochromatic laser, the optical lattice potential $V^{(1)}_{g/e}(\boldsymbol{r})$ felt by atoms in each state g/e can then be written in terms of the total electric field $\boldsymbol{E}(\boldsymbol{r})$ as [28]

$$V_{g/e}(\boldsymbol{r}) = \mp\tfrac{1}{2}\alpha_{am}|\boldsymbol{E}(\boldsymbol{r})|^2. \tag{1}$$

Ground-state atoms are trapped near the maxima of the intensity $\propto |\boldsymbol{E}(\boldsymbol{r})|^2$, while excited-state atoms are trapped near the minima. Importantly, the antimagic wavelength should be far detuned from any resonance so as to avoid spontaneous emission in the experiment. In the following, we will consider optical lattices at the Yb antimagic wavelength $\lambda_{am} \approx 1120$ nm [22,29]. The energy will thus be measured in units of the recoil energy $E_R/h = (h/2m\lambda^2_{am}) \approx 900$ Hz, corresponding to a temperature of about $T_R \approx 40$ nK.

B. Band-structure calculation for the primary lattices

The primary lattice is created by three coplanar laser beams of equal wavelength λ_{am} and intensity, and wave vectors $\boldsymbol{k}_{1,2,3}$ that intersect at angles $2\pi/3$ [see Fig. 2(a)]. We choose the polarizations of the beams to be normal to the lattice plane, so that the complex amplitudes of the corresponding electric fields take the form $\boldsymbol{E}_i = E_0\mathbf{e}_z\, e^{i\boldsymbol{k}_i\cdot\boldsymbol{r}}$. The coherent superposition of the individual electric fields results in the intensity distribution illustrated in Fig. 2(c). The intensity maxima (minima) of this pattern lie on a triangular (honeycomb) lattice that traps g (e) atoms according to Eq. (1) [30,31], as illustrated in Fig. 1(b). In the following we label A and B the two inequivalent sites of the honeycomb lattice formed by intensity minima, and C the sites of the triangular lattice formed by intensity maxima. We write the light-shift

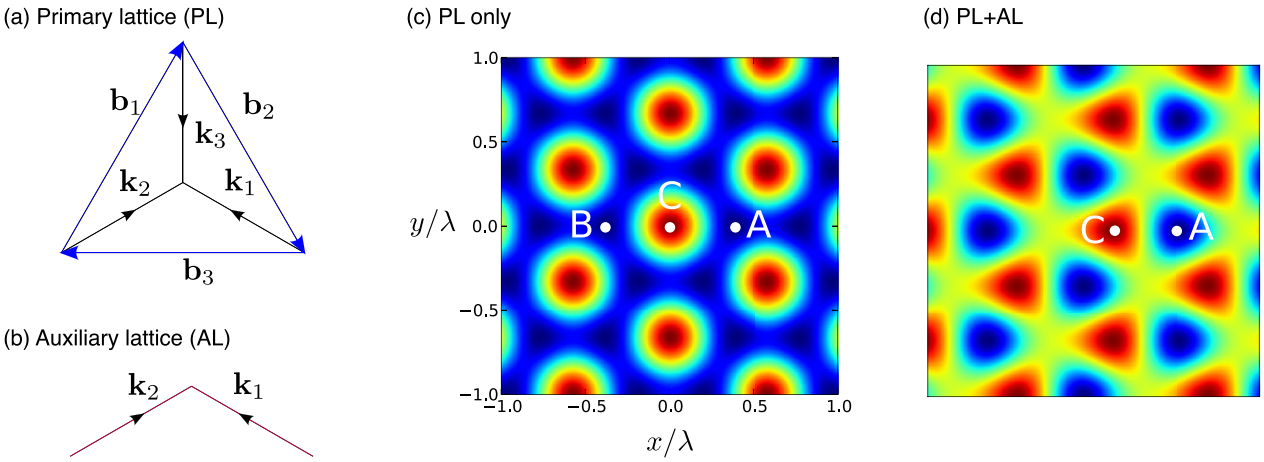

FIG. 2. (Color online) (a) Laser beams configuration for the primary lattice: the wave vectors $\boldsymbol{k}_{1,2,3}$ of the three lasers and the elementary reciprocal lattice vectors $\boldsymbol{b}_{1,2,3}$ are shown. (b) Laser beams configuration for the auxiliary lattice. Note that primary and auxiliary fields add incoherently due to the choice of polarizations. (c) The intensity distribution $|\boldsymbol{E}(\boldsymbol{r})|^2$ for the primary lattice: red (blue) colors correspond to high (low) intensity regions. The inequivalent lattice sites of the corresponding honeycomb (A, B) and triangular (C) lattices are indicated. (d) The intensity distribution $|\boldsymbol{E}(\boldsymbol{r})|^2$ for the total lattice potential obtained by adding the auxiliary lattice. The inequivalent lattice sites of the corresponding honeycomb lattice (A, C) are indicated.

potentials acting on g/e as

$$V^{(1)}_{g/e}(\boldsymbol{r}) = \mp V_0 \left[3 + 2\sum_{j=1}^{3} \cos(\boldsymbol{b}_j \cdot \boldsymbol{r}) \right], \qquad (2)$$

where we introduced the three vectors $\boldsymbol{b}_\alpha = \frac{1}{2}\varepsilon_{\alpha\beta\gamma}(\boldsymbol{k}_\beta - \boldsymbol{k}_\gamma)$ ($\varepsilon_{\alpha\beta\gamma}$ is the fully antisymmetric tensor), also shown in Fig. 2(a). We note that any phase shifts that appear in general in the arguments of the three cosines in Eq. (2) can be eliminated by a proper choice of the origin.

We have studied the band structure of each of the two uncoupled lattices $V^{(1)}_{g/e}(\boldsymbol{r})$ from first principles using the method and code published by Walters and co-workers [32]. The Bloch states were computed and used to construct a localized basis spanned by the maximally localized generalized Wannier functions [33]. Knowledge of the Wannier functions in turn enables one to compute the parameters of a faithful tight-binding model describing dynamics in the lowest bands for each lattice. The band-structure calculation also signals the limits of validity of this tight-binding model; see also Ref. [34]. We will consider in the following the (arbitrary) criterion for the validity of this model: the width W_s of the lowest s band is one order of magnitude lower than the gap $\Delta_{\rm sp}$ separating this band from the higher lying p band.

We start with the honeycomb lattice potential $V^{(1)}_e(\boldsymbol{r})$ felt by atoms in state e, and present the results of the full band-structure calculations in Fig. 3(a). The tight-binding model relevant to the two lowest-energy bands—analogous to the well-known bands of graphene that touch at the Dirac points [35]—is parametrized by a NN hopping matrix element J_{AB} connecting inequivalent sites [red line in Fig. 3(a)] and a NNN hopping matrix element connecting equivalent sites, $J_A = J_B$

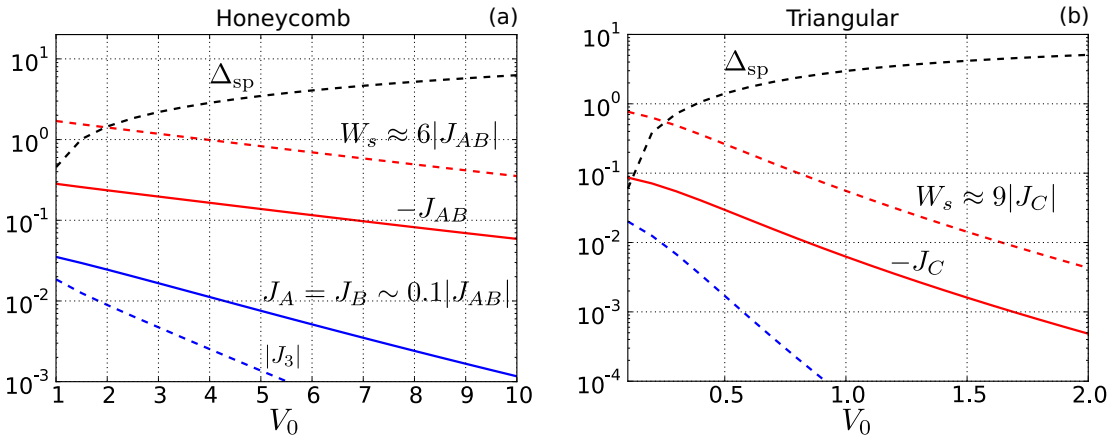

FIG. 3. (Color online) Band-structure parameters for the main optical lattice shown in Fig. 2(c), as a function of the potential strength V_0: (a) the honeycomb lattice felt by the e states and (b) the triangular lattice felt by the g states. Both panels show the width of the lowest Bloch band W_s ($W_s = 6|J_{AB}|$ for the honeycomb lattice and $W_s = 9|J_C|$ for the triangular lattice), the band gap $\Delta_{\rm sp}$ separating it from the higher band, and the hopping amplitudes. All quantities are energies, expressed in units of the recoil energy E_R.

[blue line in Fig. 3(a)]. The NNN hopping amplitude is positive and at least an order of magnitude smaller that the NN hopping. For comparison, the amplitude of the third-order transition is also included: $|J_3|$ is the absolute value of the matrix element connecting a given site to the diametrically opposite site across a honeycomb cell. This element is negative, and is the largest of all neglected higher-order contributions. The lowest two bands have an energy width W_s (given by $W_s = 6|J_{AB}|$ in the tight-binding approximation), which is plotted as a red dashed line to compare it to the band gap $\Delta_{\rm sp}$ separating the ground s bands from the higher-lying p bands (black dashed line). We see that a two-band approximation is well justified for $V_0 \gtrsim 5E_R$. This range also corresponds to $|J_3| \lesssim J_A/10$. We conclude that for $V_0 > 5\,E_R$, the ground band is well isolated from the higher-lying ones and that a faithful two-site tight-binding model can be formulated including only NN and NNN transitions.

The triangular lattice potential felt by the g state is given by $V_g^{(1)}(\boldsymbol{r}) = -V_e^{(1)}(\boldsymbol{r})$, whereby the minima and maxima exchange their positions. The corresponding C sites are separated by higher barriers than in the honeycomb lattice, and the distance between nearest-neighboring sites of the triangular lattice is equal to the distance between next-nearest-neighboring sites of the honeycomb lattice. As a consequence, for a given depth V_0 the tunneling rates in the triangular lattice are drastically smaller than in the honeycomb lattice. Figure 3(b) summarizes the numerical results of the Wannier-structure study for the case of the triangular lattice. The red line shows the absolute value of the (negative) NN hopping element J_C, which is compared to the band gap (black dashed line) and NNN hopping (blue dashed line). We see that for $V_0 > 0.5\,E_R$ the tight-binding model is well justified. Overall, the validity of single-band and tight-binding approximations are determined by the honeycomb lattice parameters. In the range $V_0 > 5E_R$, tunneling between C sites in the triangular lattice is weaker by orders of magnitude than for A or B sites. Although this seems like a serious concern for an experimental implementation, we will see later that introducing the auxiliary lattice cures this imbalance.

C. Coupling the two sublattices

We now connect the two sublattices by a laser resonantly coupling the two internal states g and e and thereby induce hopping between the otherwise unconnected sublattices. We call this configuration the "hybrid lattice" in the following. Following Ref. [36], we express the laser-assisted hopping matrix element between A and C sites, respectively hosting states e and g, as

$$J(\boldsymbol{r}_A,\boldsymbol{r}_C) = \frac{\hbar\Omega}{2}\int d^2r\, w_A(\boldsymbol{r}-\boldsymbol{r}_A)e^{i\boldsymbol{p}\cdot\boldsymbol{r}}w_C(\boldsymbol{r}-\boldsymbol{r}_C), \qquad (3)$$

where the real-valued Wannier functions w_A and w_C are centered at their respective lattice sites $\boldsymbol{r}_A$ and $\boldsymbol{r}_C$. Here, Ω is the Rabi frequency characterizing the strength of the light-atom coupling, and $\boldsymbol{p}$ is the recoil momentum transferred to the hopping atom. Since the product of the Wannier functions is well localized near the midpoint of the line connecting the two sites, laser-induced hopping matrix elements are well approximated by

$$J(\boldsymbol{r}_A,\boldsymbol{r}_C) = J_{AC}e^{i\,\boldsymbol{p}\cdot(\boldsymbol{r}_A+\boldsymbol{r}_C)/2}, \qquad (4)$$

where J_{AC} is independent of $\boldsymbol{p}$ [36]. By symmetry, one obtains $J(\boldsymbol{r}_A,\boldsymbol{r}_C) = J(\boldsymbol{r}_C,\boldsymbol{r}_A)^*$, and equivalent expressions for the hopping between B and C sites.

Importantly, the hopping matrix elements in Eq. (4) contain space-dependent phases determined by the laser's wave vector $\boldsymbol{p}$. The sum of the phase factors along the boundary of a region $\triangle$ can be identified with the circulation of a synthetic vector potential penetrating the region $\triangle$. In the following, we use the term "flux" through a region $\triangle$ to refer to the synthetic flux given by the circulation of these phases along the boundary $\partial\triangle$. In the present work, we seek a lattice configuration that gives rise to topological band structures with nonzero Chern numbers [3,4]. As realized by Haldane [13], a necessary condition to generate such topological band structures is to build a model that explicitly breaks time-reversal symmetry. Thus a simple way to identify whether our hybrid honeycomb-triangular lattice indeed supports potentially nonzero Chern numbers is to examine its behavior under time reversal.

We will now demonstrate that the hybrid lattice is actually *invariant* under this transformation. We show the flux patterns obtained from Eq. (4) in Fig. 4(a) for two chosen subplaquettes patterns: the first one is spanned by A-C and A-A links, and the other by B-C and B-B links. Time reversal affects the lattice by reversing the sign of the fluxes. From the flux patterns shown in Fig. 4(a), it is clear that this transformation leaves the honeycomb sublattice unchanged up to a discrete rotation. A similar analysis applies to other subplaquette configurations, such as those spanned by C-C links. From this analysis, we conclude that the laser-coupled hybrid lattice remains time-reversal invariant even with laser-assisted tunneling, due to the high degree of symmetry between the A and B sites of the honeycomb sublattice. This also suggests that breaking this symmetry (e.g., by adding an on-site perturbation acting on the B sites only) will naturally generate a configuration that will change under time reversal. This is the situation that we are going to analyze in the following section.

III. ADDING THE AUXILIARY LATTICE: BUILDING THE HALDANE MODEL

A. Auxiliary lattice

In order to remove the A/B symmetry of the honeycomb lattice, we introduce an auxiliary lattice $V_{g/e}^{(2)}$ produced by two additional beams with wave vectors $\boldsymbol{k}_1$ and $\boldsymbol{k}_2$ and in-plane polarizations [see Fig. 2(b)]. The additional lasers are described by electric fields $\boldsymbol{E}_1^{(2)} = E_2 e^{i\boldsymbol{k}_1\cdot\boldsymbol{r}}(\frac{1}{2},\frac{\sqrt{3}}{2})$ and $\boldsymbol{E}_2^{(2)} = E_2 e^{i\boldsymbol{k}_2\cdot\boldsymbol{r}+i\theta}(\frac{1}{2},-\frac{\sqrt{3}}{2})$, where θ is the relative phase shift between the two fields. Their coherent superposition produces a standing wave that adds incoherently to the existing main lattice $V_{g/e}^{(1)}$ due to the orthogonality of polarizations, i.e., $|\boldsymbol{E}_{\rm tot}(\boldsymbol{r})|^2 = |\boldsymbol{E}^{(1)}(\boldsymbol{r})|^2 + |\boldsymbol{E}^{(2)}(\boldsymbol{r})|^2$. The potentials corresponding to this auxiliary lattice read

$$V_{g/e}^{(2)}(\boldsymbol{r})^2 = \mp V_2[2-\cos(\boldsymbol{b}_3\cdot\boldsymbol{r}-\theta)]. \qquad (5)$$

The relative phase θ cannot be eliminated by a change of origin, and—together with the beam amplitudes—allows one

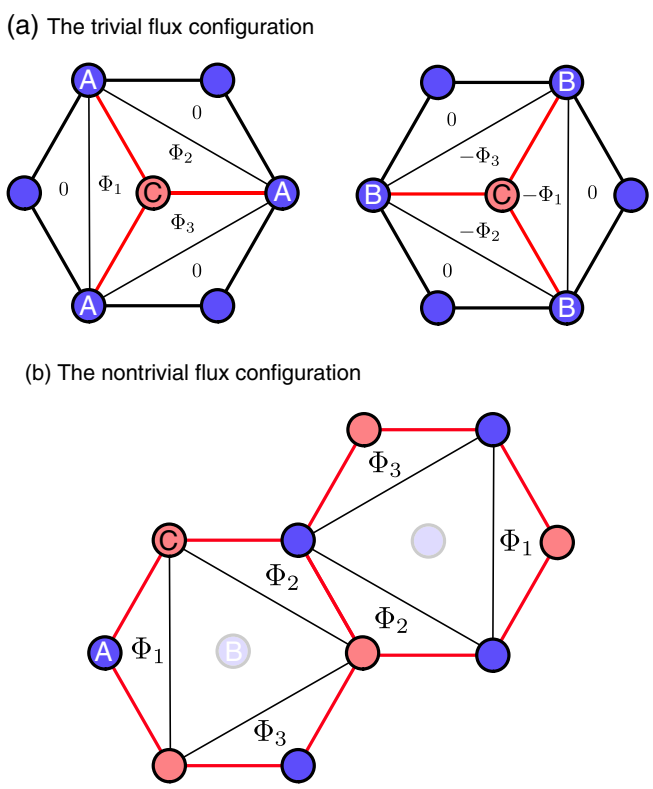

FIG. 4. (Color online) (a) Flux pattern for the hybrid honeycomb-triangular lattice with laser coupling. The phases accompanying the laser-assisted hopping (4) lead to nonzero fluxes $\pm\Phi_{1,2,3}$ within the triangular subplaquettes shown on the figure. The fluxes are given by $\Phi_1 = \boldsymbol{p}\cdot\boldsymbol{a}_3/4\pi, \Phi_2 = -\boldsymbol{p}\cdot\boldsymbol{a}_2/4\pi, \Phi_3 = \boldsymbol{p}\cdot\boldsymbol{a}_1/4\pi$, where $\boldsymbol{p}$ is the recoil momentum and $\boldsymbol{a}_{1,2,3}$ are defined in Fig. 6. Time reversal changes $\Phi_j \to -\Phi_j$, and therefore merely transforms A sites to B sites (and vice versa). Since A and B are related by a discrete symmetry (Π rotation around the axis perpendicular to the lattice plane), we conclude that the laser-coupled hybrid lattice does not break time-reversal symmetry. (b) Flux pattern for the main lattice perturbed by the auxiliary lattice introduced in Sec. III. The B sites are eliminated from the lowest energy band by a strong on-site perturbation. The resulting low-energy tight-binding model is no longer invariant under time reversal.

to move the position of the auxiliary lattice relative to the lattice $V^{(1)}_{g/e}$ and tune its depth. This way, the overall lattice geometry $V^{(1)}_{g/e} + V^{(2)}_{g/e}$ can be tuned. For a strong enough potential, the B sites of the primary honeycomb lattice $V^{(1)}_e$ are effectively eliminated from the dynamics [see Fig. 2(d)] leading to the desired laser-coupled honeycomb lattice illustrated in Fig. 1(c).

B. Perturbative analysis

To gain insight into the influence of the auxiliary lattice, let us first discuss the behavior of the band structure of the main hybrid lattice for a *weak* on-site perturbation. We simplify the analysis by assuming that the system is well represented by a tight-binding model for the ground bands and by reducing the number of parameters. We take the absolute value of the (negative) NN hopping amplitude as the unit of energy so that $J_{AB} = -1$, and set the laser-induced hopping $J_{AC} = J_{BC} = 1$. The intrasublattice NNN hoppings are considered to be uniform over the lattice $J_2 = J_A = J_B$, and $J_C \ll J_2$. We then add a perturbation ϵ_B that modifies the on-site energy of all the B sites, modeling the effect of a *weak* external potential that aims to lift the spectrum degeneracy and open gaps, but still remains weak enough not to perturb significantly the band structure of the uncoupled lattices.

The tight-binding model is then defined by the momentum space Hamiltonian

$$H(\boldsymbol{k}) = \begin{pmatrix} J_2 f\left(\boldsymbol{k}+\frac{1}{2}\boldsymbol{p}\right) & g(\boldsymbol{k}) & h(\boldsymbol{k}) \\ g^*(\boldsymbol{k}) & J_2 f\left(\boldsymbol{k}+\frac{1}{2}\boldsymbol{p}\right)+\epsilon_B & h^*(\boldsymbol{k}) \\ h^*(\boldsymbol{k}) & h(\boldsymbol{k}) & J_C f\left(\boldsymbol{k}-\frac{1}{2}\boldsymbol{p}\right) \end{pmatrix}, \tag{6}$$

where

$$f(\boldsymbol{k}) = 2\sum_{j=1}^{3}\cos\left(\boldsymbol{a}_j\cdot\boldsymbol{k}\right),$$

$$g(\boldsymbol{k}) = -\sum_{j=1}^{3} e^{i\boldsymbol{\delta}_j\cdot(\boldsymbol{k}+\boldsymbol{p}/2)}, \quad h(\boldsymbol{k}) = \sum_{j=1}^{3} e^{-i\boldsymbol{\delta}_j\cdot\boldsymbol{k}},$$

where the vectors $\boldsymbol{a}_j$ and $\boldsymbol{\delta}_j$ are defined in the caption of Fig. 6. We have analyzed the band structure through a direct diagonalization, varying the parameters in a wide range. In general, one finds three bands, whose topological character can be established by computing the Chern number through the numerical method of Ref. [37]. For $\epsilon_B = 0$, the two lowest bands touch at the Dirac points for any value of $\boldsymbol{p}$. A finite $\epsilon_B > 0$ opens a gap Δ separating these two bands.

Figure 5(a) shows the magnitude of Δ for $J_C \ll J_2$, and indicates the opening of gaps of a different nature as the perturbation ϵ_B is increased. The figure also indicates the Chern number ν associated with the lowest isolated band. The Chern number has been computed using the method of Ref. [37], which is based on an efficient discretization of Berry's curvature inspired by lattice gauge theory. A large trivial gap ($\nu = 0$) is first opened for small ϵ_B around the time-reversal-invariant configuration ($\boldsymbol{p} = 0$). For large ϵ_B, nontrivial gaps with Chern numbers $\nu = \pm 1$ open at finite $\boldsymbol{p} \neq 0$. Nonzero Chern numbers $\nu = \pm 1$ imply that the lowest-energy band is associated with a nontrivial topological order [21]: setting the Fermi energy within the gap leads to a Chern insulating phase, characterized by chiral edge modes [17,18,42–44]. We identify these nontrivial Chern insulating phases with those that were previously reported in Ref. [21], namely, the phases resulting from the Haldane-like model obtained by only considering the presence of A and C sites (i.e., removing the B sites of the hybrid lattice). The opening of this topological gap is further analyzed in Figs. 5(b) and 5(c), by varying the hopping J_C. These plots show that even for unrealistically large hopping between the C sites of the primitive triangular lattice ($J_C \sim J_2$), a very large on-site perturbation ϵ_B is required to generate a topological phase.

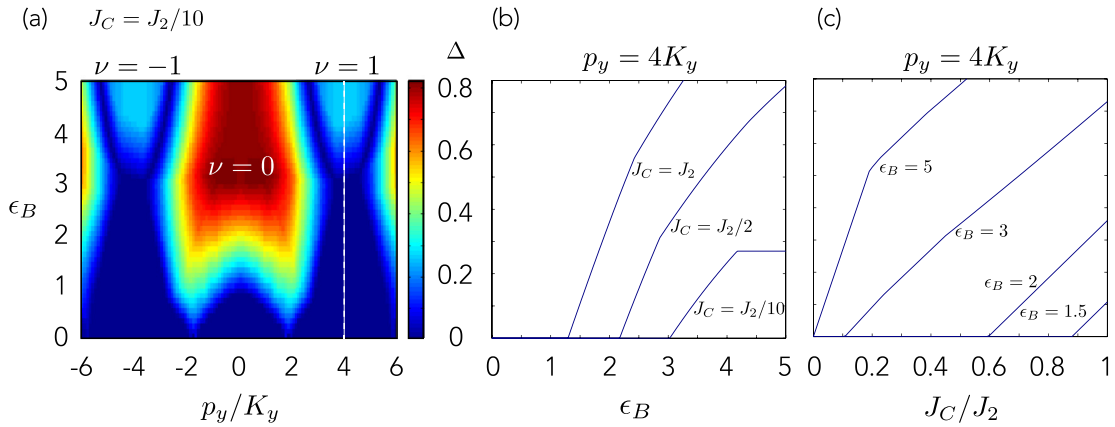

FIG. 5. (Color online) Band structure of the simplified tight-binding model (6) for the laser-coupled hybrid lattice. (a) Size of the main gap Δ as a function of the on-site perturbation ϵ_B and the recoil momentum p_y for $J_2 = 0.3\,J$, $p_x = 0$, and $J_C = J_2/10$. The large gap centered around $\boldsymbol{p} = 0$ is associated with a zero Chern number, $\nu = 0$, whereas the small gaps at $p_y \approx \pm 4K_y$ are associated with the nontrivial Chern numbers $\nu = \pm 1$. Here, the gap Δ and the perturbation ϵ_B are expressed in units of the NN hopping J. (b) Cut through the diagram (a) for $p_y = 4K_y$ and increasing values of the ratio J_C/J_2. (c) Size of the main gap as a function of J_C/J_2 for increasing values of the perturbation ϵ_B. Here $K_y = 2\pi/a3\sqrt{3}$ and $a = 2\lambda_{\rm am}/3\sqrt{3}$ is the lattice spacing of the primitive honeycomb lattice.

C. Band-structure calculations and tunneling parameters

For very large $\epsilon_B \gg J_{AB}$, the perturbative analysis presented above breaks down as the lattice geometry becomes strongly distorted. We have performed a full band-structure calculation based on the full potential to reevaluate the proper parameters for the tight-binding model of the hybrid lattice in the lowest band. Although the auxiliary lattice leads to on-site energies that are the same for all equivalent sites (A, B, or C), it does not respect the original triangular point symmetry of the primary potential landscape and affects the potential landscapes away from the maxima or minima. As a consequence, for arbitrary θ, the hopping amplitudes between neighboring potential minima are generally direction dependent. Numerical work reveals that choosing the values $\theta = \pi/6$ and $V_2 = 3V_1$, as shown in Fig. 2(d), is optimal to preserve—albeit approximately—the triangular point symmetry of the potential landscape. The calculations presented in the following are performed using these values.

Figure 6 summarizes the results. Panel (a) shows a fragment of the lattice. The blue (red) contour lines depict the shapes of the calculated real-valued maximally localized Wannier functions on a single site A (three surrounding sites C). We see that the Wannier orbitals have rounded triangular shape that follows the shape of the potential well in the vicinity of the potential minima. Although not immediately conspicuous in the contour plots, the Wannier orbitals *do not* have the full D_3 symmetry of the equilateral triangle; instead, they are only symmetric with respect to reflection in the x axis. This is a consequence of the striped auxiliary interference pattern and is reflected in a slight directional dependence of hopping amplitudes; see Fig. 1(c).

The calculated hopping matrix elements and characteristics of the energy bands are shown in panels (b) and (c) of Fig. 6.

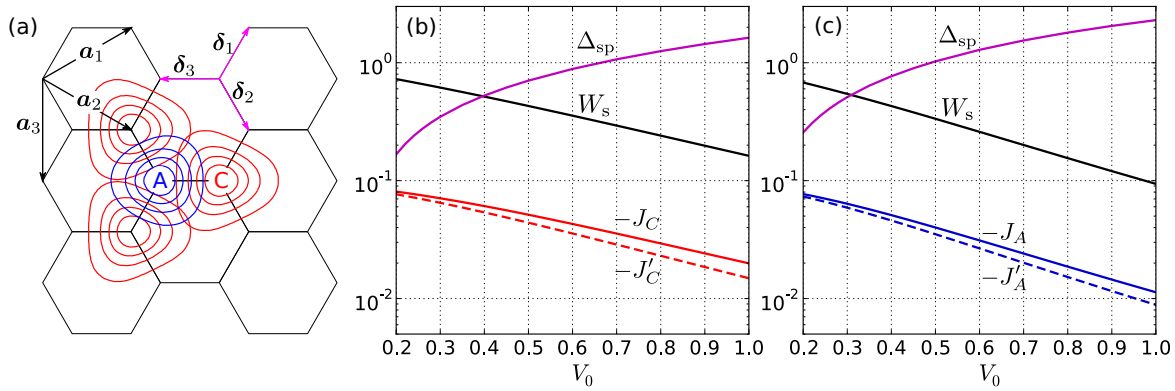

FIG. 6. (Color online) (a) Fragment of the honeycomb lattice AC, corresponding to the total potential combining the main and auxiliary lattices, simultaneously showing the elementary translation vectors and the shape of the Wannier orbitals. The contour levels are drawn at 0.2,0.4,0.6, and 0.8 times each orbital's maximum value. The vectors are given by $\boldsymbol{\delta}_1 = a/2(1,\sqrt{3})$, $\boldsymbol{\delta}_2 = a/2(1,-\sqrt{3})$, $\boldsymbol{\delta}_3 = a(-1,0)$, $\boldsymbol{a}_1 = \boldsymbol{\delta}_1 - \boldsymbol{\delta}_3$, $\boldsymbol{a}_2 = \boldsymbol{\delta}_2 - \boldsymbol{\delta}_3$, and $\boldsymbol{a}_3 = \boldsymbol{a}_2 - \boldsymbol{a}_1 = \boldsymbol{\delta}_2 - \boldsymbol{\delta}_1$, where $a = 2\lambda_{\rm am}/3\sqrt{3}$ is the primitive lattice spacing. Panels (b) and (c) show the width of the lowest Bloch band W_s, the band gap separating from the higher band $\Delta_{\rm sp}$, and the Hubbard parameters for the respective sublattices C and A. All quantities in (b) and (c) are energies, expressed in units of the recoil energy E_R.

All the plotted parameters have the dimensions of the energy and are expressed in terms of the recoil energy E_R. The two panels correspond to the different triangular sublattices, and are completely analogous. Thus we restrict the discussion to the behavior of g atoms shown in panel (b). The full and dashed red lines show the dependence of the hopping amplitudes between NNN sites of type C. As expected, these hopping elements display a weak directional dependence. Thus transitions connecting two sites in the $\pm\boldsymbol{a}_3$ direction (J'_C) are slightly weaker than transitions connecting neighboring C sites in the $\pm\boldsymbol{a}_{1(2)}$ directions (J_C). The full black and purple lines indicate, respectively, the dependence of the width of the lowest s band Δ_s and the band gap $\Delta_{\rm sp}$ to the higher p band. We have also verified that higher-order hopping transitions are negligible. Using the same criterion as before ($\Delta_{\rm sp} \gtrsim 10W_s$), we conclude that a single-band tight-binding approximation becomes justified as soon as the modulation strength exceeds $V_0 \approx 1\,E_R$.

We stress that the obtained tunneling parameters are now all similar in magnitude, unlike the situation without auxiliary lattice, and that they only weakly depend on the direction despite the absence of triangular point symmetry in the strict sense. For example, the choice $V_0 = 1\,E_R$ leads to values

$$\begin{aligned} J_A &= -0.011E_R, \quad J'_A = -0.009E_R, \\ J_C &= -0.020E_R, \quad J'_C = -0.015E_R. \end{aligned} \tag{7}$$

We also verified that the same conclusion applies to the intersublattice NN transitions, that is, the hopping amplitudes show only a weak dependence on the direction of the AC link given by $\boldsymbol{\delta}_{1,2,3}$.

D. Tight-binding model

In the tight-binding approximation, the model is represented by the $\boldsymbol{k}$-space Hamiltonian

$$\mathcal{H}(\boldsymbol{k}) = \begin{pmatrix} F\left(J_A, J'_A, \boldsymbol{k} + \frac{1}{2}\boldsymbol{p}\right) & J_{AC}h(\boldsymbol{k}) \\ J_{AC}h^*(\boldsymbol{k}) & F\left(J_C, J'_C, \boldsymbol{k} - \frac{1}{2}\boldsymbol{p}\right) \end{pmatrix}, \tag{8}$$

where

$$F(J, J', \boldsymbol{k}) = 2J\sum_{j=1}^{2}\cos(\boldsymbol{k}\cdot\boldsymbol{a}_j) + 2J'\cos(\boldsymbol{k}\cdot\boldsymbol{a}_3),$$

and the recoil momentum $\boldsymbol{p}$ enters the arguments of these functions as a shift in the reciprocal space.

We calculate the band and topological structure numerically using the realistic parameter values obtained from the band-structure modeling at the potential modulation strength $V_0 = 1\,E_R$. NNN hopping amplitudes are listed in Eq. (7) and take values in the vicinity of $J_A, J_C \approx -0.015E_R$. Guided by our previous work [21], we set the strength of the laser-assisted NN transitions to $J_{AC} \approx 3|J_A| = 0.050E_R$, which corresponds to using the Rabi frequency $\hbar\Omega \approx E_R$ in Eq. (3). Figure 7 shows the Chern number of the lowest band, which has been numerically computed using the method of Ref. [37]. This confirms that the topological phases are indeed readily accessible in this regime. The Chern number patterns are periodic in $\boldsymbol{p}$ with a hexagonal unit cell twice the size of the ordinary Brillouin zone. This is the consequence of the fractional argument $\boldsymbol{p}/2$ entering the matrix elements of the Hamiltonian matrix (8).

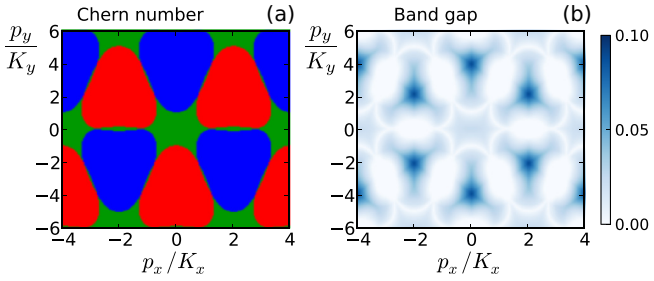

FIG. 7. (Color online) Topological band structure in the tight-binding regime. The left panel shows the dependence of the lower-band Chern number on the Cartesian components of the recoil momentum. The latter are expressed in terms of the vector $\boldsymbol{K} = (2\boldsymbol{b}_1 + \boldsymbol{b}_2)/3 = (\sqrt{3}\pi/\lambda_{\rm am}, \pi/\lambda_{\rm am})$ pointing to a Dirac point of the reciprocal lattice. Red and blue areas denote Chern numbers ± 1; green areas are topologically trivial. The right panel shows the gap separating the two bands with opposite Chern numbers. The band gap is expressed in units of the recoil energy E_R.

The obtained phase diagram in Fig. 7(a) is dominated by areas corresponding to topologically nontrivial regimes. A possible experimental detection of topological phases requires that the two bands characterized by Chern numbers ± 1 are separated by substantial band gaps. Panel (b) shows that the band gap can exceed the coupling strength J_{AC} or, in the best cases, even approach $\Delta = 2J_{AC} = 0.10E_R$. We also note that the gap attains the maximum values on a lattice spanned by the vectors $2\boldsymbol{K} = (2K_x, 2K_y)$ and $2\boldsymbol{K}' = (2K_x, -2K_y)$ in the $\boldsymbol{p}$ plane. Thus the six maximum-band-gap points closest to the origin correspond to the recoil momenta $\boldsymbol{p} = 4\pi/\lambda_{\rm am}$ and are nearly reachable employing the largest possible recoil momenta $\boldsymbol{p}_{\rm max} = 2\pi/\lambda_{\rm ge}$ with the resonant wavelength $\lambda_{\rm ge} = 578$ nm.

E. Detection of the Chern insulating phase

Different methods to detect topological order in cold-atom setups have been recently proposed. Two routes are generally envisaged: (a) measure the Chern number [20,38–41] or (b) detect the presence of chiral edge modes [17,18,42–44].

In two-band models, described by the general Hamiltonian

$$H(\boldsymbol{k}) = \epsilon(\boldsymbol{k})\hat{1}_{2\times 2} + \boldsymbol{d}(\boldsymbol{k})\cdot\hat{\boldsymbol{\sigma}}, \tag{9}$$

such as the Haldane-like system considered here, the Chern number is directly related to the vector field $\boldsymbol{d}(\boldsymbol{k})$, through the winding-number expression

$$\nu = \frac{1}{4\pi}\int_{\mathbb{T}^2}\frac{\boldsymbol{d}}{|\boldsymbol{d}|^3}\cdot\left(\partial_{k_x}\boldsymbol{d}\times\partial_{k_y}\boldsymbol{d}\right)d^2\boldsymbol{k}, \tag{10}$$

which counts the number of times the vector $\boldsymbol{d}(\boldsymbol{k})/|\boldsymbol{d}|$ covers the unit sphere as $\boldsymbol{k}$ is varied over the Brillouin zone. Following Ref. [20], the vector $\boldsymbol{d}(\boldsymbol{k})$ could be reconstructed through spin-resolved time-of-flight measurements, allowing for a "pixelated" measure of the Chern number.

More generally, it has been shown that releasing a Fermi gas initially prepared in a Chern insulating phase and acting on the cloud with an external linear potential (i.e., a synthetic

"electric" field $\boldsymbol{E}$) leads to a clear transverse (Hall) drift of the cloud: measuring the center-of-mass displacement in the direction transverse to the field $\boldsymbol{E}$ provides a direct measure of the Chern number ν [40]. Alternatively, signatures of the Berry's curvature $\mathcal{F}(\boldsymbol{k})$ could be detected through Bloch oscillations [38,39], offering an alternative way to reconstruct the Chern number $\nu \approx (1/2\pi i)\sum_{\boldsymbol{k}} \mathcal{F}(\boldsymbol{k})$.

Edge modes could be directly visualized through the methods of Ref. [42], which allows one to detect the propagation of edge states on a dark background (i.e., in a region unoccupied by the many bulk states). Alternatively, the linear dispersion proper to chiral modes could be identified through spectroscopy measurements [17,18,43].

IV. CONCLUSIONS

In summary, we have introduced and analyzed a realistic scheme to realize a Chern insulator using cold atoms. In this scheme, one exploits (i) the presence of a long-lived excited state in addition to the actual ground state, which is characteristic to alkaline-earth-metal or ytterbium atoms, and (ii) the existence of a frequency range where the polarizabilities of the two relevant states differ in sign. This allows one to exploit both intensity maxima and minima of an optical lattice to trap the two internal states, simultaneously avoiding heating from spontaneous emission. Based on first-principle calculations, we validate the applicability of the tight-binding approach in certain parameter regimes, and demonstrate the emergence of a generalized Haldane model, with laser-induced complex nearest-neighbor transitions and natural real-valued next-nearest-neighbor transitions. We show that topological phases are indeed readily accessible, with the topological band gaps on the order of $0.1E_R \sim 100$ Hz, indicating that the topological properties could be detected at sufficiently low temperatures $\sim$nK using currently existing proposals based on Chern-number measurement [20,38–40] or edge-state detection [17,18,42–44]. Finally, we emphasize that our proposal to implement the Haldane model using long-lived excited states follows an earlier proposal [22,36] to realize the paradigmatic Hofstadter model [45], suggesting that the versatility of this scheme could be further exploited to realize other lattice systems of interest.

ACKNOWLEDGMENTS

N.G. is supported by the Université Libre de Bruxelles (ULB). This research was also funded by the European Social Fund under the Global Grant measure, by Ville de Paris under the Emergences program [AtomHall], and by the European Research Council under the EU Seventh Framework Program (FP/2007-2013) [StG MANYBO GA 258521]. Discussions with J. Dalibard, J. Beugnon, A. Eckardt, G. Juzeliūnas, and J. Ruseckas are gratefully acknowledged. E.A. thanks T. H. Johnson for correspondence and providing a prepublication version of the Wannier code.

[1] M. Z. Hasan and C. L. Kane, Rev. Mod. Phys. **82**, 3045 (2010).
[2] X.-L. Qi and S.-C. Zhang, Rev. Mod. Phys. **83**, 1057 (2011).
[3] D. J. Thouless, M. Kohmoto, M. P. Nightingale, and M. den Nijs, Phys. Rev. Lett. **49**, 405 (1982).
[4] M. Kohmoto, Ann. Phys. (N.Y.) **160**, 343 (1985).
[5] K. von Klitzing, Rev. Mod. Phys. **58**, 519 (1986).
[6] I. Carusotto and C. Ciuti, Rev. Mod. Phys. **85**, 299 (2013); M. Hafezi, E. A. Demler, M. D. Lukin, and J. M. Taylor, Nat. Phys. **7**, 907 (2011); M. C. Rechtsman *et al.*, Nature (London) **496**, 196 (2013); M. Hafezi, S. Mittal, J. Fan, A. Migdall, and J. M. Taylor, Nat. Photon. **7**, 1001 (2013).
[7] I. Bloch, J. Dalibard, and W. Zwerger, Rev. Mod. Phys. **80**, 885 (2008).
[8] J. Dalibard, F. Gerbier, G. Juzeliūnas, and P. Öhberg, Rev. Mod. Phys. **83**, 1523 (2011).
[9] N. Goldman, G. Juzeliūnas, P. Öhberg and I. B. Spielman, arXiv:1308.6533v1.
[10] M. Aidelsburger, M. Atala, S. Nascimbène, S. Trotzky, Y.-A. Chen, and I. Bloch, Phys. Rev. Lett. **107**, 255301 (2011).
[11] M. Aidelsburger, M. Atala, M. Lohse, J. T. Barreiro, B. Paredes, and I. Bloch, Phys. Rev. Lett. **111**, 185301 (2013).
[12] H. Miyake, G. A. Siviloglou, C. J. Kennedy, W. C. Burton, and W. Ketterle, Phys. Rev. Lett. **111**, 185302 (2013).
[13] F. D. M. Haldane, Phys. Rev. Lett. **61**, 2015 (1988).
[14] P. Hauke *et al.*, Phys. Rev. Lett. **109**, 145301 (2012).
[15] C. Wu, Phys. Rev. Lett. **101**, 186807 (2008).
[16] L. B. Shao, S.-L. Zhu, L. Sheng, D. Y. Xing, and Z. D. Wang, Phys. Rev. Lett. **101**, 246810 (2008).
[17] T. D. Stanescu, V. Galitski, and S. Das Sarma, Phys. Rev. A **82**, 013608 (2010).
[18] X.-J. Liu, X. Liu, C. Wu, and J. Sinova, Phys. Rev. A **81**, 033622 (2010).
[19] N. Goldman, F. Gerbier, and M. Lewenstein, J. Phys. B: At. Mol. Opt. Phys. **46**, 134010 (2013).
[20] E. Alba, X. Fernandez-Gonzalvo, J. Mur-Petit, J. K. Pachos, and J. J. Garcia-Ripoll, Phys. Rev. Lett. **107**, 235301 (2011).
[21] N. Goldman, E. Anisimovas, F. Gerbier, P. Öhberg, I. B. Spielman, and G. Juzeliūnas, New J. Phys. **15**, 013025 (2013).
[22] F. Gerbier and J. Dalibard, New J. Phys. **12**, 033007 (2010).
[23] Z. W. Barber, C. W. Hoyt, C. W. Oates, L. Hollberg, A. V. Taichenachev, and V. I. Yudin, Phys. Rev. Lett. **96**, 083002 (2006).
[24] N. D. Lemke, A. D. Ludlow, Z. W. Barber, T. M. Fortier, S. A. Diddams, Y. Jiang, S. R. Jefferts, T. P. Heavner, T. E. Parker, and C. W. Oates, Phys. Rev. Lett. **103**, 063001 (2009).
[25] W. Yi, A. J. Daley, G. Pupillo, and P. Zoller, New J. Phys. **10**, 073015 (2008).
[26] A. V. Gorshkov, M. Hermele, V. Gurarie, C. Xu, P. S. Julienne, J. Ye, P. Zoller, E. Demler, M. D. Lukin, and A. M. Rey, Nat. Phys. **6**, 289 (2010).
[27] S. G. Porsev, A. Derevianko, and E. N. Fortson, Phys. Rev. A **69**, 021403 (2004).

[28] R. Grimm, M. Weidemüller, and Y. B. Ovchinnikov, Adv. At. Mol. Opt. Phys. **42**, 95 (2000).

[29] V. A. Dzuba and A. Derevianko, J. Phys. B: At. Mol. Opt. Phys. **43**, 074011 (2010).

[30] G. Grynberg and C. Robilliard, Phys. Rep. **355**, 335 (2001).

[31] C. Becker, P. Soltan-Panahi, J. Kronjäger, S. Dörscher, K. Bongs, and K. Sengstock, New J. Phys. **12**, 065025 (2010); P. Soltan-Panahi *et al.*, Nat. Phys. **7**, 434 (2011); P. Windpassinger and K. Sengstock, Rep. Prog. Phys. **76**, 086401 (2013).

[32] R. Walters, G. Cotugno, T. H. Johnson, S. R. Clark, and D. Jaksch, Phys. Rev. A **87**, 043613 (2013). See also the project's web page at http://ccpforge.cse.rl.ac.uk/gf/project/mlgws/ for further information.

[33] N. Marzari, A. Mostofi, J. Yates, I. Souza, and D. Vanderbilt, Rev. Mod. Phys. **84**, 1419 (2012).

[34] K. L. Lee, B. Grémaud, R. Han, B.-G. Englert, and C. Miniatura, Phys. Rev. A **80**, 043411 (2009).

[35] A. H. Castro Neto, F. Guinea, N. M. R. Peres, K. S. Novoselov, and A. K. Geim, Rev. Mod. Phys. **81**, 109 (2009).

[36] D. Jaksch and P. Zoller, New J. Phys. **5**, 56 (2003).

[37] T. Fukui, Y. Hatsugai, and H. Suzuki, J. Phys. Soc. Jpn. **74**, 1674 (2005). The Chern-number-calculation method introduced in this reference can be summarized as follows. Every link connecting two sites of the discretized Brillouin zone, say $\boldsymbol{k}_1$ and $\boldsymbol{k}_2$, is associated with a link operator $U_{12} = \langle u(\boldsymbol{k}_1)|u(\boldsymbol{k}_2)\rangle/\mathcal{N}$, where $|u(\boldsymbol{k})\rangle$ denotes the eigenstate of the band $E(\boldsymbol{k})$ of interest, and where $\mathcal{N}$ is a normalization factor. In lattice gauge theory, the curvature $\mathcal{F}(\boldsymbol{k})$ is obtained by performing a loop product $\mathcal{F}(\boldsymbol{k}_1) = \ln U_{12}U_{23}U_{34}U_{41}$ around a unit plaquette. The Berry's curvature can thus be evaluated at each point $\boldsymbol{k}_j$ through a direct diagonalization of the Hamiltonian. The Chern number is then obtained by summing over the discretized Brillouin zone: $\nu = (1/2\pi i)\sum_j \mathcal{F}(\boldsymbol{k}_j)$.

[38] H. M. Price and N. R. Cooper, Phys. Rev. A **85**, 033620 (2012).

[39] D. A. Abanin, T. Kitagawa, I. Bloch, and E. Demler, Phys. Rev. Lett. **110**, 165304 (2013).

[40] A. Dauphin and N. Goldman, Phys. Rev. Lett. **111**, 135302 (2013).

[41] X.-J. Liu, K. T. Law, T. K. Ng, and P. A. Lee, Phys. Rev. Lett. **111**, 120402 (2013).

[42] N. Goldman, J. Dalibard, A. Dauphin, F. Gerbier, M. Lewenstein, P. Zoller, and I. B. Spielman, Proc. Natl. Acad. Sci. U.S.A. **110**, 6736 (2013).

[43] N. Goldman, J. Beugnon, and F. Gerbier, Phys. Rev. Lett. **108**, 255303 (2012).

[44] V. W. Scarola and S. Das Sarma, Phys. Rev. Lett. **98**, 210403 (2007).

[45] D. R. Hofstadter, Phys. Rev. B **14**, 2239 (1976).

II

Three-level Haldane-like model on a dice optical lattice

T. Andrijauskas, E. Anisimovas, M. Račiūnas, A. Mekys, V. Kudriašov, I. B. Spielman, and G. Juzeliūnas

Physical Review A **92**, 033617 (2015).

as the work contains at least 10% new material not covered by APS's copyright and does not contain more than 50% of the text (including equations) of the original article. The APS will extend the author of a “derived work” the right to all papers published in APS journals.

As the author (or the author's employer) of an APS-published article, may I use copies of part or all of my article in the classroom?

Yes, the author or his/her employer may use all or part of the APS-prepared version for educational purposes without requesting permission from the APS as long as the appropriate bibliographic citation is included.

As the author of an APS-published article, may I use figures, tables, graphs, etc. in future publications?

Yes, as the author you have the right to use figures, tables, graphs, etc. in subsequent publications using files prepared and formatted by you or the APS-prepared versions. The appropriate bibliographic citation must be included.

As the author of an APS-published article, may I include my article or a portion of my article in my thesis or dissertation?

Yes, the author has the right to use the article or a portion of the article in a thesis or dissertation without requesting permission from APS, provided the bibliographic citation and the APS copyright credit line are given on the appropriate pages.

As the author of an APS-published article, may I give permission to a colleague or third party to republish all or part of the article in a print publication?

Yes, as the author you may grant permission to third parties to republish print versions of the article provided the APS-published version (e.g., the PDF from the online journal, or a copy of the article from the print journal) is not used for this purpose. The article may not be published in another journal, and the third party may not charge a fee. The appropriate bibliographic citation and notice of the APS copyright must be included.

As the author of an APS-published article, may I give permission to a colleague or third party to republish all or part of the APS-published version in an online journal, book, database compilation, etc.?

No, an author may not grant permission in this case. To request permission to republish APS-copyrighted material, please refer to the “Reuse & Permissions” link that can be found on each APS article page.

As the author of an APS-published article, may I provide a PDF of my paper to a colleague or third party?

The author is permitted to provide, for research purposes and as long as a fee is not charged, a PDF copy of his/her article using either the APS-prepared version or the author prepared version.

As a third party (not an author), may I republish an article or portion of an article published by APS?

PHYSICAL REVIEW A **92**, 033617 (2015)

Three-level Haldane-like model on a dice optical lattice

T. Andrijauskas,[1] E. Anisimovas,[1] M. Račiūnas,[1] A. Mekys,[1] V. Kudriašov,[1] I. B. Spielman,[2,3] and G. Juzeliūnas[1]
[1]*Institute of Theoretical Physics and Astronomy, Vilnius University, A. Goštauto 12, Vilnius LT-01108, Lithuania*
[2]*Joint Quantum Institute, University of Maryland, College Park, Maryland 20742-4111, 20742, USA*
[3]*National Institute of Standards and Technology, Gaithersburg, Maryland 20899, USA*
(Received 5 May 2015; published 21 September 2015)

We consider ultracold atoms in a two-dimensional optical lattice of the dice geometry in a tight-binding regime. The atoms experience a laser-assisted tunneling between the nearest neighbor sites of the dice lattice accompanied by the momentum recoil. This allows one to engineer staggered synthetic magnetic fluxes over plaquettes, and thus pave a way towards the realization of topologically nontrivial band structures. In such a lattice the real-valued next-nearest neighbor transitions are not needed to reach a topological regime. Yet, such transitions can increase a variety of the obtained topological phases. The dice lattice represents a triangular Bravais lattice with a three-site basis consisting of a hub site connected to two rim sites. As a consequence, the dice lattice supports three energy bands. From this point of view, our model can be interpreted as a generalization of the paradigmatic Haldane model which is reproduced if one of the two rim sublattices is eliminated. We demonstrate that the proposed upgrade of the Haldane model creates a significant added value, including an easy access to topological semimetal phases relying only on the nearest neighbor coupling, as well as enhanced topological band structures featuring Chern numbers higher than one leading to physics beyond the usual quantum Hall effect. The numerical investigation is supported and complemented by an analytical scheme based on the study of singularities in the Berry connection.

DOI: 10.1103/PhysRevA.92.033617 PACS number(s): 67.85.−d, 37.10.Jk, 73.43.−f

I. INTRODUCTION

Optical lattices have firmly established themselves as a modern and versatile tool to study fundamental physics in a clean environment with various physical parameters being under experimentalist's control and often extensively tunable [1–3]. One is typically interested in implementing a paradigmatic Hamiltonian that clearly demonstrates a particular phenomenon or an effect. A list of recent successes features, to mention just a few examples, realization of the Harper-Hofstadter [4–6] and Haldane models [7], direct observation and control of the Dirac points [8], creation of artificial magnetic fluxes via lattice shaking [9] and reproduction of models of magnetism [10], and engineering of a spin-dependent optical lattice resulting from a combination of Raman coupling and radio-frequency magnetic fields [11].

In particular, access to topological band structures is of enormous interest [12–14]. The presence of the topological order is signaled by a nonzero Chern index reflecting a nonvanishing integral of the Berry curvature over the entire two-dimensional Brillouin zone. A topological band supported by a spatially periodic optical lattice acts as a model of a Landau level. The unique band structure consisting of a ladder of Landau levels defines an apparent insulator with current-carrying edge states and has traditionally been associated with the presence of an external magnetic field. In cold-atom setups, however, the topological character becomes an intrinsic property of the band and is not necessarily associated with the presence of a physical magnetic field [14,15]. Synthetic fluxes piercing the lattice plaquettes may be imparted by the lattice shaking [9,14,16–18], laser-assisted tunneling [14,19–21] or using synthetic dimensions [22].

Many of the breakthroughs mentioned in the introductory paragraph can be classified as mimicking or reproduction of phenomena known from the condensed matter physics. However, significant contributions from cold-atom systems to *extending* the known physics should also be recognized [1,2,14,21,23]. Perhaps the most obvious examples relate to the construction of topological bands with the values of the Chern index greater than one [24–30], which is a central topic of the present paper. The properties of such a band is not a direct sum of the properties of several Landau levels, and reach beyond the traditional (integer or fractional) quantum Hall physics [31,32].

Indeed, the study of bands with higher Chern numbers has been particularly relevant in connection to the so-called fractional Chern insulators [33–35]. Although many-body interactions, which play the central role in these studies, are beyond the scope of the present contribution, we stress that many insights into the nature of the fractional topological states were obtained from somewhat artificial lattice constructs often involving many layers [25] or distant-neighbor hoppings [26,27,36]. Ongoing efforts [37–40] are also based on the Harper-Hofstadter model that in principle supports subbands of arbitrarily high Chern numbers. Here, one also has to defy rather stringent requirements posed by large magnetic unit cells, low particle densities, and a large number of subbands implying small topological band gaps [40]. In the present paper we focus on exploring the potential offered by relatively *simple* and thus more realistic lattice models. We construct a generalization of the Haldane model [41–45] by coupling three rather than two triangular sublattices. In this way, the honeycomb lattice featured in the Haldane model is upgraded to the dice lattice [46–51] which supports a three-band model with a clean access to interesting topological configurations, such as bands characterized by the Chern number equal to 2. In the dice-lattice model it is just a complex valued nearest-neighbor (NN) coupling that is sufficient to generate a *staggered* synthetic magnetic flux and reach nontrivial setups

including a topological semimetal phase. On the other hand, for spatially periodic hexagonal lattices, nontrivial phases cannot be reached just by having the complex-valued nearest-neighbor coupling, one should add a real-valued next-neighbor coupling [42–44]. Note that the dice lattice affected by a *uniform* magnetic flux was used to demonstrate a novel and intriguing mechanism of localization of wave packets in Aharonov-Bohm cages [52–54].

The paper is structured as follows. In Sec. II, we introduce the lattice geometry and derive the 3×3 momentum-space Hamiltonian encapsulating the physics. Then, Sec. III describes the obtained results starting from phases obtained in the presence of NN couplings alone and proceeding to more complex configurations requiring next-nearest neighbor (NNN) transitions. We conclude with a brief summarizing Sec. V.

II. THE MODEL

A. Lattice geometry

We consider a dice lattice, which consists of three triangular sublattices. One of them is called a *hub* sublattice. It is coupled to other two *rim* sublattices, that in turn are not coupled with each other. Let us denote the hub sublattice by B and the rim sublattice by A and C. The vectors that connect the nearest lattice sites are (Fig. 1)

$$\boldsymbol{\delta}_1 = \frac{a}{2}(\boldsymbol{e}_x + \sqrt{3}\boldsymbol{e}_y), \quad \boldsymbol{\delta}_2 = \frac{a}{2}(\boldsymbol{e}_x - \sqrt{3}\boldsymbol{e}_y), \quad \boldsymbol{\delta}_3 = -a\boldsymbol{e}_x, \tag{1}$$

where a is the distance between two such sites. The elementary lattice vectors,

$$\boldsymbol{a}_1 = a(3\boldsymbol{e}_x + \sqrt{3}\boldsymbol{e}_y)/2, \quad \boldsymbol{a}_2 = a(3\boldsymbol{e}_x - \sqrt{3}\boldsymbol{e}_y)/2, \tag{2}$$

define a rhombic elementary cell. The set of lattice vectors $\boldsymbol{r}_{\boldsymbol{n}} = n_1\boldsymbol{a}_1 + n_2\boldsymbol{a}_2$ (with integers n_1 and n_2) span the hub sublattice B (Bravais lattice). The two rim sublattices are defined in the following way. The first rim sublattice A is shifted from the hub sublattice B by the vector $\boldsymbol{\delta}_1$ in such a way that sublattices A and B alone make a honeycomb lattice.

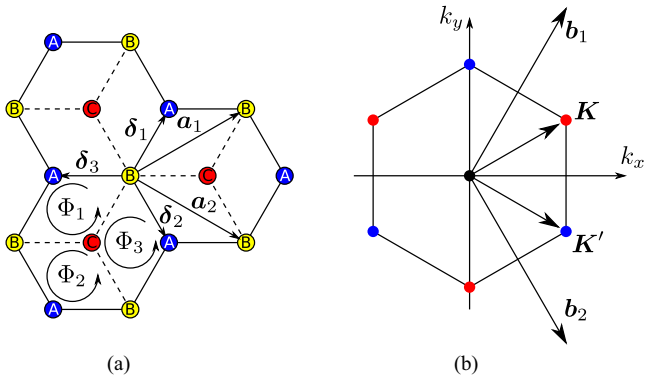

FIG. 1. (Color online) (a) Dice lattice. The blue, green, and red sites correspond to three different triangular sublattices A, B, and C. Solid lines show couplings between the sites A and B. Dashed lines show couplings between the sites B and C. The primitive lattice vectors are $\boldsymbol{a}_1$ and $\boldsymbol{a}_2$. Nearest sites are connected with the vectors $\boldsymbol{\delta}_1$, $\boldsymbol{\delta}_2$, and $\boldsymbol{\delta}_3$. (b) Hexagonal first Brillouin zone of the reciprocal lattice defined by the primitive reciprocal lattice vectors $\boldsymbol{b}_1$ and $\boldsymbol{b}_2$. Two inequivalent corners are at the points $\boldsymbol{K}$ (red) and $\boldsymbol{K}'$ (blue).

The second rim sublattice C is shifted to the opposite direction by $-\boldsymbol{\delta}_1$ (see Fig. 1). Let us introduce a set of vectors, that span all the lattice sites:

$$\boldsymbol{r}_{\boldsymbol{n},s} = \boldsymbol{r}_{\boldsymbol{n}} + s\boldsymbol{\delta}_1. \tag{3}$$

Here the index $s = 0, \pm 1$ labels the three sublattices. The sites of the hub sublattice ($s = 0$) coincide with the lattice vectors: $\boldsymbol{r}_{\boldsymbol{n},0} = \boldsymbol{r}_{\boldsymbol{n}}$. The sites of the rim sublattices A and C shifted by $\pm\boldsymbol{\delta}_1$, i.e., $\boldsymbol{r}_{\boldsymbol{n},+1} = \boldsymbol{r}_{\boldsymbol{n}} + \boldsymbol{\delta}_1$ and $\boldsymbol{r}_{\boldsymbol{n},-1} = \boldsymbol{r}_{\boldsymbol{n}} - \boldsymbol{\delta}_1$.

It is convenient to introduce an additional lattice vector $\boldsymbol{a}_3 = \boldsymbol{a}_1 - \boldsymbol{a}_2$. The set of the three lattice vectors $\boldsymbol{a}_i$ ($i = 1,2,3$) together with the opposite vectors $-\boldsymbol{a}_i$ connect all next-nearest lattice sites, and can be related to $\boldsymbol{\delta}_i$ as $\boldsymbol{a}_1 = \boldsymbol{\delta}_1 - \boldsymbol{\delta}_3$, $\boldsymbol{a}_2 = \boldsymbol{\delta}_2 - \boldsymbol{\delta}_3$, and $\boldsymbol{a}_3 = \boldsymbol{\delta}_1 - \boldsymbol{\delta}_2$.

The basic reciprocal lattice vectors,

$$\boldsymbol{b}_1 = \frac{2\pi}{3a}(\boldsymbol{e}_x + \sqrt{3}\boldsymbol{e}_y), \quad \boldsymbol{b}_2 = \frac{2\pi}{3a}(\boldsymbol{e}_x - \sqrt{3}\boldsymbol{e}_y), \tag{4}$$

are orthogonal to the lattice vectors, $\boldsymbol{a}_i \cdot \boldsymbol{a}_j = 2\pi\delta_{ij}$, $i,j = 1,2$. The first Brillouin zone is hexagonal with two inequivalent corners $\boldsymbol{K}$ and $\boldsymbol{K}'$ positioned at $\boldsymbol{K} = (2\boldsymbol{b}_1 + \boldsymbol{b}_2)/3$ and $\boldsymbol{K}' = (\boldsymbol{b}_1 + 2\boldsymbol{b}_2)/3$. In terms of the Cartesian coordinates these points are given by

$$\boldsymbol{K} = \frac{2\pi}{9a}(3\boldsymbol{e}_x + \sqrt{3}\boldsymbol{e}_y), \quad \boldsymbol{K}' = \frac{2\pi}{9a}(3\boldsymbol{e}_x - \sqrt{3}\boldsymbol{e}_y), \tag{5}$$

as one can see in Fig. 1.

B. Tight-binding model

We shall make use of the tight-binding model in which the single-particle states $|\boldsymbol{r}_{\boldsymbol{n},s}\rangle$ represent the Wannier-type wave functions localized at each lattice site $\boldsymbol{r}_{\boldsymbol{n},s}$, with $s = 0, \pm 1$ being the sublattice index. In the language of the second quantization these single-particle states read $|\boldsymbol{r}_{\boldsymbol{n},s}\rangle = c^\dagger(\boldsymbol{r}_{\boldsymbol{n},s})|\text{vac}\rangle$, where $|\text{vac}\rangle$ is the Fock vacuum state, $c^\dagger(\boldsymbol{r}_{\boldsymbol{n},s})$ and $c(\boldsymbol{r}_{\boldsymbol{n},s})$ being the creation and annihilation operators of an atom in the corresponding localized state.

The full Hamiltonian of the system consist of three terms,

$$H = H_1 + H_2 + H_3. \tag{6}$$

The first term H_1 describes the laser-assisted tunneling [14,18–21,42,44,55] of atoms between the sites of the hub sublattice B ($s = 0$) and its nearest neighboring sites that belong to the rim sublattices A and C with $s = \pm 1$:

$$H_1 = \sum_{\boldsymbol{n}} \sum_{s=\pm 1} J^{(s)} \sum_{i=1}^{3} e^{i p_s \cdot (\boldsymbol{r}_{\boldsymbol{n}} + s\boldsymbol{\delta}_i/2)} c^\dagger(\boldsymbol{r}_{\boldsymbol{n}}) c(\boldsymbol{r}_{\boldsymbol{n}} + s\boldsymbol{\delta}_i) + \text{H.c.}, \tag{7}$$

where $J^{(s)}$ are the coupling amplitudes. Such generalization of dice optical lattice with two different hopping parameters $J^{(+)}$ and $J^{(-)}$ is already discussed in Ref. [56]. The laser-assisted tunneling is accompanied by the transfer of the recoil momentum $\boldsymbol{p}_s$ with $s = \pm 1$, to be labeled simply by $\boldsymbol{p}_\pm \equiv \boldsymbol{p}_{\pm 1}$. In the present situation $\boldsymbol{p}_+$ can generally differ from $\boldsymbol{p}_-$ because the transitions between the different sublattices can be induced by different lasers. Note that the nearest neighbor hopping alone is sufficient to generate fluxes through rhombic plaquettes,

$$\Phi_i = \pm(\boldsymbol{p}_+ - \boldsymbol{p}_-) \cdot \boldsymbol{a}_i/2, \tag{8}$$

with $\boldsymbol{a}_i$ representing a diagonal vector of the plaquette in question. Yet the magnetic flux over the whole hexagonal plaquette remains zero.

The second term H_2 takes into account the tunneling between the next-nearest neighboring sites belonging to the same sublattice with $s = 0,\pm1$:

$$H_2 = \sum_{\boldsymbol{n}} \sum_{s=0,\pm1} J_2^{(s)} \sum_{i=1}^{3} c^\dagger(\boldsymbol{r}_{\boldsymbol{n},s}) c(\boldsymbol{r}_{\boldsymbol{n},s} + \boldsymbol{a}_i) + \text{H.c.} \quad (9)$$

This term describes the usual (not laser-assisted) hopping transitions between nearest sites in each of the three triangular sublattices, and $J_2^{(s)}$ with $s = 0,\pm1$ are the corresponding matrix elements for the tunneling between the atoms belonging to the sth sublattice.

The third term H_3 describes the energy mismatch for the particles populating the different sublattices:

$$H_3 = \sum_{\boldsymbol{n}} \sum_{s=0,\pm1} \varepsilon_s c^\dagger(\boldsymbol{r}_{\boldsymbol{n},s}) c(\boldsymbol{r}_{\boldsymbol{n},s}). \quad (10)$$

The on-site energies ε_s are the diagonal matrix elements of the Hamiltonian in the basis of the Wannier states. Without a loss of generality we can take the on-site energy of the hub sublattice B to be zero: $\varepsilon_0 = 0$. The on-site energies of other *rim* sublattices are to be labeled as $\varepsilon_{\pm1} \equiv \varepsilon_\pm$.

Since the first term H_1 involves complex phase factors that depend on the elementary cell number $\boldsymbol{n}$, the full Hamiltonian H is not translationally invariant. Yet, we will transform the annihilation operators according to $c(\boldsymbol{r}_{\boldsymbol{n},0}) \to c(\boldsymbol{r}_{\boldsymbol{n},0})$ and $c(\boldsymbol{r}_{\boldsymbol{n},s}) \to c(\boldsymbol{r}_{\boldsymbol{n},s}) \exp(-\mathrm{i}\boldsymbol{p}_s \cdot \boldsymbol{r}_{\boldsymbol{n}})$ with $s = \pm1$, and perform the corresponding transformation for the creation operators. This gauge transformation makes the full Hamiltonian (6) translationally invariant.

Transition to the reciprocal space is carried out by introducing new operators,

$$\begin{aligned} c_s(\boldsymbol{k}) &= \frac{1}{\sqrt{N}} \sum_{\boldsymbol{k}} c(\boldsymbol{r}_{\boldsymbol{n},s}) e^{-i\boldsymbol{k}\cdot\boldsymbol{r}_{\boldsymbol{n}}}, \\ c(\boldsymbol{r}_{\boldsymbol{n},s}) &= \frac{1}{\sqrt{N}} \sum_{\boldsymbol{k}} c_s(\boldsymbol{k}) e^{i\boldsymbol{k}\cdot\boldsymbol{r}_{\boldsymbol{n}}}, \end{aligned} \quad (11)$$

together with the Hermitian conjugated creation operators $c_s^\dagger(\boldsymbol{k})$. Here N is a number of elementary cells in the quantization area, and the vectors $\boldsymbol{r}_{\boldsymbol{n}} = \boldsymbol{r}_{\boldsymbol{n},0}$ (defined in Sec. II A) are located at the sites of the hub lattice. In terms of the new operators the Hamiltonian (6) splits into its $\boldsymbol{k}$ components:

$$H = \sum_{\boldsymbol{k}} H(\boldsymbol{k}), \quad H(\boldsymbol{k}) = [c_+^\dagger(\boldsymbol{k}) \quad c_0^\dagger(\boldsymbol{k}) \quad c_-^\dagger(\boldsymbol{k})] \mathcal{H}(\boldsymbol{k}) \begin{bmatrix} c_+(\boldsymbol{k}) \\ c_0(\boldsymbol{k}) \\ c_-(\boldsymbol{k}) \end{bmatrix}, \quad (12)$$

where $\mathcal{H}(\boldsymbol{k})$ is a 3×3 matrix:

$$\mathcal{H}(\boldsymbol{k}) = \begin{bmatrix} \varepsilon_+ + 2J_2^{(+)} f(\boldsymbol{k} - \boldsymbol{p}_+) & J^{(+)} g(\boldsymbol{k} - \boldsymbol{p}_+/2) & 0 \\ J^{(+)} g^*(\boldsymbol{k} - \boldsymbol{p}_+/2) & 2J_2^{(0)} f(\boldsymbol{k}) & J^{(-)} g(\boldsymbol{k} - \boldsymbol{p}_-/2) \\ 0 & J^{(-)} g^*(\boldsymbol{k} - \boldsymbol{p}_-/2) & \varepsilon_- + 2J_2^{(-)} f(\boldsymbol{k} - \boldsymbol{p}_-) \end{bmatrix}. \quad (13)$$

Here we also added an extra phase factor to the transformed operators $c_s(\boldsymbol{k}) \to c_s(\boldsymbol{k}) e^{i\boldsymbol{p}_s \cdot s\boldsymbol{\delta}_1/2}$. The functions,

$$f(\boldsymbol{k}) = \sum_{i=1}^{3} \cos(\boldsymbol{k} \cdot \boldsymbol{a}_i), \quad g(\boldsymbol{k}) = e^{i\boldsymbol{k}\cdot\boldsymbol{\delta}_1} \sum_{i=1}^{3} e^{-i\boldsymbol{k}\cdot\boldsymbol{\delta}_i}, \quad (14)$$

entering Eq. (13) are translationally symmetric in the reciprocal space,

$$f(\boldsymbol{k} + \boldsymbol{G}) = f(\boldsymbol{k}), \quad g(\boldsymbol{k} + \boldsymbol{G}) = g(\boldsymbol{k}), \quad (15)$$

where $\boldsymbol{G} = n_1\boldsymbol{b}_1 + n_2\boldsymbol{b}_2$ is a reciprocal lattice vector, n_1 and n_2 being integers. Consequently the matrix Hamiltonian $\mathcal{H}(\boldsymbol{k})$ is also fully translationally invariant in the reciprocal space $\mathcal{H}(\boldsymbol{k}) = \mathcal{H}(\boldsymbol{k} + \mathbf{G})$. Note that Berry curvature in general depends on the choice of Fourier transformation (11), while the corresponding Chern number does not [57,58]. Furthermore, the functions $f(\boldsymbol{k})$ and $g(\boldsymbol{k})$ obey the following reflection properties,

$$f(\boldsymbol{k}) = f(-\boldsymbol{k}), \quad g(\boldsymbol{k}) = g^*(-\boldsymbol{k}). \quad (16)$$

All this helps to consider various symmetries of the matrix Hamiltonian (13).

III. PHASES OF NONINTERACTING FERMIONS

A. Chern numbers and symmetries of the system

Since the momentum-space Hamiltonian (13) represents a three-level system, there are three energy bands characterized by energies $E_n(\boldsymbol{k})$, with $n = 1,2,3$. Each energy band has a Chern number c_n to be defined in Eq. (17). We also identify two possible band gaps. The first band gap Δ_{12} measures the energy between the first ($n = 1$) and second ($n = 2$) bands, the second band gap Δ_{23} corresponding to the energy between the second ($n = 2$) and the third ($n = 3$) bands.

The Chern number c_n for the nth band is defined in terms of a surface integral of a Berry curvature over the first Brillouin zone (FBZ) [14,59]:

$$c_n = -\frac{1}{2\pi} \int_{\text{FBZ}} d^2k \, F_n(\boldsymbol{k}). \quad (17)$$

The Berry curvature $F_n(\boldsymbol{k})$ can be expressed in terms of the eigenvectors $|u_{n,k}\rangle$ of the reciprocal space Hamiltonian (13)

as

$$F_n(\boldsymbol{k}) = i\left(\frac{\partial}{\partial k_x}\langle u_{n,\boldsymbol{k}}|\right)\left(\frac{\partial}{\partial k_y}|u_{n,\boldsymbol{k}}\rangle\right) - i\left(\frac{\partial}{\partial k_y}\langle u_{n,\boldsymbol{k}}|\right)\left(\frac{\partial}{\partial k_x}|u_{n,\boldsymbol{k}}\rangle\right). \quad (18)$$

It is well defined as long the eigenenergies $E_n(\boldsymbol{k})$ are not degenerate for any fixed value of $\boldsymbol{k}$. Therefore the Chern number c_n can be ascribed to the nth band if the latter does not touch any other bands. If the Fermi energy is situated in a band gap, the Chern number is directly related to Hall conductivity due to chiral edge states of the occupied bands [60] via $\sigma_{xy} = -e^2 c_n/\hbar$ [61–63]. For numerical calculation we make use of the discretized version of the Berry curvature (18) described in Ref. [64].

For both *rim* sublattices A and C, we set on-site energies of to be symmetrically shifted away from the zero point $\varepsilon_+ = -\varepsilon_- = \varepsilon$. We also take the tunneling amplitudes to be equal $J^{(+)} = J^{(-)} = J$, $J_2^{(+)} = J_2^{(0)} = J_2^{(-)} = J_2$ and assume the recoil momenta to be opposite $\boldsymbol{p}_+ = -\boldsymbol{p}_- = \boldsymbol{p}$ for both *rim* sublattices A and C. The choice of opposite recoil momenta ensures the maximum flux, because the magnetic flux through a rhombic plaquette Φ_i given by Eq. (8) is proportional to the difference of these vectors. Under these conditions, the matrix representation of the $\boldsymbol{k}$-space Hamiltonian becomes

$$\mathcal{H}(\boldsymbol{k}) = \begin{bmatrix} \varepsilon + 2J_2 f(\boldsymbol{k}-\boldsymbol{p}) & Jg(\boldsymbol{k}-\boldsymbol{p}/2) & 0 \\ Jg^*(\boldsymbol{k}-\boldsymbol{p}/2) & 2J_2 f(\boldsymbol{k}) & Jg(\boldsymbol{k}+\boldsymbol{p}/2) \\ 0 & Jg^*(\boldsymbol{k}+\boldsymbol{p}/2) & -\varepsilon + 2J_2 f(\boldsymbol{k}+\boldsymbol{p}) \end{bmatrix}. \quad (19)$$

This form of the Hamiltonian exhibits some symmetries. The first symmetry involves inversion of the on-site energies $\varepsilon \to -\varepsilon$ followed by the unitary transformation that changes the first row with the third one (i.e., interchanges the *rim* sublattices A and C), as well as the momentum inversion $\boldsymbol{k} \to -\boldsymbol{k}$. Using the reflection properties of the functions f and g given by Eq. (16), one arrives at the same Hamiltonian (19). The second symmetry is $J \to -J$, which is a simple gauge transformation. Using these two symmetries we see that the change $J_2 \to -J_2$ gives $\mathcal{H}(\boldsymbol{k}) \to -\mathcal{H}(\boldsymbol{k})$. To sum up, all the three mentioned symmetries are $(\varepsilon \to -\varepsilon, \mathcal{H} \to \mathcal{H})$, $(J \to -J, \mathcal{H} \to \mathcal{H})$, and $(J_2 \to -J_2, \mathcal{H} \to -\mathcal{H})$.

B. Numerical analysis

In this subsection, we numerically study the Chern phases of noninteracting fermions. In order to present dependence of the Chern number on the parameters ε, J, J_2, and $\boldsymbol{p}$ we adopt a similar presentation of the phase diagram scheme as in Ref. [44]. We choose the energy unit to be the nearest-neighbor tunneling amplitude J. For the recoil momentum $\boldsymbol{p}$, we express the p_x component in the units of K_x and the component p_y in the units of K_y, where $\boldsymbol{K}$ is one of the FBZ corners, defined in Eq. (5). In all the phase diagrams we present the dependence of the Chern number $c_n = c_n(p_x, p_y)$ on the components of the recoil momentum $\boldsymbol{p}$ using different colors for each possible values of c_n. The areas corresponding to a topologically trivial phase with a zero Chern number are shown in green ($c_n = 0$). On the other hand, the areas corresponding to nontrivial Chern phases are shown in yellow ($c_n = 1$), red ($c_n = 2$), cyan ($c_n = -1$), and blue ($c_n = -2$). Additionally we display Chern number labels in all the presented phase diagrams.

First we characterize topological properties of the band structure if there is no next-nearest neighbor coupling (J_2=0). In Fig. 2 we show the Chern number phase diagrams for $\varepsilon = J$. One can identify regions where the Chern numbers are $\{c_1, c_2, c_3\} = \{0,0,0\}$, $\{-1,2,-1\}$, and $\{1,-2,1\}$. In the first type of the regions (green color) we have topologically trivial regions. In other regions there are nonzero Chern numbers with band gaps $\Delta_{12} = \Delta_{23} = 0$. Analysis of the band structure in these regions shows that the bands do not overlap and touch indirectly. Thus by filling the first one or the first two bands we arrive at semimetallic phase with nonzero Hall conductivity. The typical spectrum of such a nontrivial semimetallic case is presented in Fig. 6. The size of the nontrivial regions in the $\boldsymbol{p}$ plane depends on the mismatch ε of the on-site energies of A and C sublattices. By increasing ε from zero these regions immediately appear around the points $\boldsymbol{p} = \boldsymbol{K}$ and become larger in size. For about $\varepsilon \approx J$ these regions have the largest area as presented in Fig. 2 for $\varepsilon = J$. For even larger values of ε the nontrivial regions shrink back to the points $\boldsymbol{K}$ and finally we are left only with the trivial phase {0,0,0} everywhere. The analytical treatment, presented in Sec. IV gives the value of

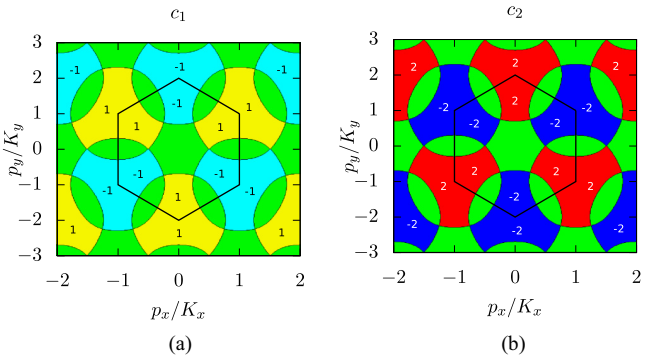

FIG. 2. (Color online) Chern number dependence on the recoil momentum $\boldsymbol{p}$ in the case $\varepsilon = J$ and $J_2 = 0$. (a) The phase diagram of the lowest band Chern number c_1. (b) The corresponding phase diagram for the middle band. Since the sum of Chern numbers over all three bands is zero, the third band gives the same phase diagram as the first one ($c_1 = c_3$). The green regions correspond to the Chern number zero. The yellow, red, cyan, and blue regions correspond to the Chern numbers 1, 2, −1, and −2, respectively. Nonzero Chern numbers are also displayed as labels. The hexagon represents the FBZ in the $\boldsymbol{p}$ plane.

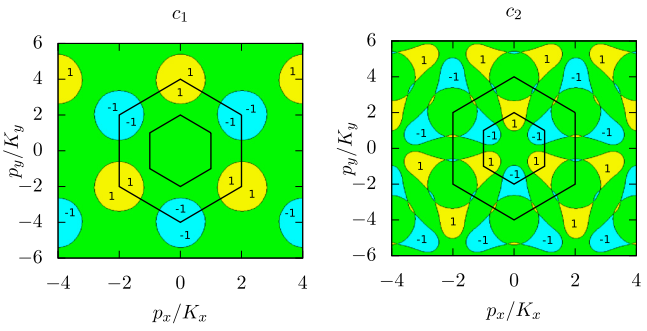

FIG. 3. (Color online) Chern number dependence on the recoil momentum $\boldsymbol{p}$ in the case $\varepsilon = 2J$ and $J_2 = 0.3J$. (a) The Chern number c_1 of the lowest band; (b) the Chern number c_2 of the middle band. For the third band (not shown here) we have $c_3 = -(c_1 + c_2)$. The green, yellow, red, cyan, and blue regions correspond to the Chern numbers 0, 1, 2, -1, and -2, respectively. Nonzero Chern numbers are also displayed as labels. A smaller hexagon shows the FBZ corresponding to the case $J_2 = 0$. Since the introduction of nonzero J_2 changes the periodicity of the $\boldsymbol{p}$ dependence, we also show a bigger hexagon, which is now the FBZ in the $\boldsymbol{p}$ plane.

$\varepsilon = \frac{3\sqrt{2}}{2}J$ for which the semimetal regions completely disappear. For $J_2 = 0$ there are no other types of phases than the trivial and semimetallic discussed above. Nonzero band gaps appear only in the regions of trivial phase.

For the case $J_2 = 0$, the change $\boldsymbol{p} \to \boldsymbol{p} + \boldsymbol{G}$, where $\boldsymbol{G}$ is the reciprocal lattice vector, corresponds to a gauge transformation. Thus there is a symmetry ($\boldsymbol{p} \to \boldsymbol{p} + \boldsymbol{G}, \mathcal{H} \to \mathcal{H}$). In the phase diagram (Fig. 2) we also show the FBZ in the $\boldsymbol{p}$ plane, which is a hexagon with two inequivalent corners positioned at points $\boldsymbol{K}$ and $\boldsymbol{K}'$.

Now let us analyze effects of the nonzero next-nearest neighbor coupling. For this we set $J_2 = 0.3J$ and $\varepsilon = 2J$. The phase diagrams of the Chern numbers are presented in Fig. 3. We can see regions with the Chern numbers corresponding to trivial phases $\{0,0,0\}$ and phases $\{0,\pm1,\mp1\}$ and $\{\pm1,0,\mp1\}$. In the latter two types of regions we can find points corresponding to nonzero band gaps $\Delta_{12} > 0$ and/or $\Delta_{23} > 0$ (Fig. 4). This shows that there exist topological Chern insulating phases. For example, at the point $\boldsymbol{p} = \boldsymbol{K}$, we

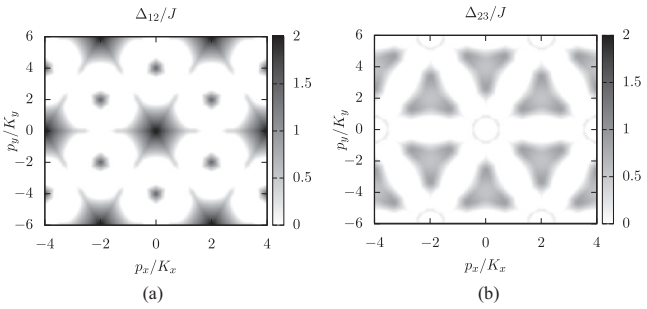

FIG. 4. Dependence of the band gap on the recoil momentum $\boldsymbol{p}$ in the case where $\varepsilon = 2J$ and $J_2 = 0.3J$. (a) The band gap Δ_{12} between the first and second bands. (b) The band gap Δ_{23} between the second and third bands.

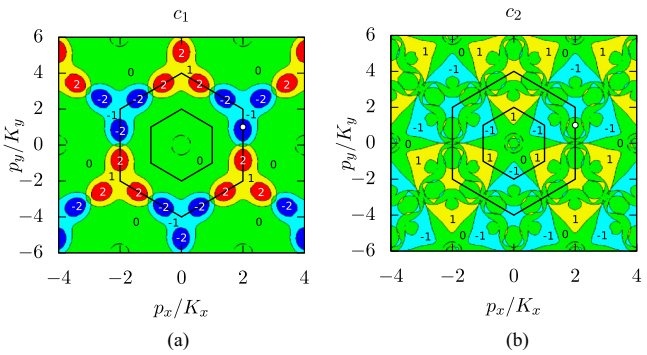

FIG. 5. (Color online) Chern number dependence on the recoil momentum in the case $\varepsilon = 0.5J$ and $J_2 = 0.5J$. (a) Chern number c_1 of the lowest band. (b) Chern number c_2 of the middle band. The color scheme and labeling are the same as in Figs. 2 and 3. The white point is $\boldsymbol{p} = (2K_x, K_y)$ where the Chern numbers are $c_1 = -2$, $c_2 = 0$, and c_3 (see the spectrum in Fig. 6).

have the Chern numbers $\{0,-1,1\}$, the band gap between the middle and highest bands being $\Delta_{23} \approx 0.26J$. Band widths in this case are about $3J$. By positioning the Fermi energy in the gap between the second and third bands one arrives at the Chern insulating phase. Another interesting point is $\boldsymbol{p} = 2\boldsymbol{K}$, which gives the Chern numbers $\{-1,0,1\}$, the band gaps $\Delta_{12} \approx 1.55J$ and $\Delta_{23} \approx 0.54J$, and the band widths of about $2J$. The bottom and top bands have nonzero Chern numbers, while it is zero for the middle band. Depending on the filling there are two types of topologically nontrivial phases. If the Fermi energy is positioned in one of the band gaps, we get a topological insulating phase. If the Fermi energy is situated within a band, the band is partially filled and supports the Chern metal phase. The discussed types of Chern number distributions over the bands are typical when J_2 is nonzero and smaller than J and ε.

In the case of nonzero NNN coupling J_2 the translation symmetry in the recoil momentum $\boldsymbol{p}$ is smaller than in the case of zero NNN couplings: One has to shift the momentum by $2\boldsymbol{G}$ rather than $\boldsymbol{G}$. In the phase diagram presented in Fig. 3 we show this by extending the FBZ, which is now a bigger hexagon.

There are more types of Chern phases when the coupling J_2 is larger than in the previous discussion and comparable to the on-site energy ε. For $\varepsilon = J_2 = 0.5J$ we find insulating phases with Chern numbers $\{\pm1,\pm1,\mp2\}$ and metallic phases with Chern numbers $\{\pm2,0,\mp2\}$ (Fig. 5). For example, in the point $\boldsymbol{p} = 2\boldsymbol{K}$ we get Chern numbers $c_1 = c_2 = -1$ and $c_3 = 2$ with band gaps $\Delta_{12} \approx 0.61J$ and $\Delta_{23} \approx 0.54J$. The width of the lower two bands are around $3J$, while the band width of the highest band is about $1.5J$. Another interesting point is $\boldsymbol{p} = (2K_x, K_y)$ where the Chern numbers are $c_1 = -2$, $c_2 = 0$, and $c_3 = 2$ (white point in Fig. 5). The bulk spectrum in this point is given in Fig. 6. Note that there is a gap $\Delta_{13} \approx 1.35J$ between the lowest and highest bands. In this gap there is a middle band with a zero Chern number. By setting the Fermi energy in this gap one gets the Chern metallic phase with the Chern number $c_1 = -2$.

To summarize the numeric analysis for $J_2 \neq 0$, the typical nontrivial Chern number distributions over the

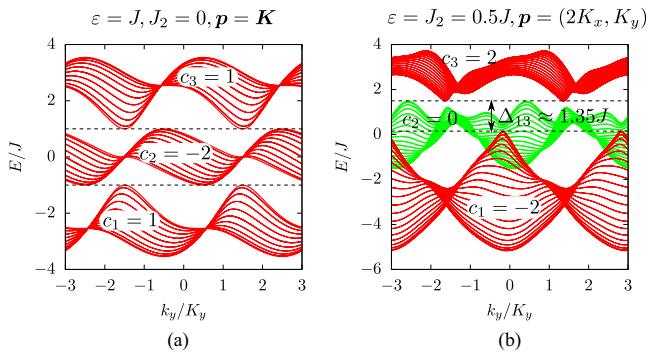

FIG. 6. (Color online) Bulk lattice spectrum projected along k_y for a number of different k_x values in the range $-K_x \leqslant k_x \leqslant K_x$. (a) The spectrum for the recoil momentum $\boldsymbol{p} = \boldsymbol{K}$ in the absence of the NNN coupling ($J_2 = 0$) and for $\varepsilon = J$ corresponding to the parameters used in Fig. 2. In that case there is no energy gap in the spectrum, but different energy bands do not directly touch each other. A topological semimetal phase is formed if the atoms fill the first energy band or the first two bands. (b) The spectrum for the recoil momentum $\boldsymbol{p} = (2K_x, K_y)$ in the case where $\varepsilon = 0.5J$ and $J_2 = 0.5J$ corresponding to the phase diagram shown in Fig. 5. Now there are two bands with nonzero Chern numbers ± 2 separated by a quasigap $\Delta_{13} \approx 1.35J$ containing a middle band with a zero Chern number.

bands are $\{0,\pm1,\mp1\}$, $\{\pm1,\mp1,0\}$, $\{\pm1,0,\mp1\}$, $\{\pm1,\pm1,\mp2\}$, $\{\pm2,\mp1,\mp1\}$, and $\{\pm2,0,\mp2\}$. One can also find the case $\{\pm1,\mp2,\pm1\}$, which is typical for $J_2 = 0$. For smaller J_2 compared to J and ε, one usually gets Chern numbers up to 1 in modulus. For larger Chern numbers (up to 2 in modulus), one needs to make the NNN-hopping J_2 be comparable to the on-site energy mismatch ε.

IV. ANALYTICAL CHERN NUMBER CALCULATION

Analytic Chern number calculation is based on integration of a Berry connection around each singularity point. The Berry connection of the nth band is defined as [14,59]

$$\boldsymbol{A}_n(\boldsymbol{k}) = i\langle u_{\boldsymbol{k},n}|\nabla_{\boldsymbol{k}}|u_{\boldsymbol{k},n}\rangle, \tag{20}$$

where $|u_{\boldsymbol{k},n}\rangle$ denotes the nth eigenvector of the matrix (13). One can express the Berry curvature (18) as the z component of the curl $\boldsymbol{B}_n = \nabla \times \boldsymbol{A}_n$, namely $F_n(\boldsymbol{k}) = \boldsymbol{e}_z \cdot \boldsymbol{B}_n$. Using the Stoke's theorem we change the integral featured in Eq. (17) over the FBZ to a contour integral around the FBZ,

$$\frac{1}{2\pi}\int_{\mathrm{FBZ}} d^2k\, F_n(\boldsymbol{k}) \rightarrow \frac{1}{2\pi}\oint_{\mathrm{FBZ}} d\boldsymbol{k}\cdot\boldsymbol{A}_n - \frac{1}{2\pi}\sum\oint_{\mathrm{singul}} d\boldsymbol{k}\cdot\boldsymbol{A}_n,$$

where the last term excludes any contribution due to unphysical gauge-dependent singular points of the Berry connection [44,65,66]. Since the $\boldsymbol{k}$-space Hamiltonian $H(\boldsymbol{k})$, given by Eqs. (13) or (19), and its eigenstates are periodic in the FBZ, $\boldsymbol{A}_n$ is also periodic. Thus the contour integral around the FBZ (the first term on the right-hand side of the above equation) is zero. Consequently the Chern number (17) can be calculated by integrating $\boldsymbol{A}_n$ around each excluded singular point [44]:

$$c_n = \frac{1}{2\pi}\sum\oint_{\mathrm{singul}} d\boldsymbol{k}\cdot\boldsymbol{A}_n, \tag{21}$$

where the sum is over all singular points in the FBZ.

Let us summarize our analytical results, details being presented in the Appendix. For the case where the recoil momentum coincides with the inverse lattice vector ($\boldsymbol{p} = \boldsymbol{G}$) we always have trivial phase with all three Chern numbers equal to zero. For the semimetal case (Fig. 2) with no NNN hopping and $\boldsymbol{p} = \boldsymbol{K}$ we find two phases, depending on the mismatch ε of the on-site energies. If $\varepsilon < \varepsilon_0 = \frac{3\sqrt{2}}{2}J$, we get Chern semimetal phase with Chern numbers $\{1,-2,1\}$. If $\varepsilon > \varepsilon_0$, we get a trivial phase $\{0,0,0\}$. In this way at larger mismatch between the on-site energies the topological phenomena disappear. This is in agreement with the numerical calculation presented in the previous section.

It is possible to apply this method for other values of the recoil momenta $\boldsymbol{p}$ and for a general nonsymmetric case with the NNN hoppings. In such calculations one needs to diagonalize the matrices of the size at most 2×2. Yet generally ordering of the eigenvalues might be a quite involved task, especially if they depend on more than one parameter.

V. CONCLUDING REMARKS

In conclusion, we have considered a two-dimensional dice lattice operating in a tight-binding regime. The laser-assisted nearest neighbor transitions are accompanied by the momentum recoils. This allows one to engineer staggered synthetic magnetic fluxes and thus facilitates realization of topologically nontrivial band structures. Real valued next-nearest neighbor transitions—although not necessary in principle to reach the topological regime—may also be present and contribute to the richness of the obtained topological phases. The considered dice lattice represents a triangular Bravais lattice with a three-site basis consisting of a hub site connected to two rim sites, providing three energy bands. Thus our model can be interpreted as a generalization of the paradigmatic Haldane model which is reproduced if one of the two rim sublattices is eliminated. We have demonstrated that the proposed upgrade of the Haldane model creates a significant added value such as (i) an easy access to topological semimetal phases relying on only the nearest neighbor coupling and (ii) enhanced topological band structures featuring Chern numbers higher than one and thus providing access to physics beyond the usual quantum Hall effect. The numerical analysis has been supported by an analytical scheme based on the study of singularities in the Berry connection.

ACKNOWLEDGMENTS

This research was supported by the Research Council of Lithuania (Grant No. MIP-082/2012). I.B.S. was partially supported by the ARO's atomtronics MURI, the AFOSR's Quantum Matter MURI, NIST, and the NSF through the PFC at the JQI.

APPENDIX: DETAILS ON ANALYTICAL CHERN NUMBER CALCULATION

1. Momentum space Hamiltonian and its eigenstates

Let us establish a general structure of the eigenstates for the matrix Hamiltonian $\mathcal{H}(\boldsymbol{k})$, Eq. (19). For this we introduce a basis of our three-level system $|s\rangle$, with $s = 0,\pm1$, and rewrite the matrix Hamiltonian in the state-vector notation as

$$\mathcal{H}(\boldsymbol{k}) = \sum_{s=0,\pm1} |s\rangle d_s(\boldsymbol{k})\langle s| + \sum_{s=\pm1} (|s\rangle g_s(\boldsymbol{k}) e^{is\alpha_s(\boldsymbol{k})}\langle 0| + \text{H.c.}), \tag{A1}$$

where $d_s(\boldsymbol{k})$ stands for the diagonal matrix elements:

$$d_s(\boldsymbol{k}) = s\varepsilon + 2J_2 f(\boldsymbol{k} - s\boldsymbol{p}). \tag{A2}$$

The off-diagonal matrix elements,

$$Jg(\boldsymbol{k} \mp \boldsymbol{p}/2) = g_\pm(\boldsymbol{k}) e^{i\alpha_\pm(\boldsymbol{k})}, \tag{A3}$$

have been represented in terms of their amplitudes $g_{\pm1}(\boldsymbol{k}) \equiv g_\pm(\boldsymbol{k})$ and phases $\alpha_{\pm1}(\boldsymbol{k}) \equiv \alpha_\pm(\boldsymbol{k})$.

Since there is no coupling between the A and C sublattices, one can perform a $\boldsymbol{k}$-dependent unitary transformation eliminating the phase factors,

$$|s\rangle \to |s,\boldsymbol{k}\rangle = |s\rangle e^{is\alpha_s(\boldsymbol{k})}, \quad s = \pm1,$$

and leave the basis vector $|0\rangle$ unchanged ($|0\rangle = |0,\boldsymbol{k}\rangle$). In the new basis the Hamiltonian (A1) is characterized by real and symmetric matrix elements. Its eigenvectors can be cast in terms of these vectors with real coefficients $C_{n,s}(\boldsymbol{k})$:

$$|u_{\boldsymbol{k},n}\rangle = \sum_{s=0,\pm1} C_{n,s}(\boldsymbol{k})|s,\boldsymbol{k}\rangle \equiv \sum_{s=0,\pm1} |s\rangle C_{n,s}(\boldsymbol{k}) e^{is\alpha_s(\boldsymbol{k})}. \tag{A4}$$

Combining Eqs. (20) and (A4), one arrives at the following expression for the Berry connection:

$$\boldsymbol{A}_n(\boldsymbol{k}) = -\sum_{s=\pm1} sC^2_{n,s}(\boldsymbol{k})\nabla_{\boldsymbol{k}}\alpha_s(\boldsymbol{k}). \tag{A5}$$

This result together with Eq. (21) will be subsequently used in finding the Chern numbers.

2. Determination of the Chern numbers: General

To determine the Chern number given by (21), one needs to study a behavior of the vector potential at its singular points. Singularities of the vector potential can emerge at the points where the phase of the coupling matrix element $g_\pm(\boldsymbol{k})e^{i\alpha_\pm(\boldsymbol{k})}$ given by Eq. (A3) is undefined. This happens if the function $g(\boldsymbol{k} - \boldsymbol{p}_\pm/2)$ goes to zero. The function $g(\boldsymbol{k})$ given by Eq. (14) is zero at the corners of the FBZ, namely at two inequivalent points $\boldsymbol{K}$ and $\boldsymbol{K}'$. Thus there are two pairs of points,

$$\boldsymbol{K}_\pm = \pm\boldsymbol{p}/2 + \boldsymbol{K}, \quad \boldsymbol{K}'_\pm = \pm\boldsymbol{p}/2 + \boldsymbol{K}', \tag{A6}$$

at which the function $g(\boldsymbol{k} \mp \boldsymbol{p}/2)$ goes to zero and its phase $\alpha_\pm(\boldsymbol{k})$ is undefined. Let us determine the coupling matrix element $g_\pm(\boldsymbol{k})e^{i\alpha_\pm(\boldsymbol{k})}$ in a vicinity of these points. Combining Eqs. (14) and (A3), the amplitude and phase of the coupling element reads up to the first order in the displacement vector $\boldsymbol{q}$, i.e., for $qa \ll 1$ with $q = |\boldsymbol{q}|$:

$$g_\pm(\boldsymbol{K}_\pm + \boldsymbol{q}) \approx \frac{3}{2}qaJ, \quad \alpha_\pm(\boldsymbol{K}_\pm + \boldsymbol{q}) \approx \frac{\pi}{3} - \varphi, \tag{A7}$$

$$g_\pm(\boldsymbol{K}'_\pm + \boldsymbol{q}) \approx \frac{3}{2}qaJ, \quad \alpha_\pm(\boldsymbol{K}'_\pm + \boldsymbol{q}) \approx -\frac{\pi}{3} + \varphi, \tag{A8}$$

where φ is a phase of the complex number $q_x + iq_y = qe^{i\varphi}$. Integrating over a small circle centered at $\mathbf{q} = 0$ surrounding each singular point of the phase, one finds

$$\oint_{|\mathbf{q}|\to0} d\boldsymbol{q}\cdot\nabla_q\alpha_\pm(\boldsymbol{K}_\pm + \boldsymbol{q}) = -2\pi,$$

$$\oint_{|\mathbf{q}|\to0} d\boldsymbol{q}\cdot\nabla_q\alpha_\pm(\boldsymbol{K}'_\pm + \boldsymbol{q}) = 2\pi,$$

where the signs are different due to the opposite phases in Eqs. (A7) and (A8). These equations together with Eqs. (21) and (A5) provide the following result for the Chern number:

$$c_n = \sum_{s=\pm1} s\big[C^2_{n,s}(\boldsymbol{K}_s) - C^2_{n,s}(\boldsymbol{K}'_s)\big], \tag{A9}$$

with $\boldsymbol{K}_{\pm1} \equiv \boldsymbol{K}_\pm$ and $\boldsymbol{K}'_{\pm1} \equiv \boldsymbol{K}'_\pm$. Therefore to find the Chern number one needs to determine the coefficients $C_{n,s}$ entering the state vector at the points $\boldsymbol{K}_\pm$ and $\boldsymbol{K}'_\pm$. If $C^2_{n,\pm} = 1$, the corresponding singular point contributes to the Chern number of the nth band. In the following we shall analyze two different situations.

3. Determination of the Chern numbers: Specific cases

Since the Hamiltonian $\mathcal{H}(\boldsymbol{k})$ given by Eqs. (19) or (A1) has a symmetry ($\varepsilon \to -\varepsilon$, $\mathcal{H} \to \mathcal{H}$), we consider only the case where $\varepsilon > 0$.

a. The case where $\boldsymbol{p} = \boldsymbol{G}$

Suppose first that the difference in the recoil momenta coincides with the inverse lattice vector $\boldsymbol{p} = \boldsymbol{G}$. In that case the coupling completely vanishes both for $\boldsymbol{k} = \boldsymbol{K}_\pm$ and also for $\boldsymbol{k} = \boldsymbol{K}'_\pm$. At these points $g(\boldsymbol{k} - \boldsymbol{p}/2) = g(\boldsymbol{k} + \boldsymbol{p}/2) = 0$, so all the states $|s\rangle$ ($s = 0,\pm1$) are decoupled, and thus the eigenstates are the bare states $|s\rangle$. The corresponding eigenenergies of the matrix Hamiltonian $\mathcal{H}(\boldsymbol{k})$, Eq. (A1), coincide with its diagonal elements $d_s(\boldsymbol{k})$ for $\boldsymbol{k} = \boldsymbol{K}_\pm$ and $\boldsymbol{k} = \boldsymbol{K}'_\pm$. Since $\boldsymbol{p} = \boldsymbol{G}$, one has $f(\boldsymbol{k} - \boldsymbol{p}) = f(\boldsymbol{k}) = f(\boldsymbol{k} + \boldsymbol{p})$, giving $d_s(\boldsymbol{k}) = s\varepsilon + 2J_2 f(\boldsymbol{k})$. Therefore the eigenstates are ordered in the same manner $d_{+1}(\boldsymbol{k}) > d_0(\boldsymbol{k}) > d_{-1}(\boldsymbol{k})$ both for $\boldsymbol{k} = \boldsymbol{K}_\pm$ and also $\boldsymbol{k} = \boldsymbol{K}'_\pm$, giving $C^2_{n,s}(\boldsymbol{K}_s) = C^2_{n,s}(\boldsymbol{K}'_s)$ with $s = \pm1$. As a result, the Chern number given by Eq. (A9) is identically equal to zero, and the system does not exhibit any topologically nontrivial phases. This is because for $\boldsymbol{p} = \boldsymbol{G}$ the flux over the rhombic plaquettes $\Phi_i = \pm\boldsymbol{p}\cdot\boldsymbol{a}_i$ is zero (modulo 2π), and there is no breaking of the time-reversal symmetry.

b. The case where $\boldsymbol{p} = \boldsymbol{K}$

As another illustration we pick the recoil momentum $\boldsymbol{p} = \boldsymbol{K}$ and take $J_2 = 0$. In that case the Chern numbers have been numerically found to be $c_1 = 1$, $c_2 = -2$, and $c_3 = 1$ (see Fig. 2). By taking $\boldsymbol{p} = \boldsymbol{K}$ the phase singularities of the coupling elements $g(\boldsymbol{k} \mp \boldsymbol{p}/2)$ emerge at the points

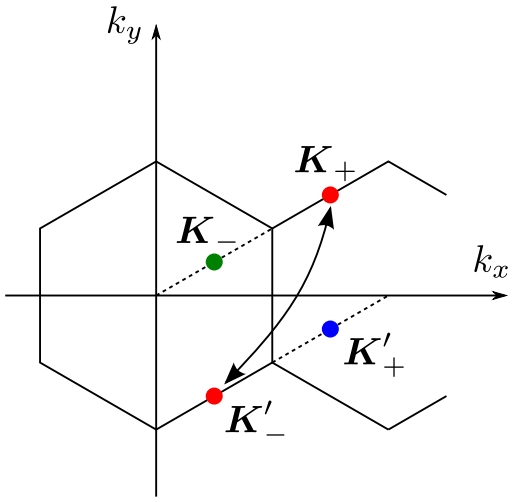

FIG. 7. (Color online) The phase singularity points $\boldsymbol{K}_\pm$ and $\boldsymbol{K}'_\pm$ of the coupling matrix elements $g(\boldsymbol{k} \mp \boldsymbol{p}/2)$ for $\boldsymbol{p} = \boldsymbol{K}$. The points $\boldsymbol{K}_+$ and $\boldsymbol{K}'_-$ are equivalent. They are shown by red dots connected with a double arrow.

$\boldsymbol{K}_\pm = \pm\boldsymbol{K}/2 + \boldsymbol{K}$ and $\boldsymbol{K}'_\pm = \pm\boldsymbol{K}/2 + \boldsymbol{K}'$, as one can see in Fig. 7. Furthermore, the point $\boldsymbol{k} = \boldsymbol{K}_+$ is equivalent to the point $\boldsymbol{k} = \boldsymbol{K}'_-$. For the latter two points we have $g(\boldsymbol{k} - \boldsymbol{p}/2) = g(\boldsymbol{k} + \boldsymbol{p}/2) = 0$, so there are no coupling matrix elements. Since $J_2 = 0$, the Hamiltonian (A1) at these points is, simply,

$$\mathcal{H}(\boldsymbol{K}_+) = \mathcal{H}(\boldsymbol{K}'_-) = \varepsilon \sum_{s=\pm1} s|s\rangle\langle s|, \tag{A10}$$

so the diagonal energies entering the Hamiltonian (A1) are $d_s(\boldsymbol{k}) = s\varepsilon$.

Eigenvalues, ordered from the lowest to the highest, are $E_1(\boldsymbol{K}_+) = E_1(\boldsymbol{K}'_-) = -\varepsilon$, $E_2(\boldsymbol{K}_+) = E_2(\boldsymbol{K}'_-) = 0$, and $E_3(\boldsymbol{K}_+) = E_3(\boldsymbol{K}'_-) = \varepsilon$. There is no degeneracy for $\varepsilon > 0$ and the coefficients $C_{n,+}(\boldsymbol{K}_+)$ and $C_{n,-}(\boldsymbol{K}'_-)$ do not change if one increases ε. The only nonzero coefficients contributing to the Chern numbers read

$$C_{3,+}(\boldsymbol{K}_+) = C_{1,-}(\boldsymbol{K}'_-) = 1. \tag{A11}$$

For the point $\boldsymbol{k} = \boldsymbol{K}_-$ the nondiagonal matrix elements of (A1) are $Jg(\boldsymbol{k} + \boldsymbol{p}/2) = 0$ and $Jg(\boldsymbol{k} - \boldsymbol{p}/2) = 3J$. Similarly for the point $\boldsymbol{k} = \boldsymbol{K}'_+$ these elements are $Jg(\boldsymbol{k} - \boldsymbol{p}/2) = 0$ and $Jg(\boldsymbol{k} + \boldsymbol{p}/2) = 3J$. Thus the Hamiltonian (A1) at these points is

$$H(\boldsymbol{K}_-) = \varepsilon \sum_{s=\pm1} s|s\rangle\langle s| + 3J(|0\rangle\langle +| + |+\rangle\langle 0|), \tag{A12}$$

$$H(\boldsymbol{K}'_+) = \varepsilon \sum_{s=\pm1} s|s\rangle\langle s| + 3J(|0\rangle\langle -| + |-\rangle\langle 0|). \tag{A13}$$

Eigenvalues of the $H(\boldsymbol{K}_-)$ are $E^{(0)}(\boldsymbol{K}_-) = -\varepsilon$ and $E^{(\pm)}(\boldsymbol{K}_-) = \frac{1}{2}(\varepsilon \pm \sqrt{\varepsilon^2 + 36J^2})$, and those of $H(\boldsymbol{K}'_+)$ are $E^{(0)}(\boldsymbol{K}'_+) = \varepsilon$ and $E^{(\pm)}(\boldsymbol{K}'_+) = \frac{1}{2}(-\varepsilon \pm \sqrt{\varepsilon^2 + 36J^2})$. They

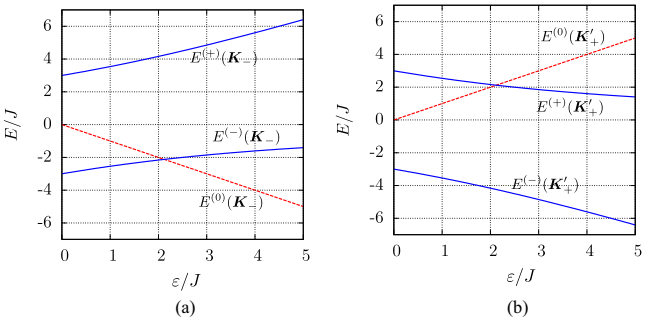

FIG. 8. (Color online) Dependence of eigenvalues of the Hamiltonian $H(\boldsymbol{k})$ on the on-site energy ε for $\boldsymbol{p} = \boldsymbol{K}$ in the absence of the next-nearest neighbor coupling. The eigenvalue $E^{(0)}$ is plotted in red dashed lines to distinguish it from the other eigenvalues $E^{(\pm)}$. (a) Eigenvalues at the point $\boldsymbol{k} = \boldsymbol{K}_-$. (b) Eigenvalues at the point $\boldsymbol{k} = \boldsymbol{K}'_+$. The eigenvalue crossing point $\varepsilon = \frac{3\sqrt{2}}{2}J \equiv \varepsilon_0$ corresponds to a transition from a topological semimetal phase on the left to a trivial phase on the right.

are plotted in Fig. 8. For $\varepsilon = \frac{3\sqrt{2}}{2}J \equiv \varepsilon_0$ there are degeneracies $E^{(0)}(\boldsymbol{K}_-) = E^{(-)}(\boldsymbol{K}_-) = -\varepsilon_0$ and $E^{(0)}(\boldsymbol{K}'_+) = E^{(+)}(\boldsymbol{K}'_+) = \varepsilon_0$. The eigenvalues change their order at the crossing point $\varepsilon = \varepsilon_0$, as one can see in Fig. 8.

Let us first consider the case $0 < \varepsilon < \varepsilon_0$. The eigenvalues of $H(\boldsymbol{K}_-)$ are in the increasing order: $E_1(\boldsymbol{K}_-) = E^{(-)}(\boldsymbol{K}_-)$, $E_2(\boldsymbol{K}_-) = E^{(0)}(\boldsymbol{K}_-)$, and $E_3(\boldsymbol{K}_-) = E^{(+)}(\boldsymbol{K}_-)$. On the other hand, coefficients required for the Chern number calculation are $C_{1,-}(\boldsymbol{K}_-) = 0$, $C_{2,-}(\boldsymbol{K}_-) = 1$, and $C_{3,-}(\boldsymbol{K}_-) = 0$. Similarly $H(\boldsymbol{K}'_+)$ gives the eigenvalues $E_1(\boldsymbol{K}'_+) = E^{(-)}(\boldsymbol{K}'_+)$, $E_2(\boldsymbol{K}'_+) = E^{(0)}(\boldsymbol{K}'_+)$, and $E_3(\boldsymbol{K}'_+) = E^{(+)}(\boldsymbol{K}'_+)$ and the coefficients $C_{1,+}(\boldsymbol{K}'_+) = 0$, $C_{2,+}(\boldsymbol{K}'_+) = 1$ and $C_{3,+}(\boldsymbol{K}'_+) = 0$. Combining this result together with (A11) we collect four nonzero coefficients: $C_{3,+}(\boldsymbol{K}_+)$, $C_{1,-}(\boldsymbol{K}'_-)$, $C_{2,-}(\boldsymbol{K}_-)$, and $C_{2,+}(\boldsymbol{K}'_+)$. Substituting them into Eq. (A9), we get the Chern numbers for each energy band:

$$c_1 = C^2_{1,-}(\boldsymbol{K}'_-) = 1, \tag{A14}$$

$$c_2 = -C^2_{2,+}(\boldsymbol{K}'_+) - C^2_{2,-}(\boldsymbol{K}_-) = -2, \tag{A15}$$

$$c_3 = C^2_{3,+}(\boldsymbol{K}_+) = 1. \tag{A16}$$

This result agrees with the numerical analysis presented in Fig. 2.

Now let us consider the case $\varepsilon > \varepsilon_0$. From Fig. 8 we see that the eigenvalues are reordered as $E_1(\boldsymbol{K}_-) \to E_2(\boldsymbol{K}_-)$, $E_2(\boldsymbol{K}'_+) \to E_3(\boldsymbol{K}'_+)$, so nonzero coefficients are $C_{3,+}(\boldsymbol{K}_+)$, $C_{1,-}(\boldsymbol{K}'_-)$, $C_{1,-}(\boldsymbol{K}_-)$, and $C_{3,+}(\boldsymbol{K}'_+)$. Using Eq. (A9), one can see that the Chern numbers of all bands are now zero:

$$c_1 = -C^2_{1,-}(\boldsymbol{K}_-) + C^2_{1,-}(\boldsymbol{K}'_-) = 0, \tag{A17}$$

$$c_2 = 0, \tag{A18}$$

$$c_3 = C^2_{3,+}(\boldsymbol{K}_+) - C^2_{3,+}(\boldsymbol{K}'_+) = 0. \tag{A19}$$

Thus there is a topological phase transition at $\varepsilon = \frac{3\sqrt{2}}{2}J$ corresponding to the eigenvalue crossing in Fig. 8.

[1] I. Bloch, J. Dalibard, and W. Zwerger, Rev. Mod. Phys. **80**, 885 (2008).
[2] M. Lewenstein, A. Sanpera, V. Ahufinger, B. Damski, A. Sen(De), and U. Sen, Adv. Phys. **56**, 243 (2007).
[3] P. Windpassinger and K. Sengstock, Rep. Prog. Phys. **76**, 086401 (2013).
[4] M. Aidelsburger, M. Atala, M. Lohse, J. T. Barreiro, B. Paredes, and I. Bloch, Phys. Rev. Lett. **111**, 185301 (2013).
[5] H. Miyake, G. A. Siviloglou, C. J. Kennedy, W. C. Burton, and W. Ketterle, Phys. Rev. Lett. **111**, 185302 (2013).
[6] D. R. Hofstadter, Phys. Rev. B **14**, 2239 (1976).
[7] G. Jotzu, M. Messer, R. Desbuquois, M. Lebrat, T. Uehlinger, D. Greif, and T. Esslinger, Nature (London) **515**, 237 (2014).
[8] L. Tarruell, D. Greif, T. Uehlinger, G. Jotzu, and T. Esslinger, Nature (London) **483**, 302 (2012).
[9] J. Struck, C. Ölschläger, M. Weinberg, P. Hauke, J. Simonet, A. Eckardt, M. Lewenstein, K. Sengstock, and P. Windpassinger, Phys. Rev. Lett. **108**, 225304 (2012).
[10] J. Struck, M. Weinberg, C. Ölschläger, P. Windpassinger, J. Simonet, K. Sengstock, R. Höppner, P. Hauke, A. Eckardt, M. Lewenstein, and L. Mathey, Nat. Phys. **9**, 738 (2013).
[11] K. Jiménez-García, L. J. LeBlanc, R. A. Williams, M. C. Beeler, A. R. Perry, and I. B. Spielman, Phys. Rev. Lett. **108**, 225303 (2012).
[12] M. Z. Hasan and C. L. Kane, Rev. Mod. Phys. **82**, 3045 (2010).
[13] X.-L. Qi and S.-C. Zhang, Rev. Mod. Phys. **83**, 1057 (2011).
[14] N. Goldman, G. Juzeliūnas, P. Öhberg, and I. B. Spielman, Rep. Prog. Phys. **77**, 126401 (2014).
[15] D. N. Sheng, Z.-C. Gu, K. Sun, and L. Sheng, Nat. Commun. **2**, 389 (2011).
[16] A. Eckardt, C. Weiss, and M. Holthaus, Phys. Rev. Lett. **95**, 260404 (2005).
[17] A. R. Kolovsky, Europhys. Lett. **93**, 20003 (2011).
[18] N. Goldman and J. Dalibard, Phys. Rev. X **4**, 031027 (2014).
[19] D. Jaksch and P. Zoller, New J. Phys. **5**, 56 (2003).
[20] F. Gerbier and J. Dalibard, New J. Phys. **12**, 033007 (2010).
[21] J. Dalibard, F. Gerbier, G. Juzeliūnas, and P. Öhberg, Rev. Mod. Phys. **83**, 1523 (2011).
[22] A. Celi, P. Massignan, J. Ruseckas, N. Goldman, I. B. Spielman, G. Juzeliūnas, and M. Lewenstein, Phys. Rev. Lett. **112**, 043001 (2014).
[23] T. Dubček, C. J. Kennedy, L. Lu, W. Ketterle, M. Soljačić, and H. Buljan, Phys. Rev. Lett. **114**, 225301 (2015).
[24] Y.-F. Wang, Z.-C. Gu, C.-D. Gong, and D. N. Sheng, Phys. Rev. Lett. **107**, 146803 (2011).
[25] Z. Liu, E. J. Bergholtz, H. Fan, and A. M. Läuchli, Phys. Rev. Lett. **109**, 186805 (2012).
[26] S. Yang, Z.-C. Gu, K. Sun, and S. Das Sarma, Phys. Rev. B **86**, 241112 (2012).
[27] Y.-F. Wang, H. Yao, C.-D. Gong, and D. N. Sheng, Phys. Rev. B **86**, 201101 (2012).
[28] A. Sterdyniak, C. Repellin, B. A. Bernevig, and N. Regnault, Phys. Rev. B **87**, 205137 (2013).
[29] F. Wang and Y. Ran, Phys. Rev. B **84**, 241103 (2011).
[30] D. Sticlet, F. Piéchon, J.-N. Fuchs, P. Kalugin, and P. Simon, Phys. Rev. B **85**, 165456 (2012).
[31] S. A. Parameswaran, R. Roy, and S. L. Sondhi, C. R. Phys. **14**, 816 (2013).
[32] E. J. Bergholtz and Z. Liu, Int. J. Mod. Phys. B **27**, 1330017 (2013).
[33] T. Neupert, L. Santos, C. Chamon, and C. Mudry, Phys. Rev. Lett. **106**, 236804 (2011).
[34] N. Regnault and B. A. Bernevig, Phys. Rev. X **1**, 021014 (2011).
[35] A. G. Grushin, A. Gómez-León, and T. Neupert, Phys. Rev. Lett. **112**, 156801 (2014).
[36] D. Sticlet and F. Piéchon, Phys. Rev. B **87**, 115402 (2013).
[37] A. Kol and N. Read, Phys. Rev. B **48**, 8890 (1993).
[38] R. N. Palmer and D. Jaksch, Phys. Rev. Lett. **96**, 180407 (2006).
[39] G. Möller and N. R. Cooper, Phys. Rev. Lett. **103**, 105303 (2009).
[40] G. Moller and N. R. Cooper, arXiv:1504.06623.
[41] F. D. M. Haldane, Phys. Rev. Lett. **61**, 2015 (1988).
[42] E. Alba, X. Fernandez-Gonzalvo, J. Mur-Petit, J. K. Pachos, and J. J. Garcia-Ripoll, Phys. Rev. Lett. **107**, 235301 (2011).
[43] G. Juzeliūnas and I. B. Spielman, Physics **4**, 99 (2011).
[44] N. Goldman, E. Anisimovas, F. Gerbier, P. Öhberg, I. B. Spielman, and G. Juzeliūnas, New J. Phys. **15**, 013025 (2013).
[45] E. Anisimovas, F. Gerbier, T. Andrijauskas, and N. Goldman, Phys. Rev. A **89**, 013632 (2014).
[46] B. Sutherland, Phys. Rev. B **34**, 5208 (1986).
[47] D. Bercioux, D. F. Urban, H. Grabert, and W. Häusler, Phys. Rev. A **80**, 063603 (2009).
[48] G. Möller and N. R. Cooper, Phys. Rev. Lett. **108**, 045306 (2012).
[49] M. Rizzi, V. Cataudella, and R. Fazio, Phys. Rev. B **73**, 144511 (2006).
[50] A. A. Burkov and E. Demler, Phys. Rev. Lett. **96**, 180406 (2006).
[51] D. Bercioux, N. Goldman, and D. F. Urban, Phys. Rev. A **83**, 023609 (2011).
[52] J. Vidal, R. Mosseri, and B. Douçot, Phys. Rev. Lett. **81**, 5888 (1998).
[53] C. C. Abilio, P. Butaud, T. Fournier, B. Pannetier, J. Vidal, S. Tedesco, and B. Dalzotto, Phys. Rev. Lett. **83**, 5102 (1999).
[54] J. L. Movilla and J. Planelles, Phys. Rev. B **84**, 195110 (2011).
[55] J. Ruostekoski, G. V. Dunne, and J. Javanainen, Phys. Rev. Lett. **88**, 180401 (2002).
[56] A. Raoux, M. Morigi, J.-N. Fuchs, F. Piéchon, and G. Montambaux, Phys. Rev. Lett. **112**, 026402 (2014).
[57] T. S. Jackson, G. Möller, and R. Roy, arXiv:1408.0843.
[58] E. Dobardžić, M. Dimitrijević, and M. V. Milovanović, Phys. Rev. B **91**, 125424 (2015).
[59] D. Xiao, M.-C. Chang, and Q. Niu, Rev. Mod. Phys. **82**, 1959 (2010).
[60] Y. Hatsugai, Phys. Rev. Lett. **71**, 3697 (1993).
[61] M. Kohmoto, Ann. Phys. **160**, 343 (1985).
[62] M. Kohmoto, Phys. Rev. B **39**, 11943 (1989).
[63] D. J. Thouless, M. Kohmoto, M. P. Nightingale, and M. den Nijs, Phys. Rev. Lett. **49**, 405 (1982).
[64] T. Fukui, Y. Hatsugai, and H. Suzuki, J. Phys. Soc. Jpn. **74**, 1674 (2005).
[65] Y. Hatsugai, J. Phys. Soc. Jpn. **74**, 1374 (2005).
[66] M. Hafezi, A. S. Sørensen, M. D. Lukin, and E. Demler, Europhys. Lett. **81**, 10005 (2008).

III

Topological lattice using multi-frequency radiation

Tomas Andrijauskas, I B Spielman and Gediminas Juzeliūnas

New Journal of Physics **20**, 055001 (2018).

New Journal of Physics
The open access journal at the forefront of physics

Deutsche Physikalische Gesellschaft DPG
IOP Institute of Physics

Published in partnership with: Deutsche Physikalische Gesellschaft and the Institute of Physics

OPEN ACCESS

RECEIVED
20 June 2017

REVISED
26 February 2018

ACCEPTED FOR PUBLICATION
19 March 2018

PUBLISHED
3 May 2018

PAPER

Topological lattice using multi-frequency radiation

Tomas Andrijauskas[1], **I B Spielman**[2,3] **and Gediminas Juzeliūnas**[1]

[1] Institute of Theoretical Physics and Astronomy, Vilnius University, Saulėtekio 3, LT-10222 Vilnius, Lithuania
[2] Joint Quantum Institute, University of Maryland, College Park, MD 20742-4111, United States of America
[3] National Institute of Standards and Technology, Gaithersburg, MD 20899, United States of America

E-mail: gediminas.juzeliunas@tfai.vu.lt

Keywords: artificial gauge fields, Floquet, flux lattice

Abstract

We describe a novel technique for creating an artificial magnetic field for ultracold atoms using a periodically pulsed pair of counter propagating Raman lasers that drive transitions between a pair of internal atomic spin states: a multi-frequency coupling term. In conjunction with a magnetic field gradient, this dynamically generates a rectangular lattice with a non-staggered magnetic flux. For a wide range of parameters, the resulting Bloch bands have non-trivial topology, reminiscent of Landau levels, as quantified by their Chern numbers.

1. Introduction

Ultracold atoms find wide applications in realizing condensed matter phenomena [1–4]. Since ultracold atom systems are ensembles of electrically neutral atoms, various methods have been used to simulate Lorentz-type forces, with an eye for realizing physics such as the quantum Hall effect (QHE). Lorentz forces are present in spatially rotating systems [5–11] and appear in light-induced geometric potentials [12, 13]. The magnetic fluxes achieved with these methods are not sufficiently large for realizing the integer or fractional QHE. In optical lattices, larger magnetic fluxes can be created by shaking the lattice potential [14–17], combining static optical lattices along with laser-assisted spin or pseudo spin coupling [12, 13, 18–24]; current realizations of these techniques are beset with micro motion and interaction induced heating effects. Here we propose a new method that simultaneously creates large artificial magnetic fields and a lattice that may overcome these limitations.

Our technique relies on a pulsed atom-light coupling between internal atomic states along with a state-dependent gradient potential that together create a two-dimensional periodic potential with an intrinsic artificial magnetic field. With no pre-existing lattice potential, there are no *a priori* resonant conditions that would otherwise constrain the modulation frequency to avoid transitions between original Bloch bands [25]. For a wide range of parameters, the ground and excited bands of our lattice are topological, with nonzero Chern number. Moreover, like Landau levels the lowest several bands can all have unit Chern number.

The manuscript is organized as follows. Firstly, we describe a representative experimental implementation of our technique directly suitable for alkali atoms. Secondly, because the pulsed atom-light coupling is time-periodic, we use Floquet methods to solve this problem. Specifically, we employ a stroboscopic technique to obtain an effective Hamiltonian. Thirdly, using the resulting band structure we obtain a phase diagram which includes a region of Landau level-like bands each with unit Chern number.

2. Pulsed lattice

Figure 1 depicts a representative experimental realization of the proposed method. A system of ultracold atoms is subjected to a magnetic field with a strength $B(X) = B_0 + B'X$. This induces a position-dependent splitting $g_F\mu_B B$ between the spin up and down states; g_F is the Land g-factor and μ_B is the Bohr magneton. Additionally, the atoms are illuminated by a pair of Raman lasers counter propagating along $\mathbf{e}_y$, i.e., perpendicular to the detuning gradient. The first beam [up-going in figure 1(a)] is at frequency $\omega^+ = \omega_0$, while the second [down-going in figure 1(a)] contains frequency components $\omega_n^- = \omega_0 + (-1)^n(\delta\omega + n\omega)$; the difference frequency

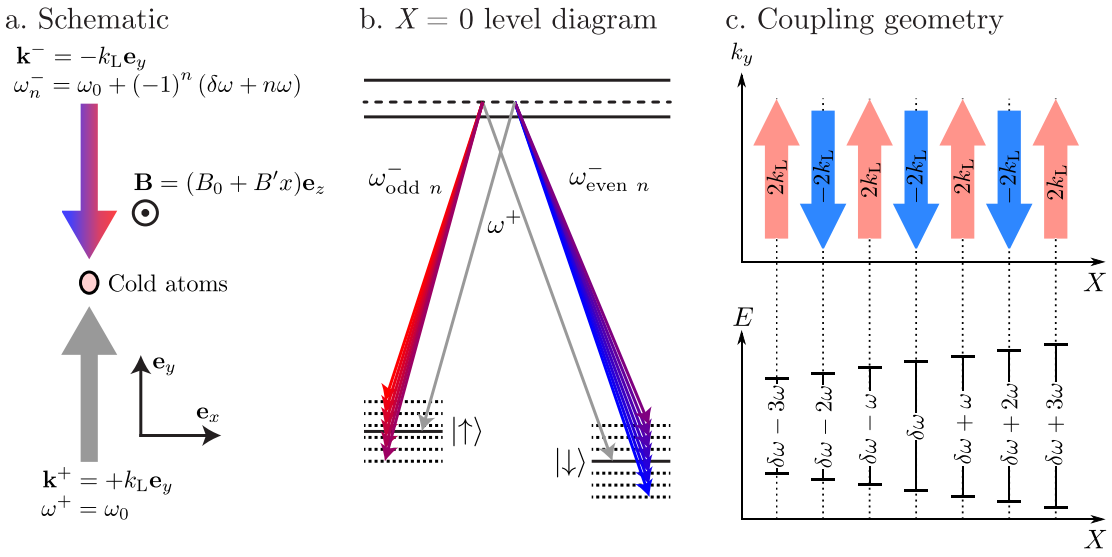

Figure 1. Floquet flux lattice. (a) Experimental schematic depicting a cold cloud of atoms in a gradient magnetic field, illuminated by a pair of counter-propagating laser beams tuned near two-photon Raman resonance. The down-going beam includes sidebands both to the red and blue of the carrier (ω_0) in resonance at different spatial positions along $\mathbf{e}_x$. (b) Level diagram showing even and odd sidebands linking the $|\uparrow\rangle$ and $|\downarrow\rangle$ states with differing detuning from resonance at $X = 0$. (c) Spatially dependent coupling. Bottom: different frequency components are in two-photon resonance in different X positions. Top: the recoil kick associated with the Raman transition is along $\pm\mathbf{e}_y$ and thus alternates spatially depending on whether the Raman transition is driven from the red or blue sideband of the down-going laser beam.

between these beams contains frequency combs centered at $\pm\delta\omega$ with comb teeth spaced by 2ω, as shown in figure 1(b). In our proposal, the Raman lasers are tuned to be in nominal two-photon resonance with the Zeeman splitting from the large offset field B_0 such that $g_F\mu_B B_0 = \hbar\delta\omega_0$, making the frequency difference $\omega^-_{n=0} - \omega^+$ resonant at $X = 0$, where $B = B_0$. Intuitively, each additional frequency component ω^-_n adds a resonance condition at the regularly spaced points $X_n = n\hbar\omega/g_F\mu_B B'$, however, transitions using even-n sidebands give a recoil kick opposite from those using odd-n sidebands (see figure 1(c)). Each of these coupling-locations locally realizes synthetic magnetic field experiment performed at the National Institute of Standards and Technology [26], arrayed in a manner to give a rectified artificial magnetic field with a nonzero average that we will show is a novel flux lattice.

In practice only a finite number of lattice teeth are needed, owing to the finite spatial extent of a trapped atomic gas. In rough numbers the spatial extent of a quantum degenerate gas is 20 μm, and if we select a very large gradient corresponding to a lattice spacing of 0.5 μm, this gives just 40 comb teeth. Generating the frequency comb is straightforward. In the laboratory, acoustic-optical modulators (AOMs) frequency-shift laser beams by an amount defined by a laboratory radiofrequency (rf) source. Therefore creating a comb is a matter of first creating a frequency comb—simple with rf—and then feeding that signal into the AOM. This sort of frequency synthesis is routine in the ultracold atom labs.

We formally describe our system by first making the rotating wave approximation (RWA) with respect to the large offset frequency ω_0. This situation is modeled in terms of a spin-1/2 atom of mass M and wave-vector $\boldsymbol{K} = -\mathrm{i}\boldsymbol{\nabla}$ with a Hamiltonian

$$H(t) = H_0 + V(t). \tag{1}$$

The first term is

$$H_0 = \frac{\hbar^2\boldsymbol{K}^2}{2M} + \frac{\Delta(X)}{2}\sigma_3, \tag{2}$$

where $\Delta(X) = \Delta' X$ describes the detuning gradient along $\mathbf{e}_x$, and $\sigma_3 = |\uparrow\rangle\langle\uparrow| - |\downarrow\rangle\langle\downarrow|$ is a Pauli spin operator. In the RWA only near-resonant terms are retained, giving the Raman coupling described by

$$V(t) = V_0\sum_n [\mathrm{e}^{\mathrm{i}(K_0 Y - 2n\omega t)} + \mathrm{e}^{\mathrm{i}(-K_0 Y - (2n+1)\omega t)}]|\downarrow\rangle\langle\uparrow| + \text{H.c.} \tag{3}$$

The first term describes coupling from the sidebands with even frequencies $2n\omega$, whereas the second term describes coupling from the sidebands with odd frequencies $(2n + 1)\omega$. The recoil kick is aligned along $\pm\mathbf{e}_y$ with opposite sign for the even and odd frequency components. In writing equation (3) we assumed that the coupling amplitude V_0 and the associated recoil wavenumber K_0 are the same for all frequency components. The

coupling Hamiltonian $V(t)$ and therefore the full Hamiltonian $H(t)$ are time-periodic with period $2\pi/\omega$, and we accordingly apply Floquet techniques.

3. Theoretical analysis

The outline of this section is as follows. (1) We begin the analysis of the Hamiltonian given by equation (1) by moving to dimensionless units; (2) subsequently derive an approximate effective Hamiltonian from the single-period time evolution operator; (3) provide an intuitive description in terms of adiabatic potentials; and (4) finally solve the band structure, evaluate its topology and discuss possibilities of the experimental implementation.

3.1. Dimensionless units

For the remainder of the manuscript we will use dimensionless units. All energies will be expressed in units of $\hbar\omega$, derived from the Floquet frequency ω; time will be expressed in units of inverse driving frequency ω^{-1}, denoted by $\tau = \omega t$; spatial coordinates will be expressed in units of inverse recoil momentum K_0^{-1}, denoted by lowercase letters $(x, y) = K_0(X, Y)$. In these units, the Hamiltonian (1) takes the form

$$h(\tau) = \frac{H(\tau/\omega)}{\hbar\omega} = E_r \boldsymbol{k}^2 + \frac{1}{2}\boldsymbol{\Omega}(\tau)\cdot\boldsymbol{\sigma}, \tag{4}$$

where $E_r = \hbar^2 K_0^2/(2M\hbar\omega)$ is the dimensionless recoil energy associated with the recoil wavenumber K_0; $\boldsymbol{k} = \boldsymbol{K}/K_0$ is the dimensionless wavenumber. The dimensionless coupling

$$\boldsymbol{\Omega}(x, y, \tau) = (2\,\mathrm{Re}\,u(y, \tau), 2\,\mathrm{Im}\,u(y, \tau), \beta x) \tag{5}$$

includes a combination of position-dependent detuning and Raman coupling. Here $\beta = \Delta'/(\hbar\omega k_0)$ describes the linearly varying detuning in dimensionless units; the function $u(y, \tau) = v_0\sum_n\{\exp[\mathrm{i}(y - 2n\tau)] + \exp[\mathrm{i}(-y - (2n + 1)\tau)]\}$ is a dimensionless version of the sum in equation (3) with $v_0 = V_0/(\hbar\omega)$.

In the time domain the coupling given by equation (5) is

$$\frac{1}{2}\boldsymbol{\Omega}(\tau)\cdot\boldsymbol{\sigma} = \frac{1}{2}\beta x\sigma_3 + \sum_l v_l(y)\delta(\tau - \pi l), \tag{6}$$

with

$$v_l(y) = \pi v_0[\mathrm{e}^{\mathrm{i}y} + (-1)^l\mathrm{e}^{-\mathrm{i}y}]|\downarrow\rangle\langle\uparrow| + \mathrm{H.c.} \tag{7}$$

In this way we have separated the spatial and temporal dependencies in the coupling (6).

3.2. Effective Hamiltonian

We continue our analysis by deriving an approximate Hamiltonian that describes the complete time evolution over a single period from $\tau = 0 - \epsilon$ to $\tau = 2\pi - \epsilon$ with $\epsilon \to 0$. This evolution includes a kick v_0 at the beginning of the period $\tau_+ = 0$ and a second kick v_1 in the middle of the period $\tau_- = \pi$; between the kicks the evolution includes the kinetic and gradient energies. In the full time period, the complete evolution operator is a product of four terms:

$$U(2\pi, 0) \equiv \lim_{\epsilon\to 0} U(2\pi - \epsilon, 0 - \epsilon) = U_0 U_{\mathrm{kick}}^{(1)} U_0 U_{\mathrm{kick}}^{(0)}. \tag{8}$$

Here

$$U_0 = \exp\left\{-\mathrm{i}\pi\left[E_r\boldsymbol{k}^2 + \frac{1}{2}\sigma_3\beta x\right]\right\} \tag{9}$$

is the evolution operator over a half period, generated by kinetic energy and gradient. The operator

$$U_{\mathrm{kick}}^{(l)} = \exp\left[-\mathrm{i}v_l(y)\right] \tag{10}$$

describes a kick at $\tau = l\pi$.

We obtain an effective Hamiltonian by assuming that the Floquet frequency ω greatly exceeds the recoil frequency, $1 \gg E_r$, allowing us to ignore the commutators between the kinetic energy and functions of coordinates in equation (8). We then rearrange terms in the full time evolution operator (8) and obtain (see appendix)

$$U_{\mathrm{eff}} = \exp\left[\{-\mathrm{i}2\pi([E_r\boldsymbol{k}^2 + v_{\mathrm{eff}})]\}\right], \tag{11}$$

where $\nu_{\rm eff}$ is an effective coupling defined by

$$\exp(-i2\pi\nu_{\rm eff}) = e^{-i\pi\sigma_3\beta x/2}U^{(1)}_{\rm kick}e^{-i\pi\sigma_3\beta x/2}U^{(0)}_{\rm kick}. \tag{12}$$

The function $\nu_l(y)$ entering the kick operators $U^{(l)}_{\rm kick}$ is spatially periodic along the y direction with a period 2π. This period can be halved to π by virtue of a gauge transformation $U = \exp(-iy\sigma_3/2)$. Subsequently, when exploring energy bands and their topological properties, this prevents problems arising from using a twice larger elementary cell. Following this transformation the evolution operator becomes

$$U_{\rm eff} = \exp\{-i2\pi[E_{\rm r}(\boldsymbol{k} + \sigma_3\boldsymbol{e}_y/2)^2 + \nu_{\rm eff}]\}, \tag{13}$$

where $\nu_l(y)$ featured in the kick operators $U^{(l)}_{\rm kick}$ has now the spatial periodicity π along the y direction, i.e. it should be replace to

$$\nu_l(y) = \pi\nu_0[e^{i2y} + (-1)^l]|\downarrow\rangle\langle\uparrow| + \text{H.c.} \tag{14}$$

The algebra of Pauli matrices allows us to write the effective coupling $\nu_{\rm eff}(\boldsymbol{r})$ featured in the evolution equations (12) and (13) as:

$$\nu_{\rm eff}(\boldsymbol{r}) = \frac{1}{2}\boldsymbol{\Omega}_{\rm eff}(\boldsymbol{r})\cdot\boldsymbol{\sigma}, \tag{15}$$

where $\boldsymbol{\Omega}_{\rm eff} = (\Omega_{\rm eff,1}, \Omega_{\rm eff,2}, \Omega_{\rm eff,3})$ is a position-dependent effective Zeeman field which takes the analytic form

$$\exp(-i2\pi\nu_{\rm eff}) = q_0 - iq_1\sigma_1 - iq_2\sigma_2 - iq_3\sigma_3. \tag{16}$$

Here q_0, q_1, q_2 and q_3 are real functions of the coordinates (x, y), allowing to express the effective Zeeman field as

$$\boldsymbol{\Omega}_{\rm eff} = \pi^{-1}\frac{\boldsymbol{q}}{||\boldsymbol{q}||}\arccos q_0, \tag{17}$$

where $\boldsymbol{q}$ is a shorthand of a three dimensional vector (q_1, q_2, q_3). In general the equation (16) gives multiple solutions that correspond for different Floquet bands. Our choice (17) picks only to the two bands that lie in the energy window from $-1/2$ to $1/2$ covering a single Floquet period.

Comparing (12) and (16) and multiplying four matrix exponents give explicit expressions

$$q_0 = \cos f_1\cos f_2\cos(\pi\beta x), \tag{18}$$

$$q_1 = \sin f_1\cos f_2\cos(y + \pi\beta x) - \cos f_1\sin f_2\sin(y), \tag{19}$$

$$q_2 = \sin f_1\cos f_2\sin(y + \pi\beta x) + \cos f_1\sin f_2\cos(y), \tag{20}$$

$$q_3 = \cos f_1\cos f_2\sin(\pi\beta x) - \sin f_1\sin f_2 \tag{21}$$

with

$$f_1(y) = 2\pi\nu_0\cos(y), \tag{22}$$

$$f_2(y) = 2\pi\nu_0\sin(y). \tag{23}$$

These explicit expressions show that the resulting effective Zeeman field (17) and the associated effective coupling (15) are periodic along both $\boldsymbol{e}_x$ and $\boldsymbol{e}_y$, with spatial periods $a_x = 2/\beta$ and $a_y = \pi$ respectively. Therefore, although the original Hamiltonian containing the spin-dependent potential slope $\propto x\sigma_3$ is not periodic along the x direction, the effective Floquet Hamiltonian is. The spatial dependence of the Zeeman field components $\Omega_{\rm eff,1}$, $\Omega_{\rm eff,2}$ and $\Omega_{\rm eff,3}$ is presented in the figure 2 for $\beta = 0.6$ giving an approximately square unit cell. In figure 2 we select $\nu_0 = 0.25$ where the absolute value of the Zeeman field $\Omega_{\rm eff}$ is almost uniform, as is apparent from the nearly flat adiabatic bands shown in figure 3 below.

3.3. Adiabatic evolution and magnetic flux

Before moving further to an explicit numerical analysis of the band structure, we develop an intuitive understanding by performing an adiabatic analysis of motion governed by effective Hamiltonian

$$h_{\rm eff}(\boldsymbol{r}) = E_{\rm r}(\boldsymbol{k} + \sigma_3\boldsymbol{e}_y/2)^2 + \frac{1}{2}\boldsymbol{\Omega}_{\rm eff}\cdot\boldsymbol{\sigma} \tag{24}$$

featured in the evolution operator $U_{\rm eff}$, equation (13). The coupling field $\boldsymbol{\Omega}_{\rm eff}(\boldsymbol{r})$ is parametrized by the spherical angles $\theta(\boldsymbol{r})$ and $\phi(\boldsymbol{r})$ defined by

$$\cos\theta = \frac{\Omega_{\rm eff,3}}{\Omega_{\rm eff}}, \tag{25}$$

$$\tan\phi = \frac{\Omega_{\rm eff,2}}{\Omega_{\rm eff,1}}. \tag{26}$$

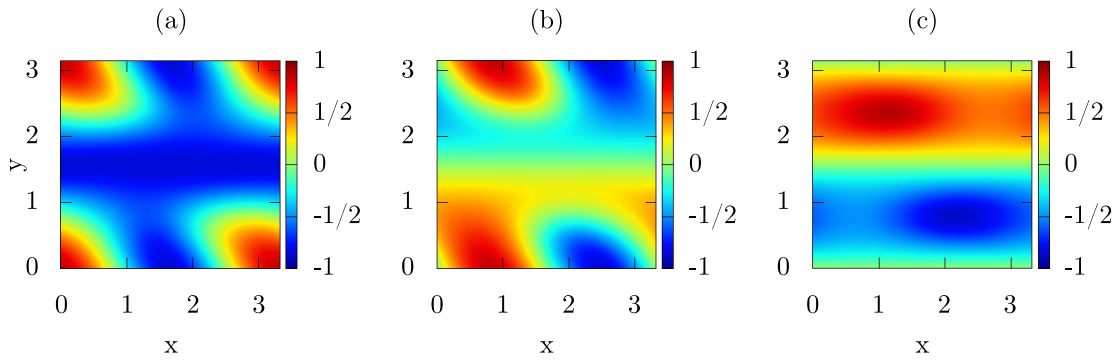

Figure 2. Coupling components (a) $\Omega_{\mathrm{eff},1}(\boldsymbol{r})$, (b) $\Omega_{\mathrm{eff},2}(\boldsymbol{r})$ and (c) $\Omega_{\mathrm{eff},3}(\boldsymbol{r})$ for $v_0 = 0.25$ and $\beta = 0.6$ calculated using equations (17)–(23). The corresponding eigenvalues of the coupling $v_\pm(\boldsymbol{r}) = \pm\Omega_{\mathrm{eff}}/2$ are presented by the thick red solid lines in the figure 3.

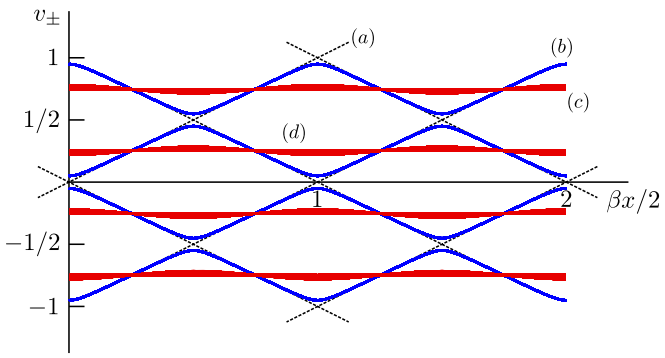

Figure 3. Adiabatic Floquet potentials given by equation (29) for $\beta = 0.6\ \mu$s. (a) Thin black dotted lines denote the spin-dependent gradient slopes without including the Raman coupling ($v_0 = 0$); (b) thin blue solid lines denote effective adiabatic potentials for weak Raman coupling ($v_0 = 0.05$) (c) red solid lines denote nearly flat adiabatic potentials that are achieved for stronger Raman coupling ($v_0 = 0.25$). All the curves are projected into x plane for various y values. A weak y dependence of the adiabatic potentials is seen to appear in the strong coupling case (c) making the superimposed red lines thicker.

This gives the effective coupling [12]

$$\frac{1}{2}\boldsymbol{\Omega}_{\mathrm{eff}}\cdot\boldsymbol{\sigma} = \frac{1}{2}\Omega_{\mathrm{eff}}\begin{bmatrix}\cos\theta & \mathrm{e}^{-\mathrm{i}\phi}\sin\theta\\ \mathrm{e}^{\mathrm{i}\phi}\sin\theta & -\cos\theta\end{bmatrix}, \tag{27}$$

characterized by the position-dependent eigenstates

$$|+\rangle = \begin{pmatrix}\cos(\theta/2)\\ \mathrm{e}^{\mathrm{i}\phi}\sin(\theta/2)\end{pmatrix}, \qquad |-\rangle = \begin{pmatrix}-\mathrm{e}^{-\mathrm{i}\phi}\sin(\theta/2)\\ \cos(\theta/2)\end{pmatrix}. \tag{28}$$

The corresponding eigenvalues

$$v_\pm(\boldsymbol{r}) = \pm\frac{1}{2}\Omega_{\mathrm{eff}}, \tag{29}$$

are shown in figure 3 for various value of the Raman coupling v_0. As one can see in figure 3, for $v_0 = 0.25$ the resulting bands $v_\pm(\boldsymbol{r})$ (adiabatic potentials) are flat and have a considerable gap $\approx\omega/2$, a regime suitable for a description in terms of an adiabatic motion in selected bands [27].

As in [28], we consider the adiabatic motion of the atom in one of these flat adiabatic bands with the projection Schrödinger equation that includes a geometric vector potential

$$\boldsymbol{A}_\pm(\boldsymbol{r}) = \pm\frac{1}{2}(\cos\theta - 1)\nabla\phi. \tag{30}$$

This provides a synthetic magnetic flux density $\boldsymbol{B}_\pm(\boldsymbol{r}) = \nabla\times\boldsymbol{A}_\pm(\boldsymbol{r})$. The geometric vector potential $\boldsymbol{A}_\pm(\boldsymbol{r})$ may contain Aharonov–Bohm type singularities, that give rise to a synthetic magnetic flux over an elementary cell

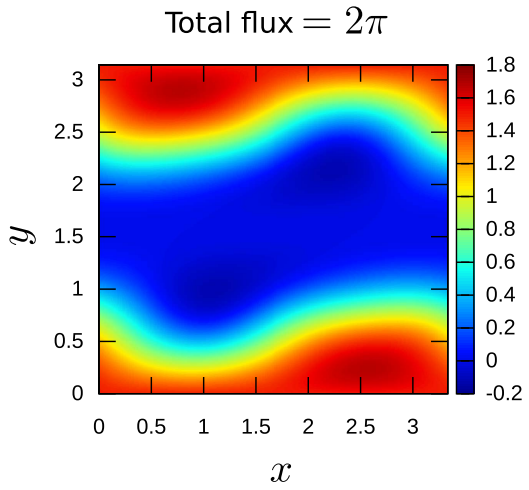

Figure 4. Geometric flux density $\boldsymbol{B}_{\pm}(\boldsymbol{r}) = \nabla \times \boldsymbol{A}_{\pm}(\boldsymbol{r})$ computed for $v_0 = 0.25$ and $\beta = 0.6$ using equation (30). The overall spatial structure of this flux density does not depend on the gradient β; rather it scales with the corresponding lattice constant $a_x = 2/\beta$.

$$\alpha_{\pm} = -\sum \oint_{\text{singul}} \mathrm{d}\boldsymbol{r} \cdot \boldsymbol{A}_{\pm}(\boldsymbol{r}). \tag{31}$$

The singularities appear at points where $\theta = \pi$, where the angle ϕ and its gradient $\nabla\phi$ are undefined and $\cos\theta = -1$. The term $\cos\theta - 1$ in (30) is nonzero and does not remove the undefined phase $\nabla\phi$. Our unit cell contains two such singularities located at $\boldsymbol{r} = (a_x, 3a_y)/4$ and $\boldsymbol{r} = (3a_x, a_y)/4$, containing the same flux, so that they do not compensate each other, giving the synthetic magnetic flux $\pm 2\pi$ in each unit cell. Note that usually the optical lattices are sufficiently deep, and the $\pm 2\pi$ flux per elementary is topologically trivial. In that case the tight binding model can be applied, with the tunneling taking place only between the nearest-neighboring sites of the square plaquette. The $\pm 2\pi$ flux over the square plaquette can then be eliminated by a gauge transformation. Yet if the lattice is shallow enough, the tight binding model is not applicable and the above arguments do not work. In the present situation, the most interesting topological lattice appears for a flat adiabatic trapping potential shown by a solid red curve in figure 3. In such a situation there are no well defined lattice sites, and the $\pm 2\pi$ flux per elementary cell results in topologically non-trivial bands explored in the next subsection.

For a weak coupling (such as $v = 0.05$) the geometric flux density $\boldsymbol{B}(\boldsymbol{r}) \equiv \boldsymbol{B}_{\pm}(\boldsymbol{r})$ is concentrated around the intersection points of the gradient slopes shown in in figure 3 and has a very weak y dependence. With increasing the coupling v, the flux extends beyond the intersection areas and acquires a y dependence. Figure 4 shows the geometric flux density $\boldsymbol{B}(\boldsymbol{r}) \equiv \boldsymbol{B}_{+}(\boldsymbol{r})$ for the strong coupling ($v_0 = 0.25$) corresponding to the most flat adiabatic bands. In this regime the flux develops stripes in the x direction and has a strong y dependence. For the whole range of coupling strengths $0 \leqslant v_0 \leqslant 1/2$ the total synthetic magnetic flux per unit cell is 2π and is independent of the Floquet frequency ω and the gradient β.

Now let us discuss the effect of an extra spin-independent trapping potential. The present scheme requires a large spin-dependent energy gradient which would have a huge influence on the relative trapping for the two spin states without the Raman coupling or for a weak Raman coupling. In that case one would expect that the stable positions for any trapped sample of the two spin states would live at entirely distinct locations, possibly with no overlap. Yet we are interested mostly in a sufficiently strong Raman coupling where the two spin states get mixed, and the atomic motion takes place in almost flat adiabatic potentials shown in red in figure 3. Therefore the atoms are no longer affected by the steep spin-dependent potential slopes, and the spin-independent trapping potential would not cause separation of different spin states. Instead, the extra spin-independent parabolic trapping potential would simply make the flat adiabatic trapping potentials parabolic. Of course, one needs to be all the time in the regime where the Raman coupling is strong compared to the characteristic energy of the spin-dependent potential slope. That is why we propose to introduce the spin-dependent potential gradient only at the final stage of the adiabatic protocol discussed in section 3.5.

3.4. Band structure and Chern numbers

We analyze the topological properties of this Floquet flux lattice by explicitly numerically computing the band structure and associated Chern number using the effective Hamiltonian (24) without making the adiabatic approximation introduced in section 3.3. Again the gradient of the original magnetic field is such that we approximately get a square lattice, $\beta = 0.6$. Furthermore, we choose the Floquet frequency to be ten times larger

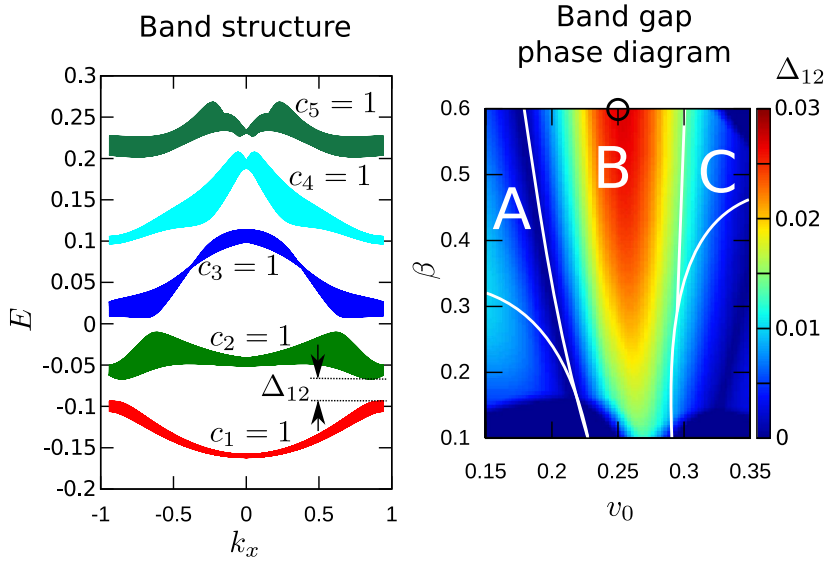

Figure 5. Left: band structure calculated using the effective Hamiltonian (24) for $v_0 = 0.25$, $\beta = 0.6$ and $E_r = 0.1$. Right: the band gap Δ_{12} between the first and second bands for $E_r = 0.1$ and various values of v_0 and β. The letters A, B and C indicate the regions where the Chern numbers of the first three bands correspond to the right, middle and left parts of the figure 6.

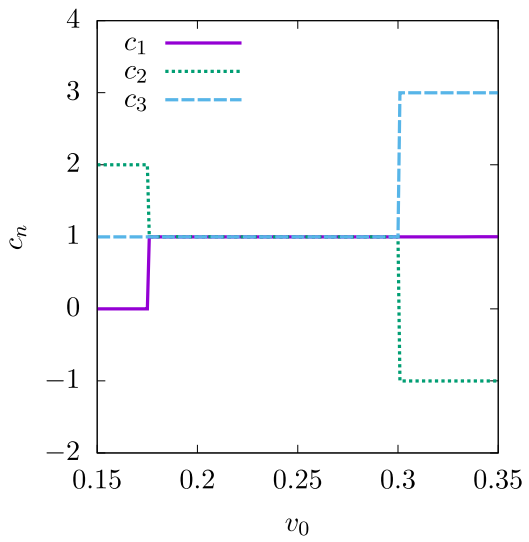

Figure 6. Dependence of Chern number for the bands calculated using the effective Hamiltonian (24) on the coupling strength v_0 for $\beta = 0.6$ and $E_r = 0.1$. Here we present the Chern numbers c_1, c_2 and c_3 of the three lowest bands.

than the recoil energy, $E_r = 0.1$. Note that one can alter the length of the plaquette along the x direction (and thus the flux density) by changing β representing the potential gradient along the x axis.

First, let us consider the case where $v_0 = 0.25$ corresponding to the most flat adiabatic potential. In this situation the Chern numbers of the first five bands appear to be equal to the unity, as one can see in the left part of figure 5. Thus the Hall current should monotonically increase when filling these bands. This resembles the QHE involving the Landau levels. Second, we check what happens when we leave the regime $v_0 = 0.25$ where the adiabatic potential is flat, and consider lower and higher values of the coupling strength v_0. Near $v_0 = 0.175$ we find a topological phase transition where the lowest two energy bands touch and their Chern numbers change to $c_1 = 0$ and $c_2 = 2$, while the Chern numbers of the higher bands remain unchanged, illustrated in figure 6. In a vicinity of $v_0 = 0.3$ there is another phase transition, where the second and third bands touch, leading to a new distribution of Chern numbers: $c_1 = 1, c_2 = -1, c_3 = 3, c_4 = 1$. Interestingly the Chern numbers of the second and the third bands jump by two units during such a transition.

Finally, we explore the robustness of the topological bands. The right part of figure 5 shows the dependence of the band gap Δ_{12} between the first and second bands on the coupling strength v_0 and the potential gradient β.

One can see that the band gap is maximum for $\nu_0 = 0.25$ when the adiabatic potential is the most flat. The gap increases by increasing the gradient β, simultaneously extending the range of the ν_0 values where the band gap is nonzero. Therefore to observe the topological bands, one needs to take a proper value of the Raman coupling $\nu_0 \approx 0.25$ and a sufficiently large gradient β, such as $\beta = 0.6$.

We now make some numerical estimates to confirm that this scheme is reasonable. We consider an ensemble of ^{87}Rb atoms, with $|\uparrow\rangle = |f = 2,\ m_F = 2\rangle$ and $|\downarrow\rangle = |f = 1,\ m_F = 1\rangle$; the relative magnetic moment of these hyperfine states is $\approx$2.1 MHz G^{-1}, where 1 G $= 10^{-4}$ T. For a reasonable magnetic field gradient of 300 G/cm, this leads to the $\Delta'/\hbar \approx 2\pi \times 600$ MHz cm$^{-1} = 2\pi \times 60$ kHz μm^{-1} detuning gradient. For ^{87}Rb with $\lambda = 790$ nm laser fields the recoil frequency is $\omega_r/2\pi = 3.5$ kHz. Along with the driving frequency $\omega = 10\omega_r$, this provides the dimensionless energy gradient $\beta = \Delta'/(\hbar\omega k_0) \approx 1.3$, allowing easy access to the topological bands displayed in figure 5.

3.5. Loading into dressed states

Adiabatic loading into this lattice can be achieved by extending the techniques already applied to loading into Raman dressed states [29]. The loading technique begins with a Bose–Einstein condensate (BEC) in the lower energy $|\downarrow\rangle$ state in a uniform magnetic field B_0. Subsequently one slowly ramps on a single off resonance RF coupling field and the adiabatically ramp the RF field to resonance (at frequency $\delta\omega$). This RF dressed state can be transformed into a resonant Raman dressed by ramping on the Raman lasers (with only the $\omega_0 + \delta\omega$ frequency on the k^- laser beam) while ramping off the RF field. The loading procedure then continues by slowly ramping on the remaining frequency components on the k^- beam, and finally by ramping on the magnetic field gradient (essentially according in the lattice sites from infinity). This procedure leaves the BEC in the $q = 0$ crystal momentum state in a single Floquet band.

4. Conclusions

Initial proposals [30–32] and experiments [26] with geometric gauge potentials were limited by the small spatial regions over which these existed. Here we described a proposal that overcomes these limitations using laser coupling reminiscent of a frequency comb: temporally pulsed Raman coupling. Typically, techniques relying on temporal modulation of Hamiltonian parameters to engineer lattice parameters suffer from micro-motion driven heating. Because our method is applied to atoms initially in free space, with no optical lattice present, there are no *a priori* resonant conditions that would otherwise constrains the modulation frequency to avoid transitions between original Bloch bands [25].

Still, no technique is without its limitations, and this proposal does not resolve the second standing problem of Raman coupling techniques: spontaneous emission process from the Raman lasers. Our new scheme extends the spatial zone where gauge fields are present by adding sidebands to Raman lasers, ultimately leading to a $\propto\sqrt{N}$ increase in the required laser power (where N is the number of frequency tones), and therefore the spontaneous emission rate. As a practical consequence it is likely that this technique would not be able reach the low entropies required for many-body topological matter in alkali systems [13], but straightforward implementations with single-lasers on alkaline-earth clock transitions [33, 34] are expected to be practical.

Acknowledgments

We thank Immanuel Bloch, Egidijus Anisimovas and Julius Ruseckas for helpful discussions. This research was supported by the Lithuanian Research Council (Grant No. MIP-086/2015). IBS was partially supported by the ARO's Atomtronics MURI, by AFOSR's Quantum Matter MURI, NIST, and the NSF through the PCF at the JQI.

Appendix. Stroboscopic evolution operator

The stroboscopic evolution operator (8) reads explicitly

$$U(2\pi, 0) = U_0 U_{\rm kick}^{(1)} U_0 U_{\rm kick}^{(0)} = \mathrm{e}^{-\mathrm{i}\pi\left[E_{\rm r}\boldsymbol{k}^2 + \frac{1}{2}\sigma_3\beta x\right]}\mathrm{e}^{-\mathrm{i}\nu_1(y)}\mathrm{e}^{-\mathrm{i}\pi\left[E_{\rm r}\boldsymbol{k}^2 + \frac{1}{2}\sigma_3\beta x\right]}\mathrm{e}^{-\mathrm{i}\nu_0(y)}. \tag{32}$$

In the main we have approximated the evolution operator by equation (11). To estimate the validity of the latter equation, let us make use of the Baker–Campbell–Hausdorff formula

$$e^X e^Y = e^Z \quad \text{with} \quad Z = X + Y + \frac{1}{2}[X, Y] + \ldots \tag{33}$$

and consider this expansion up to the leading term $\frac{1}{2}[X,\ Y]$, essentially the second term in the Magnus expansion.

Neglecting the commutation between $E_{\rm r}\boldsymbol{k}^2$ and $\sigma_3\beta x$, one can write

$$U_0 = {\rm e}^{-{\rm i}\pi\left[E_{\rm r}\boldsymbol{k}^2+\frac{1}{2}\sigma_3\beta x\right]} \approx {\rm e}^{-{\rm i}\pi E_{\rm r}\boldsymbol{k}^2}{\rm e}^{-{\rm i}\frac{\pi}{2}\sigma_3\beta x}. \tag{34}$$

The error in doing so is approximately $-{\rm i}\frac{\pi}{4}E_{\rm r}\beta\sigma_3[x,\ \boldsymbol{k}^2] = \frac{\pi}{2}E_{\rm r}\beta k_x\sigma_3$. Since $E_{\rm r}\beta \ll 1$, this provides a small momentum shift along the x direction. Furthermore, we shall neglect the commutation between $E_{\rm r}\boldsymbol{k}^2$ and $v_l(y)$. The error in doing so is approximately $-{\rm i}\frac{\pi}{2}E_{\rm r}\sigma_{x,y}[y,\ \boldsymbol{k}^2] = \pi E_{\rm r}k_y\sigma_3$. Since the Floquet frequency ω greatly exceeds the recoil frequency $E_{\rm r} \ll 1$ and $\beta < 1$, this also provides a small momentum shift along the y direction. With these assumptions, one has

$$U(2\pi,\ 0) = U_0U^{(1)}_{\rm kick}U_0U^{(0)}_{\rm kick} \approx {\rm e}^{-{\rm i}2\pi E_{\rm r}\boldsymbol{k}^2}{\rm e}^{-{\rm i}2\pi v_{\rm eff}},$$

where

$${\rm e}^{-{\rm i}2\pi v_{\rm eff}} = {\rm e}^{-{\rm i}\pi\sigma_3\beta x/2}{\rm e}^{-{\rm i}v_1(y)}{\rm e}^{-{\rm i}\pi\sigma_3\beta x/2}{\rm e}^{-{\rm i}v_0(y)}.$$

Finally under the above assumptions one can merge the exponents in $U(2\pi,\ 0)$, giving equation (11).

References

[1] Bloch I, Dalibard J and Zwerger W 2008 Many-body physics with ultracold gases *Rev. Mod. Phys.* **80** 885–964
[2] Greiner M, Mandel O, Esslinger T, Hänsch T W and Bloch I 2002 Quantum phase transition from a superfluid to a mott insulator in a gas of ultracold atoms *Nature* **415** 39–44
[3] Lewenstein M, Sanpera A and Ahufinger V 2012 *Ultracold Atoms in Optical Lattices: Simulating Quantum Many-Body Systems* (Oxford: Oxford University Press)
[4] Lewenstein M, Sanpera A, Ahufinger V, Damski B, Sen (De) A and Sen U 2007 Ultracold atomic gases in optical lattices: mimicking condensed matter physics and beyond *Adv. Phys.* **56** 243–379
[5] Abo-Shaeer J R, Raman C, Vogels J M and Ketterle W 2001 Observation of vortex lattices in Bose–Einstein condensates *Science* **292** 476–9
[6] Cooper N R 2008 Rapidly rotating atomic gases *Adv. Phys.* **57** 539–616
[7] Fetter A L 2009 Rotating trapped Bose–Einstein condensates *Rev. Mod. Phys.* **81** 647
[8] Gemelke N, Sarajlic E and Chu S 2010 Rotating few-body atomic systems in the fractional quantum Hall regime arXiv:1007.2677
[9] Madison K W, Chevy F, Bretin V and Dalibard J 2001 Stationary states of a rotating Bose–Einstein condensate: routes to vortex nucleation *Phys. Rev. Lett.* **86** 4443–6
[10] Matthews M R, Anderson B P, Haljan P C, Hall D S, Wieman C E and Cornell E A 1999 Vortices in a Bose–Einstein condensate *Phys. Rev. Lett.* **83** 2498–501
[11] Wright K C, Blakestad R B, Lobb C J, Phillips W D and Campbell G K 2012 Driving phase slips in a superfluid atom circuit with a rotating weak link *Phys. Rev. Lett.* **110** 025302
[12] Dalibard J, Gerbier F, Juzeliūnas G and Öhberg P 2011 Colloquium: artificial gauge potentials for neutral atoms *Rev. Mod. Phys.* **83** 1523–43
[13] Goldman N, Juzeliūnas G, Öhberg P and Spielman I B 2014 Light-induced gauge fields for ultracold atoms *Rep. Prog. Phys.* **77** 126401
[14] Eckardt A 2017 Colloquium: atomic quantum gases in periodically driven optical lattices *Rev. Mod. Phys.* **89** 011004
[15] Jotzu G, Messer M, Desbuquois R, Lebrat M, Uehlinger T, Greif D and Esslinger T 2014 Experimental realisation of the topological Haldane model with ultracold fermions *Nature* **515** 237–40
[16] Struck J, Ölschläger C, Weinberg M, Hauke P, Simonet J, Eckardt A, Lewenstein M, Sengstock K and Windpassinger P 2012 Tunable gauge potential for neutral and spinless particles in driven optical lattices *Phys. Rev. Lett.* **108** 225304
[17] Windpassinger P and Sengstock K 2013 Engineering novel optical lattices *Rep. Prog. Phys.* **76** 086401
[18] Aidelsburger M, Atala M, Lohse M, Barreiro J T, Paredes B and Bloch I 2013 Realization of the Hofstadter Hamiltonian with ultracold atoms in optical lattices *Phys. Rev. Lett.* **111** 185301
[19] Cooper N 2011 Optical flux lattices for ultracold atomic gases *Phys. Rev. Lett.* **106** 175301
[20] Goldman N, Budich J C and Zoller P 2016 Topological quantum matter with ultracold gases in optical lattices *Nat. Phys.* **12** 639–45
[21] Jaksch D and Zoller P 2003 Creation of effective magnetic fields in optical lattices: the Hofstadter butterfly for cold neutral atoms *New J. Phys.* **5** 56
[22] Javanainen J and Ruostekoski J 2003 Optical detection of fractional particle number in an atomic Fermi–Dirac gas *Phys. Rev. Lett.* **91** 150404
[23] Miyake H, Siviloglou G A, Kennedy C J, Burton W C and Ketterle W 2013 Realizing the Harper Hamiltonian with laser-assisted tunneling in optical lattices *Phys. Rev. Lett.* **111** 185302
[24] Osterloh K, Baig M, Santos L, Zoller P and Lewenstein M 2005 Cold atoms in non-Abelian gauge potentials: from the Hofstadter 'moth' to lattice gauge theory *Phys. Rev. Lett.* **95** 010403
[25] Weinberg M, Ölschläger C, Sträter C, Prelle S, Eckardt A, Sengstock K and Simonet J 2016 Multiphoton interband excitations of quantum gases in driven optical lattices *Phys. Rev.* A **92** 043621
[26] Lin Y J, Compton R L, Jimenez-Garcia K, Porto J V and Spielman I B 2009 Synthetic magnetic fields for ultracold neutral atoms *Nature* **462** 628–32
[27] Yi W, Daley A J, Pupillo G and Zoller P 2008 State-dependent, addressable subwavelength lattices with cold atoms *New J. Phys.* **10** 073015
[28] Juzeliūnas G and Spielman I B 2012 Flux lattices reformulated *New J. Phys.* **14** 123022
[29] Lin Y-J, Compton R L, Perry A R, Phillips W D, Porto J V and Spielman I B 2009 Bose–Einstein condensate in a uniform light-induced vector potential *Phys. Rev. Lett.* **102** 130401
[30] Günter K J, Cheneau M, Yefsah T, Rath S P and Dalibard J 2009 Practical scheme for a light-induced gauge field in an atomic Bose gas *Phys. Rev.* A **79** 011604

[31] Juzeliūnas G, Ruseckas J, Öhberg P and Fleischhauer M 2006 Light-induced effective magnetic fields for ultracold atoms in planar geometries *Phys. Rev.* A **73** 025602
[32] Spielman I B 2009 Raman processes and effective gauge potentials *Phys. Rev.* A **79** 063613
[33] Kolkowitz S, Bromley S L, Bothwell T, Wall M L, Marti G E, Koller A P, Zhang X, Rey A M and Ye J 2017 Spin–orbit-coupled fermions in an optical lattice clock *Nature* **542** 66
[34] Livi L F *et al* 2016 Synthetic dimensions and spin–orbit coupling with an optical clock transition *Phys. Rev. Lett.* **117** 220401

FOR NOTES

FOR NOTES

Vilnius University Press
Universiteto st. 1, LT-01513 Vilnius
E-mail: info@leidykla.vu.lt
www.leidykla.vu.lt
Print run: 10